

©2014
Jesse Kohl
ALL RIGHTS RESERVED

ENHANCING SURFACE PLASMON PROPAGATION AND LEAKAGE IN
PLANAR THIN FILM AND TUBULAR METALLIC NANOSTRUCTURES
FOR VISIBLE-LIGHT-BASED ORGANIC OPTOELECTRONICS

by

JESSE KOHL

A dissertation submitted to the

Graduate School-New Brunswick

Rutgers, The State University of New Jersey

In partial fulfillment of the requirements

For the degree of

Doctor of Philosophy

Graduate Program in Materials Science & Engineering

Written under the direction of

Deirdre M. O'Carroll

And approved by

New Brunswick, New Jersey

OCTOBER, 2014

Abstract of The Dissertation

Enhancing Surface Plasmon Propagation and Leakage in Planar Thin Film and Tubular Metallic Nanostructures for Visible-Light-Based Organic Optoelectronics

by JESSE KOHL

Dissertation Director:

Deirdre M. O'Carroll

Optical fields can be confined and propagated on subwavelength volumes by coupling to surface plasmon polariton (SPP) modes supported by metallic nanostructures. However, SPPs are inherently lossy modes, specifically in the visible regime with losses upwards of 1000 cm^{-1} , resulting in short mode propagation lengths [1,2]. SPPs are also a significant loss channel (up to 46.8% loss) in visible-light-based optoelectronics such as organic light-emitting diodes, significantly reducing light outcoupling efficiency [3-6].

Theoretical calculations in the literature have demonstrated that light-emitting organic semiconducting conjugated polymers can compensate for the intrinsic losses of SPPs [2,7-11]. Engineering plasmon-polymer

interactions may also aid in reducing loss at metal electrodes and increase light outcoupling efficiency in OLEDs [2,7-11]. In this study, a fundamental understanding of efficient SPP/polymer emitter coupling, towards the development of low-loss electrodes for visible-light-based organic optoelectronics through the investigation of two distinct structures: (1) semiconductor-metal-insulator (SMI) waveguides and (2) tubular metallic nanostructures.

Dispersion relations were solved for the SMI waveguides over a range of metal film thickness and emitter dielectric constants. Solutions demonstrate that at visible wavelengths, SPP mode propagation lengths and magnetic field leakage are enhanced to lengths $>1300\text{ }\mu\text{m}$ and $>74\text{ }\mu\text{m}$, respectively, through the optimization of the metal film thickness and by the addition of an organic polymer gain medium. These findings were experimentally validated by collecting pump power dependent emission spectra of SMI waveguides fabricated over a range of metal film thicknesses with controlled emitter dipole orientation.

Large area arrays of gold nanotubes were synthesized with wall thickness (WT) tuned from 30 nm to $>140\text{ nm}$. Their optical response was characterized as a function of wall thickness and excitation condition via polarized bright-field/dark-field microscopy and darkfield scattered light

spectroscopy. Resonant frequency, mode propagation length and mode type were found to be tunable based on tube geometry and excitation condition. Full-field 3-dimensional electromagnetic simulations were carried out to corroborate the experimental results and develop a fundamental understanding of the optical response of these structures for applications as low-loss patterned metal electrodes.

Acknowledgement

I would like to begin my acknowledging my mother and late father, Cathy and Paul Kohl, who were both the first generations in their families to graduate from college and go on to earn higher degrees. They imbued in my sister and me the value of higher education and selflessly to potentiate our passions. Prior to being accepted to the Materials Science and Engineering Program at Rutgers I worked at Corning Incorporated for two Rutgers Ceramic Engineering alums, Dr. Matthew J Dejneka and Dr. Thomas R Chapman. I acknowledge these individuals for sharing their passion for science with me, which catalyzed my interest in earning a PhD in materials science.

Upon entering Rutgers, the first group of individuals I interacted was the department staff including Claudia Kuchinow, Phyllis Cassell, John Yaniero, Nancy Pamula, and Janet Pesinski. They are an exemplary group who has all made my experience within the department a very positive one. My academic experience at Rutgers has been shaped by numerous professors in the department whom I have taken classes from and collaborated with. These individuals include Prof. George Sigel, Prof. Stephan H. Garofolini, Prof. Richard Lehman, Prof. M. John Matthewson, Prof. Victor A. Greenhut, and Prof. Armen Khachaturyan. I would like to acknowledge the Materials Science and Engineering Graduate Director, Prof. Lisa C. Klein, for her dedication to the graduate students and open door policy. She has been a great advocate who has helped me greatly throughout the course of my studies. One individual who has greatly influenced me during my experience at Rutgers is Professor Mei Chee Tan. Prof. Tan is not only a remarkable scientist but an equally skilled and dedicated educator, who mentored me and numerous other students during her time at Rutgers.

I would like to acknowledge my research collaborators, Micha Fireman, Joseph A Pantina, Ryan Belfar, Emily Esposito, and Joshua Vichare, as well as my research group

members Christopher Petoukhof, Binxing Yu, Catrice Carter, Zeqing Shen, Benjamin Agyei, Tuffour, Gary Cheung, and Sarah Goodman. An important part of my education at Rutgers was having the opportunity to be an NSF IGERT trainee in the Nanotechnology for Clean Energy IGERT program. This program has not only provided generous funding, but provided opportunities to cross-pollinate with the global scientific community. With this, I gratefully acknowledge Prof. Manish Chowalla and Dr. Johanna Bernstein.

I would like to also acknowledge my thesis committee members Prof. Frederic Cosandey, Prof. James Harrington, and Prof. Piotr Piotrowiak for their time and willingness to serve on my committee. I also owe a great debt of gratitude to my adviser Prof. Deirdre M. O'Carroll. She is a consummate scientist, a gifted teacher, and has made my experience at Rutgers remarkably positive and productive. Working under her expert tutelage has grown my scientific knowledge beyond my expectations and has grown my passion for science.

Chapters 2 and 4 of this dissertation were based upon two first author publications written by the author of this dissertation, J. Kohl [130,171]. Chapter 2 is based upon the publication titled “Enhancing surface plasmon leakage at the metal/semiconductor interface: towards increased light outcoupling efficiency in organic optoelectronics,” in which a set of dispersion relations were solved for a semiconductor-metal-insulator plasmonic waveguide [130]. In this work, J. Kohl was responsible for solving the dispersion relations, interpreting the solutions, and writing the manuscript [130]. Chapter 4 was based upon the publication titled “Surface plasmon and photonic mode propagation in gold nanotubes with varying wall thickness,” in which a comprehensive experimental and theoretical study of gold nanotubes was presented [171]. J. Kohl was responsible for interpretation of the experimental results, the design and execution of the theoretical study, and the writing of the manuscript [171].

Table of Contents

Abstract of The Dissertation	ii
Acknowledgement	v
List of Table Captions	xi
List of Figure Captions.....	xiii
Chapter Figures	xiii
Appendix Figures.....	xxvi
List of Acronyms.....	xxxv
1 Background and Scope of Investigation.....	1
1.1 Introduction	1
1.2 Background	7
1.2.1 The Diffraction Limit and Evanescent Waves	7
1.2.2 Electromagnetic Waves and Surface Plasmons	10
1.2.3 Dielectric Functions of Metals	12
1.2.4 Surface Plasmons at a Single Metal Interface.....	15
1.2.5 SPP Propagation in Insulator-Metal-Insulator (IMI) Waveguides	17
1.2.6 Organic Semiconducting Conjugated Polymers.....	18
1.2.7 Excitation of Surface Plasmons	19
1.3 Thesis Overview and Objectives	22
2 Dispersion Relation Calculations of Planar Asymmetric Insulator-Metal-Insulator and Semiconductor-Metal-Insulator Waveguides towards Increased Light Outcoupling Efficiency in Organic Optoelectronics	28
2.1 Abstract.....	28
2.2 Introduction	29
2.3 Methods.....	32
2.3.1 Reproduction of Burton and Cassidy Dispersion Relation Solutions	32
2.3.2 Solving Dispersion Relation of Planar Asymmetric F8BT-Ag-SiO ₂ SMI Waveguides	34
2.4 Results and Discussion	37
2.5 Conclusion.....	49
3 Experimental Fabrication and Characterization of Semiconductor-Metal-Insulator Waveguides of Varying Metal Film Thicknesses	51
3.1 Abstract.....	51

3.2	Introduction	52
3.3	Methods.....	55
3.3.1	Waveguide Glass Substrate and Cover Preparation	55
3.3.2	Thermal Evaporation of Ag Films	56
3.3.3	Polymer Film Deposition	57
3.3.4	Assembly of ISI and ISMI Waveguides	58
3.3.5	Grinding and polishing ISMI Waveguides	59
3.3.6	Apparatus Used to Collect Pump Power Dependent Emission Spectra	59
3.3.7	Measurement of Incident Excitation Power Density and Energy per Pulse	62
3.3.8	Procedure for Collecting Pump Power Dependent Emission Spectra	63
3.3.9	Procedure for Collecting Polarized Pump Power Dependent Emission Spectra ...	66
3.3.10	Method of Emission Spectra Analysis	67
3.3.11	Absorption Spectra of ISMI Waveguides	67
3.3.12	Finite Difference Time Domain Simulations of SMI Waveguides	68
3.3.13	Experimental Methods to Vary and Control PFO Molecular Dipole Orientation ..	70
3.3.14	Optical Characterization of PFO Molecular Chain Orientation	72
3.3.15	Synchrotron Characterization of PFO Molecular Chain Orientation	73
3.4	Results and Discussion	77
3.4.1	Pump Power Dependent Emission Spectra of Neat PFO ISI and ISMI Waveguides 77	
3.4.2	Absorption Spectroscopy and FDTD Simulations of PFO SMI Waveguide	88
3.4.3	Comparison of Pump Power Dependent Emission Spectra of ISMI Waveguides with Varying Ag Metal Film Thickness to Theoretical Dispersion Relations	94
3.4.4	Characterization of Polymer Molecular Dipole Orientation	100
3.4.5	Background on GIWAXS/GISAXS	101
3.4.6	Characterization of PFO Molecular Dipole Orientation as a Function of Processing Conditions	105
3.4.7	Discussion of Molecular Dipole Orientation in PFO Films	117
3.5	Conclusions	118
4	Surface plasmon and photonic mode propagation in gold nanotubes with varying wall thickness	120
4.1	Abstract.....	120
4.2	Introduction	121

4.3	Methods.....	123
4.3.1	Electrodeposition Conditions.....	123
4.3.2	Sample Preparation	125
4.3.3	Scattered-Light Spectroscopy of Gold Nanotubes.....	125
4.3.4	Electromagnetic Simulations	126
4.4	Results and Discussion	127
4.5	Conclusions	143
5	Theoretical and Experimental Study of Surface Plasmon Resonance as a Function of Incident Polarization for Single Gold Nanowire/Nanotube Heterostructures	147
5.1	Abstract.....	147
5.2	Introduction	148
5.3	Methods.....	150
5.3.1	Sample Preparation	150
5.3.2	SEM Analysis of Single AuNW/NT Heterostructure and Image Analysis	151
5.3.3	Polarized Bright-field/Dark-field Imaging of Single Gold Nanotubes	151
5.3.4	Polarized Bright-field/Dark-field Image RGB and Grayscale Intensity Analysis...	159
5.3.5	Polarized Dark-field Scattered Light Single Nanostructure Spectroscopy of Single NW/NT Heterostructures.....	161
5.3.6	FDTD Simulations of Single Gold NW and NTs of Representative Geometries of the “tube 1” NW/NT heterostructure.....	165
5.4	Results and Discussion	166
5.4.1	FESEM Analysis of a Single Gold NW/NT Heterostructure	167
5.4.2	Polarized True Color Bright-field and Dark-field Images and Analysis of Single NW/NT Heterostructures.....	169
5.4.3	Polarized Dark-field Scattered-Light Single Nanostructure Spectroscopy of Single Gold NW/NT Heterostructures	175
5.4.4	Computational and Theoretical Analysis of the Plasmonic Response of Single Gold NW/NT Heterostructures as a Function of Incident Polarization	178
5.5	Conclusion.....	187
6	Summary and Future Work.....	189
6.1	Preface	189
6.2	Planar Thin-Film Semiconductor-Metal-Insulator Waveguides.....	189
6.3	Tubular metallic Nanostructures	195

Appendix A.....	201
A1. Mathematica Code used to reproduce N_{eff} and L for Burton and Cassidy Asymmetric Silica-Gold-Silica IMI Waveguide	201
A2. Mathematica Code used to Solve Dispersion Relations for a F8BT/Ag/SiO ₂	205
Appendix B.....	209
Appendix C.....	215
Appendix D.....	230
Appendix E	238
Appendix F	245
F1. Polarized True Color Bright-field and Dark-field Images and Analysis of Single NW/NT Heterostructures Collected during Method Optimization	245
F2. Polarized Dark-field Scattered-Light Single Nanostructure Spectroscopy of Single Gold NW/NT Heterostructures Collected during Method Optimization	253
Bibliography	263

List of Table Captions

Table 3.1 Schematic overview of the optical bench setup designed for gain and loss coefficient measurements via the variable stripe length (VSL) and shifting excitation spot (SES) methods. Inset images show the aperture configurations for VSL and SES measurements.

Table 3.2 Heat treatment temperature, time, and cooling methods for 100 nm neat PFO films on bare VWR glass substrates, VWR glass substrates coated with 100 nm Ag metal, and bare 1 mm thick microscope slide glass.

Table. 3.2 Heat treatment temperature, time, and cooling methods for 100 nm neat PFO films on bare VWR glass substrates, VWR glass substrates coated with 100 nm Ag metal, and bare 1 mm thick microscope slide glass.

Table 4.1 Summary of the theoretical and experimentally observed trends surface plasmon mode type and peak resonance as a function of wall thickness and inner diameter under the three different excitation conditions: end on (i), normal excitation with polarization parallel (0°) (ii), and perpendicular (90°) (iii), with respect to the long axis of the structure).

Table AA1 ϵ values for the substrate (SiO_2) and cover (F8BT) media for the three dispersion relation conditions. Table AA2. Boundary conditions (A and B) for the real part of the complex surface plasmon polariton wavevector, k^r , at specific metal film thickness ranges (t_{start} to t_{end}) for the four mode solutions (SB, SL, AB, and AL) for the three dispersion relation conditions (PRSS,

CSS, and CG). Metal film thicknesses are entered into Lines 10 and 11 and boundary conditions (A and B) are entered into Line 12 of the code.

Figure AF1. True color bright-field and dark-field images of gold NW/NT heterostructure “tube 1” under in-phase excitation and collection polarization varied in 10° increments from 90° WRT to the long axis of the heterostructure (Condition 1) to 0° WRT to the long axis of the heterostructure. Inset in all images are schematics of the excitation direction and incident polarization, where \vec{k} denotes the excitation propagation direction and \vec{E} denotes polarization of the electric field. All scale bars = $200\ \mu\text{m}$.

List of Figure Captions

Chapter Figures

Fig. 1.1 Schematic plot of processing speed (Hz) versus device length scale or size (nm) for conventional photonic, electronic, and hybrid optoelectronic technologies [19,20]. Color available in electronic copy.

Figure 1.2. The numerical aperture (NA) of a lens (shown in blue) with respect to an image or focal point, P , depends on the half-angle, θ , of the maximum cone of light that can enter or exit the lens. D is the diameter of the lens.

Figure 1.3. (a) Schematic of the magnetic field (H_y) of an SPP mode propagating along a metal–dielectric interface in the z -direction (where red lines indicate the Electric field and the + and – symbols represent changes in the magnetic field charge distribution). (b) A cross-sectional schematic of the perpendicular electric field, E_y , of an SPP mode, which decays in the x - z . Parts (a) and (b) of this figure were adapted from [49]. Color available in electronic copy.

Figure 1.4. Plot of ϵ' versus wavelength for silver ($\omega = 2.18 \cdot 10^{15} s^{-1}, \gamma = 4.353 \cdot 10^{12} s^{-1}$) and gold ($\omega = 2.183 \cdot 10^{15} s^{-1}, \gamma = 6.46 \cdot 10^{12} s^{-1}$) of both the Drude model and the empirical constants of Palik [77]. The plasma frequency and damping constants used to calculate the optical constants for the Drude model were taken from [80]. Color available in electronic copy.

Figure 1.5. Plot of ϵ'' versus wavelength for silver ($\omega = 2.18 \cdot 10^{15} s^{-1}, \gamma = 4.353 \cdot 10^{12} s^{-1}$) and gold ($\omega = 2.183 \cdot 10^{15} s^{-1}, \gamma = 6.46 \cdot 10^{12} s^{-1}$) of both the Drude model and the empirical

constants of Palik [77]. The plasma frequency and damping constants used to calculate the optical constants using the Drude model were taken from [80]. Color available in electronic copy.

Figure 2.1. Illustrations of (a) a generic OLED exhibiting a tightly-bound SPP mode at the metal electrode propagating in the z -direction, and (b) the F8BT-Ag-SiO₂ SMI waveguide studied in this work . (c-f) Schematic representations of $|H_y|$ versus x cross-sections for: (c) SB, (d) SL, (e) AB, and (f) and AL for an antisymmetric IMI waveguide (where $0 < \left(\left| \epsilon_{\text{cover}} - \epsilon_{\text{substrate}} \right| / \epsilon_{\text{substrate}} \right) \times 100 < 1\%$). Blue dotted line in (e, f) represents H_y versus x cross-sections of the AB and AL modes, respectively. Color available in electronic copy.

Figure 2.2. Independently reproduced plot of the effective mode index versus metal film thicknesses for the four SPP mode symmetries supported by the slightly asymmetric silica-gold-silica IMI waveguide presented in the Burton and Cassidy work [82]. Color available in electronic copy.

Figure 2.3. Independently reproduced plot of propagation length L versus metal film thicknesses for the slightly symmetric IMI silica-gold-silica waveguide presented in the Burton and Cassidy work [82]. Color available in electronic copy.

Figure 2.4. (a-c) N_{eff} and (d-f) $\text{Log}_{10}(L)$ versus t calculated for (a, d) the PRSS case, (b, e) the CSS case and (c, f) the CG case for all four SPP modes supported by the F8BT-Ag-SiO₂ SMI waveguide.

Figure 2.5. D as a function of t , in F8BT (a,c,e,g) and SiO₂ (b,d,f,h) for: (a,b) SB; (c,d) SL; (e,f) AB; (g,h) AL for three SMI waveguide dielectric constant cases.

Figure 2.6. (a) H_y and (b-g) $|H_y|$ calculated at $t = 47$ nm (a,b,d,f) and $t = 80$ nm (c,e,g) for the SB (a-c), SL (d,e), AB (f,g) and AL (h,i) modes for all three SMI waveguide dielectric constant cases. Schematic illustrations of the F8BT-Ag-SiO₂ SMI waveguide inset in (b,c) represent the $|H_y|$ of the highly radiative ‘leaky’ SB mode at $t = 47$ nm and the tightly-bound SB mode $t = 80$ nm, respectively. AL mode not included. Color available in electronic copy.

Figure. 3.1 Schematic overview of the optical bench setup designed for gain and loss coefficient measurements via the variable stripe length (VSL) and shifting excitation spot (SES) methods, which instead was used to collect pump power emission spectra. Inset image shows cylindrical lens, aperture to control slit width, and sample holder. Color available in electronic copy.

Figure 3.2. Schematic representation of polarization gain measurements taken of SMI waveguides with outcoupled edge emission polarized parallel to the plane of the waveguide (0°) (a) and polarized perpendicular to the plane of the waveguide (90°) (b).

Figure 3.3. Schematic of Full-field electromagnetic simulations of SMI waveguide analogs under 355 or 460 nm plane wave excitation with 948 nm thick glass superstrate, a 100 nm thick PFO film, an Ag metal film of 35, 50, 65, and 100 nm thickness, and glass substrate of 90, 105, 120, or 155 nm thickness.

Figure 3.4. Measurement of temperature versus time with a handheld thermal probe placed on the hotplate stage used to conduct the thermal treatments of PFO films at 2 temperature settings on the hotplate dial: 200 and 280° C.

Figure 3.5. Schematic of the principal components of the NSLS Beamline X9 from the undulator source (at the right) to the end station hutch (large black box). Abbreviations used: gate valve (GV); double-crystal monochromator (DCM); Kirkpatrick-Baez (KB); horizontal/vertical focusing mirrors (HFM/VFM); ion chamber beam-position monitor (IC BPM); slits (S1, S2, S3); upstream/downstream monitor (usmon/dsmon) [133].

Figure 3.6. (a) Photograph of the X9 Beamline optical components with the double-crystal monochromator (on the right) and the KB horizontal/vertical bimorph adaptive focusing mirrors (on the left). b) The long vacuum-compatible chamber of NSLS Beamline X9 that contains both the SAXS (at the far end) and WAXS detectors (designed by Scott Coburn). c) Position of the WAXS and SAXS detectors relative to the X-ray beam. d) View from the X-ray beam in the direction of the detectors. This view indicates the overlapping region, which can be seen from the SAXS images. [4] Color available in electronic copy.

Figure 3.7. Compilation of glass/PFO/glass ISI waveguide emission spectra at varying pump power densities ranging from 0.06 to 0.86 W/cm². Inset is same spectra re-scaled to visually depict the significant line narrowing with increasing pump power density.

Figure 3.8. Glass/PFO/Glass ISI waveguide (a) emission intensity at the peak emission wavelength (I_{max}) with linear fits below and above the ASE threshold, (b) full-width-half-maximum, (c) and peak emission wavelength (λ_{max}) as a function of excitation power density.

Figure 3.9. Gain spectra of glass/PFO/Ag/glass waveguides with Ag film thicknesses of 35, 45, 50, 55, 65, and 100 nm under excitation power densities of (a) 6.97E-6, (b) 0.06, (c) 0.21, (d) 0.29, (e) 0.41, (f) 0.48, (g) 0.542, (h) 0.69, (i) 0.86 W/cm². Color available in electronic copy.

Figure 3.10. Log plot of I_{max} as a function of pump power density of glass/PFO/Ag/glass waveguides with Ag film thicknesses of 0, 35, 45, 50, 55, 65, and 100 nm.

Figure 3.11. Fitted plots I_{max} as a function of pump power density from spectra of glass/PFO/Ag/glass ISMI waveguides with Ag film thicknesses (t_m) of (a) 0, (b) 35, (c) 45, (d) 50, (e) 55, (f) 65, and (g) 100 nm.

Figure 3.12. Full-width-half-maximum (FWHM) of the emission spectra of glass/PFO/Ag/Glass Emission waveguides with Ag film thicknesses of 0, 35, 45, 50, 55, 65, and 100 nm as a function of excitation power density.

Figure 3.13. Peak emission wavelength (λ_{max}) of gain spectra of neat PFO insulator-semiconductor-metal-insulator waveguide with Ag film thicknesses of 0, 35, 45, 50, 55, 65, and 100 nm as a function of excitation power density.

Fig. 3.14 Absorption spectra plotted as percent transmittance versus wavelength of glass/PFO/Ag/glass waveguides with Ag film thicknesses of 0 (no Ag film), 35, 65, and 100 nm. Color available in electronic copy.

Fig. 3.15 Simulated 2D electric field profiles of a 355 nm plane wave source incident on PFO-Ag-glass waveguides with Ag metal film thicknesses of 35, 50, 65, and 100 nm. Shown in (a) and (b) are the real and imaginary components of the electric field, respectively, (c) is the absolute intensity and (d) is the absolute intensity squared of the electric field. Color available in electronic copy.

Fig. 3.16 Simulated 2D electric field profiles of a 460 nm plane wave source incident on a PFO/Ag/glass SMI waveguide with Ag metal film thicknesses of 35, 50, 65, and 100 nm. Shown in (a) and (b) are the real and imaginary components of the electric field, respectively, (c) is the absolute intensity and (d) is the absolute intensity squared of the electric field. Color available in electronic copy.

Figure 3.17. Theoretically calculated symmetric bound (SB) mode propagation length (L) (a) and semiconductor layer penetration depth (D) as a function of Ag metal film thickness for a F8BT/Ag/glass semiconductor-metal-insulator waveguide. (d-f) show I_{\max} , ASE threshold, and ASE slope efficiency, respectively of glass/PFO/Ag/glass ISMI waveguides with Ag metal film thicknesses of 35, 45, 50, 55, 65, and 100 nm under an excitation pump power density of 0.76 W/cm^2 .

Figure 3.18. In a grazing incidence experiment the beam travelling in vacuum with refractive index n_0 is incident upon the sample of refractive index n_1 at angle θ_0 may be in general both partially transmitted through the interface and partially reflected. The transmitted beam is propagated at a grazing angle θ_t with respect to the surface and may be reflected from other interfaces in the sample, such as the film/substrate interface illustrated here. In this case, the radiation reflected from the two interfaces interferes, yielding a distinctive pattern characteristic

of the film thickness [136]. k_0 is the wavevector, k_s is the direction of the scattered beam, and q is the change in momentum as a result of the scattering process ($q = k_s - k_0$).

Figure 3.19. a) In a generic scattering apparatus X-rays generated by the source are collimated and often monochromated before striking the sample. The scattered beam may then be analyzed for direction or energy or both before being detected [1]. b) In classical small angle X-ray scattering the incident beam is perpendicular to the sample surface and the entire sample thickness is probed

Figure 3.20 Absorption spectra of 100 nm PFO films on VWR glass in as spin cast (neat) form, vapor annealed, heated to 120°, 180°, 200°, and 280° C. Heat treated samples were quenched on glass or metal plates. Color available in electronic copy.

Figure 3.21. Absorption spectra of 100 nm PFO films on thin VWR glass and thick microscope slide glass substrates heated at 200° C for 1 hour and cooled on a glass plate (a), and heated for 280° C for 30 minutes and quenched on a metal plate. Color available in electronic copy.

Figure 3.22. Line scans of GIWAXS profiles of neat PFO film atop 100 nm Ag on VWR glass at incident angles of 0.07° (a,b) and 0.09° (c,d) in the q_r (a,c) and q_z (c,d) directions.

Figure 3.23. Line scans of GIWAXS profiles of PFO film atop 100 nm Ag on VWR glass heat treated at 120° C and quenched on a metal plate at incident angles of 0.07° (a,b) and 0.09° (c,d) in the q_r (a,c) and q_z (c,d) directions.

Figure 3.24. Line scans of GIWAXS profiles of PFO film atop 100 nm Ag on VWR glass heat treated at 180° C and quenched on a metal plate at incident angles of 0.07° (a,b) and 0.09° (c,d) in the q_r (a,c) and q_z (c,d) directions.

Figure 3.25. Line scans of GIWAXS profiles of PFO film atop 100 nm Ag on VWR glass heat treated at 200° C and quenched on a glass plate at incident angles of 0.07° (a,b) and 0.09° (c,d) in the q_r (a,c) and q_z (c,d) directions.

Figure 3.26. Line scans of GIWAXS profiles of PFO film atop 100 nm Ag on VWR glass heat treated at 280° C and quenched on a metal plate at incident angles of 0.07° (a,b) and 0.09° (c,d) in the q_r (a,c) and q_z (c,d) directions.

Figure 4.1. (a) Schematic showing the gold nanotube growth process [electrodeposition and pore-widening steps (i), (ii), and (iii) carried out under ultrasonication]. (b)–(d): SEM images of gold nanotubes deposited after AAO pore widening in H₃PO₄ for 60, 30, and 15 minutes, respectively. (e)–(g): Dark-field spectra, using unpolarized, end-on halogen lamp excitation, acquired from the samples imaged in (b)–(d), respectively. Top left corner insets in (e) to (g): True-color dark-field images of the nanotube arrays; scale bars are 25 μ m. Color available in electronic copy.

Figure 4.2. (a) Dark-field spectra using unpolarized, normally incident, halogen lamp excitation, acquired along the length of a single, nanotube/nanowire heterostructure [regions where the spectra were acquired from are indicated in with Roman numerals (d)]. Progressing downward along the structure, a red shift in resonance is evident as it becomes more tube-like. (b) Bright-field and (c) dark-field true-color optical images of the heterostructure. (d) SEM image of the NW/NT region of the structure. Color available in electronic copy.

Figure. 4.3. Electric-field intensity vs wavelength spectra for (a) and (b) the SPP, and (c) and (d) the photonic modes for (a) and (c) end-on excitation, and (b) and (d) transversely polarized normal excitation (spectra fitted with a double Gaussian). Inset in plots (a) and (b) are schematic representations of the end-on and normal excitation schemes, respectively. Green/gray arrows indicate excitation direction (k) and red/dark gray arrows indicate the polarization direction (E). Radial 2-D electric-field intensity profiles of (simulated AuNTs of 30-, 60-, and 140-nm WT under (e) end-on and (f) transversely polarized normal excitation at wavelengths corresponding to the maximum intensity in the corresponding SPP spectra shown in (a) and (b). Scale bars = 150 nm; color bars in (e) and (f) represent electric-field intensity. Color available in electronic copy.

Figure 4.4. Simulated (a) and (b) SPP and (c) and (d) photonic mode decay profiles of single gold nanotubes under end-on excitation with constant 200-nm inner diameter and WT of 30, 60, and 140 nm with an excitation wavelength of (a)–(c) 660 nm and (b)–(d) 770 nm. Axial 2-D electric-field intensity profiles of the tube cross-section under (e) 660 nm and (f) 770 nm end-on excitation (x axis scale bar = 150 nm; color bars represent electric field intensity). Inset in (a) is a schematic of the excitation conditions. Green/gray arrows indicate excitation direction (k) and red/dark gray arrows indicate the polarization direction (E). Color available in electronic copy.

Figure 4.5. FDTD simulated electric-field profiles of the surface plasmon resonances on the surface (a) and in the core (b) of the gold nanotubes with fixed length and wall thickness of 5 μm and 30 nm, respectively, with inner diameters (ID) ranging from 15 nm to 150 nm.

Figure 4.6. Schematic of plasmon hybridization model for tubular metallic nanostructures of thick (a) and thin walls (b), showing the coupling or hybridization between the core mode of a cavity (ω_c) and the surface mode of a wire (ω_w) resulting in two hybridized modes, a lower energy

symmetric mode (ω_-) and a higher energy antisymmetric mode (ω_+) Figure adapted from [150,151,163].

Figure 5.1. Schematics of sample placement and location of the excitation and collection polarizers (a,b), and of the incident polarization on the sample (c,d) in polarization convention 1 (C1) (a,c) where polarization is parallel to the y-axis and convention 2 (C2) (b,d) where polarization is parallel to the x-axis. Samples were oriented parallel (position I) or perpendicular (position II) to the x-direction on the microscope stage. In position I, incident polarization was parallel (0°) and perpendicular (90°) WRT to the long axis of the structure in conditions 2 (C2) and 1 (C1) (a,c), respectively. In position II, incident polarization was parallel (0°) and perpendicular (90°) WRT to the long axis of the structure in conditions 1 (C1) and 2 (C2) (a,c), respectively. Color available in electronic copy.

Figure 5.2. Spectra on blank glass with polarized excitation and collection in C1 (a) and C2 (b) polarization conditions with excitation polarizer (i) in phase with the collection polarizer, (ii) 10° clockwise WRT to the collection polarizer and (iii) 10° counterclockwise WRT to the excitation polarizer. (c) Compilation of spectra in (a) and (b) illustrating the 4X increase in signal throughput of the C2 polarization condition relative to C1. Shown in (d) are spectra on blank glass with polarized collection only in C1 and C2 polarization conditions showing a 6X increase signal throughput of the C2 polarization condition relative to C1. Color available in electronic copy.

Figure 5.3. True color bright-field image of a NW/NT heterostructure “tube 1” with marked regions where RGB and grayscale analysis were conducted: (R1) broken wire region, (R2) undamaged wire region, and (R3) tube region. Color available in electronic copy.

Figure. 5.4. True color bright-field image of nanowire/nanotube heterostructure “tube 1” with 15 x 15 pixel blue boxes indicating the regions where the RGB and grayscale analysis were collected. Color available in electronic copy.

Figure 5.5. Schematic of the bright-field/dark-field microscope integrated with an imaging spectrometer. (1) Out-coupled light from the back of the microscope is reduced in diameter with a reverse Galilean beam expander. (2) The light then travels down a periscope mount to a (3) 45 degree mirror and through a (4) 100 mm focal length achromatic doublet onto the Andor 303is imaging spectrometer. Color available in electronic copy.

Figure 5.6. FESEM micrographs of gold NW/NT heterostructure “tube 1” taken on a flat stage (a-c) and at a tilt angle of 60° (d-f) at (a) 37 kX, (b, e) 100 kX, (c) 200 kX, (d) 50 kX, and (f) 150 kX.

Figure 5.7. True color bright-field (a) and dark-field (b) images of gold NW/NT heterostructure “tube 1” for polarizations ranging from 0° to 90° in 10° increments with both excitation and collection polarizers fixed in the C2 condition and varying polarization by rotating the sample.

Beside each image is a schematic of the excitation direction and polarization, where \vec{k} denotes the excitation propagation direction and \vec{E} denotes polarization of the electric field. All scale bars = 2 μm . Color available in electronic copy.

Figure 5.8. Percentages of red (R), green (G), and blue (B) pixels on a blank region of (a) & (b) shown in Fig. 5.7 (a,b) on the (c,d) nanotube region and (e,f) nanowire region of NW/NT heterostructure “tube 1” under as a function of incident polarization under bright-field (a,c,e) and dark-field (b,d,f) illumination. Color available in electronic copy.

Figure 5.9. Spectrometer CCD images of gold NW/NT heterostructure “tube 1” when parallel (a) and perpendicular (b,c) to the spectrometer input slits with bounded regions schematically depicting the areas from which spectra of the nanowire (a,c) and nanotube (a,b) regions of the heterostructure were collected. Beside each image is a schematic of the excitation direction and polarization, where \vec{k} denotes the excitation propagation direction and \vec{E} denotes polarization of the electric field. Incident polarization with respect to the long axis of the structure is 90° in (a) and 0° in (b,c).

Figure 5.10. Dark-field scattered light spectra of the NT (a) and NW (b) regions of gold NW/NT heterostructure “tube 1” for 0° and 90° polarization with respect to the long axis of the structure (dual excitation and collection polarization in the C2 condition was employed). Color available in electronic copy.

Figure 5.11. Simulated NT resonant spectra extracted from NT core (a,b) and NT surface (c,d) spectra under parallel (0°) (a,c) and perpendicularly (90°) polarized (b,d) under normal incidence broadband plane wave excitation. Inset at left are schematic representations of the normal incidence excitation conditions with 0° and 90° polarization. Color available in electronic copy.

Figure 5.12 Cross-sectional (a-d), and radial (e-h), 2-D electric-field intensity profiles plotted of the NT at the peak resonant wavelengths of the core mode under 0° (a,b,e,f), and 90° (c,d,f,h)

incident polarization, with (b,d,f,h) and without (a,c,e,g) a silicon substrate. The inset in each profile is a schematic of the excitation direction and polarization, where \vec{k} denotes the excitation propagation direction and \vec{E} denotes the polarization of the electric field. All scale bars = 100 nm. Color available in electronic copy.

Figure 5.13 Cross-sectional (a-d), and radial (e-h), 2-D electric-field intensity profiles plotted of the AuNT at the peak resonant wavelengths of the surface mode under 0° (a,b,e,f), and 90° (c,d,f,h) polarization, with (b,d,f,h) and without (a,c,e,g) a silicon substrate. The inset in each profile is a schematic of the excitation direction and polarization, where \vec{k} denotes the excitation propagation direction and \vec{E} denotes polarization of the electric field. All scale bars = 100 nm. Color available in electronic copy.

Figure 5.14. Simulated surface mode spectra of the NW without the presence of a silicon substrate under parallel (0°) and perpendicularly (90°) polarized normal incidence broadband plane wave excitation.

Appendix Figures

Figure AB1. Schematic of the variable stripe length method (VSL). The amplified spontaneous emission is collected from the edge of the sample as a function of excitation stripe length, t . Color available in electronic copy.

Figure AB2. Schematic of the excited stripe on the surface of the planar waveguide. L is the total length of the amplifier, t excitation stripe length projected on the sample surface, dt is the change in excitation stripe length, $\Omega(t)$ is the solid angle defined by the exit facet of the waveguide and the of the excitation stripe edge on the sample surface. $\Omega(t) = \Omega$ when $t = L$.

Figure AB3. Schematic of shifting excitation spot technique (SES). t is the excitation stripe length (which is fixed) and x is distance of the stripe from the edge of the waveguide. Color available in electronic copy.

Figure AC1. Gain spectra of a PFO-only ISI waveguide (a,b) and ISMI waveguides with metal film thicknesses of 35, 50, 65, and 100 nm (c,d) under 355 nm excitation with power densities of 0.64 W/cm^2 (a,c) and 0.835 W/cm^2 (b,d). Color available in electronic copy.

Figure AC2. Peak emission wavelength (a), peak emission intensity (b), and FWHM (c) of PFO-only waveguides (0 nm Ag) and SMI waveguides with Ag film thicknesses of 35, 50, 65, and 100 nm under power densities of 0.64 and 0.835 W/cm^2 . The plot of emission intensity (c) was scaled to show trend in the Ag metal containing SMI waveguides only.

Figure AC3. Gain spectra of a neat PFO-only waveguide with unpolarized emission, emission polarized parallel (0°) and perpendicular (90°) to the plane of the waveguide excited with power densities of 0.64 W/cm^2 (a) and 0.835 W/cm^2 (b). Color available in electronic copy.

Figure AC4. Gain spectra of a neat PFO SMI waveguide Ag film thicknesses of 35, 50, 65, and 100 nm excited with power densities of 0.64 W/cm^2 (a,b) and 0.835 W/cm^2 (c,d) with emission polarized parallel (0°) (a,c) and perpendicular (90°) (b,d) to the plane of the waveguide. Color available in electronic copy.

Figure AC5. Peak emission wavelength (a-c), peak emission intensity (d-f), and FWHM (g-i) of PFO-only waveguides (0 nm Ag) and SMI waveguides with Ag film thicknesses of 35, 50, 65, and 100 nm under power densities of 0.64 and 0.835 W/cm^2 with unpolarized emission (a,d,g), emission polarized parallel (0°) (b,e,h) and perpendicular (90°) (c,f,i) to the plane of the waveguide. Color available in electronic copy.

Figure AC6 (a) Spectrometer CCD image of the outcoupled edge emission from a neat PFO SMI waveguide with 50 nm Ag film thickness focused to a $4500 \mu\text{m}$ diameter spot and (b) corresponding spectrum of outcoupled edge emission. Vertical red lines in (a) denote the $250 \mu\text{m}$ diameter region where spectrum in (b) was collected.

Figure AC7. (a) Images of the outcoupled edge emission from a neat PFO SMI waveguide with 50 nm Ag film thickness. Regions bounded in red are where gain spectra shown in (b) were collected. (c) Analysis of peak emission wavelength, maximum emission intensity and FWHM of spectra in (b). Color available in electronic copy.

Figure AC8. Spectrometer CCD images of the outcoupled edge emission from a neat PFO SMI waveguide with 50 nm Ag film thickness focused to a 4500 μm diameter spot (a) and an 800 μm diameter spot (b) with the spectrometer input aperture slits fully open (a,b) and closed to 250 μm in diameter (c).

Figure AC9. Gain spectra of a PFO-only waveguide (a) and SMI waveguides with metal film thicknesses of 35 (b), 50 (c), 65 (d), and 100 nm (d), under 355 nm excitation with a power density of 0.64 W/cm². Shown in (f) is a compilation plot of spectra shown in (a)-(e).

Figure AC10. Peak emission wavelength (a), peak emission intensity (b), and FWHM (c) of waveguides with Ag film thicknesses of: 0 (PFO only), 35, 50, 65, and 100 nm under a power density of 0.64 W/cm² as a function of metal film thickness.

Figure AD1. Gain spectra of a neat PFO insulator-semiconductor-insulator waveguide (0 nm Ag) under excitation power densities of (a) 6.97E-6, (b) 2.3E-5, (c) 0.043, (d) 0.06, (e) 0.08, (f) 0.15, (g) 0.21, (h) 0.25, (i) 0.29, (j) 0.41, (k) 0.48, (l) 0.54, (m) 0.542, (n) 0.58, (o) 0.69, (p) 0.76, (q) 0.812, and (r) 0.86 W/cm².

Figure AD2. Gain spectra of a 35 nm Ag film thickness neat PFO insulator-semiconductor-metal-insulator waveguide under excitation power densities of (a) 6.97E-6, (b) 2.3E-5, (c) 0.043, (d) 0.06, (e) 0.08, (f) 0.15, (g) 0.21, (h) 0.25, (i) 0.29, (j) 0.41, (k) 0.48, (l) 0.54, (m) 0.542, (n) 0.58, (o) 0.69, (p) 0.76, (q) 0.812, and (r) 0.86 W/cm².

Figure AD3. Gain spectra of a 45 nm Ag film thickness neat PFO insulator-semiconductor-metal-insulator waveguide under excitation power densities of (a) 6.97E-6, (b) 2.3E-5, (c) 0.043, (d)

0.06, (e) 0.08, (f) 0.15, (g) 0.21, (h) 0.25, (i) 0.29, (j) 0.41, (k) 0.48, (l) 0.54, (m) 0.542, (n) 0.58, (o) 0.69, (p) 0.76, (q) 0.812, and (r) 0.86 W/cm².

Figure AD4. Gain spectra of a 50 nm Ag film thickness neat PFO insulator-semiconductor-metal-insulator waveguide under excitation power densities of (a) 6.97E-6, (b) 2.3E-5, (c) 0.043, (d) 0.06, (e) 0.08, (f) 0.15, (g) 0.21, (h) 0.25, (i) 0.29, (j) 0.41, (k) 0.48, (l) 0.54, (m) 0.542, (n) 0.58, (o) 0.69, (p) 0.76, (q) 0.812, and (r) 0.86 W/cm².

Figure AD5. Gain spectra of a 55 nm Ag film thickness neat PFO insulator-semiconductor-metal-insulator waveguide under excitation power densities of (a) 6.97E-6, (b) 2.3E-5, (c) 0.043, (d) 0.06, (e) 0.08, (f) 0.15, (g) 0.21, (h) 0.25, (i) 0.29, (j) 0.41, (k) 0.48, (l) 0.54, (m) 0.542, (n) 0.58, (o) 0.69, (p) 0.76, (q) 0.812, and (r) 0.86 W/cm².

Figure AD6. Gain spectra of a 65 nm Ag film thickness neat PFO insulator-semiconductor-metal-insulator waveguide under excitation power densities of (a) 6.97E-6, (b) 2.3E-5, (c) 0.043, (d) 0.06, (e) 0.08, (f) 0.15, (g) 0.21, (h) 0.25, (i) 0.29, (j) 0.41, (k) 0.48, (l) 0.54, (m) 0.542, (n) 0.58, (o) 0.69, (p) 0.76, (q) 0.812, and (r) 0.86 W/cm².

Figure AD7. Gain spectra of a 100 nm Ag film thickness neat PFO insulator-semiconductor-metal-insulator waveguide under excitation power densities of (a) 6.97E-6, (b) 2.3E-5, (c) 0.043, (d) 0.06, (e) 0.08, (f) 0.15, (g) 0.21, (h) 0.25, (i) 0.29, (j) 0.41, (k) 0.48, (l) 0.54, (m) 0.542, (n) 0.58, (o) 0.69, (p) 0.76, (q) 0.812, and (r) 0.86 W/cm².

Figure AE.1 GIWAXS profiles of bare VWR glass collected at incident angles ranging from 0.05° to 0.4°. Color available in electronic copy.

Figure AE2. GIWAXS profiles of 100 nm Ag on VWR glass collected at incident angles ranging from 0.05° to 0.4° . Color available in electronic copy.

Figure AE3. GIWAXS profiles of 100 nm neat PFO on bare VWR glass collected at incident angles ranging from 0.05° to 0.4° . Color available in electronic copy.

Figure AE4. GIWAXS profiles of 100 nm neat PFO atop 100 nm Ag on VWR glass collected at incident angles ranging from 0.05° to 0.4° . Color available in electronic copy.

Figure AE5. GIWAXS profiles of 100 nm PFO on bare VWR glass heat treated at 120°C for 30 minutes and quenched on a metal plate collected at incident angles ranging from 0.05° to 0.4° . Color available in electronic copy.

Figure AE6. GIWAXS profiles of 100 nm PFO atop 100 nm Ag on VWR glass heat treated at 120°C for 30 minutes and quenched on a metal plate collected at incident angles ranging from 0.05° to 0.4° . Color available in electronic copy.

Figure AE7. GIWAXS profiles of 100 nm PFO on bare VWR glass heat treated at 180°C for 30 minutes and quenched on a metal plate collected at incident angles ranging from 0.05° to 0.4° . Color available in electronic copy.

Figure AE8. GIWAXS profiles of 100 nm PFO atop 100 nm Ag on VWR glass heat treated at 180°C for 30 minutes and quenched on a metal plate collected at incident angles ranging from 0.05° to 0.4° . Color available in electronic copy.

Figure AE9. GIWAXS profiles of 100 nm PFO on bare VWR glass heat treated at 200° C for 60 minutes and cooled on a glass plate collected at incident angles ranging from 0.05° to 0.4°. Color available in electronic copy.

Figure AE10. GIWAXS profiles of 100 nm PFO atop 100 nm Ag on VWR glass heat treated at 200° C for 60 minutes and cooled on a glass plate collected at incident angles ranging from 0.05° to 0.4°. Color available in electronic copy.

Figure AE11. GIWAXS profiles of 100 nm PFO on bare VWR glass heat treated at 280° C for 30 minutes and quenched on a metal plate collected at incident angles ranging from 0.05° to 0.4°. Color available in electronic copy.

Figure AE12. GIWAXS profiles of 100 nm PFO atop 100 nm Ag on VWR glass heat treated at 280° C for 30 minutes and quenched on a metal plate collected at incident angles ranging from 0.05° to 0.4°. Color available in electronic copy.

Figure AE13. GIWAXS profiles of 100 nm PFO on bare VWR glass vapor annealed in toluene vapor for 60 minutes collected at incident angles ranging from 0.05° to 0.4°. Color available in electronic copy.

Figure AE14. GIWAXS profiles of 100 nm PFO atop 100 nm Ag on VWR glass vapor annealed in toluene vapor for 60 minutes collected at incident angles ranging from 0.05° to 0.4°. Color available in electronic copy.

Figure AF1. True color bright-field and dark-field images of gold NW/NT heterostructure “tube 1” under in-phase excitation and collection polarization varied in 10° increments from 90° WRT to the long axis of the heterostructure (Condition 1) to 0° WRT to the long axis of the heterostructure. Inset in all images are schematics of the excitation direction and incident polarization, where \vec{k} denotes the excitation propagation direction and \vec{E} denotes polarization of the electric field. All scale bars = 200 μm . Color available in electronic copy.

Figure AF2. True color bright-field and dark-field images of a gold NW/NT heterostructure “tube 2” under in-phase excitation and collection polarization varied in 10° increments from 90° WRT to the long axis of the heterostructure (Condition 1) to 0° WRT to the long axis of the heterostructure (images taken at 10°, 20°, 40°, 50°, 60°, and 70° polarization are not shown). Inset in all images are schematics of the excitation direction and polarization, where \vec{k} denotes the excitation propagation direction and \vec{E} denotes polarization of the electric field. All scale bars = 2 μm . Color available in electronic copy.

Figure AF3. (a) Grayscale intensity analysis of the dark-field images of the NT region of gold nanowire/nanotube heterostructure “tube 2” under (i) collection polarization only, (ii) excitation polarization only, and (iii) dual excitation and polarization from 0° to 90° WRT to the long axis of the heterostructure, (b) percentage blue and (c) percentage red pixels of the tube region of darkfield images under dual polarization from 0° to 90° WRT to the long axis of the heterostructure. Green pixel analysis (not shown) was inconclusive.

Figure AF4. True color bright-field (a,c,e,g,i) and dark-field (b,d,f,h,j) images of gold NW/NT heterostructure “tube 1” under (a,b) unpolarized excitation and collection, (c,d,g,h) polarized

excitation and collection (dual), and (e,f,i,j) polarized collection only at 0° polarization (c-f) and 90° polarization (g-j) with respect to the long axis of the heterostructure. Beside all images are schematics of the excitation direction and polarization, where \vec{k} denotes the excitation propagation direction and \vec{E} denotes polarization of the electric field. All scale bars = 2 μm. Color available in electronic copy.

Figure AF5. Spectrometer CCD images of gold NW/NT heterostructure “tube 2” in full view (a-e, and p-t, of the nanowire (f,h,j,l,n,u,w,y,aa,cc) and nanotube (g,i,k,m,o,v,x,z,bb,dd) regions only (where spectra were collected) when the long axis of the structure was parallel (a-o) and perpendicular (p-td) to the x-direction of the microscope stage under: (i) unpolarized excitation and collection (a,f,g,p,u,v), (ii) polarization in condition 1 (C1) with both excitation and collection polarization (b,h,l,q,w,x) and with collection polarization only (c,j,k,r,y,z) and (iii) polarization in condition 2 (C2) with both excitation and collection polarization (d,l,m,s,aa,bb) and with collection polarization only (e,n,o,t,cc,dd). Resultant polarization incident on the structure is denoted in the top right corner of each image.

Figure AF6. Unpolarized dark-field scattered light spectra of the NW and NT regions of heterostructure “tube 2” when parallel (0°) and perpendicular (90°) WRT to the x-direction of the microscope stage. Color available in electronic copy.

Figure AF7. Dark-field scattered light spectra of the tube region of gold nanowire/nanotube heterostructure “tube 2” under 0° and 90° incident polarization with: collection polarization only (a,b) and dual excitation and collection polarization (c,d) with polarization set in condition 1 (C1) (a,c) and polarization set in condition 2 (C2) (b,d). Color available in electronic copy.

Figure AF8. Dark-field scattered light spectra of the NW region of gold NW/NT heterostructure “tube 2” under 0° and 90° incident polarization with: collection polarization only (a,b) and dual excitation and collection polarization (c,d) with polarization set in condition 1 (C1) (a,c) and polarization set in condition 2 (C2) (b,d). Color available in electronic copy.

List of Acronyms

AB: Antisymmetric Bound

AL: Antisymmetric Leaky

ASE: Amplified Stimulated Emission

AuNT: Gold Nanotube

CG: Complex Gain

CSS: Complex Steady State

FDTD: Finite-Difference-Time-Domain

ID: Inner Diameter IMI: Insulator-Metal-Insulator waveguide

ISI: Insulator-Semiconductor-Insulator Waveguide

ISMI: Insulator-Semiconductor-Metal-Insulator Waveguide

LDOS: Local Density of Optical States

LED: Light Emitting Diode

NT: Nanotube

NW: Nanowire

OD: Outer Diameter

OLED: Organic Light Emitting Diode

PRSS: Purely Real Steady State

RSPP: Radiative Surface Plasmon Polariton

SB: Symmetric Bound

SES: Shifting Excitation Spot

SL: Symmetric Leaky

SP: Surface Plasmon

SPP: Surface Plasmon Polariton

VSL: Variable Stripe Length

WT: Wall Thickness

1 Background and Scope of Investigation

1.1 Introduction

Over the course of human history, an understanding of light and how to manipulate its flow has ushered in a myriad of imaging technologies such as the microscope and telescope, which have broadened our collective understanding of the natural world. In conjunction, light plays roles in a host of modern day industrial, medical, consumer, and communication technologies. Realization of efficient conversion of light into electricity via solar-photovoltaic cells may also play a central role in developing a carbon-neutral renewable energy source to address the ever-increasing demand for the earth's finite supply of fossil fuels. Equally as important as solar light harvesting technology is the efficient conversion of electrical energy to light through the development of solid state light emitting diodes LEDs which are expected to significantly improve the energy efficiency of both general lighting and portable display technologies.

Light may also play a profound role in future terahertz computing technologies. As computer circuitry has become more advanced, there has been a concerted effort to make them faster, more computationally powerful and smaller, while at the same time minimizing energy consumption [10]. Light is the fastest means of sending information and the concept of developing computer chips that operate via light or light-like signals, instead of electricity has been actively discussed for several decades [13]. Because photons are not as strongly interacting as electrons and holes, they significantly broaden information bandwidth. Optical networks already provide large bandwidths (upwards of 100 Gbits/s) that even the fastest state-of-the-art electronic processors (with bandwidths on the order of 10 Gbits/s) are unable to compete with on that metric (see Fig.1.1) [14,15]. Realization of densely integrated hybrid opto-electronic circuitry could allow terahertz speed data processing at length scales smaller than the free-space

wavelength of light (see Fig.1.1). This would facilitate a significant increase in the volume and energy efficiency of data processing.

The realization of practical photonic-based computer chips faces many hurdles. Firstly, optical fields localized in a cavity can have a length no smaller than approximately half the optical wavelength. Therefore, optical devices operating in the visible regime can have dimensions no smaller than a few hundred nanometers(see Fig. 1.1). Conversely, the fundamental components of electronic computer circuitry are rapidly approaching length scales in the tens of nanometers (see Fig. 1.1) [16]. This fundamental mismatch between the ability to confine light and down-size optical circuitry has limited practical integration of optical components with conventional electronic circuitry. This implies the need to develop the necessary building blocks of modern photonics such as optical logic switches, waveguides, coherent light emitting sources, and interconnects on length scales significantly smaller than the wavelength of light, such that they are compatible with electronic circuitry. This can be achieved by coupling conventional light (photons) to surface plasmons. Surface plasmons or SPs are transverse-magnetic modes that exist along a metal-dielectric or metal-semiconductor interface. They result from collective oscillations of the conduction electrons of the metal and can produce both localized resonances (localized surface plasmons) and propagating modes (surface plasmon polaritons or (SPPs)). Surface plasmons may allow electromagnetic signals travelling close to the speed of light in vacuum to be confined on length-scales unachievable with conventional photonics and facilitate the manipulation and propagation of light below the diffraction limit [17,18]. Thus, at present, plasmonic devices (i.e., those employing surface plasmons) may be regarded as the ‘missing-link’ between conventional photonic technology and highly-integrated hybrid opto-electronic circuitry

(see Fig 1.1) [17,18].

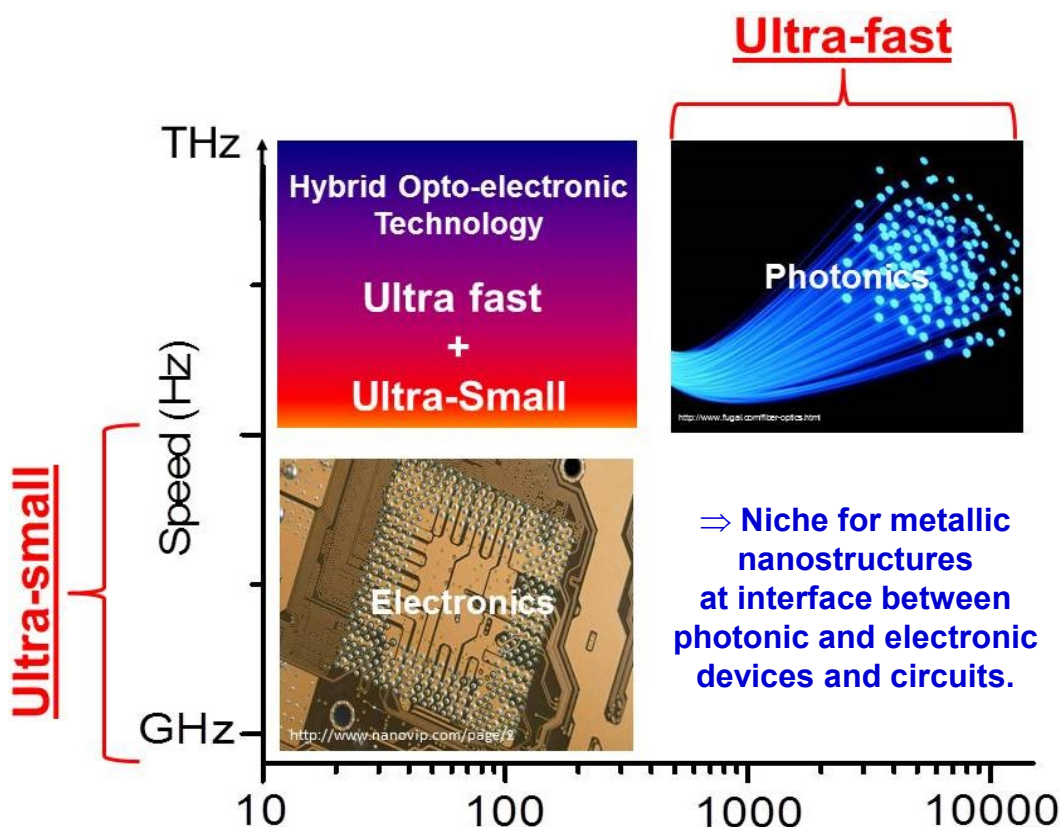


Fig. 1.1 Schematic plot of processing speed (Hz) versus device length scale or size (nm) for conventional photonic, electronic, and hybrid optoelectronic technologies [19,20]. Color available in electronic copy.

Furthermore, the ability to focus and confine light to sub-wavelength length scales has the potential to benefit a host of existing and emerging large-area opto-electronic technologies[10,21,22]. In the case of thin film photovoltaics, better light management on the nanometer scale may increase light absorption efficiency while allowing for a reduction in the volume of the active semiconductor material used to absorb incident light, thereby increasing the open circuit voltage [23]. This may ultimately lead to higher device efficiency and a decrease in manufacturing cost through the use of less active material [23]. Lighting technologies such as light-emitting diodes (LEDs) may be made more energy efficient by introducing structures that produce strong nanoscopic field enhancements to the semiconductor material to increase the local

density of optical states (LDOS), and allow the semiconductor material to radiate more efficiently than in conventional devices. According to Fermi's Golden Rule the radiative decay rate is directly proportional to the LDOS [24]. Therefore, by increasing the LDOS using highly-localized surface plasmons, the radiative transition rate, and, hence, quantum efficiency can be enhanced (quantum efficiency = radiative decay rate/(radiative decay rate + non-radiative decay rate)). Similarly, the rate of spontaneous emission can be modified and enhanced through the matching of the emission rate with a resonant cavity. This is known as the Purcell effect [25]. The enhancement factor F_p of the is given by the following relation called the Purcell Factor:

$$F_p = \frac{3}{4\pi^2} \left(\frac{\lambda_c}{n}\right)^3 \left(\frac{Q}{V}\right), \quad (1)$$

where (λ_c/n) is the wavelength within the material and Q and V are the quality factor and mode volume of the cavity, respectively. Therefore, for plasmonic cavities below the diffraction limit (i.e., cavities with ultra-small mode volume) very large Purcell factors can be achieved [26].

Increasing confinement and photonic mode density may also enhance the performance of conventional light lasers and has important implications in the field of quantum information technology in which a single quantum emitter must be efficiently coupled to photonic circuitry.

An underlying challenge for the practical development of plasmonic technologies such as nanoscopic waveguides, light emitters and efficient nanoscale light management structures is to minimize intrinsic losses that surface plasmons exhibit. These losses are ohmic in nature and are due to the strong energy dissipation present in metals at optical frequencies approaching the plasma frequency of the metal (non-negligible imaginary component of the dielectric constant). Other sources of loss relating to SPs include dark-modes and higher order modes (i.e., multipoles). This is especially problematic in the visible and near-UV regime where strong damping of the plasmonic fields occurs and SP mode losses on the order of $1,000 \text{ cm}^{-1}$ are typical[1,2]. Therefore, eliminating loss is of paramount importance when designing plasmonic

opto-electronic devices such as plasmonic interconnects, where a propagating surface plasmon mode is sent over macroscopic distances (tens of microns). In 1989 Sudarkin and Demkovich proposed the introduction of a gain material, analogous to that used in optical lasers to compensate and overcome the intrinsic loss [27]. This seminal work has ushered in a host of theoretical and experimental work exploring a host of gain media to compensate for intrinsic losses in plasmonic metallic nanostructures [12,24,28-31].

One particularly promising category of gain media is fluorescent organic semiconducting (conjugated) polymers. There are many families of conjugated polymer materials that exhibit high gain cross-sections such as polyphneylenevinylenes, polyparaphenylene, and polyfluorenes [32]. They are synthesized from low-cost, earth-abundant elements (carbon, hydrogen, sulfur, oxygen) and are readily solution processed at ambient temperatures [32]. They have very large absorption and emission cross-sections (absorption coefficient $\sim 10 \text{ cm}^{-1}$) and can exhibit photoluminescence quantum efficiencies of over 80% in solid films [2,33-35]. These properties occur because of the large exciton binding energies exhibited by conjugated materials (Frenkel excitons) leading to large oscillator strengths, in addition to significant Stokes shifted separation between the absorption and fluorescence emission spectra [2]. The achievable gain per unit volume of conjugated polymers can be inherently higher than laser dyes, which must be diluted to avoid self-quenching [2]. Amplified stimulated emission, lasing and high net gain ($> 60 \text{ cm}^{-1}$) have been demonstrated in sub-micron thick films, wires and other geometries of such polymers [33-35]. The excitation and emission wavelengths of conjugated polymers are also highly tunable, allowing coverage of nearly the entire visible spectrum [11].

These aforementioned attributes make these polymers attractive for a host of next-generation visible-light-based optoelectronic devices. Currently the most widely utilized organic semiconducting polymers are PPVs, which currently are utilized in a variety of organic electronic applications such as LEDs and potentially thin film transistors [36,37]. Additionally, these

polymers have potential applications in a host of green and renewable energy technologies such as organic photovoltaic solar cells and solid-state LED lighting and displays [37]. In conjunction with these applications, organic semiconducting polymers may provide a well-suited material system to provide gain compensation for plasmonic nanostructures operating in the visible regime [38].

Development of a fundamental understanding of efficient surface plasmon-organic semiconductor emitter coupling may help reduce loss in conventional, electrically-driven optoelectronic devices such as organic light emitting diodes (OLEDs). In particular, surface plasmons have been identified as a major loss channel in OLEDs and other electrically-driven optoelectronic devices [21-24, 39-42]. This arises from excitation of tightly-bound surface plasmon modes at the metal electrode, which trap light energy at the interface and in turn reduce the overall light outcoupling efficiency, g_{out} , of a light-emitting device. For OLEDs, loss to tightly bound surface plasmon modes can be upwards of 20-46.8% [3-6]. The major approaches taken to minimize optical energy loss to SPP modes in OLEDs include: (i) introduction of Bragg gratings or other wavelength-scale corrugated microstructures to fulfill the energy and momentum conservation of trapped modes and light propagating in air [3,6,43,44]; (ii) anisotropic orientation of the molecular dipole emitters of the active organic layer to an in-plane configuration that avoids coupling to bound SPP modes (limited to extended or anisotropic molecules) [3,4,43,44]; and (iii) use of high-index prisms in to extract SPPs and waveguided modes [3]. Other approaches include development of electrodes fabricated from metals with SPP energies larger or smaller than the device operating energies so that they do not couple with photons emitted by the device [4,6], and addition of spacer layers to control the degree of coupling to SPP modes [6,39]. The aforementioned strategies have potential to reduce SPP losses but may introduce new leakage or optical dissipation channels, require additional and potentially complex fabrication, and significant changes to the device architecture [6]. Compelling evidence suggests that if the SPP

mode character and leakage into the semiconductor emitter can be controlled rather than suppressed entirely, SPPs may boost performance in a host of visible-light-based optoelectronic devices such as organic photovoltaics, organic lasers, and OLEDs [21-24, 39-42]. By enhancing surface plasmon leakage, a significant fraction of SPP mode amplitude can be shifted into the organic semiconductor emitter layer, thereby decreasing the amount of optical energy lost to parasitic coupling to tightly bound SPP modes. Additionally, shifting an increased fraction of the mode energy into the polymer emitter layer promotes increased SPP propagation length because there is less damping of the mode by absorption in the metal.

1.2 Background

1.2.1 The Diffraction Limit and Evanescent Waves

The minimum spot size in which light can be focused by conventional optical elements such as lenses and mirrors is dictated by the wavelength of the light and the refractive index of the medium through which it is propagating. The classical limit, achieved with highly focused laser beams used in data storage and confocal microscopy systems, can afford resolution on the order of $\lambda/4$ [45,46]. In optics, the smallest focused spot size of light that a perfect lens with a circular aperture can achieve is called the Airy disk and it is limited by the diffraction of light. Diffraction occurs when the wavefront of light is obstructed by an optical component or feature. Thus, when focused by an optical lens component, the light wavefronts cannot be tapered to a point but instead form an Airy disc with a central spot with radius r , of [46]:

$$r = 1.22\lambda/2NA, \quad (2)$$

where λ is the wavelength of light and NA is the numerical aperture of the lens (i.e., the focal length of the lens divided by the diameter) of the lens.

This limit has important implications for the minimum distance between two features that can be resolved using conventional light microscopy. German physicist Ernst Abbe is credited with the full derivation of the diffraction limit of an optical microscope and the equation [45]:

$$d_{res} \approx \frac{\lambda}{2NA}, \quad (3)$$

where d_{res} is the minimum resolvable distance between two features, λ is the wavelength of light and NA is the numerical aperture of the microscope objective lens (which is calculated as the sin of the half angle, Θ , multiplied by the refractive index of the medium); see Figure 1.2 [45]. The numerical aperture is a dimensionless number that characterizes the range of angles over which the system can accept or emit light.

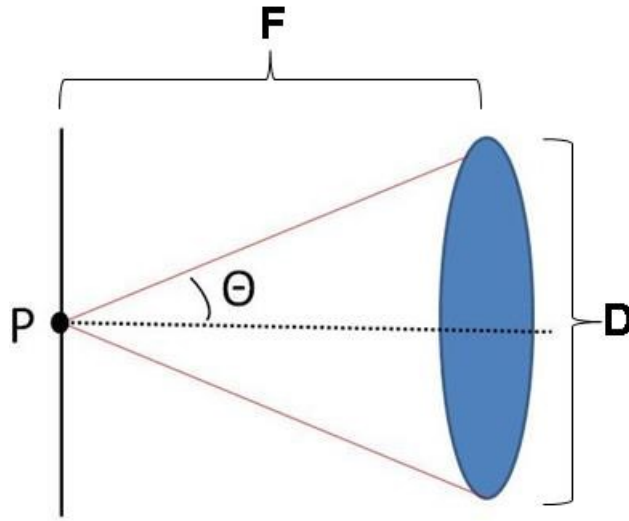


Figure 1.2. The numerical aperture (NA) of a lens (shown in blue) with respect to an image or focal point, P , depends on the half-angle, Θ , of the maximum cone of light that can enter or exit the lens. D is the diameter of the lens.

Evanescent waves are central to the field of nano-optics and are important for understanding how optical fields can be confined to subwavelength dimensions. The word itself is derived from the Latin word *evanescere*, which can mean *vanishing from notice* or *imperceptible*

[47]. In classical theory, electromagnetic fields and electrons are completely confined within the region of confinement. However, in reality the field distribution of light in a waveguide extends or ‘leaks’ beyond the physical boundaries of the waveguide [46,48]. The light that leaks beyond the boundary of the waveguide is an electromagnetic field called an evanescent wave. Unlike the behavior of plane waves, evanescent waves can have large in-plane wavevectors. Additionally, the field amplitude of an evanescent wave decays exponentially with distance, x , into the medium with lower refractive index and can be calculated as follows (see Figure 3) [46,48]:

$$E_x(x) = E_0 \exp(-x/D_{pen}), \quad (4)$$

where E_0 is the electric field at the boundary of the waveguide and D_{pen} is the penetration depth. Penetration depth values for visible light are typically 50 - 100 nm and can be calculated as follows [46,48]:

$$D_{pen} = \frac{\lambda}{4\pi n_1 [\sin^2 \theta - (\frac{n_2}{n_1})^2]^{1/2}} \quad (5)$$

where n_2 and n_1 are the indices of refraction of the two media ($n_1 > n_2$) and θ is the angle of incidence relative to the surface normal of guided light at the boundary of the waveguide. Note that θ must be greater than the critical angle in the waveguide material, i.e., the evanescent wave is excited by guided waveguide modes only. Because the penetration depth is typically much smaller than the free-space wavelength, evanescent waves such as surface plasmon polaritons (SPPs) are useful for subwavelength-scale optical applications (see Fig. 1.3).

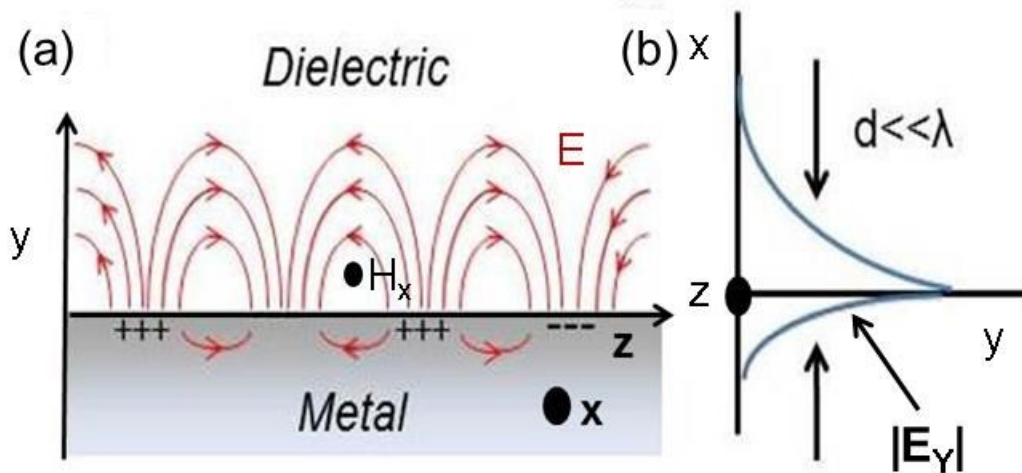


Figure 1.3. (a) Schematic of the magnetic field (H_y) of an SPP mode propagating along a metal–dielectric interface in the z -direction (where red lines indicate the Electric field and the + and – symbols represent changes in the magnetic field charge distribution). (b) A cross-sectional schematic of the perpendicular electric field, E_y , of an SPP mode, which decays in the x - z . Parts (a) and (b) of this figure were adapted from [49]. Color available in electronic copy.

1.2.2 Electromagnetic Waves and Surface Plasmons

From a historical perspective, the study of surface electromagnetic waves started in the early 20th century. In 1907, Zenneck theoretically analyzed the surface wave property of a planar boundary between free-space and a half space with a finite conductivity [50]. He termed these “Zenneck waves”. Later, in 1909 Sommerfeld postulated that by treating the earth’s atmosphere or upper half as a pure dielectric and the ground or lower portion as a conductor, that radio waves could propagate parallel and adjacent to the surface of the earth, following its curvature [51]. These waves are referred to as Sommerfeld waves, gliding waves, or Norton surface waves. Later, in 1941, Fano theorized that surface electromagnetic waves resulted in Wood’s anomalies in metal diffraction gratings [52].

Woods anomalies, observed on diffraction gratings for only p-polarized light are narrow spectral regions that show a sharp change in diffracted energy [53]. The physical explanation is the following: consider a reflection grating which produces a range of diffracted light in

successive orders diffracted away from the normal [54]. In some order, at some critical wavelength, the diffracted light lies in the plane of the grating. It is not possible for light beyond this point to be diffracted behind the glass of the grating. The power which would be sent into the forbidden region is redistributed back into the allowed orders [54]. The power appears as an addition, to the spectrum response, with a sharp cut on at the critical wavelength and a steep decline to the red. The additional power is in no sense a reflection or a ghost image, but a genuine enhancement of efficiency of the grating, as if the light from two orders has been combined [54]. As can be imagined from the physical explanation, which involves light passing near the plane of the grating, the additional efficiency is highly polarization dependent - a Wood's anomaly is almost entirely polarized [54]. While Woods was unable to provide any interpretation for these phenomena, and the notion of surface plasmon polaritons did not appear until nearly a half century later, Woods must be considered the initiator of plasmonics [54]. Later work by Ritchie, Stern, Ferrell and Powell on the treatment of the characteristic energy losses of fast electrons passing thorough thin metal films, predicted the existence of self-sustained collective oscillations at metal surfaces (i.e., surface plasmons) [55-60]. Further revealed that the energy loss results from excitation of a surface plasma oscillation (the quanta of which Stern and Ferrell called the Surface Plasmon [61]) in which part of the restoring electric field extends beyond the specimen boundary. The surface plasmon oscillations can therefore be affected by the presence of any film or contaminant on the specimen surface [62-64]. This effect was later described in terms of excitation of electromagnetic evanescent waves at the surface of the metal, and in the 1970's evanescent waves where described as a means to study ultra-thin metal films and coatings [65]. Seminal work by Kretschmann and Raether allowed the direct optical observation of surface plasmons through attenuated total reflection (ATR) experiments [66]. Their work ushered in great interest and exploration of surface plasmons for a host of nanophotonic, metamaterial and biological sensing applications [13,18,21, 67-70].

In a more contemporary and formal definition, surface plasmon polaritons are transverse magnetic waves that propagate along a metal –dielectric interface where there is a change in sign of the real part of the dielectric permittivity across the interface; see Figure 1.3. They are evanescently confined in the x-direction and their fields decay exponentially into both materials. The term “surface plasmon polariton” implies the hybrid nature of these waves as they result from resonant coupling between conventional light waves (photons) and collective oscillations of the free conduction electrons of the metal (i.e., plasmons) [71].

More quantitatively, surface plasmon polaritons (SPPs) are the eigenmodes of a metal-dielectric interface and are solutions of Maxwell’s equations that can be formulated in the absence of an incident field [72]. On a flat interface between metal-dielectric half-spaces with dielectric constants, ϵ_d (dielectric) and ϵ_m (metal). Assuming the interface is normal to the x-direction and the SPPs propagate such that the wavevector in the y-direction, k_y , is negligible, the SPP wavevector, k_z , is related to the optical frequency, ω , through the following dispersion relation [72]:

$$k_z = k_0 \sqrt{\frac{\epsilon_d \epsilon_m}{(\epsilon_d + \epsilon_m)}} \quad (6)$$

where $k_0 = 2\pi/\lambda$ is the free-space wavevector, where λ is the free-space operating wavelength.

1.2.3 Dielectric Functions of Metals

To further define the origin of surface plasmon polaritons, it is necessary to discuss the dispersive dielectric constants or relative permittivity of metals, ϵ_m , and look specifically at the Drude and Lorentz models that describe the optical response of metals. The Drude model for a free electron gas is based upon the understanding that metals contain a significant number of free electrons that are not bound to any atoms and can move freely without experiencing any restoring

forces [73]. Thus, it implies that the spring constant (or damping factor) is zero and the natural resonant frequency of the electrons, ω_0 , is ∞ . Therefore, the complex relative permittivity of metals described by the free-electron Drude model is [73,76]:

$$\varepsilon_m = 1 - \frac{\omega_p^2}{\omega^2 + i\gamma\omega} = \varepsilon'_m + i\varepsilon''_m \quad (7)$$

where the real and imaginary parts of ε_m can be defined as:

$$\varepsilon'_m = 1 - \frac{\omega_p^2}{\omega^2 + \gamma^2} \quad (8)$$

$$\varepsilon''_m = \frac{\omega_p^2 \gamma}{\omega(\omega^2 + \gamma^2)} \quad (9)$$

For certain metals the plasma frequency, ω_p , is greater than the damping constant, γ , (Au, Ag, Al, Cu, Be, Cr, Ni, Pd, Pt, Ti, Na and W) [77]. For large frequencies close to ω_p , $\omega \gg \gamma$ resulting in negligible damping. Thus the real part of the dielectric function (ε'_m) dominates and simplifies to:

$$\varepsilon'_m = 1 - \left(\frac{\omega_p}{\omega}\right)^2 \quad (10)$$

which defines the dielectric function of an un-damped free-electron plasma. At frequencies less than the plasma frequency, the dielectric constant of the metal exhibits negative values. The Drude model is an adequate optical dielectric function for metals in general but only over a limited range of energies. Above energies of 1.9 eV there exist strong discrepancies, specifically for gold [78]. More accurate full-spectrum optical characterization of metals requires the use of empirical optical constants.

The Lorentz dipole oscillator model is more accurate than the Drude model for describing the dielectric function of metals near the plasma frequency, as it considers how bound electrons

within a metal atom interact with an external electromagnetic (EM) wave at frequency, ω . The Lorentz dipole oscillator model is defined by the following equations [79]:

$$\epsilon'_m = 1 + \frac{\omega_p^2(\omega_p^2 - \omega^2)}{(\omega_0^2 - \omega^2)^2 + \gamma^2 \omega^2} \quad (11)$$

$$\epsilon''_m = \frac{\omega_p^2 \gamma \omega}{(\omega_0^2 - \omega^2)^2 + \gamma^2 \omega^2}. \quad (12)$$

By combining the Drude and Lorentz models a more complete expression for the dielectric constants of metals is obtained (Drude-Lorentz model). For the research conducted in this thesis, gold and silver will be the primary metals of study. Therefore, included below in Figures 1.4 and 1.5 are plots of ϵ' and ϵ'' versus wavelength, respectively, using the Drude model as compared with the empirical constants of Palik [77]. For all of electromagnetic simulations and computational studies presented in this dissertation, the empirical dielectric constants of Palik were employed [77].

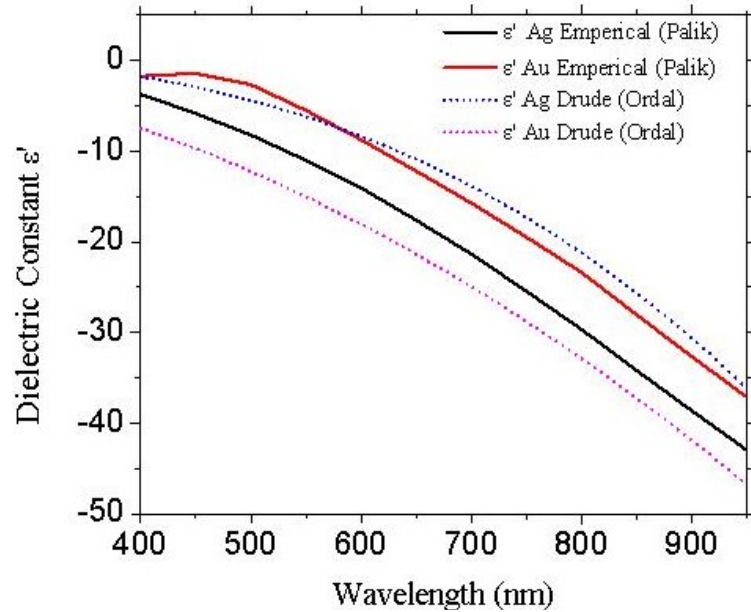


Figure 1.4. Plot of ϵ' versus wavelength for silver ($\omega = 2.18 \cdot 10^{15} \text{ s}^{-1}$, $\gamma = 4.353 \cdot 10^{12} \text{ s}^{-1}$) and gold ($\omega = 2.183 \cdot 10^{15} \text{ s}^{-1}$, $\gamma = 6.46 \cdot 10^{12} \text{ s}^{-1}$) of both the Drude model and the empirical constants of Palik [77]. The plasma frequency and damping constants used to calculate the optical constants for the Drude model were taken from [80]. Color available in electronic copy.

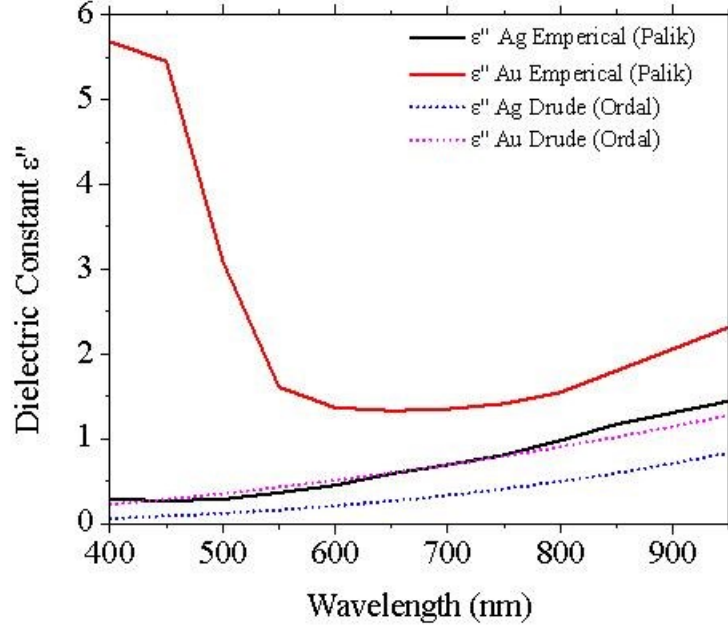


Figure 1.5. Plot of ϵ'' versus wavelength for silver ($\omega = 2.18 \cdot 10^{15} \text{ s}^{-1}$, $\gamma = 4.353 \cdot 10^{12} \text{ s}^{-1}$) and gold ($\omega = 2.183 \cdot 10^{15} \text{ s}^{-1}$, $\gamma = 6.46 \cdot 10^{12} \text{ s}^{-1}$) of both the Drude model and the empirical constants of Palik [77]. The plasma frequency and damping constants used to calculate the optical constants using the Drude model were taken from [80]. Color available in electronic copy.

1.2.4 Surface Plasmons at a Single Metal Interface

Dispersion relations provide great insight into the how SPP mode energy is distributed within the layers of the structure it is propagating in, as well as an insight into how lossy a given mode may be [81-84]. Depending on the architecture of the structure in which the SPP mode is propagating, there can be multiple SPP modes, each with a distinct dispersion relation solution [82,84]. The solution, termed k , is the complex plasmon polariton wavevector, which has both a real (k_r) and imaginary (k_i) component. From the real (k_r) and imaginary (k_i) components of the complex surface plasmon polariton wavevector, the mode effective index, N_{eff} , and characteristic SPP mode propagation length, L , can be calculated for all four modes of each of the three dielectric constant cases according to [82]:

$$N_{\text{eff}} = k_r / k_0 \quad (5)$$

$$L = 1 / k_i . \quad (6)$$

The mode effective index (N_{eff}) gives direct insight into which layer of the structure the majority of the mode energy resides, and the propagation length describes the $1/e$ propagation length of the mode, which gives insight into how lossy the mode is [82,84]. Additionally, from the dispersion relation solutions, the SPP mode penetration depth, D in the each of the layers of the structure can be calculated, which gives insight into the spatial distribution of the mode [82,84]. These calculations will be discussed in depth in Chapter 2; however, it is important to briefly describe the significance of the information that is gleaned from dispersion relation solutions.

Before providing a background on insulator-metal-insulator (IMI) slab waveguides, the equations to describe surface plasmons at a single metal-dielectric interface will be presented. The dispersion relation k_z of SPPs propagating along the z direction of a single flat interface between a semi-infinite metal and dielectric is [81]:

$$k_z = \frac{\omega}{c} \sqrt{\frac{\epsilon_m \epsilon_d}{\epsilon_m + \epsilon_d}} \quad (13)$$

$$k_{x\,m,d}^2 = \epsilon_{m,d} \left(\frac{\omega}{c}\right)^2 - k_z^2 \quad (14)$$

where k_z is the in-plane wavevector.

Work by Dionne *et al.* solved the SPP dispersion relation using the equation for a single silver-silica interface [81]. The work clearly described the SPP propagation along a single interface and illustrated the difference when the dispersive dielectric constant of the metal was treated with the Drude free-electron gas model versus using empirical optical constants. When the metal was described by the Drude free-electron gas model without damping it resulted in

$\epsilon_m(\omega) = 1 - \omega_p^2/\omega^2$ with $\omega_p = 8.85 \times 10^{15} \text{s}^{-1}$ [81] and showed the existence of a plasmon bandgap, (or forbidden zone where the plasmons cannot occur) between the surface plasmon frequency ω_{sp} and the plasma frequency, ω_p . ω_{sp} was defined as the frequency where $\epsilon'_m = -\epsilon_m$ and so $\omega_{sp} = \omega_p/(1 + \epsilon_2)^{1/2}$ [81]. Thus, it is the negative real part of the dielectric function of metals that allows the propagation of surface plasmons.

When empirical constants (of Johnson and Christy) were used to solve the dispersion relation of the silver-silica interface, Dionne *et al.* showed that there were significant differences in the surface plasmon dispersion compared to that when the Drude model was used to describe the metal [81]. When empirical constants were used they took into account both the free-electron and interband damping [81]. In contrast with the Drude model, it showed that plasmon modes were allowed through the entire 400 - 950 nm frequency range. The radiative surface plasmon mode was observed at frequencies which satisfy the relation $\epsilon'' > |\epsilon'|$. At low energies, as the SPP wavevector approached the light line (used to distinguish between guided and non-guided modes in a dielectric slab waveguide) it terminated at a finite limit ω_{sp} . At intermediate frequencies between the SPP and radiative surface plasmon polaritons (RSPP) modes (which are highly leaky modes), there was a transitional mode with negative phase velocities [81]. The bound nature of SPP modes resulted in their dispersion curves lying to the right of the light line of the dielectric material [85]. This momentum mismatch between light and SPPs of the same frequency requires special optical coupling techniques such as prism coupling or gratings to bridge the difference and these will be described in Section 3.8.

1.2.5 SPP Propagation in Insulator-Metal-Insulator (IMI) Waveguides

The basis for understanding the SPP propagation in semiconductor-metal-insulator (SMI) waveguides studied in this thesis are based upon theoretical work by Burton and Cassidy [82]. In

their work, a comprehensive set of dispersion relations were solved for a planar asymmetric IMI waveguide consisting of a gold film sandwiched between a silica cover and substrate [82]. It is referred to as asymmetric waveguide because the refractive indices of the cover (n_{cover}) and substrate media are not equal. ($n_{substrate}$). In the Burton and Cassidy work, the IMI waveguide dispersion relations were solved over a range of metal film thicknesses, while the cover and substrate were considered infinitely thick media [82]. Their results have been independently reproduced in Chapter 2 and are discussed in detail.

1.2.6 Organic Semiconducting Conjugated Polymers

Organic semiconducting conjugated polymer materials for electronic and photonic devices have been largely motivated by their extensive processability, spectral tunability and low cost [35]. Tuning molecular morphology and structural order can be employed to influence the local molecular order or conformation in conjugated polymer systems and thereby control the mechanisms of formation, transport and harvesting of excited states for device applications [35]. Indeed, following the development of high purity organic materials synthesis routes, organic electronic and photonic devices have become commercially viable. Recent reports on the global market for products such as organic light emitting displays, organic solar cells, organic thin film transistors and other electronic products made from organic materials estimated growth from €14 billion by 2012 to €25 billion by 2014 [86]. As a result, large numbers of major US, European, and Japanese companies, including 3M, Dow Corning, DuPont, GE, Infineon, IBM, Philips and Pioneer are already heavily involved in organic electronics and photonics.

Polyfluorenes are attractive materials for photonics applications since they exhibit high photoluminescence quantum efficiencies (up to 70 %), large stimulated emission cross-sections ($\sim 10^{-15} \text{ cm}^2$) and absorption coefficients ($\sim 2 \times 10^5 \text{ cm}^{-1}$) and have chemically tunable emission wavelengths [87-91]. The peak gain wavelengths of these organic conjugated polymers do not

overlap with the fluorescence spectra. For example, the fluorescence spectra of PFO results in the emission of blue light (415 – 420 nm) in conjunction with two vibronic side bands (439 – 445 nm and 470 – 475 nm) assigned to 0-0, 0-1, and 0-2 intra-chain singlet transitions. Much of the S_1 to S_0 (0-0) transition is re-absorbed due to its energy being in close proximity to the onset wavelength of the absorption spectrum. The emission from the 0-2 transition is diminished due to excited state absorption. However, the intermediate S_1 - S_0 (0-1) transition results in the peak gain wavelength [92-94].

1.2.7 Excitation of Surface Plasmons

The dispersion relations for surface plasmons describe certain implications with respect to how coupling can occur between photons and surface plasmons. If the dispersion relation is thought of in terms of energy and momentum [83,84], the surface plasmon always has a larger momentum than a photon of the same frequency in free space. Because energy and momentum are always conserved, in order for a free-space photon to be converted into a surface plasmon, additional momentum must be provided. Thus, light incident on a smooth metal surface from free-space will never excite a surface plasmon [52,53,66]. Generally speaking, there are three primary methods used to provide the required additional momentum. The first is to introduce features to the metal, such as surface texturing, a grating, or simply a single surface bump [12,22]. A grating coupler matches the wavevectors by increasing the parallel wavevector component by an amount related to the grating period [12,22]. This method, while less frequently utilized, is critical to the theoretical understanding of the impact of surface roughness on surface plasmon propagation length. Moreover, simple isolated sub-wavelength surface defects such as a groove, a slit or a corrugation on an otherwise planar surface acts like a point dipole radiating with a range of wavevectors and provides a mechanism by which free-space radiation and surface plasmons can exchange energy and hence couple [55,95,96].

The second method is more complex. When light travels in a material of refractive index $n > 1$ the wavevector in free space, k , is scaled by the refractive index and, so, increases to the value kn within the material [22,96] If the light wave experiences total internal reflection on the inner surface of the material, it produces an evanescent (exponentially decaying) wave extending beyond the medium with wavevector value kn that can equal that of the surface plasmon wavevector. Therefore, if the evanescent wave is brought sufficiently close a metal surface it can directly excite a surface plasmon. The mismatch of momentum between photons and plasmons described above makes it harder to excite them, but it has an upside – a surface plasmon, once excited at a metal-air interface, cannot radiate back into a photon unless it hits another surface feature. Only in 1998 with the publication of a seminal work by T. W. Ebbesen *et al.* was greater attention given to the potential of field enhancement and long-range surface plasmon propagation at shorter visible wavelengths [97]. This work considered the amount of light transmitted through a rectangular array of subwavelength-sized holes in a thin silver plate. Their findings were contrary to much of the theoretical work conducted since the 1950s, which had established that very little light was transmitted through subwavelength-sized holes. Ebbesen *et al.* found that the amount of transmitted light was a factor of ten greater than predicted [97]. This enhancement was attributed to the coupling/propagation of surface plasmons on the silver plate.

A third method of exciting surface plasmon modes is the coupling of fluorescent dipole emitters (such as polyfluorenes) to metal thin films or nanostructures at optical frequencies. This type of coupling is currently of interest because plasmonic nanostructures exhibit strong electromagnetic field concentrations and can act as the intermediary between photons from high-yield dipole emitters and the atomic and molecular length scales. Such coupling has been successfully utilized to implement electrically pumped surface plasmon polariton emitters, demonstrate enhanced emission and absorption of emitters [98-101] and plasmon lasers or SPASER type devices [102,103]. Experiments in the 1970's showed that the fluorescence

lifetime of a dipole emitter near a metal surface can be greatly modified by the reflection and absorption, or coupling to the metal surface [104]. At large separation distances between the emitter and the metal's surface (> 300 nm) the dipole emitter decays through traditional far-field radiative processes (i.e., fluorescence). At intermediate separation distances (10 nm – 300 nm), the fluorescence lifetime oscillates as a function the distance and coupling to a surface plasmon mode can occur [104]. The oscillations in the fluorescence lifetime are due to the metal effectively acting as a mirror for the electric field of the emitter. The interference between the reflected wave and the initial wave gives rise to the observed oscillations. At small separation distances (< 10 nm), the lifetime monotonically decreases as the dipole approaches the metal surface and damping or quenching occurs. This decrease is due to *non-radiative* energy transfer from the excited dipole to the metal, which leads to the formation of surface plasmon polariton waves and lossy surface waves. Both are non-radiative energy transfer processes but the energy which is converted to propagating surface plasmon polaritons can be recovered with the appropriate geometry that allows momentum matching with photons and can result in a surface plasmon coupled emission [105,106]. Dipole orientation also plays a critical role in the degree of coupling which occurs between the emitter and metals surface [107]. A parallel dipole (s-polarized) is cancelled out by its own image on the metal surface, while a perpendicularly polarized dipole (p-polarized) can be coupled to a surface plasmon mode and its emission can be enhanced.

Enhancement of the spontaneous emission rate due to surface plasmons has been theoretically calculated [108] and experimentally measured for different emitting materials [109]. Coupling of a semiconductor quantum well to localized surface plasmon resonances has led to an emission rate 92 times faster than the free space emission [110] and light-emitting diodes structures using this effect to enhance the emission have been proposed [111]. To calculate the emission rate, the dipole field interaction is treated as a perturbation and a Fermi's golden rule

can be applied [110,112]. As previously discussed, conjugated polymers are attractive materials to provide gain for surface plasmon propagation. The processable nature of organic semiconducting polymers allows orientation of the emitting polymer chains (or dipole emitters) for effective excitation of surface plasmons.

1.3 Thesis Overview and Objectives

The key objectives of this study are the development of: (1) efficient surface plasmon/organic polymer emitter coupling, towards the development of low-loss electrodes for visible-light-based organic optoelectronics; and (2) macroscale surface plasmon propagation for hybrid optoelectronics circuitry. Compelling evidence suggests that if the SPP mode character and leakage into the semiconductor can be controlled rather than suppressed entirely, SPPs may boost performance in a host of visible-light-based optoelectronic devices including organic photovoltaics, organic lasers, and OLEDs [21-24, 39-42]. As described previously in the introduction, organic semiconducting conjugated polymers are suitable gain media to compensate for intrinsic SPP losses due to their high quantum efficiency, tunable emission, and most importantly, the ability to control the orientation of the molecular dipole emitters; which is expected to play a critical role in the degree and efficiency of SPP-emitter coupling.

To validate the hypothesis that the introduction of an organic conjugated polymer gain medium in combination with optimization of the metal film thickness can enhance SPP propagation length and mode leakage, a simple model system consisting of a planar thin-film organic semiconductor-metal-insulator (SMI) waveguide was studied. While SMI waveguides do not exhibit true subwavelength-scale SPP propagation, they closely resemble the metal electrode/semiconductor interface in electrically-driven visible-light-based optoelectronics. Additionally, they provide a well-suited system to fundamentally understand and study plasmon/polymer interactions because it is relatively facile to fabricate and tune layer thickness.

The system studied in this thesis consisted of a silver metal film atop a silica substrate with a cover or ‘superstrate’ layer consisting of the organic conjugated polymer poly(9,9-dioctylfluorene-2,7-diyl) (PFO). PFO was selected as the gain medium used in the SMI waveguides because its photophysics and processing are well characterized and it is readily commercially available [34,35]. Silver was the metal of choice for these waveguides because its surface plasmon wavelength can be tuned close to the peak gain wavelength of PFO (which occurs near the $S_1 \rightarrow S_0$ 0-1 singlet exciton transition wavelength of ~ 455 nm) [34, 38].

These SMI waveguides were first computationally studied by solving a set of dispersion relations for the structure over a range of metal film thicknesses and polymer emitter dielectric constants (i.e., different emission regimes, e.g., steady state versus stimulated emission). These dispersion relation calculations were more rigorous compared to the majority of dispersion relation calculations presented in the literature because all layers of the waveguide (the cover, metal film, and substrate) were treated as complex materials (i.e., those with both real and imaginary dielectric constants). In contrast, the majority of the previously published examples treated the cover and substrate media as purely real materials (i.e., without absorption loss), which resulted in significant underestimations of the SPP loss. While treating all three layers of the SMI waveguide as complex materials made solving the dispersion relations more computationally challenging, a more accurate assessment of SPP losses was achieved. Additionally, this treatment allowed the dispersion relations to be solved for different emitter emission regimes, which gave insight into the degree of loss compensation these organic conjugated polymers can provide when stimulated emission (gain) is induced in them. From the dispersion relation solutions, calculations of mode effective index, propagation length, penetration depth and magnetic field confinement, were carried out. From these data, it was shown that at visible wavelengths, surface plasmon mode propagation length and magnetic field

leakage of $>1300\ \mu\text{m}$ and $>74\ \mu\text{m}$, respectively, can be achieved through the optimization of the metal film thickness and by the addition of an organic polymer gain medium.

To experimentally validate the trends predicted by the dispersion relation solutions, a set of planar Insulator-Semiconductor-Metal-Insulator (ISMI) waveguides were fabricated. They consisted of 100 nm thick as-spin-cast ('neat') PFO films on thermally evaporated Ag metal films, with thicknesses ranging from 0 to 100 nm, sandwiched between a glass substrate and superstrate. The waveguided "edge" emission spectra from the fabricated planar ISMI waveguides was then studied over a range of optical excitation pump power densities. From these emission spectra, the peak emission intensity, amplified spontaneous emission (ASE) threshold, and ASE slope efficiency were compared as a function of metal film thickness. It was found that ISMI waveguides with Ag metal film thicknesses between 45 and 50 nm exhibited the greatest emission intensity, lowest ASE threshold and greatest ASE slope efficiency. These measurements provide compelling indirect evidence of the theoretically predicted ability to tune and optimize plasmon-polymer emitter coupling as a function of metal film thickness.

Additional experimental work presented herein has laid the ground work for the study of SPP-polymer emitter coupling as a function of polymer molecular dipole orientation, something which was not possible in the dispersion relations. This was achieved by preparing thin (100 nm) PFO films and using different treatment methods to promote in- and out-of-plane molecular dipole orientation and varying degrees of crystallinity. While it was beyond the scope of this thesis to fabricate waveguides at varying metal film thicknesses with multiple polymer molecular dipole orientations, methods to prepare amorphous, in-plane oriented and semi-crystalline PFO films were developed. Characterization of the polymer dipole orientation and crystallinity was carried out using grazing-incidence small- and wide-angle x-ray scattering measurement facilities at Brookhaven National Lab.

In parallel with the SMI waveguide research, a comprehensive body of both theoretical and experimental work was conducted on tubular metallic plasmonic nanostructures, which have been identified as potential candidates for molecular sensing, subwavelength resonator cavities for coherent nanoscale emitters, and other chip-scale optoelectronic circuitry applications. Tubular metallic nanostructures can be regarded as ‘rolled-up’ thin-film IMI-type waveguides and it has been shown that certain aspects of their plasmonic responses are analogous.

The target application of the nanotubes studied in this thesis were subwavelength optoelectronic applications, they were deliberately synthesized with a large (200 nm) inner diameters (ID), significantly larger than those studied in the literature ($ID < 35$ nm) [113-115]. The large ID of served two functions: (1) it would allow the tubes to be more readily in-filled with an organic polymer emitter to serve as a resonator cavity; and (2) the large ID could potentially support photonic modes, which may be used to couple to the SPP modes supported on the surface of the tube.

Owing to the fact that tubular metallic structures are a more complex geometry than planar thin film waveguides a fundamental understanding of their optical response as a function of wall thickness, inner diameter, excitation geometry, and polarization must be fully understood before attempting to successfully introduce an emitter material and optimize a waveguide or resonator behavior. To fundamentally understand the optical response of these structures, arrays of large 200 nm ID, 2 to 3- μ m-long gold nanotubes (AuNTs) with wall thicknesses ranging from 30 to 140 nm were synthesized in collaboration with Micha Fireman (Caltech/UCSB). The plasmonic response of both the large-area arrays and single nanowire-nanotube heterostructures were experimentally measured as a function of wall thickness, and incident excitation geometry with bright-field and dark-field microscopy and dark-field scattered-light spectroscopy. It was found that the resonant energy of the surface plasmon modes could be tuned by varying the wall

thickness and inner diameter. This in-turn allows the structure to be tailored for a given optical response.

Three-dimensional finite-difference-time-domain (FDTD) electromagnetic simulations were conducted on single nanotubes of corresponding geometries to those that were experimentally fabricated to identify and understand the modes supported by these structures as a function of wall thickness, inner diameter, excitation geometry, and polarization. These simulations demonstrated that large 200 nm ID AuNTs support three different mode types that depend on excitation direction and polarization: (1) when excitation is incident at the AuNT end, which we refer to as end-on excitation, propagating SPP modes are excited along the length of the nanotube walls, analogous to that of planar metal films and IMI waveguides [82]. (2) In addition to the propagating SPP mode, a photonic mode is excited in the core of the nanotube. Similarly, for excitation normal to the nanotube long axis (which we refer to as normal excitation), with electric field polarized parallel to the nanotube long axis, both a propagating SPP mode and a photonic mode are supported. (3) For excitation normal to the nanotube and polarized transverse to the long axis, a localized surface plasmon resonant mode not previously documented in the literature for nanotubes of this size was detected. This simulated localized surface plasmon resonance was akin to a localized ring-resonator-type surface plasmon mode, described by Apter *et. al* for low-aspect-ratio annular ring-shaped metallic structures [116]. Such resonant modes are desirable for a host of applications due to their narrower spectral width and tunability.

To experimentally confirm the presence the ring-resonator-type mode polarized bright-field and dark-field image analysis and polarized dark-field scattered-light spectroscopy were conducted on single nanowire/nanotube heterostructures. In doing so, the optical response of these structures was characterized and the first experimental evidence of ring resonator-type surface plasmon modes was observed. It was found that the nanotubes support both a photonic mode in the core of the structure and surface plasmon modes on the surface. When polarization is

shifted from 0° to 90° with respect to the long axis of the structure, the nanotube ceased to support propagating SPP mode and supported a lower-energy resonant mode characteristic of a ring-resonator-type localized surface plasmon resonance. The photonic mode in the core of the nanotube was found to redshift (in theory) when polarization was varied from 0° to 90° and likely contributed to the measured dark-field spectral response of the nanotubes.

The knowledge developed through this study of the optical response of tubular metallic nanostructures as a function of structure geometry and excitation condition has enabled initial experimental confirmation the presence of localized ring-resonator modes, and has paved the path towards successfully introducing a polymer gain medium in the core or surface of the nanotube. Furthermore, knowledge gained from the theoretical and experimental study of conjugated polymer emitter/plasmon coupling in SMI waveguides provides insight into how to optimize such coupling in more complex geometries such as the metallic nanotubes.

2 Dispersion Relation Calculations of Planar Asymmetric Insulator-Metal-Insulator and Semiconductor-Metal-Insulator Waveguides towards Increased Light Outcoupling Efficiency in Organic Optoelectronics

2.1 Abstract

The light outcoupling efficiency of organic light-emitting optoelectronic devices is severely limited by excitation of tightly-bound surface plasmon polaritons at the metal electrodes. To gain insight into low-loss plasmon-polymer coupling, a set of dispersion relations for a planar asymmetric organic semiconductor-metal-insulator, SMI, waveguide (consisting of F8BT-Ag-SiO₂ materials) were solved over a range of metal film thicknesses and dielectric constant conditions. The dispersion relation solutions demonstrate that by tuning metal film thickness, and the emission regime of the organic semiconductor, a significant fraction of surface plasmon polariton mode amplitude can be leaked into the active semiconductor layer, thereby decreasing the amount of optical energy trapped by the metal. At visible wavelengths, mode leakage increases by factors of up to 3.8 and 88 by tuning metal film thickness and by addition of gain, respectively.

The method used to solve these dispersion relations was based on a modified version of dispersion relations solved by Burton and Cassidy for an asymmetric silica-gold-silica insulator-metal-insulator (IMI) waveguide [82]. Unlike the Burton and Cassidy dispersion relation treatment, and others in the literature, our modified method presented in this work treats of all three layers of the SMI waveguide as complex materials (i.e., with both real and imaginary components of the complex dielectric constants). This approach, while more computationally intensive yields more physically accurate surface plasmon absorption loss values, and allowed the dispersion relations to be solved for different polymer emission regimes (e.g., steady state and stimulated emission). To validate our approach taken to solve the modified dispersion relations

for the planar asymmetric F8BT-Ag-SiO₂ SMI waveguide, the original Burton and Cassidy dispersion relations were independently reproduced and these solutions are also presented herein.

The work reported in this chapter has enabled the development and optimization of a set of experimentally fabricated SMI waveguide analogs with varying metal film thickness that are presented in Chapter 3. The experimental results show clear agreement in the behavior that is predicted by the modified dispersion relations presented in this chapter.

2.2 Introduction

Organic light-emitting diode (OLED) performance is significantly limited by poor light outcoupling efficiency, g_{out} (20% - 33.7%) [3-6,43,44] manifesting from: (1) non-radiative exciton decay within the organic semiconductor as heat to one of the electrodes (5.3% loss) [4,5]; (2) guided photonic modes within the device (9.3% - 35.2% loss) [2,42]; and, (3) significantly, to tightly-bound surface plasmon polariton (SPP) modes at the metal electrodes (20.5 - 46.8% loss) (see Fig. 2.1(a)) [3-6]. The major approaches taken to minimize optical energy loss to SPP modes in OLEDs include: (i) introduction of Bragg gratings or other wavelength-scale corrugated microstructures to fulfill the energy and momentum conservation of trapped modes and light propagating in air [3,6,43,44]; (ii) anisotropic orientation of the molecular dipole emitters of the active organic layer to an in-plane configuration that avoids coupling to bound SPP modes (limited to extended or anisotropic molecules) [3,43]; and (iii) using high index prisms to extract SPPs and waveguided modes [2]. Other approaches include developing electrodes fabricated from metals with SPP energies larger or smaller than the device operating energies so that they do not couple with photons emitted by the device [4,6], and adding spacer layers to control the degree of coupling to SPP modes [6,39]. The aforementioned strategies have potential to reduce SPP losses but may introduce new leakage or optical dissipation channels, and require additional and potentially complex fabrication, or significant changes to the device architecture [5].

Compelling evidence suggests that if the SPP mode character and leakage into the semiconductor can be controlled rather than suppressed entirely, SPPs may boost performance in a host of visible-light-based optoelectronic devices including OLEDs, organic photovoltaics, and organic lasers [21-24,31,39,41,42]. Here, we have taken a theoretical approach towards mitigating optical loss to tightly-bound by solving a set of three dispersion relations for a semiconductor-metal-insulator (SMI) asymmetric planar waveguide, which serves as a direct analogue to a metal electrode/organic semiconductor interface. Through calculations of mode effective index, propagation length, penetration depth and magnetic field confinement, we demonstrate that by tuning metal film thickness and emission regime, a significant fraction of SPP mode amplitude can leak into the organic semiconductor emitter layer, thereby decreasing the amount of optical energy lost to parasitic coupling to tightly bound SPP modes.

Prior to solving modified dispersion relations for the planar asymmetric F8BT-silver-silica semiconductor-metal-insulator (SMI) waveguide studied in this thesis (see Fig. 2.1(b)), dispersion relations solutions for a slightly asymmetric silica-gold-silica insulator-metal-insulator (IMI) waveguide originally solved by Burton and Cassidy were independently reproduced to validate the approach taken herein. [82]. The Burton and Cassidy waveguide was termed ‘slightly asymmetric’ because the silica cover and substrate had slightly different refractive index values, hence, it was not a truly symmetric structure. This slightly broken symmetry plays an important role in the number of mode solutions that IMI-type waveguides can support [82].

Both the Burton and Cassidy IMI waveguide and the SMI waveguide studied in this chapter are slightly asymmetric structures, which in-turn give rise to two distinct SPP mode symmetries (symmetric and antisymmetric), and two distinct SPP mode leakage types (bound and leaky), giving rise to four distinct SPP modes: symmetric bound (SB), symmetric leaky (SL), antisymmetric bound (AB), and antisymmetric leaky (AL) (see Fig. 2.1(c)-(d)). In perfectly symmetric IMI waveguides, the bound and leaky modes become degenerate, resulting in only two

distinct mode types, a symmetric and an antisymmetric mode [82,84]. The character of the four SPP mode types as well as their mathematical origin will be discussed in greater detail in the results and discussion section.

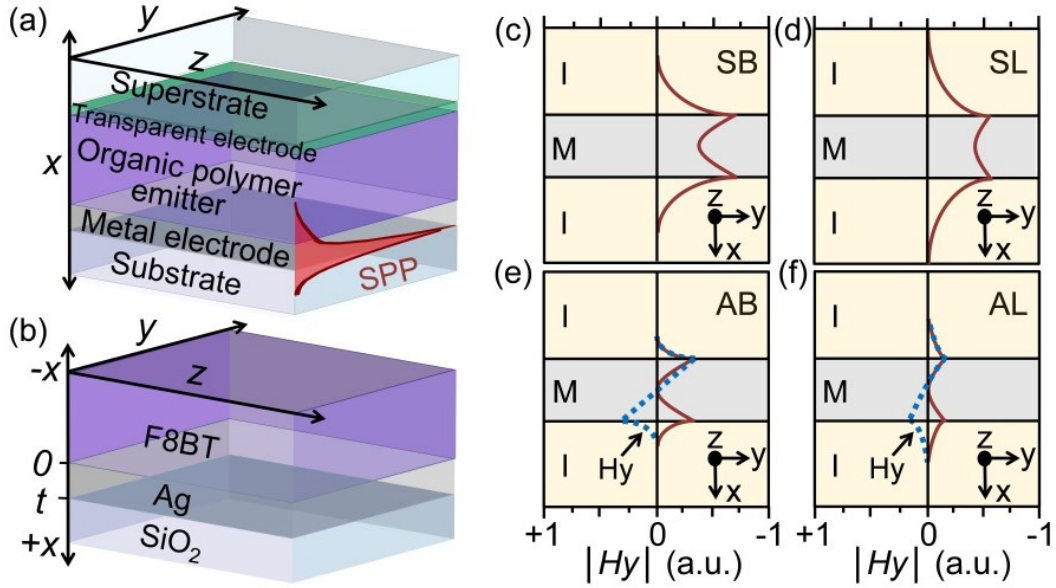


Figure 2.1. Illustrations of (a) a generic OLED exhibiting a tightly-bound SPP mode at the metal electrode propagating in the z-direction, and (b) the F8BT-Ag-SiO₂ SMI waveguide studied in this work . (c-f) Schematic representations of $|H_y|$ versus x cross-sections for: (c) SB, (d) SL, (e) AB, and (f) and AL for an antisymmetric IMI waveguide (where $0 < \left(\left(\frac{|\epsilon_{\text{cover}} - \epsilon_{\text{substrate}}|}{\epsilon_{\text{substrate}}} \right) \times 100 \right) < 1\%$). Blue dotted line in (e, f) represents H_y versus x cross-sections of the AB and AL modes, respectively. Color available in electronic copy.

2.3 Methods

2.3.1 Reproduction of Burton and Cassidy Dispersion Relation Solutions

In this study, SPP propagation is in the z-direction with the electric and magnetic field components decaying in the x-z and x-y planes, respectively (see Fig. 2.1(c)-(f)). The Burton and Cassidy IMI waveguide dispersion relations (see below) were solved at a fixed wavelength of 1.3 μm for a structure comprised of a gold thin film of finite thickness, taken to have a complex dielectric constant, $(\epsilon_{\text{metal}})$ (i.e., $\epsilon_{\text{metal}} = \epsilon_{\text{metal}}^r + i\epsilon_{\text{metal}}^i$, where $\epsilon_{\text{metal}}^r$ and $i\epsilon_{\text{metal}}^i$ are the real and imaginary components, respectively) of $-72.1 + i2.3$ sandwiched between two infinitely thick silica layers (i.e., the cover and substrate) of slightly different refractive indices, taken to have purely real dielectric constants (ϵ) (i.e., lacking an imaginary permittivity component: $\epsilon_{\text{cover}} = \epsilon_{\text{cover}}^r$ and $\epsilon_{\text{substrate}} = \epsilon_{\text{substrate}}^r$) of 2.1316 and 2.098, respectively [82]. As mentioned in the introduction, the silica cover and substrate had slightly different refractive indices to break the symmetry of the structure so that all four SPP mode types could be studied.

While some of the seminal theoretical IMI-type waveguide studies consider the cover and substrate dielectric medium to have a complex dielectric constant (i.e., $\epsilon_{\text{cover}} = \epsilon_{\text{cover}}^r + i\epsilon_{\text{cover}}^i$, where $\epsilon_{\text{cover}}^r$ and $i\epsilon_{\text{cover}}^i$ are the real and imaginary components, respectively), many of these studies assume both that both dielectric constants of the cover and substrate media are purely real (i.e., the imaginary component is neglected; $\epsilon_{\text{cover}} = \epsilon_{\text{cover}}^r$ and $\epsilon_{\text{substrate}} = \epsilon_{\text{substrate}}^r$), and only the metal film is taken to have a complex dielectric constant (i.e., $\epsilon_{\text{metal}} = \epsilon_{\text{metal}}^r + i\epsilon_{\text{metal}}^i$) [82,117,118]. This was done to minimize the computational intensity of solving the dispersion relation to yield the complex plasmon polariton wavevector, k . In some systems, because low loss dielectric media such as SiO_2 were utilized, neglecting the imaginary component of the complex dielectric constant (i.e., loss) and taking the dielectric constant to be a purely real was a valid simplifying

assumption [82]. However, in making this assumption, SPP propagation lengths and in-turn loss could be overestimated.

Dispersion relations (Eqs. 1-4) for the Burton and Cassidy IMI waveguide were solved iteratively over a range of metal film thicknesses of 20-100 nm by bounding the real (k^r) and imaginary (k^i) components of the complex plasmon polariton wavevector, k (where $k = k^r + ik^i$), using the Wolfram Mathematica® 8 “NMinimize” function which finds the global minimum of a problem with constraints (see Appendix A Section A1 for Wolfram Mathematica® dispersion relation code and boundary conditions used for the solutions) [82]:

$$\frac{\alpha_1 \varepsilon_2}{\alpha_2 \varepsilon_1} + \frac{(\varepsilon_0 \alpha_1 + \varepsilon_1 \alpha_0) + (\varepsilon_0 \alpha_1 - \varepsilon_1 \alpha_0) \exp(-2\alpha_1 t)}{(\varepsilon_0 \alpha_1 + \varepsilon_1 \alpha_0) - (\varepsilon_0 \alpha_1 - \varepsilon_1 \alpha_0) \exp(-2\alpha_1 t)} = 0$$

(1)

where

$$\alpha_0^2 = k^2 - k_0^2 \varepsilon_0 \quad (2)$$

$$\alpha_1^2 = k^2 - k_0^2 \varepsilon_1 \quad (3)$$

$$\alpha_2^2 = k^2 - k_0^2 \varepsilon_2 \quad (4)$$

and where α_0 , α_1 , and α_2 are decay constants and ε_0 , ε_1 , and ε_2 are the dielectric constants of the SiO₂ cover, the thin gold film and the SiO₂ cover media respectively, t is the thickness of the gold film, and k_0 is the free space wavenumber ($k_0 = 2\pi / \lambda$). NMinimize can return values indicating a solution but which are not physically reasonable or accurate. Thus, the values for k^r and k^i were only accepted when the left hand side of the dispersion relation (Eq. 1) had magnitudes $< 10^{-15}$.

From the real (k^r) and imaginary (k^i) components of the complex surface plasmon polariton wavevector, the mode effective index, N_{eff} , and characteristic SPP mode propagation length, L , were calculated for all four modes according to [82]:

$$N_{eff} = k^r / k_0 \quad (5)$$

$$L = 1 / k^i \quad (6)$$

2.3.2 Solving Dispersion Relation of Planar Asymmetric F8BT-Ag-SiO₂ SMI Waveguides

As for the Burton and Cassidy dispersion relations, SPP propagation for planar asymmetric F8BT-Ag-SiO₂ SMI waveguides is in the z-direction with the electric and magnetic field components decaying in the x-z and x-y planes, respectively (see Fig. 2.1). The SMI waveguide was comprised of a silver film of thickness, t , which extended from 0- t along the x-axis and two infinite dielectric/semiconductor slabs: a SiO₂ substrate, which extended from t to $+x$ along the x-axis and an F8BT (poly[(9,9-di-*n*-octylfluorenyl-2,7-diyl)-*alt*-(benzo[2,1,3]thiadiazol-4,8-diyl)]) cover, which extended 0 to $-x$, along the x-axis (see Fig. 2.1(b)). Dispersion relations were solved at a fixed wavelength, λ , of 576 nm (which correlates to the peak gain wavelength of F8BT [120]) for three dielectric constant cases, where the imaginary components of the complex dielectric constants (ϵ), of the SiO₂ substrate and F8BT cover were varied. The complex dielectric constant of silver at 576 nm for all three cases was fixed at $-12.5681 + i0.854591$ [77]. The complex dielectric constant for F8BT at 576 nm under steady state excitation was calculated using empirically-derived expressions for the standard critical point exciton model from Campoy-Quiles *et al.* (see Eq. (1) in [120] and Table 1 in [120] and [121]). The first dielectric constant case, defined as Purely Real Steady State (PRSS) was solved to establish the characteristics of a system without absorption losses in the substrate or cover (i.e., lacking an imaginary dielectric constant component: $\epsilon = \epsilon^r$, where ϵ^r is the real part of the cover or substrate dielectric constant).

For the PRSS case, $\epsilon_{SiO_2} = 2.13$ and $\epsilon_{F8BT} = 3.6446$. The second dielectric constant case, defined as Complex Steady State (CSS), was solved for when the cover and substrate media were considered to have complex dielectric constants (where $\epsilon = \epsilon^r + i\epsilon^i$ and ϵ^r and ϵ^i are the real and imaginary components, respectively), which accounted for absorption losses in both media. For the CSS case, $\epsilon_{SiO_2} = 2.13 + i0.0015$ and $\epsilon_{F8BT} = 3.6446 + i0.2358$. Both the PRSS and CSS dielectric constant cases are assumed to represent a regime where the F8BT undergoes spontaneous emission. The third case, defined as Complex Gain (CG), took account for absorption loss in the SiO₂ substrate but was solved for when the F8BT can provide loss compensation (i.e., gain) to the propagating SPP modes (i.e., when the F8BT undergoes stimulated emission and a population inversion). The extrinsic, or net gain of F8BT measured in aqueous solution can be $\geq 10,000 \text{ cm}^{-1}$, but in solid-state waveguide geometries this value is often lower due to a degree of solid state emission quenching/reabsorption, which contribute to lower net gain in the solid state. [122-124]. For the CG dispersion relation, a net gain of 47 cm^{-1} was assumed - a relatively modest assumption for F8BT in planar thin film geometries, where net gains upwards of 79 cm^{-1} have been measured [122-124]. Gain can be mathematically reflected in the complex dielectric constant of a material by a negative imaginary component (ϵ^i) [125]. To relate the value of ϵ^i for F8BT to a net gain of 47 cm^{-1} at 576 nm, the following expression was used [125]: $\gamma_{net} = -k_0 \epsilon^i / (\epsilon^r)^{1/2}$ where γ_{net} is the net power gain coefficient, k_0 is the free space wavenumber ($k_0 = 2\pi / \lambda$). Thus, for the CG case,

$$\epsilon_{SiO_2} = 2.13 + i0.0015 \text{ and } \epsilon_{F8BT} = 3.6446 - i0.00083.$$

Dispersion relations (Eqs. 1-4 in Section 2.3.1) for the three dielectric constant cases were solved iteratively by bounding the real (ϵ^r) and imaginary (ϵ^i) components of the complex plasmon polariton wavevector, k , using the Wolfram Mathematica® 8 “NMinimize” function as before (see Appendix A Section A2 for Wolfram Mathematica® dispersion relation code and boundary conditions used for the solutions).

Note, in Equations 1-4 from [82] (see in Section 2.3.1), the original convention took the decay constants α_0, α_1 , and α_2 , and the dielectric constants $\varepsilon_0, \varepsilon_1$, and ε_2 to be that of the cover, the thin metal film, and the substrate media, respectively. However, for the F8BT-Ag-SiO₂ studied in this work, the assignments of the cover and substrate media have been reversed in Equations 1-4 in section 2.3.1 (i.e., the decay constants, α_0, α_1 , and α_2 , and dielectric constants, $\varepsilon_0, \varepsilon_1$, and ε_2 are that of the substrate (SiO₂), the thin silver film and the cover (F8BT) media, respectively). The assignment used for this work resulted in solutions that were indistinguishable from those solved with the cover and substrate assignments in [82]; however, solutions were more directly obtained with the reversed cover and substrate assignment. This enabled solutions to be more rapidly obtained for the three dielectric constant cases as a function of film thickness.

From the real (k^r) and imaginary (k^i) components of the complex surface plasmon polariton wavevector, the mode effective index, N_{eff} , and characteristic SPP mode propagation length, L , were calculated for all modes of each of the three dielectric constant cases according to Equations 5 and 6 (see Section 2.3.1) [82]. SPP mode penetration depth, D in the cover and substrate dielectric media (F8BT and SiO₂) were calculated for all four modes of each of the three dielectric constant cases using the following equation [82]:

$$D = 1 / \alpha^r \quad (7)$$

where α^r is the real part of the relevant decay constant (Eqns. 2-4). Magnetic field (H_y) and penetration depth ($f(x)$) into each of the three layers of the waveguide (SiO₂, Ag, and F8BT) were calculated at two metal film thickness, $t = 47$ nm and 80 nm for all four modes of each of the three dielectric constant cases, using the following equations [84]:

$$SiO_2 : f(x) = \left[\cosh(\alpha_1 x) + \frac{\alpha_0 \varepsilon_1}{\alpha_1 \varepsilon_0} \sinh(\alpha_1 t) \right] e^{-\alpha_2(x-t)}, \quad x > t \quad (8)$$

$$\text{Ag} : f(x) = \cosh(\alpha_1 x) + \frac{\alpha_0 \varepsilon_1}{\alpha_1 \varepsilon_0} \sinh(\alpha_1 x), \quad 0 < x < t \quad (9)$$

$$\text{F8BT} : f(x) = e^{\alpha_0 x}, \quad x < 0. \quad (10)$$

2.4 Results and Discussion

As described briefly in the introduction for IMI-type waveguides with slightly broken symmetry, such as the silica-gold-silica waveguide studied by Burton and Cassidy, two mode symmetries (symmetric and antisymmetric) and two mode leakage types (bound and leaky) are typically observed, giving rise to four distinct mode types: symmetric bound (SB), antisymmetric bound (AB), symmetric leaky (SL), and antisymmetric leaky (AL) (see Fig. 2.1(c)-(f)) [82-84,117-119]. These four modes occur when the dielectric constants of the substrate and cover are not identical ($\varepsilon_{\text{cover}} \neq \varepsilon_{\text{substrate}}$) and arise because the decay constants (α 's) are only defined as their squares (Eqs. 2-4 Section 2.3.1), thus having both positive and negative roots [117]. In perfectly symmetric structures ($\varepsilon_{\text{cover}} = \varepsilon_{\text{substrate}}$) the bound and leaky modes are degenerate and only two modes are supported: symmetric and antisymmetric modes [82,83,117]. By assigning which root is used in the dispersion relation equation for each of the three media (the cover, substrate, and gold film) four solutions arise. The SB and AB modes were found when all three decay constants were taken to be positive ($\alpha_0, \alpha_1, \alpha_2 > 0$). The SL mode was found when $\alpha_2 < 0$, $\alpha_0, \alpha_1 > 0$ and the AL mode was found when $\alpha_0 < 0$, $\alpha_1, \alpha_2 > 0$. No solutions were found when the negative root of the metal decay constant (α_1) was used in the dispersion relation solution, nor was a solution found when both α_0 and $\alpha_2 < 0$ [82].

SPP mode symmetry is typically defined by the character of the cross-sectional profile of the magnetic field (H_y) or magnitude of the magnetic field ($|H_y|$) in the metal film and is schematically represented in Figs. 2.1(c)-1(f) for a structure with only slightly broken symmetry (i.e., 1% difference between ϵ_{cover} and $\epsilon_{\text{substrate}}$) [117,118]. Symmetric modes have H_y fields that do not change sign across the metal film (Figs. 2.1(c) and 1(d)), while antisymmetric modes exhibit a zero or nodal point within the metal film (Figs. 2.1(e) and 2.1(f)) [117]. Thus, H_y fields of antisymmetric modes result in an opposite charge distribution on either side of the metal film and, hence, a significant fraction of the mode power resides within the metal, which leads to less leakage into the surrounding media and shorter SPP propagation lengths (Figs. 2.1(e) and (f)) [83]. ‘Leaky’ modes are less confined to the metal and in turn generally penetrate further into the surrounding media than ‘bound’ modes (Figs. 2.1(d) and (f)). In cases where the difference between the cover and substrate dielectric constants is larger, the magnetic field profiles can maintain their characteristic behavior, but leakage is expected to occur more significantly into the higher refractive index medium [82,83].

For the Burton and Cassidy silica-gold-silica IMI waveguide, independently reproduced plots of mode effective index (N_{eff}) and propagation length L versus metal film thickness (t) are shown in Figs. 2.2 and 2.3. These independently produced results are in excellent agreement with the Burton and Cassidy solutions [82]. Therefore, it is concluded that the code and method developed to solve these dispersion relations is valid. For a full interpretation of these results see [82].

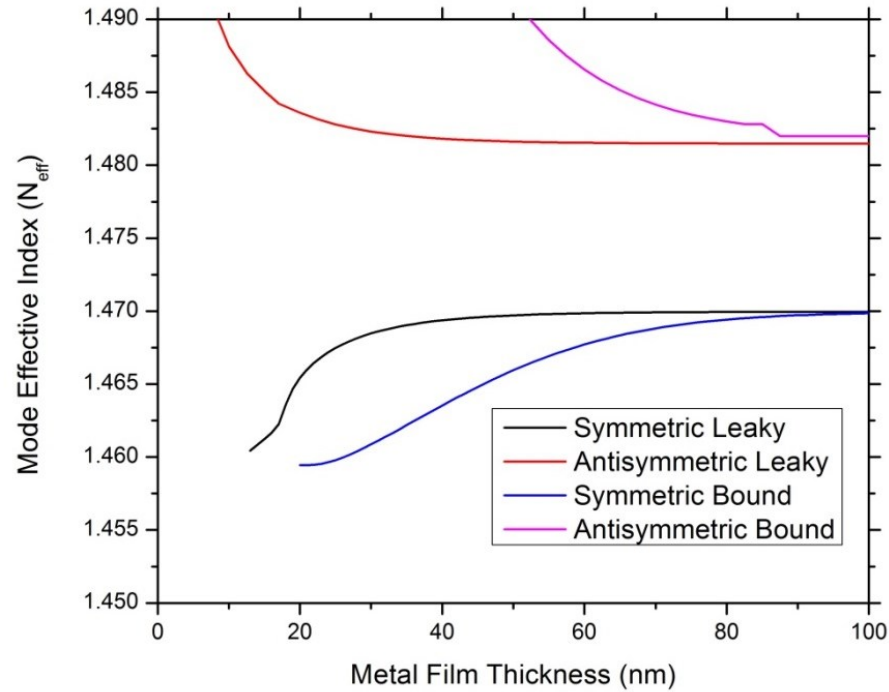


Figure 2.2. Independently reproduced plot of the effective mode index versus metal film thicknesses for the four SPP mode symmetries supported by the slightly asymmetric silica-gold-silica IMI waveguide presented in the Burton and Cassidy work [82]. Color available in electronic copy.

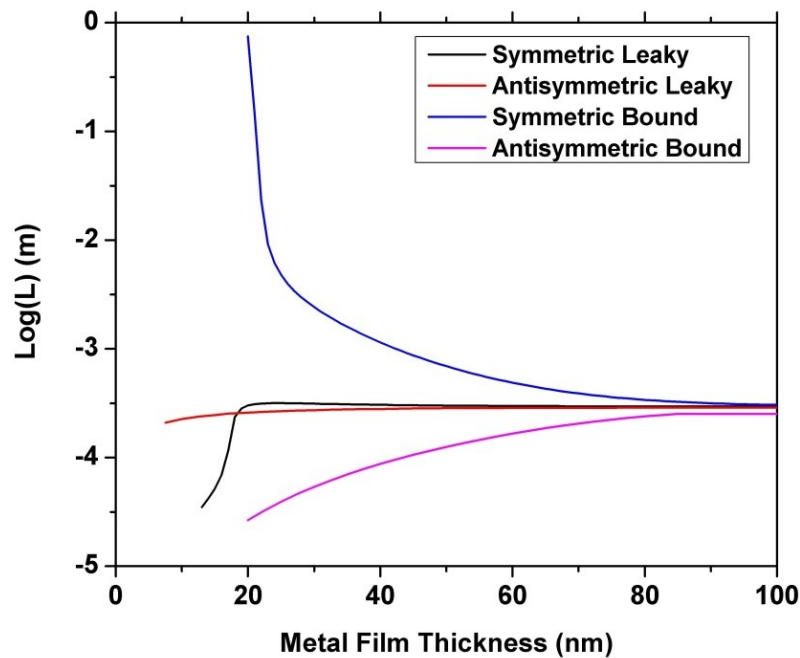


Figure 2.3. Independently reproduced plot of propagation length L versus metal film thicknesses for the slightly symmetric IMI silica-gold-silica waveguide presented in the Burton and Cassidy work [82]. Color available in electronic copy.

Analogous to the Burton and Cassidy asymmetric IMI waveguide, the planar asymmetric F8BT-Ag-SiO₂ SMI waveguide also exhibited the four distinct mode types (see Fig. 2.1(c)-(e)) for all three dielectric constant cases that were solved. Additionally, the four modes were solved with the same positive and negative root assignments as that of the Burton and Cassidy IMI waveguide: the SB and AB modes were found when all three decay constants were taken to be positive ($\alpha_0, \alpha_1, \alpha_2 > 0$), the SL mode was found when $\alpha_2 < 0$, $\alpha_0, \alpha_1 > 0$, and the AL mode was found when $\alpha_0 < 0$, $\alpha_1, \alpha_2 > 0$. No solutions were found when the negative root of the metal decay constant (α_1) was used in the dispersion relation solution, nor was a solution found when both α_0 and $\alpha_2 < 0$ [82].

For the F8BT-Ag-SiO₂ SMI structure, plots of mode effective index (N_{eff}) versus metal film thickness (t) are shown in Figs. 2.4(a)-(c) for the three dielectric constant cases (see Eq. 5 in Section 2.3.1). For all three cases, the two antisymmetric modes had greater N_{eff} values (ranging from 2.26 to 8.78) than the two symmetric modes (ranging from 1.60 to 1.64) over all calculated metal film thicknesses, and N_{eff} increased with decreasing t . A greater N_{eff} indicated that the majority of the mode energy was confined within the material with the highest dielectric constant, i.e., the metal [82]. Since the symmetric modes had the lowest N_{eff} values, it was expected that the modes penetrated much further into the insulator/semiconductor media than the antisymmetric modes. Bound modes generally had slightly higher N_{eff} values than leaky modes suggesting they were more tightly confined to the metal-insulator/semiconductor interface [82]. This was observed more clearly at $t < 40$ nm, where the disparity in N_{eff} between bound and leaky modes for both the symmetric and antisymmetric cases increased with decreasing t .

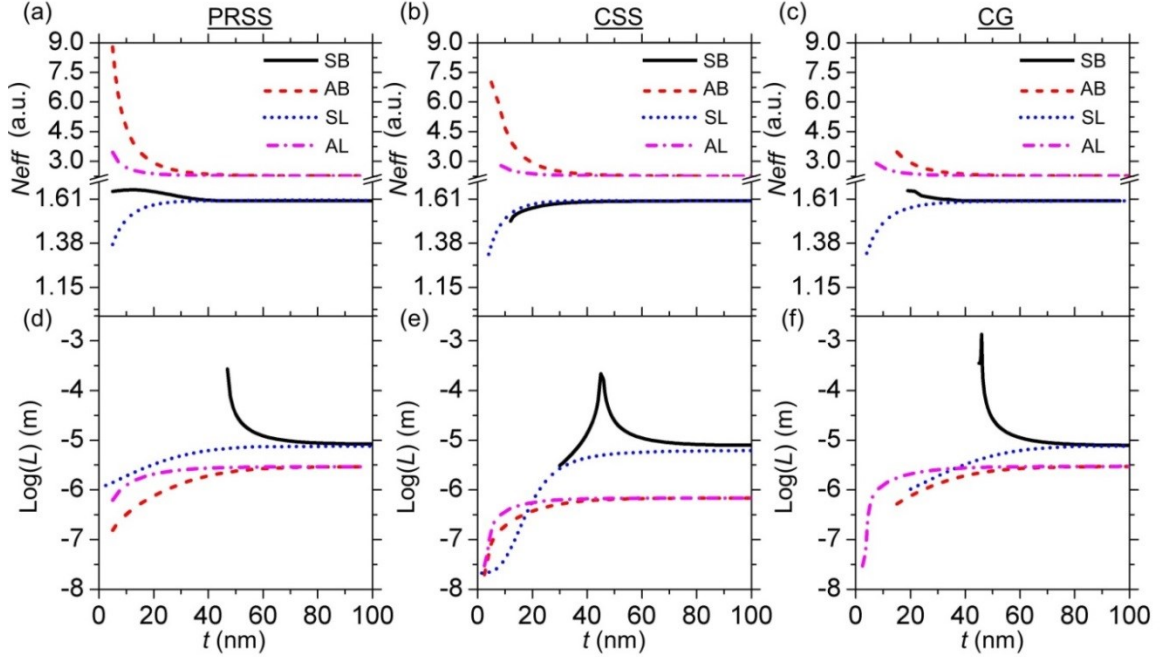


Figure 2.4. (a-c) N_{eff} and (d-f) $\text{Log}_{10}(L)$ versus t calculated for (a, d) the PRSS case, (b, e) the CSS case and (c, f) the CG case for all four SPP modes supported by the F8BT-Ag-SiO₂ SMI waveguide.

For all three dielectric constant cases, symmetric modes exhibited mode propagation length (L) values significantly larger than antisymmetric modes over the range of t (see Figs. 2.4(d)-4(f) and Eq. 6 in Section 2.3.1). The shorter L values of the antisymmetric modes were attributed to greater mode confinement within the metal. With increasing t , the bound and leaky mode solutions of the symmetric and antisymmetric modes became degenerate in L [82]. The SB mode, which had the longest L values for $45 \text{ nm} \leq t \leq 47 \text{ nm}$, was calculated to propagate $217 \text{ }\mu\text{m}$ for the CSS case, $271 \text{ }\mu\text{m}$ for the PRSS case, and $1357 \text{ }\mu\text{m}$ for the CG case. It was notable that the PRSS case overestimated L by a factor of 1.25 over the CSS case and that the CG case showed an enhancement in L of 6.25 over the CSS case. The values of L of the SB mode decreased significantly from its maximum for $t < 45 \text{ nm}$ and $t > 47 \text{ nm}$. For all three dielectric constant conditions, at larger metal film thicknesses, e.g., $t = 80 \text{ nm}$ (selected because for $t > 60 \text{ nm}$, L of all four modes were almost unchanged) L values were reduced significantly and converged to

values in the range 8.26 - 8.82 μm for the SB mode and 6.08 - 7.47 μm for the SL mode. The antisymmetric modes exhibited maximum L at $t > 60$ nm, and at $t = 80$ nm the CSS case resulted in AB and AL mode L values of 0.68 μm , i.e., more than a factor of 4 shorter than the PRSS (AB: 2.88 μm , AL: 2.93 μm) and CG (AB: 2.92 μm , AL: 2.96 μm) cases, indicating they are more lossy and, hence more tightly bound modes relative to the symmetric modes. These results show that the presence of gain in the semiconductor can enhance SB mode propagation length significantly and also underscore the importance of treating the cover and substrate as media with complex dielectric constants, so that absorption loss is taken into account and, in turn, L is not overestimated.

For PRSS and CG cases, solutions for the SB mode for L below $t = 47$ nm and 45 nm, respectively, were not included in Fig. 2.4(d) and 4(f) because the imaginary component of the complex plasmon polariton wavevector k^i (in the forward z-direction) became negative, indicating that the mode becomes highly dispersive and leaks into the surrounding cover and substrate media with little forward momentum. It is known that the SB mode can exhibit a mode cutoff at a certain metal thickness (t_{cutoff}), below which k^i becomes negative and the mode either ceases to propagate or changes character from a bound to a growing or leaky mode [84,118]. The existence of a SB mode t_{cutoff} is highly dependent on the values of the real and imaginary parts of the complex dielectric constants of the cover and substrate media [84,118]. t_{cutoff} is expected to decrease as the values of the real parts of the cover and substrate dielectric constants converge [84]. Positive imaginary components of the cover and substrate dielectric constants also results in a decrease in t_{cutoff} because the attenuation introduced by the positive imaginary component forces the mode to be more tightly confined to the metal-dielectric/semiconductor interface as opposed to leaking into the cover and/or substrate media. For the F8BT-Ag-SiO₂ SMI waveguide, the PRSS case had no imaginary dielectric constant components for either the cover or substrate ($\epsilon_{\text{SiO}_2}^i = \epsilon_{\text{F8BT}}^i = 0$); the CG case had a small negative imaginary component for F8BT to reflect

gain ($\epsilon_{F8BT}^i = -0.00083$) and only a small positive imaginary component for SiO_2 ($\epsilon_{\text{SiO}_2}^i = 0.0015$).

Based on these considerations we conclude that the SB mode exhibited a metal-film-thickness-dependent mode cutoff under the PRSS and CG conditions and the SMI structure did not support the SB mode below $t_{\text{cutoff}} \sim 45$ and 47 nm, respectively. Conversely, under the CSS condition, which had both a cover and substrate with positive imaginary components ($\epsilon_{\text{SiO}_2}^i = 0.0015$ and $\epsilon_{F8BT}^i = 0.2358$), the SB mode is supported down to a metal film thickness of less than 30 nm, well below the cutoff thickness of the PRSS and CG cases.

To further understand the spatial distribution of the SPP mode energy within the three layers of the SMI waveguide, the mode penetration depth, D , into both cover and substrate for the four modes and three dielectric constant cases were calculated over a metal film thickness range of 25 - 100 nm (see Figs. 2.5(a)-(h) and Eq. 7 Section 2.3.1). For all modes and dielectric constant cases, D was much greater in the medium with the larger dielectric constant (F8BT), particularly for symmetric modes. The symmetric modes in Figs. 2.5(a)-(d), both exhibited significantly greater D values in both SiO_2 and F8BT because they were not as tightly bound to the metal as the antisymmetric modes. As a result, the dielectric constant changes for the three cases had significant impact on D . The SB mode exhibited relatively constant D values ($D \approx 140$ nm) in SiO_2 as a function of t but penetration into F8BT increased significantly with decreasing film thickness to a value of $176 \mu\text{m}$ for the PRSS case, $0.8 \mu\text{m}$ for the CSS case and $74 \mu\text{m}$ for the CG case at a thickness of 47 nm, i.e., the approximate film thickness that yielded the longest propagation length; see Figs. 2.4(d)-4(f), 2.5(a), and 2.5(b). D of the SB mode in F8BT for the CSS case was over two orders of magnitude less than the PRSS and the CG cases. When comparing the PRSS case and the CG case, the PRSS case penetrated only slightly farther in to the F8BT.

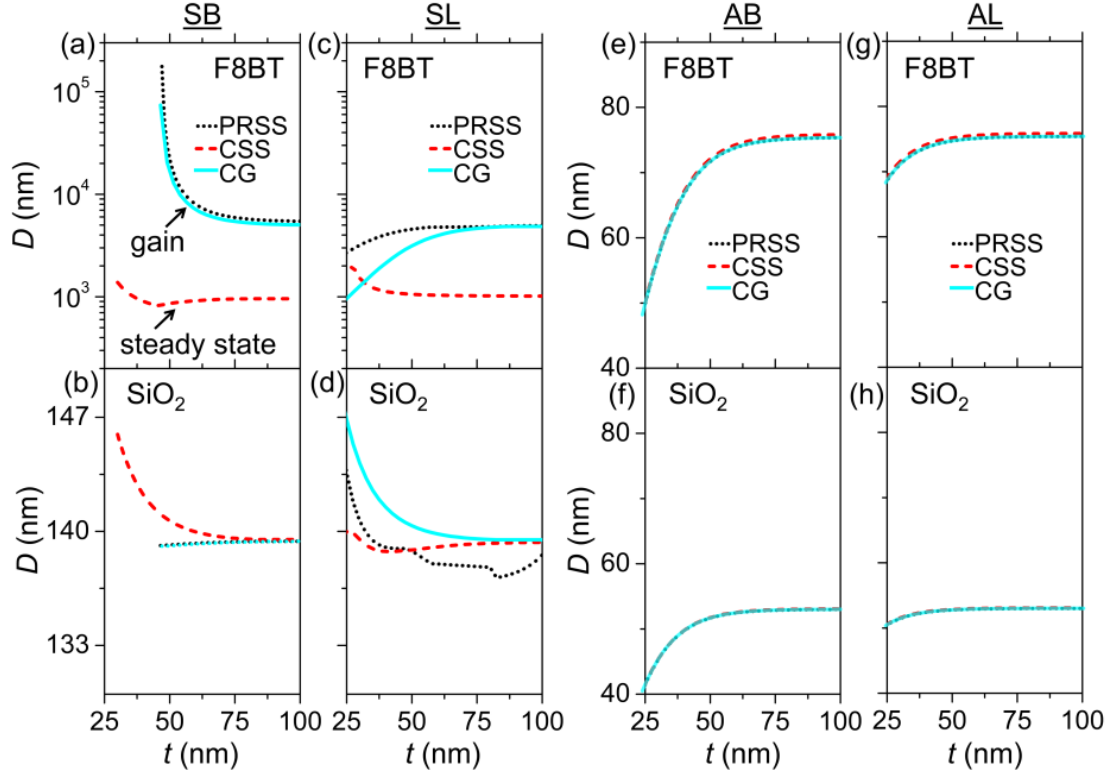


Figure 2.5. D as a function of t , in F8BT (a,c,e,g) and SiO₂ (b,d,f,h) for: (a,b) SB; (c,d) SL; (e,f) AB; (g,h) AL for three SMI waveguide dielectric constant cases.

The SL mode exhibited an almost constant D of approximately 138 nm in SiO₂ for $t > 30$ nm for the three dielectric constant cases. In contrast, the CSS case exhibited a decrease in D with decreasing $t > 30$, and the PRSS and CG cases showed an increase in D , at $t < 30$ nm (see Figs. 2.5(c) and (d)). D of the SL mode in F8BT for the PRSS and CG cases exhibited a trend of decreasing D with decreasing thickness for $t < 65$ nm, with the PRSS case having greatest overall D value of 4.96 μm at $t = 100$ nm compared to the CG case with a maximum D value of 4.86 μm at $t = 100$ nm (see Fig. 5(c)). At $t < 40$ nm, the trend in D for the SL mode in F8BT for the CSS case deviated slightly from the PRSS and CG cases and exhibited a local maximum at $t = 23.5$ nm and then rapidly decreases with decreasing t (not shown).

For the AB and AL modes (Fig. 2.5(e)-(h)), D values were small (< 55 nm in SiO₂ and < 80 nm in F8BT) and were virtually identical for the three dielectric constant cases. Small penetration

depths relative to the SB and SL modes further suggest that these were more tightly bound lossy modes that were largely confined to the metal-insulator/semiconductor interfaces. As a result, large changes in the imaginary part of the complex dielectric constants of the cover/substrate media did not appear to have a notable impact on the penetration depth of antisymmetric modes into the SiO₂ and F8BT. D was relatively constant for both the AB and AL modes for all three dielectric constant cases for $t > 40$ nm with average D values of 52 nm in SiO₂ and 74 nm in F8BT. Below $t = 40$ nm, D decreased exponentially with decreasing film thickness.

Two representative film thicknesses ($t = 47$ nm, where the maximum D and L values were observed; and $t = 80$ nm, selected because for $t > 60$ nm, D and L values for all four modes were almost unchanged) were chosen to illustrate how the cover dielectric constant (and hence the F8BT emission regime) and substrate affect H_y and $|H_y|$ leakage of the four modes (see Figs. 2.6(a)-(g) and Eqs. 8-10 in Section 2.3.1). At $t = 80$ nm, $|H_y|$ at the SiO₂/silver interface for all four modes, especially the SB mode, was greater than that at $t = 47$ nm due to decreased field leakage into the cover and substrate. $|H_y|$ leaked significantly further into the higher dielectric constant medium (F8BT) and the SB mode exhibited virtually identical magnetic field profiles in SiO₂ and silver for the three dielectric constant cases at both t values. However, the SB mode, which had the greatest field amplitude of the four SPP modes, exhibited a strong dependence of H_y and $|H_y|$ leakage into the F8BT on the dielectric constant case (see Figs. 2.6(a) and (b), respectively). At $t = 47$ nm, the PRSS and CG cases showed extreme leakage into the F8BT and did not exhibit the characteristic exponential decay into the cover and substrate media. At 75% of the amplitude at the F8BT/silver interface, the magnetic field of the SB mode for the PRSS case extended more than 50 μm into the F8BT and the CG case extended over 21 μm , whereas the CSS case only extended 0.5 μm . The SB mode supported by all three cases was still a bound mode according to convention (see Fig. 2.1(c)), albeit weakly, as the metal thickness was almost at the cutoff value at which the mode character changes to a “leaky” mode and/or ceases to propagate in the z -direction. Large SB mode field leakages at small t values have been reported in

prior studies of IMI waveguides and while the historical naming convention of the mode does not accurately reflect this leaky behavior, it is congruent with the literature [82,118,119]. At $t = 80$ nm and at 75% of the amplitude at the F8BT/silver interface, the SB mode $|H_y|$ profiles for all three cases exhibited shorter magnetic field decay lengths into the F8BT (~ 5.5 μm for the PRSS and CG cases and 0.96 μm for the CSS case) (see Fig. 2.6(c)). This extreme leakage enhancement at $t = 47$ nm compared to the tightly bound magnetic field at $t = 80$ nm is depicted in the schematic insets in Figure. 2.6(b) and (c), respectively. This substantially diminished leakage is depicted in the illustration inset in Fig. 2.6(c). This is attributed to increased mode confinement within the thicker metal slab and diminished influence by the surrounding media.

The SL mode behaved similarly to the SB mode in that $|H_y|$ leakage was greater into the F8BT than silica, and followed the same trend in leakage as a function of dielectric constant condition: $|H_y|_{\text{PRSS}} > |H_y|_{\text{CG}} > (|H_y|_{\text{CSS}})$ (see Fig. 2.6(d) and (e), and as a function of Ag film thickness). However, unlike the SB mode, the SL mode exhibited slightly greater field leakage at the 80 nm case. At $t = 47$ nm, at 75% of the amplitude at the F8BT/silver interface SL mode exhibits magnetic field leakage values of 1.28, 0.31, and 0.83 μm , for the PRSS, CSS, and CG cases, respectively. At $t = 80$ nm, at 75% of the amplitude at the F8BT/silver interface SL mode exhibits magnetic field leakage values of 1.3, 0.299, and 1.3 μm , for the PRSS, CSS, and CG cases, respectively.

The antisymmetric modes exhibited much lower $|H_y|$ values than the symmetric modes and their field profiles were largely unaffected by film thickness and dielectric constant case (see Figs. 2.6(f)-(i)). For all three dielectric constant conditions (PRSS, CSS, and CG) and the two metal film thicknesses ($t = 47$ and 80 nm), at 75% of the amplitude at the F8BT/silver interface AB and AL modes exhibited magnetic field leakage values of ranging from 0.2 – 0.22 μm . One noteworthy disparity in magnetic field leakage that the antisymmetric modes exhibited was a slightly greater magnetic field leakage into the silica substrate for the PRSS dielectric constant

condition (see Fig. 2.6(f)-(i)). This is attributed to the fact in the PRSS dielectric constant case, both the cover and substrate media are treated as purely real, which may reduce the mode confinement, allowing increased leakage into the silica substrate. However, this deviation observed in the PRSS dielectric constant case is not an to be considered a true reflection of physical reality, which is more accurately predicted by the CSS and CG dielectric constant cases that exhibit no such deviation.

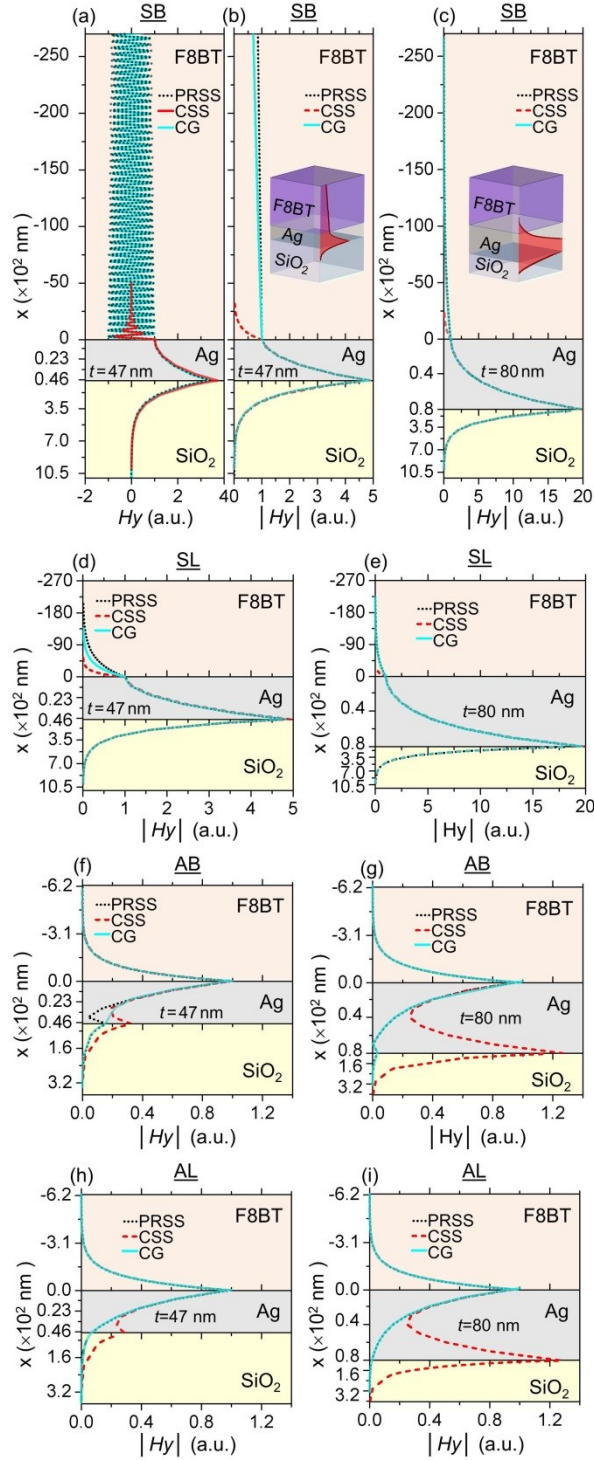


Figure 2.6. (a) H_y and (b-g) $|H_y|$ calculated at $t = 47$ nm (a,b,d,f) and $t = 80$ nm (c,e,g) for the SB (a-c), SL (d,e), AB (f,g) and AL (h,i) modes for all three SMI waveguide dielectric constant cases. Schematic illustrations of the F8BT-Ag-SiO₂ SMI waveguide inset in (b,c) represent the $|H_y|$ of the highly radiative ‘leaky’ SB mode at $t = 47$ nm and the tightly-bound SB mode $t = 80$ nm, respectively. AL mode not included. Color available in electronic copy.

2.5 Conclusion

A comprehensive set of dispersion relations were solved for a planar asymmetric F8BT-Ag-SiO₂ (SMI) waveguide over a range of metal film thicknesses, and three dielectric constant conditions. Unlike the majority of dispersion relations presented in the literature, the set that were solved included those where all three layers of the waveguide were treated as “real” materials, i.e., with complex dielectric constants. While this was more computationally intensive it allowed dispersion relations of the SMI waveguide to be solved under representative conditions of steady state and stimulated emission regimes of the F8BT emitter and accurately accounted for absorption loss in all three layers of the waveguide.

The solutions of these dispersion relations demonstrated that by tuning metal film thickness, and the emission regime of the organic semiconductor, a significant fraction of surface plasmon polariton mode amplitude could be leaked into the active semiconductor layer, thereby decreasing the amount of optical energy trapped by the metal. At visible wavelengths, mode leakage increased by factors of up to 3.8 and 88 by tuning metal film thickness and by addition of gain, respectively. This enhanced SPP field leakage and increased propagation length may lead to the ability to mitigate surface plasmon losses at metallic electrodes in organic optoelectronic devices such as OLEDs and organic lasers.

Our theoretical results may vary somewhat from experiment due to metal film quality and the fact that our calculations do not take into account a finite thickness of the cover and substrate nor the F8BT dipole orientation (which is expected to play a critical role in the degree of coupling to SPP modes at optical frequencies) [31,126-129]. A dipole oriented parallel to the plane of the polymer-metal interface is expected to be damped by its own image on the metal surface, while a dipole oriented perpendicular to the plane is expected to couple to SPP modes [31, 129]. Conversely, because the calculations here were carried out at a single wavelength coinciding with the peak gain wavelength of the F8BT and at a conservative net gain value for F8BT, the results do not fully account for optical gain that can occur over a broader spectral range (typically 552 -

600 nm) and for the higher F8BT gain values that could be achieved in practice [122,129].

Experimental work presented in Chapter 3 provides compelling evidence that validates the theoretically predicted ability to reduce parasitic SPP losses by optimizing metal film thickness and with the addition of gain.

3 Experimental Fabrication and Characterization of Semiconductor-Metal-Insulator Waveguides of Varying Metal Film Thicknesses

3.1 Abstract

The solutions of theoretical dispersion relations for planar asymmetric semiconductor-metal-insulator waveguides presented in Chapter 2 demonstrated that by optimizing metal film thickness, and the emission regime of the organic semiconductor, a significant fraction of surface plasmon polariton (SPP) mode amplitude was leaked into the active semiconductor layer, thereby decreasing the amount of optical energy trapped by the metal. In this way, a reduction in parasitic loss to tightly bound surface plasmon modes may lead to the development of low loss plasmonic electrodes for visible-light-based optoelectronics [130].

The work presented in this chapter is an experimental investigation of the theoretical predictions presented in Chapter 2. This was achieved by fabricating a set of insulator-semiconductor-metal-insulator (ISMI) waveguides with a range of Ag metal film thicknesses, and collecting excitation pump power-dependent edge emission spectra from these waveguides. By measuring the waveguided edge emission intensity at the peak wavelength (I_{max}), the threshold for amplified spontaneous emission (ASE), and the ASE slope efficiency as a function of metal film thickness, compelling experimental evidence provided validation of the theoretical calculations which showed that the most efficient SPP-semiconductor coupling occurred at a metal film thickness where the dominant SPP mode(s) exhibited the greatest propagation length (i.e., lowest loss) and greatest field leakage into the semiconductor emitter.

In conjunction with corroborating the theoretical results in Chapter 2 through optical characterization of neat PFO ISMI waveguides, amorphous and semi-crystalline PFO films were fabricated and characterized with GIWAXS measurements. These films with differing molecular ordering may be used in the future to further study polymer semiconductor-SPP coupling as a

function of molecular dipole orientation, which is expected to play a critical role in the degree and efficiency of plasmon/polymer interactions.

3.2 Introduction

As described in detail in Chapters 1 and 2 of the thesis, SPPs may provide a means of confining and propagating electromagnetic waves on subwavelength scale volumes, which may lead to the development of subwavelength optoelectronic circuitry, capable of operating both at ultra-small length scales and ultra-fast operating speeds (THz) [1,5]. Such operating speeds are not unattainable with conventional nanoscale electronic circuitry due to the relative speed of electrons versus photons [13-15]. However, macroscale subwavelength SPP propagation has been historically regarded as unfeasible due to the fact that SPPs are inherently lossy waves with short mode propagation lengths (10-100 μm) due to the non-negligible imaginary component of the complex dielectric constant of the metal (e.g., Ag, Au, Al) [1,2]. The lossy nature of SPPs also makes these modes one of the most significant loss channels in electrically-driven visible-light-based optoelectronic devices such as organic light-emitting diodes (OLEDs), where coupling into tightly bound SPP modes decreases the light outcoupling efficiency by trapping light energy at the metal electrode-emitter interface (see Chapter 2.2 for further details) [3-6].

It has been proposed that by coupling into a gain medium that a significant percentage of the intrinsic losses of SPP modes can be compensated for and SPP propagation length can be enhanced [27]. Additionally, efficient plasmon-emitter coupling and tailoring of the SPP field leakage may lead to increased light outcoupling efficiency in OLEDs and perhaps lead to the development of electrically driven organic semiconductor lasers. Numerous gain materials have been explored, including quantum dots, rare earth doped glasses and crystals, and laser dyes [28-31]. However, we have employed the use of organic semiconducting polymer emitters as gain media. The virtues of these materials are discussed in detail in Chapter 1 of this thesis, but it is

important to emphasize that while these materials exhibit high quantum efficiencies and high gain cross-sections, they offer the potential of control over the molecular dipole orientation, which is expected to play a critical role in efficient coupling or de-coupling to SPP modes. A dipole oriented parallel to the plane of the polymer-metal interface is expected to be damped by its own image on the metal surface, while a dipole oriented perpendicular to the plane is expected to couple to SPP modes [31, 129].

In Chapter 2 of this thesis, a set of theoretical dispersion relations were solved for an organic polymer semiconductor-metal-insulator waveguide over a range of metal film thicknesses (20-100 nm) and under both steady state and amplified stimulated emission (ASE) regimes. These dispersion relations show that by the introduction of a gain medium and optimizing the metal film thickness, even with a conservative net gain (47 cm^{-1}) that at visible wavelengths the SPP loss can be significantly decreased and the SPP mode leakage increases by factors of up to 3.8 and 88 by tuning metal film thickness and by addition of gain, respectively [130]. Compelling evidence suggests that if the SPP mode loss and leakage into the semiconductor can be controlled rather than suppressed entirely, SPPs may boost performance in a host of visible-light-based optoelectronic devices including organic photovoltaics, organic lasers, and OLEDs [21-24,31,39,41,42,130].

The work in this chapter was conducted to experimentally validate the theoretical dispersion relations of Semiconductor-Metal-Insulator (SMI waveguides) presented in Chapter 2 and test whether by tuning metal film thickness, low loss/efficient SPP-polymer emitter coupling can be achieved. This was carried out by fabricating a set of Insulator-Semiconductor-Metal-Insulator (ISMI) waveguides with 100 nm as-spin-case ('neat') PFO films with Ag metal film thicknesses ranging from 35 - 100 nm and collecting the resultant emission spectra from these waveguides over a range of optical excitation power densities. From these emission spectra, the

peak emission intensity, ASE threshold, and ASE slope efficiency were compared as a function of metal film thickness.

Comparison between the peak emission intensity, ASE threshold and ASE slope efficiency of the experimentally fabricated ISMI waveguides as a function of Ag metal film thickness and the theoretical dispersion relations showed strong correlation between the resultant spectral characteristics of the waveguides and the theoretically calculated SPP mode propagation length and mode penetration depth at a given metal film thickness. Compelling experimental evidence validates the theoretical predictions presented in Chapter 2, suggests that the most efficient/lowest loss emission occurs when the dominant SPP mode(s) exhibit the greatest propagation length (i.e., lowest loss) and the greatest mode penetration depth [130].

The original experimental path included the measurement of the gain and loss coefficients utilizing the variable stripe length (VSL) and shifting excitation spot (SES) methods, respectively. However, after developing these measurement techniques and building the experimental measurement setup, it was found that these techniques are most suitable for measuring the intrinsic gain and loss coefficients of planar films of a gain medium-only, not the gain and loss coefficients of SMI-type waveguides. This is due to the fact that these waveguides exhibit significantly higher gain and lower loss coefficients than a sample consisting of a gain medium thin film on a glass substrate. The reasons why high gain and more specifically low loss coefficients are not practical to measure using these techniques require a brief explanation of the measurement techniques. In the VSL technique, a strip of light is projected onto the sample and spectra are collected as the stripe length is incrementally increased (described in detail in Appendix B). In the SES technique, the loss coefficient is extracted by collecting spectra of the sample as a stripe of light (of fixed length) is incrementally traversed away from the sample edge (described in detail in Appendix B). The excitation stripe length and position was controlled by an aperture mounted on a micrometer stage. Due to the Gaussian nature of the excitation source,

there was a limited range in which the stripe could be traversed without the power density incident on the sample becoming non uniform. Due to the low loss exhibited by these samples, the stripe length and position could not be suitably varied to change the optical response without varying the incident power density. Therefore, to infer the degree and efficiency of SPP-semiconductor emitter coupling as a function of metal film thickness, emission spectra with a fixed stripe length were collected using the existing VSL/SES apparatus over a range of power density. While the VSL/SES setup that was build was not of direct utility for these experiments, the setup could potentially be modified in the future for the collection of gain or loss coefficients. Background information and a full description of the measurement system are presented in Appendix B.

Additionally, the work presented in this chapter has laid the ground work for the study of SPP-polymer emitter coupling as a function of polymer molecular dipole orientation. This was achieved by preparing 100 nm thick PFO films on glass substrates and using different treatment methods to promote in- and out-of-plane molecular dipole orientation and varying degrees of crystallinity. While it was beyond the scope of this thesis to fabricate waveguides at varying metal film thicknesses with different polymer molecular dipole orientations, methods to prepare amorphous, in-plane oriented and semicrystalline PFO films were developed and are presented herein.

3.3 Methods

3.3.1 Waveguide Glass Substrate and Cover Preparation

1 mm thick Fisherbrand plain microscope slides (Cat # 12-550D) were used as the cover or superstrate of the waveguide and were cut into squares of 2 cm dimensions using a Cutter's Mate lubricated tungsten carbide cutting wheel. Square 18 x 18 mm VWR Microcover selected 1

ounce glass squares (CAT.NO 48368-040) 030111-9) were used as the waveguide substrate. Superstrate and substrate glass were carefully cleaned by sonicating in Sparkleen solution (1 g Sparkleen cleaner in 1 L deionized water) in a clean 100 ml beaker for 15 minutes followed by manually scrubbing the surfaces of the substrates with ethanol soaked KimWipes. The substrates were transferred to a clean 100 ml beaker then re-sonicated for 20 minutes in Sparkleen solution followed by rinsing in 3 clean 100 ml beakers filled with deionized water. The substrates were then transferred to a 100 ml beaker filled with a 50/50 mixture of concentrated HCl and ethanol, covered with a watch glass and let set for 20 minutes. The substrates were then carefully rinsed in deionized water and dried using a compressed air gun.

3.3.2 Thermal Evaporation of Ag Films

Silver metal films of 35, 45, 50, 55, 65, and 100 nm were deposited on the cleaned 18 x 18 mm VWR glass substrates with an Edwards Coating System Model E306A thermal evaporator fitted with a calibrated crystal monitor to measure thickness. Prior to thermal evaporations, the vacuum chamber was scrubbed thoroughly with KimWipes soaked in acetone to remove any contaminants such as other metals, metal oxides, and carbon. Depositions were carried using a tungsten wire basket with 2-4 x brand silver metal pellets. The acoustic impedance (z) for Ag metal: 16.68×10^5 - g/cm²/s and the density (d) of Ag metal: 10.5 g/cm³, were input into the thermal evaporator control panel. The thermal evaporator was pumped down to below 9×10^{-6} mbar prior to carrying out the evaporation. Once this pressure was reached, the voltage was slowly increased incrementally (5 volts per minute) until it approached 3.2 volts and a stable current of 20.5-21 Amps. Once this current was achieved, the shutter was opened, exposing the samples to metal vapor at deposition rates ranging from 0.1 to 1 nm per minute. This low deposition rate helped reduce film roughness. In total, these thermal evaporations ranged in duration from 30 to 1.5 hours in length. After the evaporation was complete, the Ag coated glass

substrates were left in the deposition chamber under vacuum to cool to room temperature for approximately 1 hour to prevent oxidation when exposed to ambient air.

3.3.3 Polymer Film Deposition

100 nm films of PFO were spin cast onto bare 18 x 18 mm VWR glass substrates, VWR substrates coated with Ag films of varying thickness, and bare thick microscope slide glass. These films were deposited with a Laurel Technologies Corporation spin coater (Model WS-400BZ-6NPP/Lite (Rev. MS)) under continuously flowing nitrogen by drop depositing 5 μ L of a 20 mg/ml solution of PFO in chloroform from a micropipette onto the substrate spinning at 6000 rpm with a 1 minute spin cycle. Because these substrates are thin, the vacuum chuck on the spin coater would cause the samples to ‘cup’ or bow in the center when actuated. This in-turn caused the PFO film deposition to be non-uniform. To rectify this problem, the thin 18 mm square substrates were carefully affixed to a thick square piece of microscope glass with double-sided carbon tape that was then placed on the vacuum chuck of the spin coater. After spin coating, the samples were placed in a nitrogen glovebox for at least 24 hours to ensure no solvent was left on the film.

The 20 mg/ml chloroform solution was prepared by carefully weighing dry flakes of Poly(9,9-dioctylfluorenyl-2,7-diyl) (PFO) with a molecular weight (M_w) of 58,200 by GPC, from Sigma Aldrich ((CAS Number: 195456-48-5) 571652, (500 mg vial) from lot # MKBH8002V, Pcode: 1001174608,) and adding it to a measured volume of chloroform in a small capped vial. Once the PFO was added to the chloroform, a micro stir bar was placed in the mixture and the vial was capped and sealed with parafilm. The sealed vial was placed in a beaker partially filled with water that was pre-heated on a stirring hot plate pre-heated to 45° C. The magnetic stirring action was set to 700 rpm and the solution was heated and stirred for 90 minutes to ensure that the PFO had

fully dissolved in the chloroform. The sealed vessel containing the PFO/chloroform solution was cooled in ambient air to room temperature before spin casting.

3.3.4 Assembly of ISI and ISMI Waveguides

ISMI waveguides were assembled by bonding the cleaned superstrate glass onto a substrate (with the Ag film and PFO layer already deposited) using Norland NOA-63 index matched optical epoxy. NOA-63 epoxy was selected because its refractive index of $n = 1.56$ matched the refractive index of the PFO emitter ($n = 1.28$) reasonably well, while more importantly being transparent at wavelengths at the 355 nm pump wavelength that was selected to excite the waveguides. Bonding the superstrate to the layered substrate was achieved by carefully placing a drop of the epoxy (of approximately 3 mm in diameter) in the center of the superstrate glass and gently lowering the superstrate onto substrate. Light pressure was applied to ensure that the epoxy covered the entire interface between the cover and substrate. The superstrate glass was deliberately cut to slightly larger dimensions than the substrate glass, such that when excess epoxy flowed out from the interface, a bead formed along the edges of the sample to ensure that the PFO and Ag films were fully surrounded and encased in epoxy. This prevented oxidation of the PFO and Ag thin films, ensuring the sample could be safely stored in ambient air and analyzed for prolonged periods of time.

Once the epoxy film was air bubble-free, it was exposed to a handheld UV lamp of x watts for approximately 20 seconds. This short exposure started the curing process of the epoxy and allowed the sample to be handled without the position of the cover or substrate shifting. Excess epoxy was cleaned from the cover and substrate with KimWipes soaked in acetone. Once the waveguide was cleaned, it was exposed to the same UV lamp for approximately 45 to 55 minutes to fully cure the epoxy.

3.3.5 Grinding and polishing ISMI Waveguides

Once the waveguide was cured, an edge of the sample was ground and polished to an optical finish. This polished edge served as the window from which outcoupled edge emission was collected. Polishing was conducted by manually grinding and polishing the edge on a Leco Vari/pol VP-150 polishing wheel at speeds of 300 – 500 rpm with a series of Buehler silicon carbide polishing pads with grit sizes of 120, 180, 220, 400, 600, and 800, and finishing with a 1 μm polishing pad. After the sample was polished on each pad, it was placed on-edge and the angle between the sample and the table was measured to ensure that the polished surface was perpendicular to the face of the waveguide.

3.3.6 Apparatus Used to Collect Pump Power Dependent Emission Spectra

A custom designed apparatus shown schematically in Fig. 3.1 was initially built to measure gain and loss coefficients of ISMI waveguides using the variable stripe length (VSL) technique and shifting excitation spot (SES) method, respectively (described in detail in Appendix B). However, this setup was in-turn solely utilized to collect pump power dependent emission spectra of ISI and ISMI waveguides with a fixed excitation stripe length.

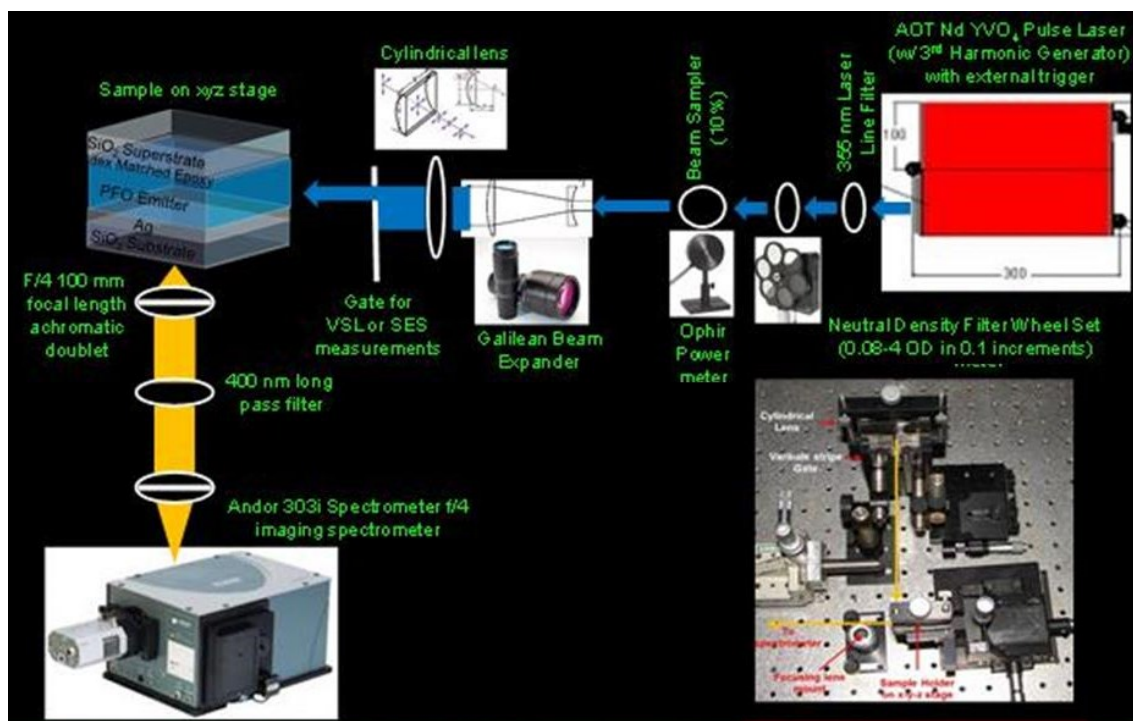


Figure. 3.1 Schematic overview of the optical bench setup designed for gain and loss coefficient measurements via the variable stripe length (VSL) and shifting excitation spot (SES) methods, which instead was used to collect pump power emission spectra. Inset image shows cylindrical lens, aperture to control slit width, and sample holder. Color available in electronic copy.

The excitation source used for the measurements was an AOT ACE NdYVO₄ pulse laser fitted with a thermoelectrically cooled 3rd harmonic generator to output a 355 nm emission. The laser has a pulse duration of 0.6 ns at repetition rates below 5000 Hz and the pulse rate was externally controlled using a BK Precision 3011 B 2 MHz function generator. The laser beam was then passed through a 355 nm band pass filter that allowed only light between 350 and 360 nm to be transmitted. The filtered laser emission was then passed through two neutral density filters fixed on wheels set to vary the incident power density on the sample. The neutral density filter wheel set was purchased from Newport (model 5215). The first filter wheel contained neutral density filters of: 0.04, 0.5, 1, 1.5, 2, and 2.5 OD and the second wheel contained neutral density filters of 0.04, 0.1, 0.2, 0.3, 0.4, and 0.5 OD, allowing the optical density of the beam incident on

the sample to be varied from 0.08 to 3.0 OD. The laser light then passes through a beam sampler set at a 45° angle with respect to the beam, which direct 10% of the incident power to an OPHIR silicon photodetector (model PD300-UV-ROHS) that was read with an OPHIR Vega Power and Energy Meter. The beam is then passed through an Edmund Optics Galilean-type zoom beam expander 1-8X, Output Clear Aperture 33 mm, UV (Stock No. #68-477) to increase the spot size from approximately 4 mm to 12 mm. The expanded beam is then projected through a XXX mm focal length cylindrical lens that projects a 0.5 mm diameter stripe onto the sample. The position and length of the stripe was controlled by a micrometer aperture.

For all emission spectra, the physical sample remains in a fixed position. The outcoupled edge emission from the sample was collected with two f/4 100 mm focal length achromatic doublets, which focused and directed the light onto the spectrometer CCD (see Fig. 2.1). Both lenses were mounted in x-y adjustable positioning mounts to allow precision alignment of the beam position, and both lens mounts were affixed to micrometer stages to allow fine adjustments of the focus and in-turn the spot size incident on the spectrometer. The incident spot size of the outcoupled edge emission from the waveguide that was projected onto the spectrometer CCD was found to be an important factor in collecting an accurate representation of the waveguide emission. For preliminary emission spectra, presented in Appendix C, a large, 4500 μm spot size was used. The problems of measurement reproducibility with such large spot sizes are described in detail in Appendix B. For the final data set; the spot size was approximately 500 μm . Before the second 100 mm focal length achromatic doublet, a 400 nm long pass was placed in the beam path to filter out any of the 355 nm excitation source. An Andor 303is imaging spectrometer with a 600 lines/mm grating was used to both image the spot incident on the spectrometer and collect spectra of the outcoupled edge emission.

3.3.7 Measurement of Incident Excitation Power Density and Energy per Pulse

To measure power density and energy per pulse incident on the sample, a careful set of measurements were collected by placing the OPHIR silicon photodetector in the plane of the sample and projecting a 2 mm stripe length of the 355 nm excitation source onto the detector. The laser was warmed up to stabilize the power for a period of 30 to 40 minutes prior to the measurements and the laser Oscillator current was set to 4.4 Amps and the Amplifier current was set to 4.5 Amps with a 25 Hz pulse rate. The neutral density filter wheels were used to vary the incident power density and the OPHIR Vega Power meter was set to average the power at the 355 nm excitation wavelength for 15 seconds. The raw average power measurements were recorded over neutral density filter wheel settings of 3.0, 2.5, 2.4, 2.2, 2.1, 2.0, 1.9, 1.7, 1.5, 1.4, 1.2, 1.1, 1.0, 0.9, 0.8, 0.7, 0.6, 0.54, 0.44, 0.24, 0.14, and 0.08 OD. By solving for the area of the stripe (0.5 mm x 2 mm) the power density was calculated for these neutral density filter wheel settings (see Table 3.1). It should be noted that certain ND filter wheel settings attenuated a greater percentage of the laser than their rated transmittance and in-turn are presented in table one in order of lowest to highest resultant average power. To calculate the energy per pulse, the measured average power in watts (i.e., joules per second) was divided by repetition rate in Hertz (cycles per second) to determine the energy in one pulse. Then, the power in one pulse was divided by the pulse duration (0.6×10^{-9} seconds) to solve for the energy per pulse (see Table 3.1).

Table 3.1. Neutral density filter wheel setting and resultant power density in μW , mW , and W per cm^2 and energy per pulse in Watts for a 2 mm stripe with a repetition rate of 25 Hz with laser Oscillator and Amplifier currents of 4.4 and 4.5 Amps, respectively.

OD	Avg. Power Density (W/cm^2)	Avg. Power Per Pulse (W)
3	2.23E-06	1.48E-04
2.5	6.97E-06	4.65E-04
2.4	1.43E-05	9.55E-04
2.2	1.91E-05	1.27E-03
2	2.35E-05	1.56E-03
2.1	2.37E-05	1.58E-03
1.9	4.32E-02	2.88E+00
1.7	6.00E-02	4.00E+00
1.5	8.01E-02	5.34E+00
1.4	1.58E-01	1.06E+01
1.2	2.15E-01	1.43E+01
1.1	2.60E-01	1.73E+01
1	2.90E-01	1.93E+01
0.8	4.19E-01	2.79E+01
0.9	4.81E-01	3.21E+01
0.54	5.41E-01	3.61E+01
0.7	5.43E-01	3.62E+01
0.6	5.82E-01	3.88E+01
0.44	6.91E-01	4.61E+01
0.24	7.69E-01	5.12E+01
0.14	8.12E-01	5.41E+01
0.08	8.60E-01	5.73E+01

3.3.8 Procedure for Collecting Pump Power Dependent Emission Spectra

Prior to the collection of any gain spectra, the laser was warmed up to stabilize the power for a period of 40 to 60 minutes prior to all measurements. For all measurements, the laser Oscillator current was set to 4.4 Amps, the Amplifier current was set to 4.5 Amps and the pulse rate was set to 25 Hz. Changing the laser Oscillator and Amplifier currents resulted in either lowering or increasing the output power, however with each change in these settings, a significant period of time (15-30 minutes) was required for the output power to stabilize. Therefore, as previously noted, the power density was varied with neutral density filters. For all measurements

the room lights as well as the computer monitor were switched off to prevent stray light from biasing the spectra. Neutral density filter wheel settings ranging from 2.5 to 0.08 OD were used to collect the gain measurements resulting in power densities ranging from $6.9\text{E-}6$ to 0.86 W/cm^2 .

Images of the outcoupled edge emission projected on the spectrometer were taken in imaging mode with the input slits in the full open position and with slit widths of 250 and 300 μm slits. All spectra were collected with grating 2 (600 lines/mm) in full vertical binning (FVB) mode over wavelength ranges of 400-542 nm or 420-562 nm with exposures ranging from 0.05 to 1 second and total accumulations ranging from 50 to 1000 to attain an acceptable signal to noise. It should be noted that the ideal method of collecting a spectrum is the use of a single exposure or an accumulation of multiple spectra, where the total accumulations is less than <20 . However, due to the wide range of emissivity over the seven ISMI waveguides, to make a valid comparison between them, all measurements had to be taken with the same conditions (i.e., same exposure time, same total acquisition time, same slit width, etc...). This however provided a significant challenge.

The brightly emitting ISMI waveguide with high gain required short exposure times ($<<0.5\text{ s}$) at high power densities to prevent saturation of the detector. This in-turn required a significant number of accumulations (>1000) for the weakly emitting samples with low gain to collect a spectrum with sufficient counts at the same settings as the high gain samples. The pitfall of using a very short exposure time ($<<0.5\text{ s}$) with the 25 Hz pulse rate that was employed was the fact that there was no trigger between when the pulse fired and when the spectrometer collected the spectrum. This led to a low average number of pulses per spectrum, which introduced a significant amount of bias in the overall peak emission intensity of the spectrum. For example, the peak emission intensity would vary significantly (30-40%) when using a 0.1 second exposure time with the 25 Hz pulse rate. Experiments were conducted by increasing the pulse rate upwards of 100 Hz and using the short 0.1 s exposure. The higher 100 Hz pulse rate solved the

issue of variation in the peak emission intensity because there were a greater average number of pulses per exposure; however this caused the spectrometer to saturate at even lower excitation power densities.

The next variable that was considered to reduce the issue of detector saturation was the spectrometer input slit width. While decreasing the slit width did let less of the signal in, it was found that if the input slit was too small ($>150\text{ }\mu\text{m}$), only a small percentage of the outcoupled edge emission was sampled. Furthermore, small input slit width biased the measurement because the character of the emission was found to change over the spot incident on the spectrometer. Therefore, with the final data set, a $150\text{ }\mu\text{m}$ input slit was selected with a $500\text{ }\mu\text{m}$ spot size incident on the spectrometer.

Considering that optimization of exposure time, pulse rate, number of acquisitions and the input slit ratio to the spot size incident on the spectrometer still did not allow collection of the gain spectra of all samples at the same acquisition settings without saturation, it was decided to use of a neutral density filter placed just prior to the spectrometer input slits to attenuate a percentage of the outcoupled edge emission of the samples that would have otherwise saturated the detector. This final solution allowed the use of a long 1 second exposure time to minimize bias from the average number of pulses per spectrum, a relatively low number of acquisitions (120), and a low 25 Hz pulse rate. The filter that used was a New Focus brand 2.5 OD filter that had a flat transmittance of 0.31% across the visible region.

To ensure that the filter attenuated a uniform percentage of the signal, a transmittance spectrum of the filter was collected and gain spectra were collected with and without the filter at the same excitation power densities. It was found that the filter consistently transmitted 0.225% of the signal, and all spectra that were collected with the filter in place were corrected by dividing the emission intensity by 0.00225.

3.3.9 Procedure for Collecting Polarized Pump Power Dependent Emission Spectra

An additional set of polarized gain spectra of SMI waveguides of varying metal film thickness were collected by placing a polarized film at the edge of the sample such that the outcoupled edge emission was projected through the polarizer and into the spectrometer (see Fig. 3.2). Polarization was set either parallel (0°) or perpendicular (90°) to the plane of the sample ((see Fig. 3.2 for schematic). Laser polarization was found to be in the plane of the substrate (i.e., vertically polarized WRT to the optical bench). These measurements were carried out at the same laser Amplified and Oscillator current settings and 25 Hz pulse rate as the other gain and loss measurements, using a 2 mm stripe incident on the sample and neutral density filter wheel settings of 0.08 and 0.54 OD, resulting in power densities of 0.835 and 0.64 W/cm^2 . Spectra were collected with grating 2 with $250 \text{ }\mu\text{m}$ slits, full vertical binning (FVB) mode with a 0.15 second exposure and 1000 accumulations over a 420-562 nm wavelength range. A corresponding set of unpolarized spectra were collected at the time with the same laser and spectrometer settings as the polarized spectra to make an accurate comparison.

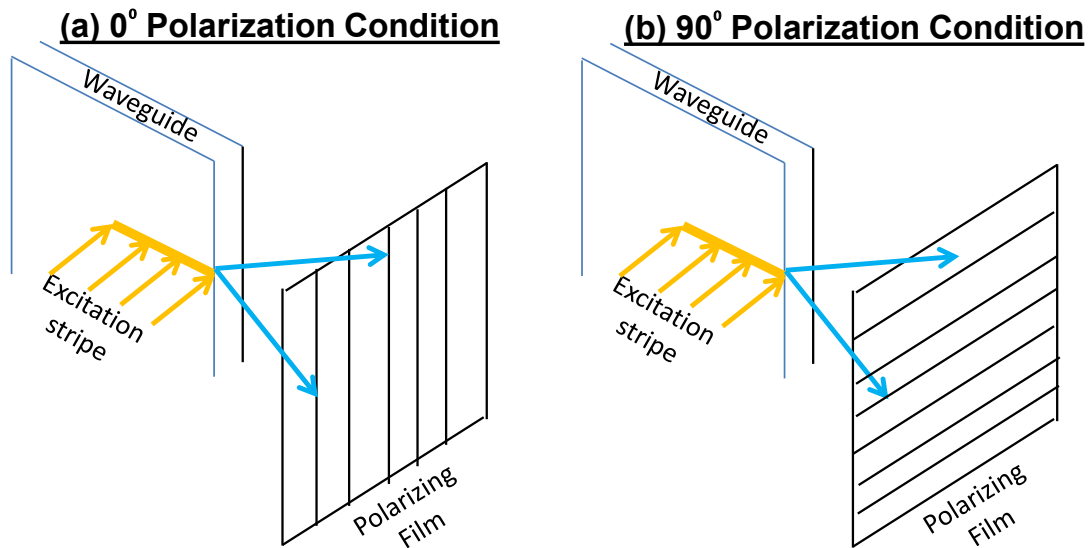


Fig. 3.2 Schematic representation of polarization gain measurements taken of SMI waveguides with outcoupled edge emission polarized parallel to the plane of the waveguide (0°) (a) and polarized perpendicular to the plane of the waveguide (90°) (b).

3.3.10 Method of Emission Spectra Analysis

All spectra were background corrected in OriginPro 8.5 software by using the “Peak Analyzer” function in the “Signal Processing” tab in “Analysis”. For spectra that were collected with a neutral density filter placed just prior to the spectrometer input slits, the raw data was corrected for the percent attenuation of the filter prior to the background correction. The full-width-half-maximum (FWHM) was manually measured by locating the wavelength at the maximum intensity on the background corrected spectra, dividing the intensity by two and finding the wavelengths at which the intensity is equal to half of the maximum intensity. Plots of peak emission wavelength, maximum intensity and FWHM versus metal film thickness in the SMI waveguide were generated. ASE threshold and ASE slope efficiency were extracted from the plots of intensity at the peak emission wavelength (λ_{max}) versus power density by fitting two linear lines to the steady state and stimulated emission regions. The ASE threshold is taken to be the x-intercept of the linear fit of the ASE region of the sample and the ASE slope efficiency is the slope of that line.

3.3.11 Absorption Spectra of ISMI Waveguides

Absorption spectra of SMI waveguides fabricated with 100 nm neat PFO (i.e., as spin cast) with metal film thicknesses of 0, 35, 50, 65, and 100 nm were collected using a 400 series SI-Photonics brand UV/VIS spectrometer. Spectra were collected from each sample in transmission mode using the ‘High Precision’ setting on the instrument, over a wavelength range of 250-900 nm. These spectra employed the use of both a deuterium and a tungsten lamp, which were calibrated prior to use such that the intensity between the two sources was within 5%. The spectrometer was blanked in ambient air, such that the total absorption of the entire waveguide was measured. Room lights were left during the measurements, but the sample holder and shutter apparatus was covered with a tunnel. Samples affixed to aperture the standard fitting on the

spectrometer. The percent transmittance of the waveguides was calculated from the measured absorbance with the following equation:

$$\%T = 1/(e^A) \quad (1)$$

where A is the absorbance and $\%T$ is the percent transmittance.

3.3.12 Finite Difference Time Domain Simulations of SMI Waveguides

Full-field electromagnetic simulations of analogs to the SMI waveguide structure with metal film thicknesses of 35, 50, 65, and 100 nm were conducted with a plane wave excitation sources at single excitation wavelengths of 355 nm and 460 nm using Lumerical Solutions Finite Difference Time Domain simulation software. The simulations (shown schematically 3.3) consisted of a superstrate layer of glass 948 nm thick adjoining a 100 nm layer of PFO, followed by an Ag metal film of 35, 50, 65, and 100 nm thicknesses, followed by a glass substrate with thicknesses of 90, 105, 120, 155 nm, depending on the thickness of the metal film. The glass substrate thickness was changed to accommodate the changes in the metal film thickness to allow the simulation to fit into the same area. This prevented having to re-design each simulation and reposition the electric and magnetic field monitors and ensured that the distance from the plane wave source with respect to the PFO-Ag interface remained constant.

For simulations carried out under 355 nm and 460 nm plane wave excitation, both the glass superstrate and substrate had the same refractive index (n) of 1.52 and were treated as purely real materials ($n = n_{real}$) due to the fact that imaginary component, (k) (i.e., the loss) is very small. However, because the imaginary components (k) of the complex refractive indices of Ag and PFO are not negligible and the fact that both the real (n) and imaginary components (k) change significantly across the visible regime, the actual n and k values for Ag and PFO at 355 and 460 nm were used in the simulations. For Ag, the n and k values are 0.20725 and 0.14346 at 355 nm and 1.4530 and 2.5672 at 460 nm, respectively. For PFO, the n and k values are 0.7916

and 0.9486 at 355 nm and 3.04432 and 0.11547 at 460 nm, respectively. The plane wave source for simulations carried out at both 355 and 460 nm excitation wavelengths was positioned at the bottom edge of the glass superstrate with propagation in the z-direction (towards the substrate) and an electric field monitor was placed through the structure to study the cross-sectional profile of the electric field in the z-direction through the PFO, Ag, and glass substrate layers of the simulated SMI waveguide (see Fig. 3.3).

To measure the real and imaginary components, the absolute intensity, and absolute intensity squared of the electric and magnetic fields through the PFO, Ag, and glass substrate layers, under both 355 and 460 nm excitation, line scans were extracted from the cross-sectional monitor in the z-direction. Plots of the real and imaginary components, the absolute intensity, and the absolute intensity squared of the electric and magnetic fields versus position in the simulated waveguide analog were generated.

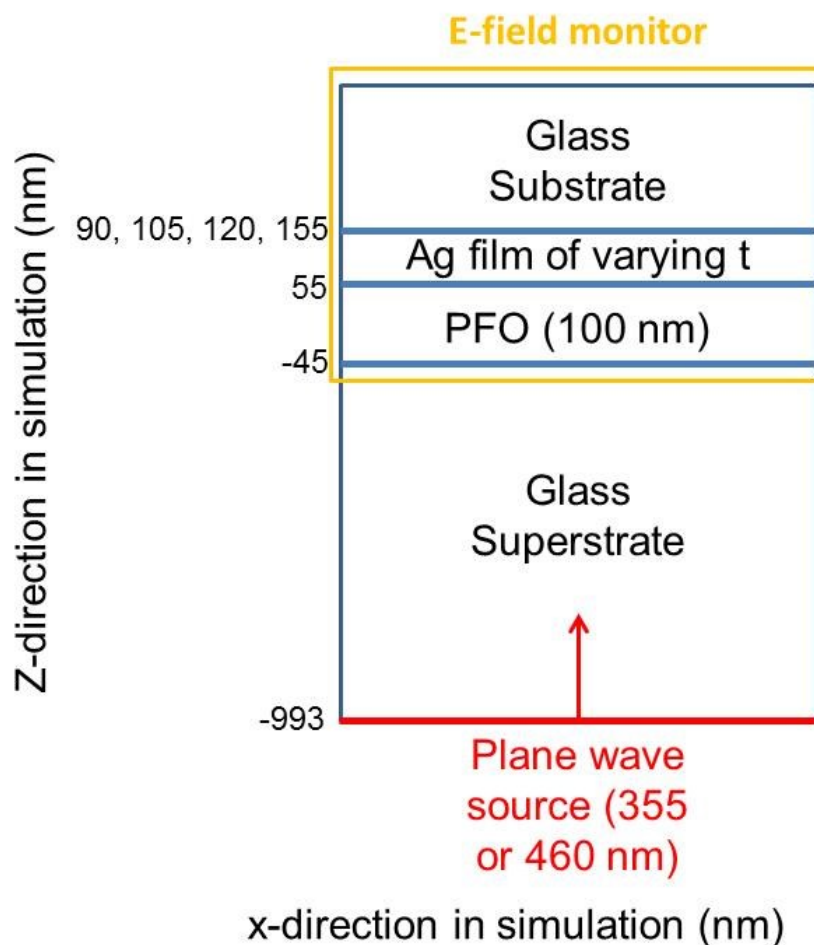


Figure 3.3 Schematic of Full-field electromagnetic simulations of SMI waveguide analogs under 355 or 460 nm plane wave excitation with 948 nm thick glass superstrate, a 100 nm thick PFO film, an Ag metal film of 35, 50, 65, and 100 nm thickness, and glass substrate of 90, 105, 120, or 155 nm thickness.

3.3.13 Experimental Methods to Vary and Control PFO Molecular Dipole Orientation

Spin cast, or ‘neat’ 100 nm PFO films on bare VWR glass substrates, VWR glass substrates coated with 100 nm Ag, and bare 1 mm thick Fisherbrand microscope slide glass were heat treated under an inert nitrogen environment at temperatures within the liquid crystalline phase for [89,131] 30 minutes at 120° and 180° C followed by rapid quenching on a metal plate, and for 60 minutes at 200° C followed by slow cooling on a glass plate to promote molecular dipole orientation and α -phase crystallites. Samples were also heat treated in an inert nitrogen

atmosphere at a temperature in the nematic liquid or glassy phase region [89,131] (above the liquid crystalline phase) at 280° C for 30 minutes followed by rapid quenching on a metal plate to produce an amorphous or ‘glassy’ sample with random dipole orientation.

These heat treatments were carried out on a hotplate in a nitrogen glovebox. The hotplate stage was carefully calibrated with a thermal probe read with a digital multimeter. It was found that the hotplate temperature was quite stable over a 30 minute duration; however the output temperature was measured to be only 60% of the temperature set on the control dial (see Fig. 3.4). Therefore, to set the desired temperature, the thermal probe was used to measure the actual temperature, which was tuned with the control dial. After the temperature was set to the desired value, the hotplate was allowed to equilibrate for 15 minutes prior to each heat treatment to ensure set point temperature stability. During the 15 minute equilibration time, measurements with the thermal probe were collected to ensure temperature stability.

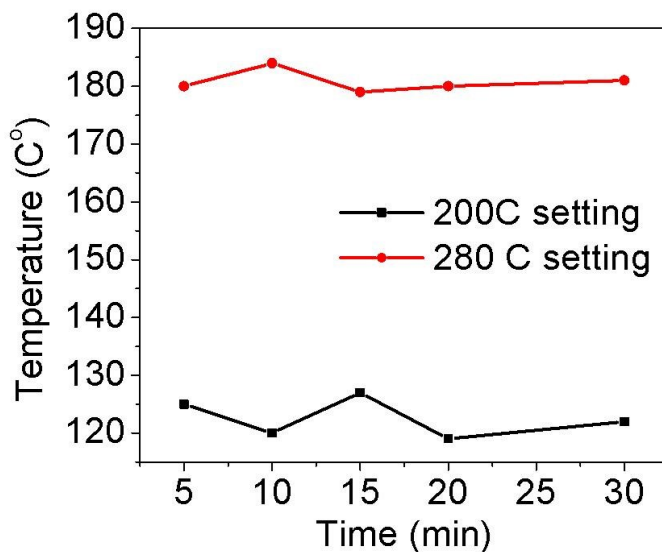


Figure 3.4. Measurement of temperature versus time with a handheld thermal probe placed on the hotplate stage used to conduct the thermal treatments of PFO films at 2 temperature settings on the hotplate dial: 200 and 280° C.

Samples were also prepared by vapor phase annealing in toluene vapor to promote molecular dipole orientation and β -phase chain orientation [131]. Vapor phase annealing was carried by taping a 20 ml glass beaker filled with approximately 10 ml of toluene to the bottom of a thoroughly cleaned glass Newman's Salsa jar. Samples (100 nm PFO on bare VWR glass substrates and those coated with 100 nm Ag) were affixed to a microscope slide using double-sided carbon tape, and the slide was rested on the lip of the 20 ml beaker such that the surface of the samples was facing the bottom of the jar. The lid of the glass salsa jar was tightly sealed and wrapped in Para Film. Vapor annealing was carried out for 1 hour. After completion, the samples were placed in the glovebox overnight prior to absorption measurements.

3.3.14 Optical Characterization of PFO Molecular Chain Orientation

To gain insight into the molecular dipole orientation and crystallinity of the 100 nm PFO films on bare VWR glass substrates and bare 1 mm thick microscope slide glass prepared with varying techniques, absorption spectra were collected on: neat PFO films, PFO films heat treated at 120°, 180°, 200°, and 280° C, and vapor-annealed PFO films using an x brand UV/VIS spectrometer. Multiple spectra were collected from each sample in transmission mode using the 'High Precision' setting on the instrument, over a wavelength range of 290-900 nm. These spectra employed the use of both a deuterium and a tungsten lamp, which were calibrated prior to use such that the intensity between the two sources was within 5%. The spectrometer was blanked with the same WVR Microcover 18 x 18 mm squares, ((CAT.NO 48368-040) 030111-9 selected 1 ounce) as used for the sample substrates. Room lights were turned off during the measurements, but the sample holder and shutter apparatus was covered with a tunnel. Samples were carefully affixed to aperture with double-sided tape so they did not have to be secured by the fitting on the spectrometer aperture which would have damaged the PFO film.

3.3.15 Synchrotron Characterization of PFO Molecular Chain Orientation

To quantify the molecular dipole orientation and crystallinity of the prepared PFO films on base VWR glass substrates, and VWR glass coated with 100 nm Ag, grazing incidence small- and wide-angle X-ray scattering (GISAXS and GIWAXS, respectively) measurements were collected using the X9 Beamline at the National Synchrotron Light Source (NSLS) at Brookhaven National Lab (BNL), NY. The X9 beamline is an undulator-based beamline that was designed and constructed around 2006-2008 and specializes in simultaneous acquisition of SAXS and WAXS data using a unique detector system [132]. A schematic illustrating the general setup of the X9 beamline is shown in Figure 3.5. The photon source for X9 beamline is mini-gap undulator (MGU) of length 360 mm with 23 x 14.5 mm periods and minimum gap separation of 3.3 mm, which provides a continuous spectrum having fundamental energy ~ 2 keV [133]. X-rays from the undulator enter the cryo-cooled double-crystal monochromator (DCM) to select the desired energy, then after passing through the DCM, monochromated X-rays are passed through a pair of 850 and 400 mm-long Kirkpatrick-Baez (KB) bimorph mirrors in order to horizontally and vertically focus the X-ray beam, respectively. The X-ray beam is then passed through 2 slits to define the beam size and divergence, followed by another pair of micro KB focusing mirrors to potentially reduce the beam size down to 10 μm ; the beam enters a third pair of slits before finally striking the sample. After scattering from the sample, the scattered X-rays travel 3.4 m to the SAXS detector and the WAXS detector is placed at a wide enough angle to collect X-rays scattered at larger angles. A beam stop is placed before the SAXS detector to partially block the unscattered/forward-scattered X-rays. [133] Pictures of the X9 end station are shown in Fig. 3.6.

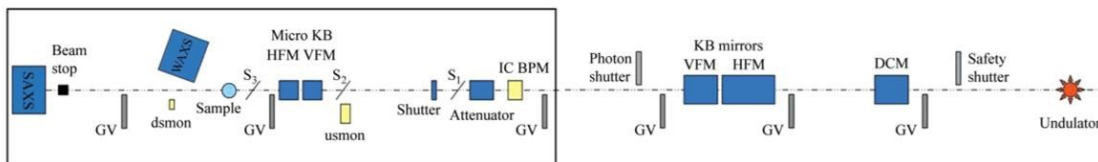


Figure 3.5. Schematic of the principal components of the NSLS Beamline X9 from the undulator source (at the right) to the end station hutch (large black box). Abbreviations used: gate valve (GV); double-crystal monochromator (DCM); Kirkpatrick-Baez (KB); horizontal/vertical focusing mirrors (HFM/VFM); ion chamber beam-position monitor (IC BPM); slits (S1, S2, S3); upstream/downstream monitor (usmon/dsmon) [133].

The WAXS detector is positioned off-axis from the direct beam such that the beam is not blocked, but X-rays scattered at wide angles can be detected [132]. One of the more recent advances in X-ray scattering is the use of Charged-Coupled Device (CCD) detectors to obtain 2D diffractograms. At the X9 beamline, a vacuum-compatible Kodak 4301E CCD sensor having 2084 x 2084 pixels (24 μm in size), custom-built by Photonic Science, is used for WAXS measurements. The detector must be vacuum compatible such that it can be placed in the vacuum chamber to receive a portion of the scattered beam [132,133]. The WAXS detector has a layer of Gadox(Tb) phosphor on its surface to convert X-rays into visible photons. The phosphor is shielded from ambient light by a black Kapton window, which still allows 98 % of the X-rays to be transmitted at 12 keV or higher [132].

The SAXS detector is a Mar 165 CCD detector, located 3.4 m from the center of the sample stage. As seen from Figure 3.6(d), there is overlap between the SAXS and WAXS detectors, specifically between $\sim 0.12 - 0.2 \text{ \AA}^{-1}$ [133]. The SAXS and WAXS data can potentially be combined automatically using software developed at the X9 beamline, and the data is calibrated using silver behenate [133]. Although simultaneous SAXS/WAXS measurements are very convenient, GIWAXS and GISAXS data at the X9 is usually collected sequentially to avoid shadowing of the WAXS detector in the GISAXS pattern as well as due to the difference in

required exposure times for the separate measurements [132]. The WAXS detector is moved a few millimeters during the GISAXS measurements, which only takes moments to complete [132].

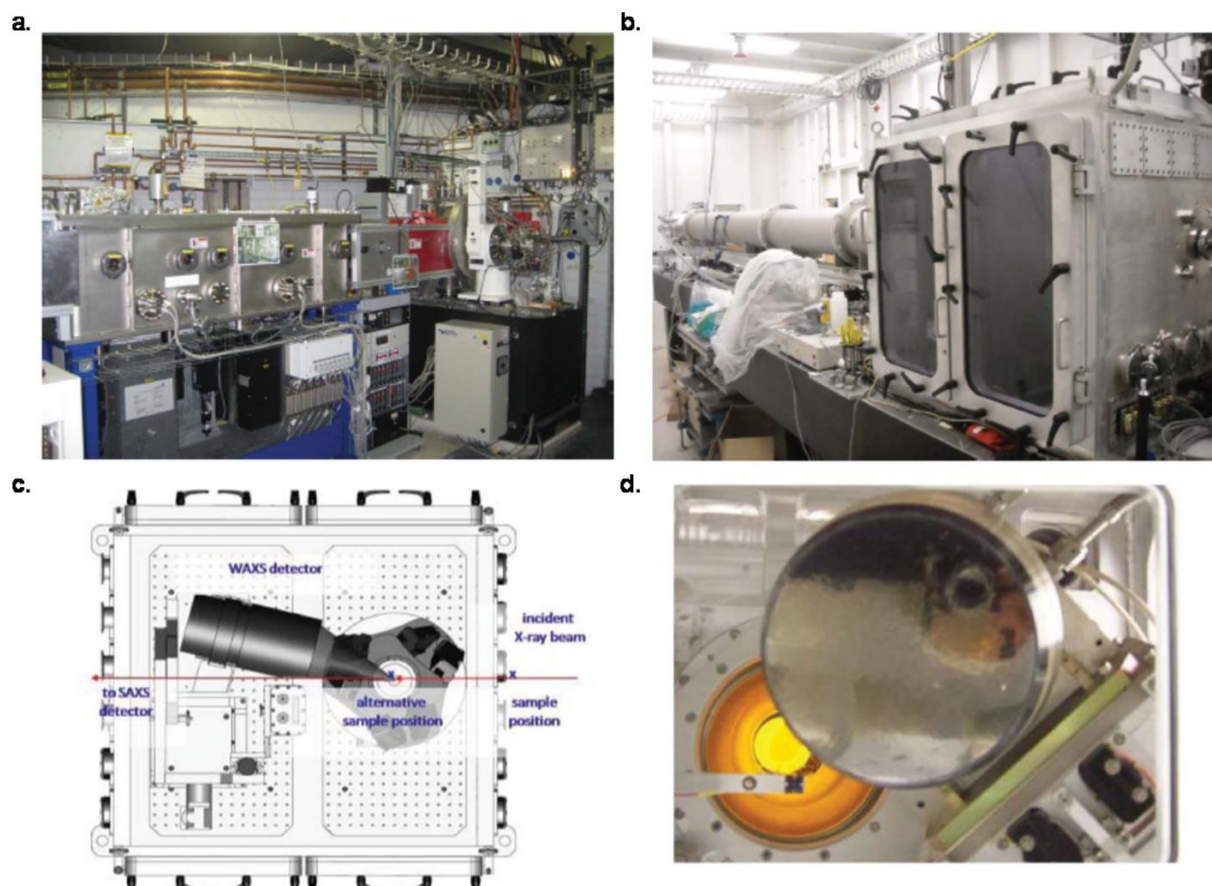


Figure 3.6. (a) Photograph of the X9 Beamline optical components with the double-crystal monochromator (on the right) and the KB horizontal/vertical bimorph adaptive focusing mirrors (on the left). b) The long vacuum-compatible chamber of NSLS Beamline X9 that contains both the SAXS (at the far end) and WAXS detectors (designed by Scott Coburn). c) Position of the WAXS and SAXS detectors relative to the X-ray beam. d) View from the X-ray beam in the direction of the detectors. This view indicates the overlapping region, which can be seen from the SAXS images. [4] Color available in electronic copy.

GIWAXS and GISAXS measurements were collected on neat PFO film, PFO films heat treated at 120°, 180°, 200°, and 280° C and vapor-annealed PFO films on bare VWR glass substrates and VWR glass coated with 100 nm Ag bare VWR glass and VWR Additional measurements were collected on bare VWR glass and VWR glass coated with a 100 nm Ag film

to serve as references. For these measurements, the incident X-ray beam ($\lambda = 0.0918$ nm) was collimated using slits and focused onto the sample position using Kirkpatrick-Biaz mirrors. This provided a 200 μm wide by 80 μm high spot at the sample position whose footprint along the sample spread out by the inverse incident angle. The sample stage was located inside the vacuum chamber (pressure ~ 40 Pa) where both the incident angle and azimuthal rotations were computer controlled. A two-dimensional charged-coupled device (CCD) detector was positioned 270 mm from the center of the sample stage to collect the GIWAXS images inside the same vacuum chamber. The GISAXS images were collected by a second CCD detector located at a distance 5 m from the sample. A rectangular beam stop was positioned to block the primary and the specular reflective beams. Data conversion to q -space was accomplished by calibration using Silver Behenate powder.

GIWAXS and GISAXS measurements were collected at angles of 0.05° , 0.06° , 0.07° , 0.08° , 0.09° , 0.1° , 0.11° , 0.12° , 0.15° , 0.2° , 0.25° , 0.3° , 0.35° , and 0.4° with acquisition times of 3, 5, 10, and 12 seconds. It was found that the most successful incident angle and acquisition times were $.07^\circ$, and 10 seconds, respectively. The feature sizes measured in the samples were smaller than could be measured using SAXS, so the subsequent analysis was centered on the GIWAXS data only. From the raw GIWAXS diffraction patterns, line scans of 10 pixels thickness were taken in the q_x (x-direction) at an angle of 2° and the q_z (y-direction) on image at angle of 88° and plotted versus intensity using view.gtk software. View.gtk is a custom program written in C by the X9 beamline staff based on the “gtk+-2 library. view.gtk is.” The key functions of this program include: displaying X-ray scattering patterns acquired on various detectors (all images are reformatted to 1024 x 1024 pixels), displaying q values for each pixel for both powder diffraction geometry and grazing incidence geometry (q_r , q_z), circular averaging of powder diffraction/solution scattering data, with user-defined mask and dezing, converting full frame grazing incidence scattering pattern to the q_r - q_z plane, line profile extraction, batch

processing of multiple data files, and annotating the scattering pattern with points (q_r , q_z), lines (straight lines on the q_r - q_z plane) or circles (constant q). View.gtk can be downloaded free from [134] and the user's manual can be downloaded from [135].

3.4 Results and Discussion

3.4.1 Pump Power Dependent Emission Spectra of Neat PFO ISI and ISMI Waveguides

Preliminary sets of unpolarized and polarized pump power dependent emission spectra of neat PFO ISI and ISMI waveguides with Ag film thicknesses of 0, 35, 50, 65, and 100 were collected and presented in the Appendix C. These preliminary measurements provided insight into the method development of the collection of emission spectra, a basic understanding of the photonic mode structure of these ISMI waveguides, and further corroboration of the trends presented in this section. The pump power dependent emission spectra presented in this section were collected within 72 hours of fabrication from a freshly fabricated set of seven waveguides made over the course of three days with 100 nm thick neat PFO films and metal film thicknesses of 0, 35, 45, 50, 55, 65, and 100 nm with the optimized measurement method that was developed see Section 3.3.8). The 0 nm Ag metal neat PFO-only waveguide is referred to as an insulator-semiconductor-insulator (ISI) waveguide and the waveguides containing Ag metal are referred to as insulator-semiconductor-metal-insulator (ISMI) waveguides.

Pump power dependent emission spectra of all neat PFO waveguides were collected at eighteen different excitation pump power densities ranging from $6.9\text{E-}6$ to 0.86 W/cm^2 . From these emission spectra, the intensity at the peak emission wavelength (I_{max}), FWHM, and the peak emission wavelength (λ_{max}) were plotted as a function of pump power density (see Section 3.3.10 for method of spectra analysis). The emission spectra of the ISI waveguide are presented in this section prior to the emission spectra of the Ag metal containing ISMI waveguides. It was

organized in this fashion to first understand the optical response of the ISI waveguide, which provided a clear baseline comparison to understand the changes in the optical response of the ISMI waveguides with varying Ag metal film thicknesses.

Pump power dependent emission spectra of the ISI waveguide are plotted as a function of excitation power density in Figure 3.7 in this section as a compilation of all spectra in one plot and as individual spectra in Figure AD1 in Appendix B to more clearly observe the evolution of the emission as a function of increasing power density. These emission spectra exhibit a spectral range of 447-460 nm, with a peak emission wavelength of 454 nm, the characteristic emission of the 0-1 transition. The trends and characteristics of these pump power dependent emission spectra are more clearly elucidated by plots of the emission intensity at the peak wavelength (I_{\max}), the FWHM, and the peak emission wavelength (λ_{\max}) as a function of excitation pump power density and presented in Figure 3.8(a), (b), and (c), respectively.

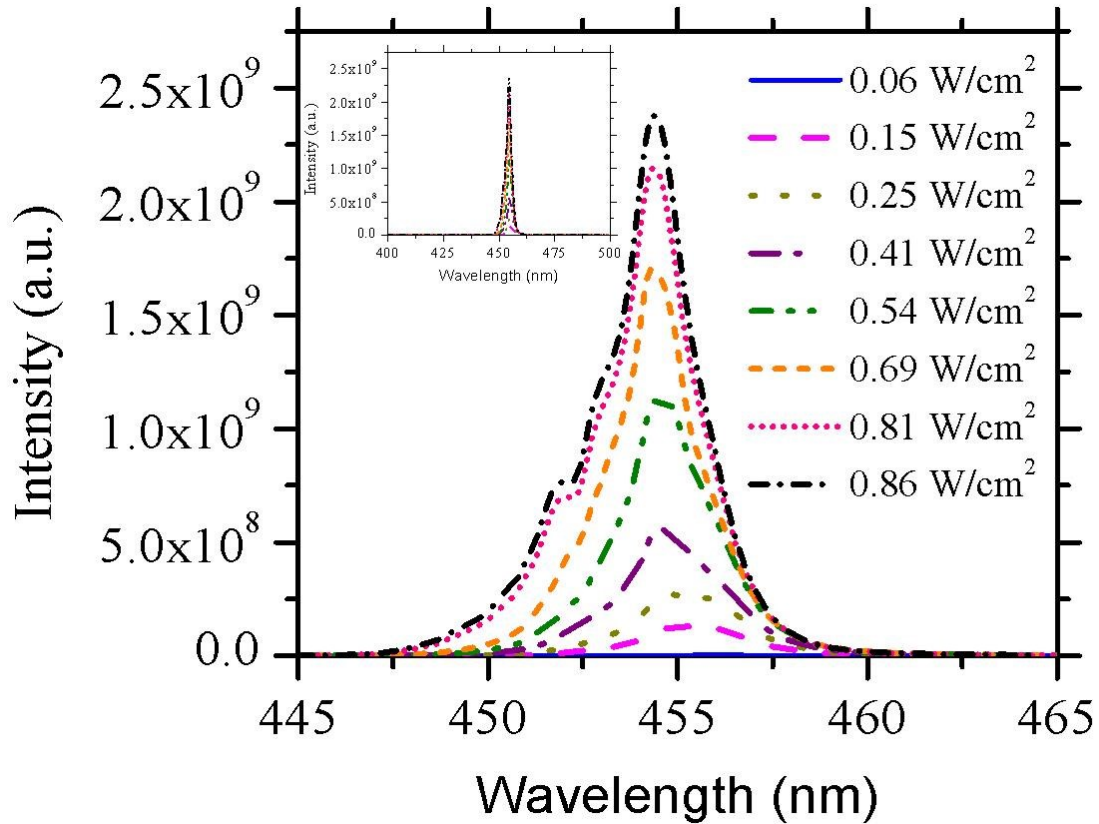


Figure 3.7. Compilation of glass/PFO/glass ISI waveguide emission spectra at varying pump power densities ranging from 0.06 to 0.86 W/cm². Inset is same spectra re-scaled to visually depict the significant line narrowing with increasing pump power density.

From the fitted plot of emission intensity at the peak emission wavelength (I_{max}), the ISI waveguide exhibits an ASE threshold of 0.17 W/cm² with a slope efficiency of 3.41E9

$\frac{\text{counts} \times \text{cm}^2}{\text{W}}$ (see Fig. 3.8(a)). Under excitation pump power densities below the ASE threshold, the sample underwent steady state fluorescence emission and exhibited FWHM's ranging from 11.74 nm at 6.9E-6 W/cm² to 3.05 nm at 0.15 W/cm² (see Fig. 3.8(b)). At excitation power densities above the ASE threshold, the ISI waveguide exhibited FWHM's ranging from 3.05 nm at a pump power density of 0.17 W/cm² down to 2.47 nm at a pump power density of 0.76 W/cm². In reality, these reported FWHM values may be narrower due to the fact that the 150 μm spectrometer input slits may limit the spectral resolution of the measurement system (see Fig. 3.8(b)). Additionally, as the excitation pump power density was increased, the ISI waveguide

exhibited a blue spectra shift (see Fig. 3.8(c)). At pump power densities below the ASE threshold, the peak emission wavelength blueshifted from 458.13 nm at a pump power density of $6.9\text{E-}6\text{ W/cm}^2$ to 455.5 nm at a pump power density of 0.15 W/cm^2 . At pump power densities at the ASE threshold and above, the peak emission wavelength further blueshifted from 455.4 nm at a pump power density of 0.17 W/cm^2 to a values ranging between 454.56 nm and 454.35 nm at pump power densities ranging between 0.41 and 0.86 W/cm^2 .

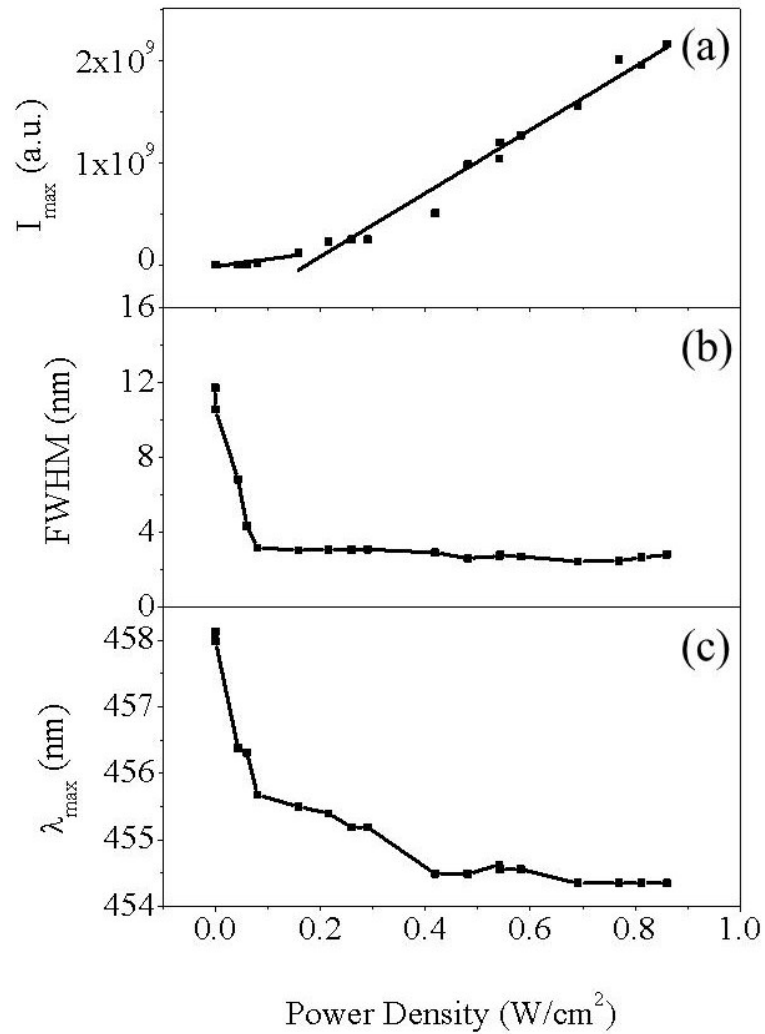


Figure 3.8. Glass/PFO/Glass ISI waveguide (a) emission intensity at the peak emission wavelength (I_{max}) with linear fits below and above the ASE threshold, (b) full-width-half-maximum, (c) and peak emission wavelength (λ_{max}) as a function of excitation power density.

Pump power dependent emission spectra of ISMI waveguides with Ag film thicknesses of 35, 45, 50, 55, 65, and 100 nm were collected at eighteen different power densities ranging from $6.9\text{E-}6$ to 0.86 W/cm^2 . Compilation plots of the emission spectra of the all ISMI waveguides at nine of the eighteen measured pump power densities are presented in this section, where there is one plot for each pump power density containing the emission spectra of all six ISMI waveguides (see Fig. 3.9(a)-(i)). Individual plots of the emission spectra for each of the six ISMI waveguides with Ag metal film thicknesses of 35, 45, 50, 55, 65, and 100 nm at all eighteen excitation pump power densities are presented in Figures. AD2, AD3, AD4, AD5, AD6, and AD7 in Appendix D, respectively, to more clearly show the spectral evolution as a function of Ag metal film thickness and excitation power density. Plots of I_{max} of all seven waveguides plotted together versus pump power density are presented in Figure 3.10 as a log plot and in Figure 3.11 on a linear scale. Plots of FWHM and λ_{max} of all six ISMI waveguides were plotted as a function of pump power density and are presented in Figures 3.12, 3.13, and 3.14, respectively. In the I_{max} , FWHM, and λ_{max} , the results for the 0 nm Ag ISI waveguide were included to serve as a facile means of comparison of the optical response of the waveguide with the introduction of Ag metal of varying film thickness (see Figs. 3.10, 3.11, 3.12, 3.13, and 3.14).

From the emission spectra (Fig. 3.9) and plots of I_{max} (Fig. 3.10 and 3.11) and FWHM (Fig. 3.12) as a function of pump power density, it is evident that the ISMI waveguides exhibited a wide range of emission intensities as a function of metal film thickness. However, all ISMI waveguides produce peak emission intensities significantly weaker than the ISI waveguide (no Ag metal). This significant decrease in emission intensity with the introduction of Ag metal into the waveguide is most clearly illustrated in the log plot of I_{max} versus pump power density of all ISMI waveguides, as well as the ISI waveguide in Figure 3.10. Comparing the relative I_{max} of the six ISMI waveguides to the neat PFO-only waveguide, the trend in I_{max} at excitation pump power densities above and below ASE, emission intensity is as follows from strongest to weakest: 0 >>

45 nm > 50 nm > 55 nm \geq 65 nm > 100 nm > 35 nm (see Fig. 3.10). The 45 nm Ag waveguide which exhibited the greatest peak emission intensity of 3.8E8 counts at a pump power density of 0.76 W/cm² is only 1.62% as intense as the non Ag metal containing ISI waveguide (see Fig. 3.10).

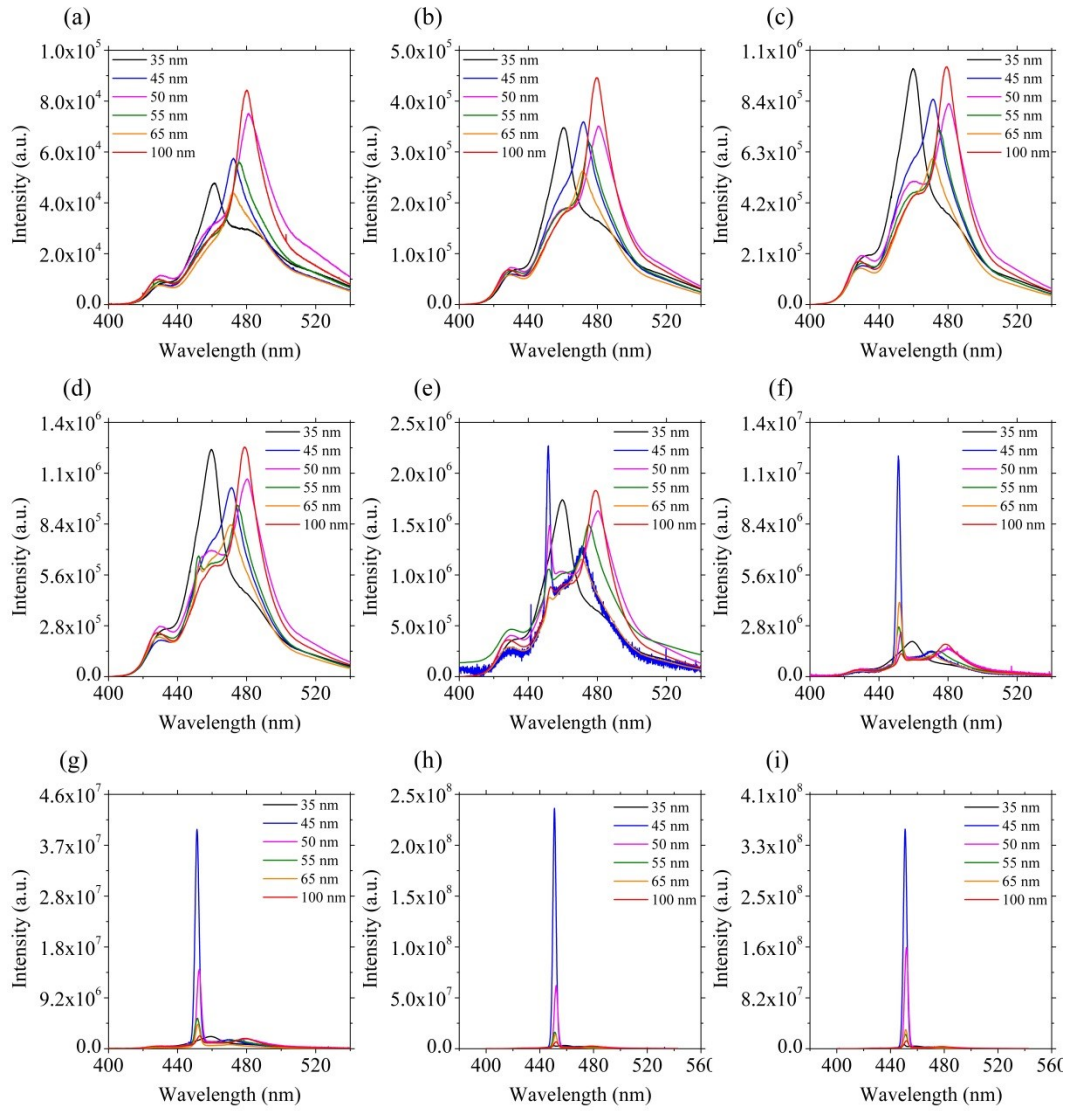


Figure 3.9. Gain spectra of glass/PFO/Ag/glass waveguides with Ag film thicknesses of 35, 45, 50, 55, 65, and 100 nm under excitation power densities of (a) 6.97E-6, (b) 0.06, (c) 0.21, (d) 0.29, (e) 0.41, (f) 0.48, (g) 0.542, (h) 0.69, (r) 0.86 W/cm². Color available in electronic copy.

Fitted linear plots of I_{max} as a function of pump power density for all ISMI waveguides, as well as the ISI waveguide are presented in Figure 3.11. From these fitted plots, the ASE threshold and slope efficiency were extracted. It was found that the trends in ASE threshold and slope efficiency as a function of metal film thickness closely mirrors that observed in I_{max} . The trend in ASE threshold as a function of metal film thickness from lowest to highest threshold is as follows: 0 nm << 45 nm < 55 nm < 65 nm < 100 nm < 50 nm < 35 nm (see Fig. 3.11). As noted previously, the ISI waveguide exhibited an ASE threshold of 0.17 W/cm². In contrast, the Ag metal containing ISMI all exhibited significantly higher ASE thresholds than the ISI waveguide with values as follows from lowest to highest: 0.46 W/cm² for the 45 nm Ag film thickness, 0.47 W cm² for Ag film thicknesses of 55, 65, and 100 nm, 0.50 W/cm² for the 50 nm Ag film thickness case, and 0.53 W/cm² for the 35 nm Ag film thickness. The 50 nm Ag film thickness ISMI waveguide, which exhibited a slightly higher ASE threshold than the 55, 65, and 100 nm Ag film waveguides, is likely an erroneous data point due to measurement error or a deviation in the Ag or PFO film thickness in the sample.

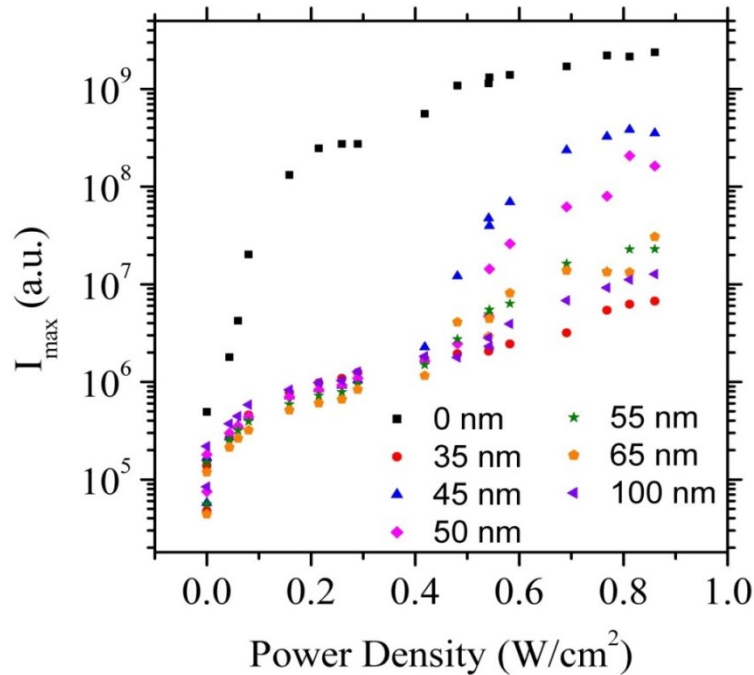


Figure 3.10. Log plot of I_{max} as a function of pump power density of glass/PFO/Ag/glass waveguides with Ag film thicknesses of 0, 35, 45, 50, 55, 65, and 100 nm.

The trend in ASE slope efficiency as a function of Ag metal film thickness was virtually identical to the trends observed in the I_{\max} and ASE threshold (see Fig. 3.11). From the highest to lowest ASE slope efficiency the trend is as follows: 0 nm >> 45 nm > 50 nm > 55 nm > 65 nm > 100 nm > 35 nm. As noted previously, the ISI waveguide exhibited the greatest ASE slope efficiency of $3.4E9 \frac{\text{counts} \times \text{cm}^2}{\text{W}}$. The slope efficiencies of the Ag metal containing waveguides from highest to lowest are as follows: 9.9E8, 5.3E8, 6.8E7, 5.8E7, 3.19E7, and 2.14E7 $\frac{\text{counts} \times \text{cm}^2}{\text{W}}$ for ISMI waveguides with Ag metal film thicknesses of 45, 50, 55, 65, 100, and 35 nm, respectively (see Fig. 3.11).

Like the ISI waveguide, all ISMI waveguides exhibited significant line narrowing and a spectral collapse of the FWHM upon reaching their respective ASE threshold (see Fig. 3.12). Below ASE, the trend in the FWHM as a function of Ag metal film thickness from broadest to narrowest is as follows: 50 nm > 55 nm > 65 nm > 45 nm > 35 nm > 100 nm > 0 nm. At pump power densities below the respective ASE threshold for each of the ISMI waveguides, the following ranges of FWHM values for each ISMI waveguide were observed: 44.63 to 29.1 nm, 27.34 to 38.43 nm, 36.74 to 38.11 nm, 30.86 to 34.55 nm, 43.07 to 20.37 nm, and 20.79 to 22.86 nm for ISMI waveguides with Ag metal film thicknesses of 50, 55, 65, 45, 35, and 100 nm, respectively.

In contrast, above their respective ASE thresholds, the trend in FWHM as a function of Ag metal film thickness is as follows from broadest to narrowest: 35 nm > 100 nm > 55 nm > 65 nm > 50 nm > 45 nm > 0 nm, with the 50, 55, and 65 nm samples having very similar FWHM (see Fig. 3.12). At a pump power densities > 0.54 W/cm² the following FWHM values for each ISMI waveguide were observed: 4.82, 4.42, 3.8, 3.26, 3.16, and 2.8 nm for ISMI waveguides with Ag metal film thicknesses of 35, 100, 55, 65, 50, and 45 nm. It is noteworthy that the ISMI waveguide with a 45 nm Ag metal film thickness exhibited the narrowest FWHM of 2.8 nm,

which was equivalent to the ISI waveguide

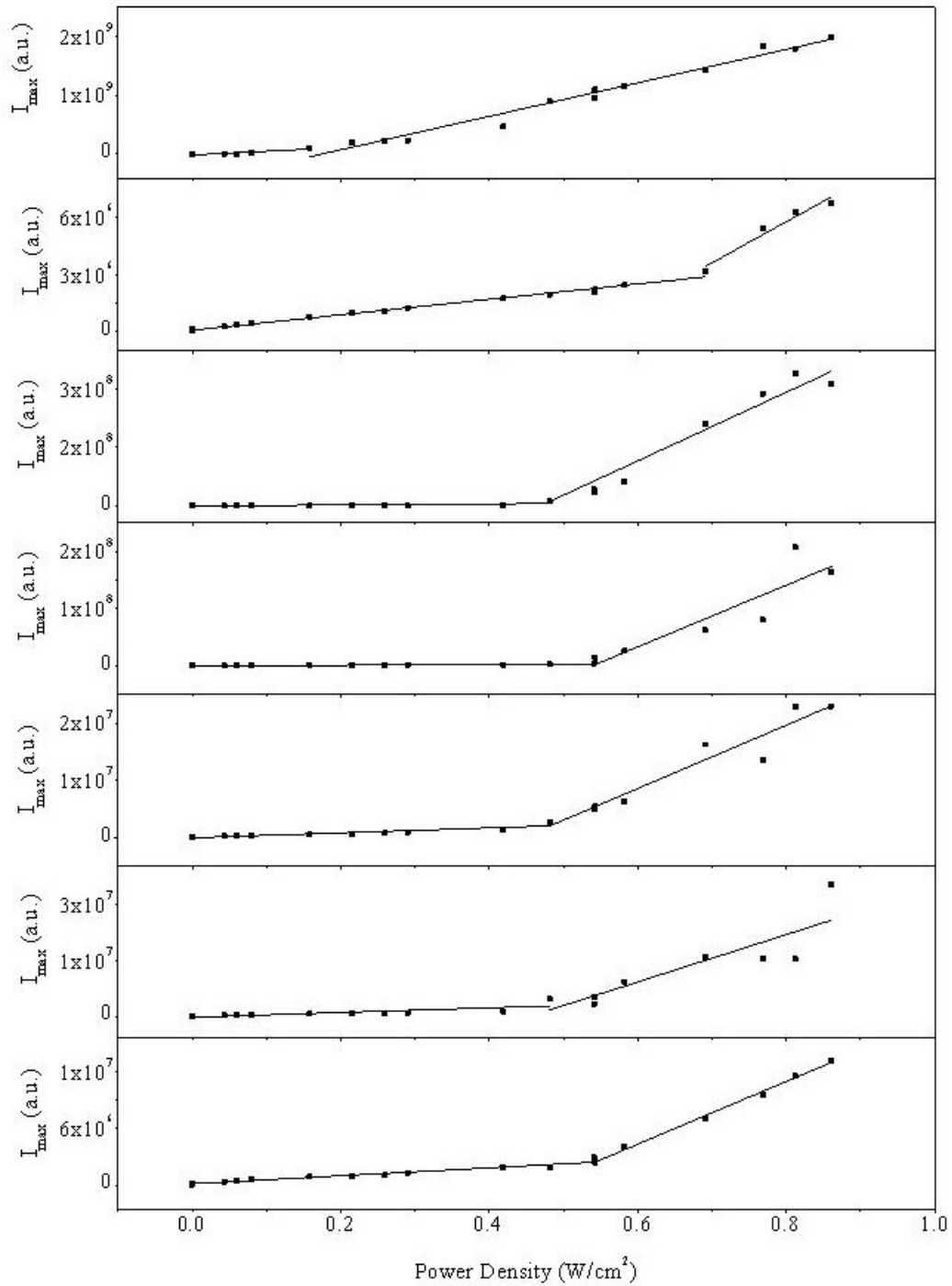


Figure 3.11. Fitted plots I_{max} as a function of pump power density from spectra of glass/PFO/Ag/glass ISMI waveguides with Ag film thicknesses (t_m) of (a) 0, (b) 35, (c) 45, (d) 50, (e) 55, (f) 65, and (g) 100 nm.

In conjunction with mapping the trends in I_{max} , FWHM, ASE threshold, and ASE slope efficiency, the trend in λ_{max} of the ISMI waveguides as a function of pump power density was studied (see Fig. 3.13). Analogous to the ISI waveguide, all ISMI waveguides exhibited a blue spectral shift with increasing excitation power density (see Fig. 3.13). Above and below each sample's respective ASE threshold, each waveguide emitted at slightly different peak wavelengths. Below the respective ASE threshold of each waveguide, the trend in λ_{max} from longest to shortest is as follows: 50 nm > 100 nm > 55 nm > 45 nm \geq 65 nm > 35 nm > 0 nm. The average λ_{max} values observed are as follows: 480.63, 479.37, 475.12, 475.12, 471.45, 459.94, and 456.32 nm for waveguides with Ag meal film thicknesses of 50, 100, 55, 45, 65, 35, and 100 nm.

Above the ASE thresholds, the trend in peak emission wavelength as a function of with metal film thickness is as follows from longest to shortest wavelength: 0 nm > 50 nm > 100 nm > 65 nm > 55 nm > 45 nm > 35 nm. However, unlike the trend in peak emission wavelength under steady state emission (below the ASE threshold), which spanned over a broad range of 24 nm, the peak emission wavelengths of all seven waveguides at or above ASE ranged between 454.45 nm (for the 0 nm Ag waveguide) to 449.8 nm (for the 35 nm Ag waveguide).

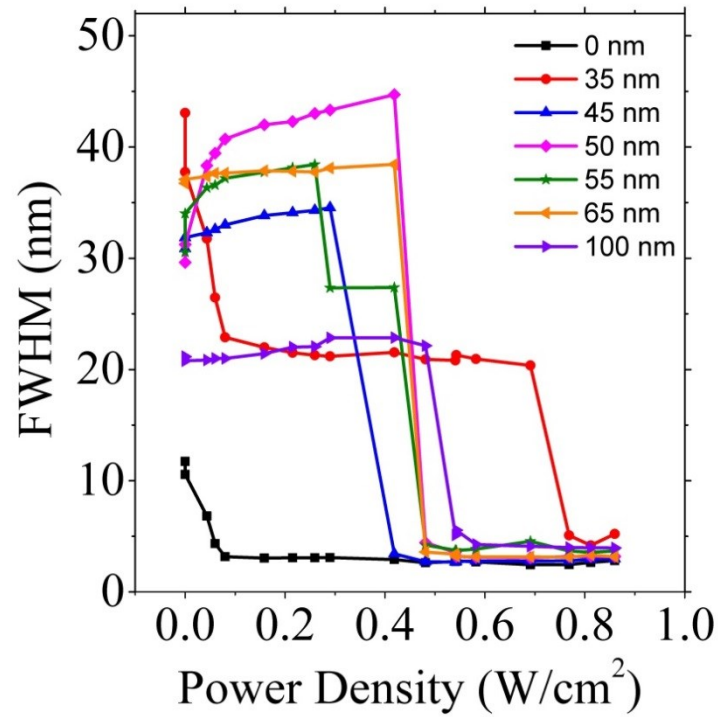


Figure 3.12. Full-width-half-maximum (FWHM) of the emission spectra of glass/PFO/Ag/Glass Emission waveguides with Ag film thicknesses of 0, 35, 45, 50, 55, 65, and 100 nm as a function of excitation power density.

The overall magnitude of the blue spectral shift with increasing power density trends as a function of Ag metal film thickness from largest to smallest shift is as follows: 50 nm > 100 nm > 45 nm > 55 nm > 65 nm > 35 nm > 0 nm. The magnitudes of the blueshifts are 28.3 nm, 27.21 nm, 24.03 nm, 23.74, 19.89 nm, 10.12 nm, and 1.86 nm for the 50, 100, 45, 55, 65, 35, and 0 nm Ag neat PFO waveguides.

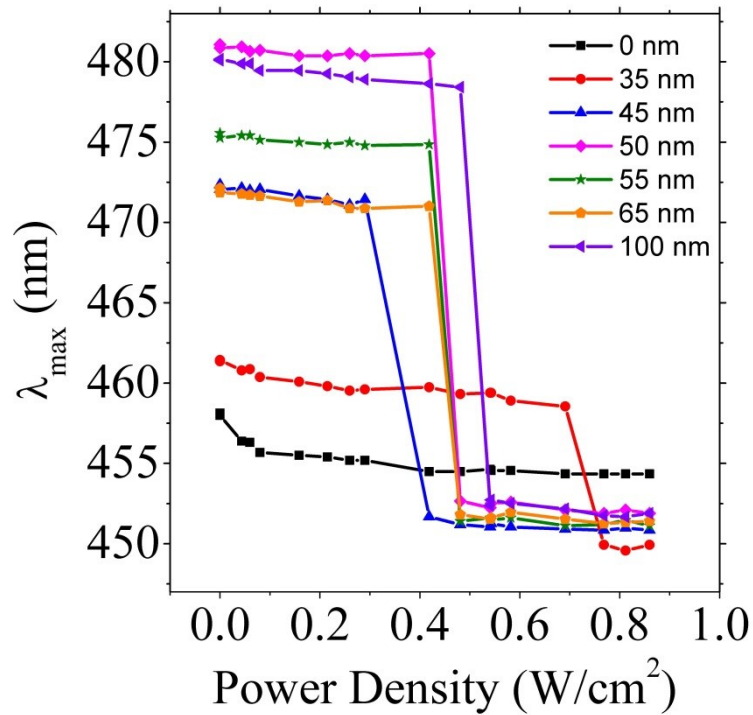


Figure 3.13. Peak emission wavelength (λ_{max}) of gain spectra of neat PFO insulator-semiconductor-metal-insulator waveguide with Ag film thicknesses of 0, 35, 45, 50, 55, 65, and 100 nm as a function of excitation power density.

3.4.2 Absorption Spectroscopy and FDTD Simulations of PFO SMI Waveguide

To clearly ascribe the origins of observed trends in I_{max} , FWHM, ASE threshold and slope efficiency, and λ_{max} of the pump power dependent emission spectra of ISMI waveguides as a function of metal film thickness, additional characterization of the waveguides was carried out. Because the 35 - 100 nm range of Ag metal film thicknesses in these ISMI waveguides falls below the optical thickness of Ag metal, it was thought that there could be significant changes in the transmittance and reflectivity of the Ag metal film across the 35 – 100 nm Ag film thickness range. Such variation could potentially have caused the excitation power density incident on the waveguide to vary as a function of Ag film thickness if the metal's reflectivity changed significantly over the range which the waveguides were fabricated. For example, if a significant

increase in transmittance occurred over the 35 – 100 nm range in these ISMI waveguide, the thin 35 nm Ag ISMI could potentially allow more of the 355 nm excitation to ‘leak’ through the waveguide than the thick 100 nm Ag film waveguide, which was expected to be significantly less transmissive and more reflective. This increased reflectivity of the thicker samples could have potentially caused an increasing fraction of the pump power to reflect back into the PFO emitter layer in the waveguide, thereby increasing the effective path length of the excitation source and in-turn increase the resultant power density. Additionally, the same changes in transmittance and reflectivity of the Ag metal film could also alter the photonic mode structure in the waveguide, if it acted as a Fabry-Perot resonator cavity. Therefore, if such phenomena were occurring within these waveguides they would need to be accounted for and understood to clearly understand the effect of SPP-polymer emitter coupling on the resultant gain spectra as a function of metal film thickness and excitation power density.

To determine if there were significant changes in transmittance and reflectivity through the ISMI waveguides of varying Ag metal films of varying thickness, absorption spectra were collected on ISMI waveguides with Ag film thicknesses of 0, 35, 65, and 100 nm (See Methods Section 3.3.11). Additionally, a set of full field electromagnetic simulations were also carried out on PFO waveguide analogs with Ag film thicknesses of 35, 50, 65, and 100 nm under wavelengths of 355 nm (the excitation wavelength used to experimentally excite the samples) and 460 nm (the peak emission wavelength of PFO) (see Section 3.3.12).

Absorption spectra of ISMI waveguides with Ag metal film thicknesses of 0, 35, 50, 65, and 100 nm are plotted in Fig. 3.14 as percent transmittance versus wavelength. All waveguides exhibit the same spectral shape, but broadband shifted to lower transmittance with increasing metal film thickness. Additionally, the percent transmittance at the 355 nm excitation wavelength is quite low (< 45% for the waveguide with no metal); suggesting that even with significant changes in the transmittance and reflectivity over the 35 - 100 nm metal film thickness range,

there is little change in the excitation power density within the waveguide because more than half of the 355 nm excitation energy is attenuated by the 100 nm PFO film before it is incident on the Ag film. Furthermore, because the spectral shape is identical for all metal film thicknesses, it suggests that there are no differences in the photonic mode structure of the waveguide as a function of metal film thickness.

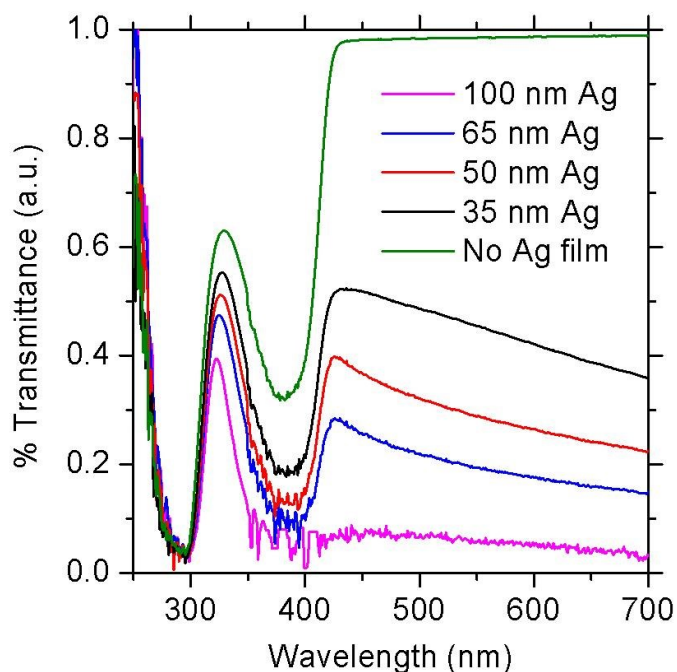


Fig. 3.14 Absorption spectra plotted as percent transmittance versus wavelength of glass/PFO/Ag/glass waveguides with Ag film thicknesses of 0 (no Ag film), 35, 65, and 100 nm. Color available in electronic copy.

The full-field electromagnetic simulations that were conducted provide more comprehensive evidence that suggest that changes the transmittance and reflectivity with varying Ag metal film thickness do not alter the excitation power density nor the photonic mode structure of the waveguide. The first simulation was conducted on SMI waveguide analogs with metal film thicknesses of 35, 50, 65, and 100 nm under excitation of a 355 nm plane wave source to understand how the pump wavelength was attenuated by the waveguide. To visualize the interaction between the 355 nm plane wave source and the three layers of the waveguide, 2D

profiles of the real and imaginary components, the absolute intensity, and the absolute intensity squared of the electric field were generated (see Fig. 3.15(a)-(d)).

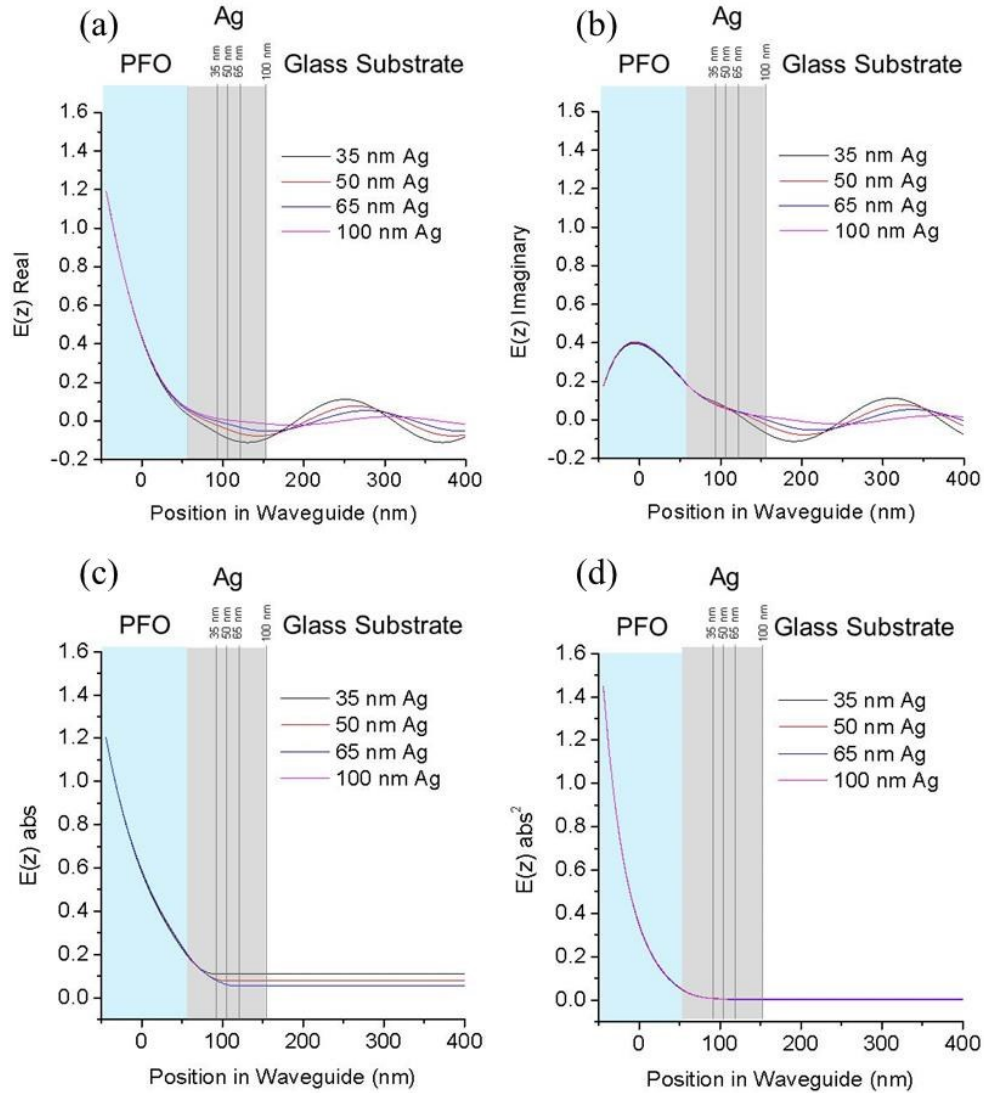


Fig. 3.15 Simulated 2D electric field profiles of a 355 nm plane wave source incident on PFO-Ag-glass waveguides with Ag metal film thicknesses of 35, 50, 65, and 100 nm. Shown in (a) and (b) are the real and imaginary components of the electric field, respectively, (c) is the absolute intensity and (d) is the absolute intensity squared of the electric field. Color available in electronic copy.

From these electric field profiles, specifically in the absolute intensity and absolute intensity squared plots (see Fig. 3.15(c) and (d)) it is evident that more than 90% of the 355 nm

pump wavelength is absorbed by the 100 nm PFO layer. This indicates that the 100 nm PFO film thickness used in all experimentally fabricated ISMI waveguides is optically thick and in-turn the excitation source interaction with the Ag film is negligible. Therefore, there is very low likelihood that the excitation path length and resultant power density incident on the waveguides varies with metal film thickness.

The second simulation conducted was identical to the previous case; however the plane wave excitation source incident on the structure was set to 460 nm, the peak emission wavelength of the PFO emitter. These simulations were conducted to determine if changes in transmittance and reflectivity of the Ag metal film with varying thickness alters the photonic mode structure of the PFO emission within the waveguide. To visualize the interaction between the 460 nm plane wave source and the three layers of the waveguide, 2D profiles of the real and imaginary components, the absolute intensity, and the absolute intensity squared of the electric field were generated (see Fig. 3.16(a)-(d)). From the 2D absolute intensity and absolute intensity squared electric field profiles shown in Fig. 3.16(c) and (d), respectively, it is observed that the electric field intensity of the photonic mode increases in the glass substrate with decreasing metal film thickness. However, the percentage of field intensity that leaks even with the thinnest 35 nm Ag film case is quite small. Additionally, the overall photonic mode profile is identical for all metal film thicknesses, suggesting that there is no fundamental difference as a function of metal film thickness.

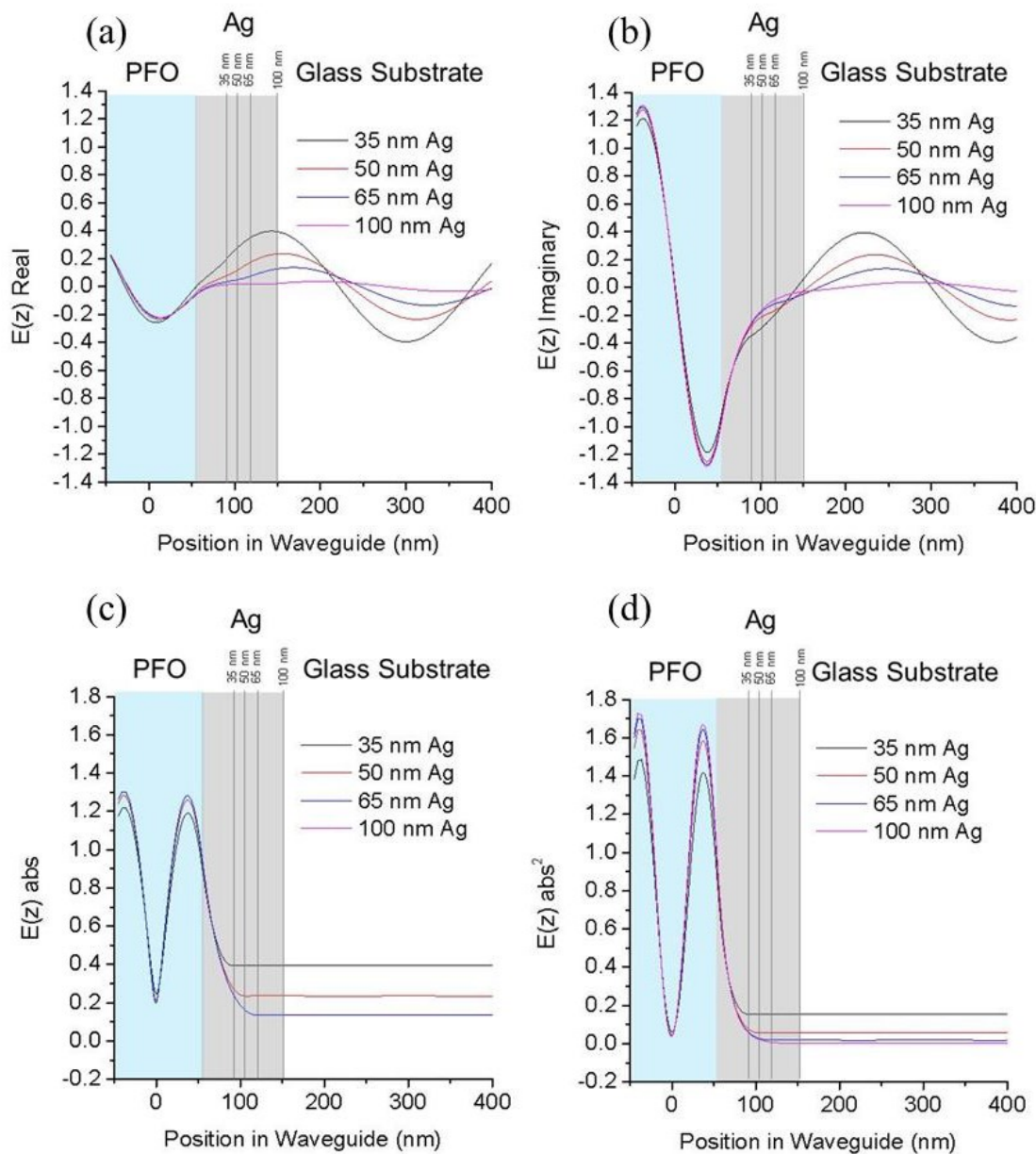


Fig. 3.16 Simulated 2D electric field profiles of a 460 nm plane wave source incident on a PFO/Ag/glass SMI waveguide with Ag metal film thicknesses of 35, 50, 65, and 100 nm. Shown in (a) and (b) are the real and imaginary components of the electric field, respectively, (c) is the absolute intensity and (d) is the absolute intensity squared of the electric field. Color available in electronic copy.

3.4.3 Comparison of Pump Power Dependent Emission Spectra of ISMI Waveguides with Varying Ag Metal Film Thickness to Theoretical Dispersion Relations

The set of gain spectra collected on ISMI waveguides with Ag metal film thicknesses of 0, 35, 45, 50, 55, 65, and 100 nm, exhibited clear trends in I_{max} , ASE threshold, ASE slope efficiency, λ_{max} , and FWHM as a function of Ag metal film thickness. Absorption spectroscopy and FDTD simulations of the SMI waveguides indicated that there is negligible variation in the excitation pump power density due changes in the Ag metal transmittance over the studied 35 - 100 nm Ag film thickness range. This was found to be due to the fact that the 100 nm PFO semiconductor layer in the waveguide was nearly optically thick at the 355 nm pump wavelength. Additionally, while a slight increase in leakage at or around the PFO emission wavelengths through the metal film with decreasing Ag metal film thickness, the simulations showed that the photonic mode structure of the waveguide remained constant over the range of metal film thicknesses, thereby ruling out any Fabry-Perot behavior or other photonic phenomena.

Based on the understanding that the excitation pump power density within the waveguides remained constant and that the photonic mode character of these waveguides was unchanged over the 35 - 100 nm Ag film thickness range, the observed trends I_{max} , ASE threshold, ASE slope efficiency, λ_{max} , and FWHM as a function of metal film thickness were attributed to the direct interaction between the PFO semiconductor emitter and excited SPP modes. While these gain measurements did not provide direct insight into which SPP modes were excited within the waveguide or the magnitude of their propagation length(s) (L) and field leakage (i.e., mode penetration depth, (D)), they did provide compelling indirect experimental evidence of the theoretically predicted trend in efficient low-loss SPP-polymer emitter coupling as a function of metal film thickness (developed in Chapter 2). By comparing the trends of the experimentally collected gain spectra of ISMI waveguides to the theoretical dispersion relations solved for the four SPP mode types supported by SMI waveguides (conducted in Chapter), a clear

relationship between the resultant strength, efficiency, and character of the ISMI waveguide emission and the theoretically predicted trends in SPP loss and field leakage, (specifically for the symmetric bound SB SPP mode) was made.

The theoretical dispersion relations solved for an F8BT-Ag-SiO₂ SMI waveguide (presented in Chapter 2) showed that these SMI waveguides supported two SPP mode symmetries (symmetric and antisymmetric) and two SPP mode leakage types (bound and leaky), giving rise to four distinct SPP mode types: symmetric bound (SB), antisymmetric bound (AB), symmetric leaky (SL), and antisymmetric leaky (AL) [82]. The SPP mode propagation lengths (L), mode penetration depths, (D) and magnetic field leakage of the four SPP mode types were studied over a range of Ag metal film thicknesses from 25-100 nm and were found to be highly tunable as a function of metal film thickness and emitter dielectric constant (i.e., excitation regime: steady state vs. ASE). Over the studied range of metal film thicknesses, the dispersion relations showed that L and D of the symmetric modes, specifically the symmetric bound (SB) mode, exhibits the longest mode propagation lengths (L) ($>1330\ \mu\text{m}$) and greatest penetration depths (D) ($>74\ \mu\text{m}$), which are highly tunable by varying the metal film thickness and emitter dielectric constant. In contrast, the two antisymmetric modes exhibited very short propagation lengths and small mode penetration depths, which varied little over the studied metal film thickness range or emitter dielectric constant (i.e., excitation regime: steady state vs. ASE). Therefore, it was not likely that the antisymmetric modes had a significant influence on the PFO semiconductor/SPP interactions over the Ag metal film thickness range that was experimentally studied. For the sake of this discussion, it is salient to remind the reader that the propagation length (L) is the inverse of the imaginary component (k_i) of the complex plasmon polariton wavevector. The imaginary component (k_i) is the loss component, thus it signifies that the antisymmetric modes that exhibit short propagation lengths, have a much larger imaginary loss component (k_i) than the symmetric modes that exhibit long propagation lengths.

The theoretical calculations of enhanced surface plasmon field leakage and propagation length of the SB mode through the variation of metal film thickness and emitter dielectric closely mirrored the observed trends in I_{max} , ASE threshold, and ASE slope efficiency of the experimentally measured ISMI waveguides. Over the studied range of Ag metal film thicknesses, the SB bound mode in the F8BT-Ag-SiO₂ SMI waveguide exhibited a SB mode cutoff at metal film thicknesses <45 nm. Solutions below the mode cutoff of 45 nm were found for the waveguide under steady state fluorescence emission and were found to have very short L values (< 300 nm)(i.e., high loss) for metal film thicknesses < 30 nm (see Fig. 3.17(a)). With increasing metal film thickness, L of the SB mode exponentially increased to maximum (>1300 μ m) at Ag metal film thicknesses between 45 and 50 nm (see Fig. 3.17(a)). At film thicknesses > 50 nm, L exponentially decreased to values on the order of 10 μ m and plateaued at film thicknesses greater than 60 nm (see Fig. 3.17(a)). The SB mode penetration depth, (D) into the organic semiconductor emitter cover layer and silica substrate mirrored the trend in mode propagation length (L) (see Fig. 3.17(b)). At metal film thicknesses of 45-50 nm, D reached a maximum, in excess of 75 μ m and 200 nm into the organic semiconductor cover and silica substrate, respectively (for the complex gain case). With increasing film thickness, the SB mode D decreased and then plateaued at metal film thickness >60 nm to values on the order of 6 μ m and 140 nm for organic semiconductor cover and silica substrate, respectively (see Fig. 3.17(b)).

Prior to a direct comparison between the trends between the pump power dependent emission spectra of ISMI waveguides and the theoretical dispersion relation results, it is important to briefly discuss the trend in mode penetration depth (D). At thick metal films (> 60 nm), the majority of the mode energy is more tightly bound within the metal film and in-turn L and D are short because the mode is damped by the lossy metal. Therefore, the majority of the mode energy is trapped at the metal-semiconductor interface. In contrast, with decreasing metal film thickness, more of the mode energy leaks into the organic semiconductor emitter cover and

silica substrate (i.e., increased D), which allows the mode to propagate in the forward direction significantly further due to decreased interaction with the lossy metal. Below certain thickness (depending on the mode and emitter dielectric constant), the metal film thickness will become too thin to support a propagating mode, and all mode energy leaks into the cover and substrate layers of the waveguide. The trend in the SB mode L and D shows that by optimizing metal film thickness, SB mode penetration depth, (D) and in-turn mode propagation length, (L) can be enhanced by reducing the amount of SPP mode energy trapped at the metal film. This reduction of SPP mode energy trapped at the metal is expected to reduce the amount of light energy from the organic semiconductor emitter trapped at the metal film and increase the light outcoupling efficiency of the emitter.

To directly compare the theoretically predicted trend of the dominant SB mode to the pump power dependent emission spectra of ISMI waveguides of varying Ag metal film thickness, a stack plot was generated with the calculated SB mode propagation length (L) (see Fig. 3.17(a), mode penetration depth (D) (see Fig. 3.17(b)) atop scatter plots of the experimentally measured I_{max} (see Fig. 3.17 (c)), ASE threshold (see Fig. 3.17 (d)), ASE slope efficiency (see Fig. 3.17 (d)), and FWHM values recorded at a pump power density of 0.76 W/cm^2 (see Fig. 3.17 (e)). The experimentally measured intensity at the peak emission wavelength (I_{max}) (see Fig. 3.17 (c)) showed the ISMI waveguide that produced the greatest I_{max} (45 nm Ag metal film thickness) has a nearly equivalent metal film thickness to that which the theory predicts that the SB mode exhibited the greatest mode propagation length (L) (i.e., the lowest loss) (see Fig. 3.17 (a)) and the greatest mode penetration depth (D) (at Ag metal film thicknesses of 45 – 47 nm) (see Fig. 3.17 (b)). At metal film thickness below 45 nm, the ISMI I_{max} decreases to a minimum for 35 nm Ag metal film ISMI (see Fig. 3.17 (c)). Correspondingly, at metal film thickness below 45 nm, the theory predicts a minimum in the SB mode propagation length (L) (i.e., the greatest loss) (see Fig. 3.17 (a)). At metal film thickness between 45 and 55 nm (see Fig. 3.17(c)), I_{max} exponentially

decreases and then linearly decreases at Ag metal films >55 nm in thickness, which is virtually identical to the trend in the theoretically predicted trend for the SB mode propagation length (L) (see Fig. 3.17X(a)) and mode penetration depth (D) (see Fig. 3.17 (b)). These findings corroborate the theoretical prediction, that the lowest loss/most-efficient SPP-emitter coupling occurs when the SPP mode propagation length is greatest (i.e., lowest loss) arising from the fact that the majority of the mode energy is shifted into the organic semiconductor emitter layer, away from the lossy metal [130].

Further corroboration that the resultant efficiency of the emission of the Ag containing neat PFO ISMI waveguides was largely dominated by the imaginary component and field distribution of the SB mode can be found by looking at the ASE threshold (see Fig. 3.17(d)) and ASE slope efficiency values (see Fig. 3.17(e)) of the experimentally measured ISMI waveguides. It was observed that the sample with the lowest ASE threshold and greatest slope efficiency (the 45 nm Ag ISMI waveguide) was at a virtually identical metal film thickness (45 - 47 nm) where the SB mode exhibited the longest L and greatest D . At metal film thickness below 45 nm, where the L of the SB mode was the shortest (i.e., the highest loss), the 35 nm Ag ISMI waveguide exhibited the highest ASE threshold see Fig. 3.17(d)) and lowest ASE slope efficiency (see Fig. 3.17(e)). This was likely attributed to the fact that the SB mode ceased to propagate at or below 45 nm, or that if it was present, it was highly dispersive, which resulted in inefficient plasmon-emitter coupling and reduced emission efficiency. As previously noted, at Ag metal film thicknesses above 45 nm the SB mode L and D exponentially decreased and plateaued at Ag film thicknesses greater than 55 nm, which is the virtually identical behavior observed in the ASE threshold and ASE slope efficiency. Only the 50 nm Ag ISMI waveguide exhibited an uncharacteristically higher ASE threshold than the other samples, which may be due to variations in polymer or metal film thickness on the sample, measurement, and or fitting error(s). FWHM of the experimentally measured pump power dependent emission spectra was included in the stack

plot in Figure 3.17(e) to further illustrate that when the SB mode exhibited the greatest L (i.e., lowest loss) and greatest D that a FWHM identical to the 0 nm Ag PFO-only waveguide was observed. Furthermore, as the Ag metal film thickness was either increased or decreased from 45 nm, the FWHM broadened due to the fact that more SPP mode energy was bound at the metal-semiconductor interface and in-turn the modes exhibited greater loss.

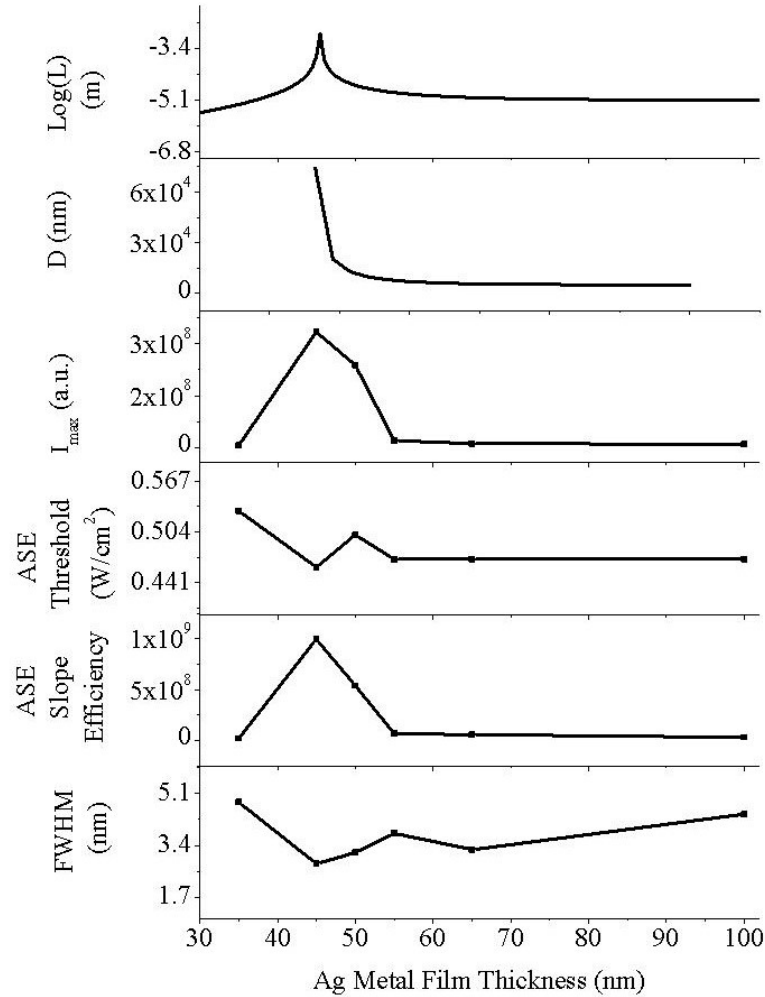


Figure. 3.17 Theoretically calculated symmetric bound (SB) mode propagation length (L) (a) and semiconductor layer penetration depth (D) as a function of Ag metal film thickness for a F8BT/Ag/glass semiconductor-metal-insulator waveguide. (d-f) show I_{max} , ASE threshold, and ASE slope efficiency, respectively of glass/PFO/Ag/glass ISMI waveguides with Ag metal film thicknesses of 35, 45, 50, 55, 65, and 100 nm under an excitation pump power density of $0.76 W/cm^2$.

There are additional considerations that must be addressed to fully understand the complex interactions between the SPP modes supported by these waveguides and the experimentally measured gain spectra. It is very likely that a detailed analysis may reveal indirect evidence that other SPP mode(s) predicted to be present play a role in the influence of the resultant gain spectra as a function of Ag film thickness and excitation power density [130]. It is likely that the tightly bound antisymmetric modes are a large source of disparity in emission intensity of the optimized 45 nm Ag neat PFO waveguide and that of the 0 nm neat PFO-only waveguide. This is due to the fact that because the propagation length (i.e., loss) of the antisymmetric modes is present and relatively constant at all Ag metal film thicknesses, that this can be considered an intrinsic loss of the system unless there is means developed to selectively couple to the long range symmetric modes or suppress the coupling to the antisymmetric modes. Furthermore, the careful control over Ag and PFO layer thickness and roughness may influence the coupling efficiency and loss. These considerations will be discussed in greater detail in Chapter 6.

3.4.4 Characterization of Polymer Molecular Dipole Orientation

Owing to the considerable effort that was devoted to the optical characterization of neat PFO ISMI waveguides of varying Ag metal film thickness, optical characterization additional of ISMI waveguides with different polymer molecular dipole orientations was outside the scope of this thesis. However, as described in the introduction, the polymer molecular ordering is expected to play a critical role in the degree and efficiency of semiconductor-SPP coupling. This section details the work conducted on the fabrication of PFO thin films of varying morphology and molecular orientation and their subsequent characterization using Grazing-Incidence small- and wide-angle X-ray Scattering (GISAXS and GIWAXS, respectively).

3.4.5 Background on GIWAXS/GISAXS

To quantify the molecular dipole orientation and crystallinity of the prepared PFO films, grazing incidence small- and wide- angle X-ray scattering (GISAXS/GIWAXS) measurements were collected using the X9 Beamline at the National Synchrotron Light Source at Brookhaven National Labs, NY. X-ray scattering techniques are of interest because they can provide information about bulk features across multiple length scales [132,136,137] based on whether small- (SAXS) or wide- (WAXS) angle X-ray scattering is utilized. Additionally, through the use of grazing incidence methods (GISAXS/GIWAXS), near-surface features and buried interfaces can be studied as these techniques essentially become surface sensitive [136,138]. In turn, GIWAXS have become important research tools for the analysis of organic thin films and devices, particularly for conjugated polymers and polymer blends in which the supramolecular and internal structures can be analyzed.

SAXS is a small-angle scattering technique where the elastic scattering of X-rays (at wavelengths on the order of 0.1 to 0.2 nm) by a sample which exhibits periodicity, crystallinity or inhomogeneities on nanometer length scales, is collected at very low angles (typically between 0.1° - 10°). This angular range contains information about the shape and size of macromolecules, characteristic distances of partially ordered materials, pore sizes, and other data. SAXS is also capable of delivering structural information of macromolecules between 5 and 25 nm, of repeat distances in partially ordered systems of up to 150 nm [139]

WAXS is an X-ray-diffraction technique that is used to determine the crystalline structure of polymers and other materials [139]. This technique specifically refers to the analysis of Bragg peaks scattered to wide angles, which (by Bragg's law) implies that they are caused by structures on sub-nanometer length scales. In principle, WAXS is the same technique as SAXS with the key difference being the distance between sample the detector is shorter and thus diffraction maxima at larger angles are observed. The diffraction pattern generated allows the determination of

chemical composition or phase composition of the film, the texture of the film (preferred alignment of crystallites), the crystallite size and presence of film stress [136]. According to this method the sample is scanned in a wide-angle X-ray goniometer, and the scattering intensity is plotted as a function of the 2θ angle. When X-rays are incident on the sample, they scatter in predictable patterns based upon the internal structure of the solid. A crystalline solid consists of regularly spaced atoms (electrons) that can be described by imaginary planes. The distance between these planes is called the d-spacing. The intensity of the d-space pattern is directly proportional to the number of electrons (atoms) that are found in the imaginary planes. Every crystalline solid will have a unique d-spacing pattern (known as the powder diffraction pattern), which is a “finger print” for that solid. Solids with the same chemical composition but different phases can be identified by their d-spacing pattern.

The SAXS and WAXS techniques described in the previous paragraphs have all been for normal incidence, where the X-rays transmit through the sample completely. A different method of obtaining X-ray scattering measurements was employed for the analysis of the polymer films that were prepared using grazing incidence, in which the incident angle (θ_0) is kept at no larger than a few degrees (Fig. 3.18) [136]. There are two major differences between X-ray scattering under grazing incidence and X-ray scattering under normal incidence. First, penetration depth into the sample is limited since the x-rays now have to travel through more of the sample when at an angle, and the penetration depth decreases rapidly with decreasing incident angle. Additionally, penetration into underlying layers such as substrates can be limited based on total reflection. As θ_0 is decreased towards zero, θ_1 the angle at which the beam travels through the sample will no longer have any real components (based on Snell's law); thus, a critical angle θ_c can be defined where, if the incident angle is less than this value, there will be no (or minimal) penetration into the substrate:

$$\theta_c = \sqrt{2}\delta_1 \quad (2)$$

where δ_1 is the real component of the refractive index [136]. An additional effect observed in grazing incidence mode is that the intensities of reflected and scattered radiation at the surface and interface becomes measureable, allowing one to probe buried interfaces as well as near-surface structures. Grazing incidence X-ray scattering is particularly useful for thin film analysis, its surface sensitivity, and its ability to study features at buried interfaces within the sample [136,138].

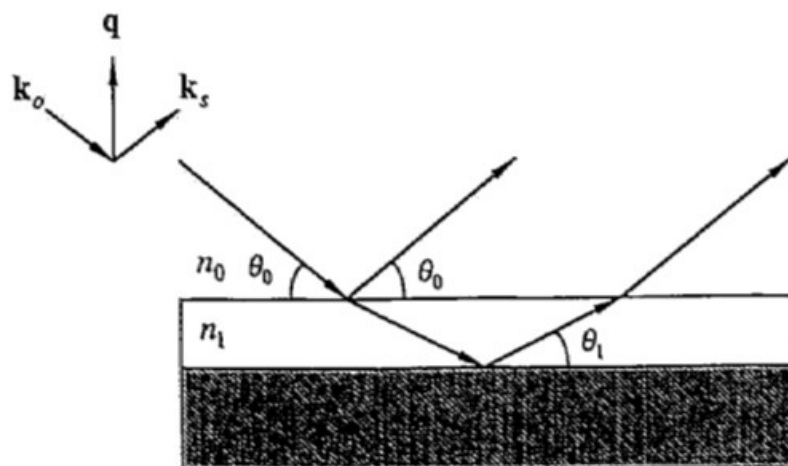


Figure 3.18. In a grazing incidence experiment the beam travelling in vacuum with refractive index n_0 is incident upon the sample of refractive index n_1 at angle θ_0 may be in general both partially transmitted through the interface and partially reflected. The transmitted beam is propagated at a grazing angle θ_t with respect to the surface and may be reflected from other interfaces in the sample, such as the film/substrate interface illustrated here. In this case, the radiation reflected from the two interfaces interferes, yielding a distinctive pattern characteristic of the film thickness [136]. k_o is the wavevector, k_s is the direction of the scattered beam, and q is the change in momentum as a result of the scattering process ($q = k_s - k_o$).

Examining the instrumentation required for GISAXS/GIWAXS measurements, there are two basic elements of X-ray scattering techniques are the X-ray source and the detection unit, which is usually either a camera or a spectrometer [136]. Figure 3.19 depicts these basic

elements, as well as other typical components of an X-ray scattering apparatus. The source can range from a typical lab X-ray tube source to a synchrotron source. The tube source commonly takes the form of either a sealed tube source or a rotating target. While the rotating target typically supplies an order of magnitude increase in intensity compared to the sealed tube, it generally is more expensive and difficult to maintain [136]. Synchrotron sources offer the advantage of high flux very high brilliance, intensity, and collimation, as well as the ability to select different X-ray energies. This makes acquisition times very short (on the order of seconds) and allows for the possibility of conducting time-resolved experiments. Additionally, the beam can be focused for imaging experiments.

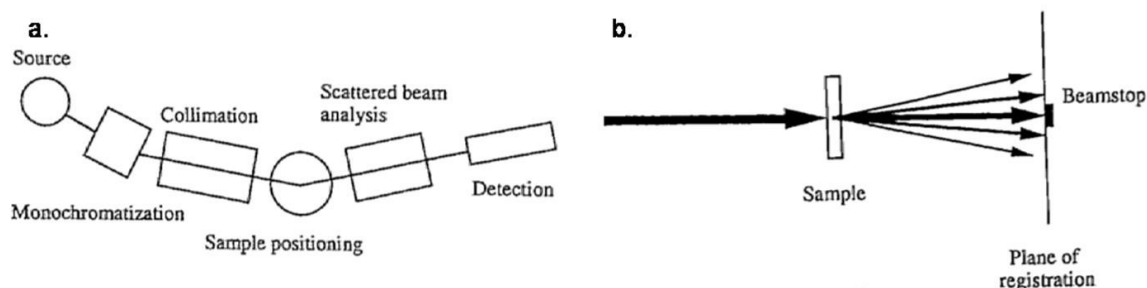


Figure 3.19. (a) In a generic scattering apparatus X-rays generated by the source are collimated and often monochromated before striking the sample. The scattered beam may then be analyzed for direction or energy or both before being detected [136]. b) In classical small angle X-ray scattering the incident beam is perpendicular to the sample surface and the entire sample thickness is probed.

Slit and point collimation have been used for focusing the beam; slit collimation typically offers more intensity, especially with the sealed tube sources [136]. Kratky-type slit collimation offers good resolution and low parasitic scattering near the primary beam, but the smearing of scattered pattern must be accounted for in the data analysis [136]. The detectors collect scattered X-rays from angles ranging from a few milliradians to a few degrees. Originally, photosensitive films were used as detectors, but these have largely been replaced by counting techniques, particularly position-sensitive counters [136]. The unscattered and forward-scattered beams are typically blocked by a beamstop, which strongly absorbs X-rays.

For Kratky camera measurements, the minimum sample area required is $1 \times 25 \text{ mm}^2$ (typically widths of 3 - 4 mm are easier to deal with) [136]. As samples become thicker, multiple scattering events become more likely, which increases the complexity of the analysis; thus, typical sample size should be limited to $\sim 1/\mu(l)$, which for a typical polymer, is around 0.1 - 2.5 mm [136].

3.4.6 Characterization of PFO Molecular Dipole Orientation as a Function of Processing Conditions

Neat 100 nm PFO films on bare VWR glass substrates, VWR glass substrates coated with 100 nm Ag, and 1 mm thick microscope slide glass were heat treated in an inert nitrogen atmosphere at temperatures within the liquid crystalline phase region to promote oriented molecular dipoles and crystallization, and in the nematic liquid phase region to produce amorphous or ‘glassy’ samples with randomly oriented molecular dipoles (see Table 3.2 for heat treatment and cooling parameters and Methods Section 3.3.13). Samples were also prepared by vapor phase annealing in toluene vapor to promote molecular dipole orientation and β -phase chain orientation (see Methods Section 3.3.13)

Table. 3.2 Heat treatment temperature, time, and cooling methods for 100 nm neat PFO films on bare VWR glass substrates, VWR glass substrates coated with 100 nm Ag metal, and bare 1 mm thick microscope slide glass.

Temperature ($^{\circ}\text{C}$)	Time (minutes)	Cooling Method
120	30	Quenched on metal plate
180	30	Quenched on metal plate
200	60	Quenched on glass plate
280	30	Quenched on metal plate

Because the temperature at which the samples are treated at was critical to the resultant crystallinity and molecular dipole orientation, careful calibration of the hot plate temperature at

the position where the samples were placed was conducted using a thermal probe (see Methods Section 3.3.13). Additionally, the cooling rate implemented upon completion of the heat treatment also plays an important role in the resultant crystallinity and molecular dipole orientation. This is why both rapid quenching on a metal plate and slow cooling on a glass plate were used. Additionally, the substrate on which the polymer is spin coated may influence the cooling rate depending on how rapidly it dissipates heat. This was the motivation for selecting two glass substrates with different thickness: the thin VWR substrate of 0.18 mm and the thick microscope slide glass of 1 mm.

To characterize the molecular dipole orientation and crystallinity of these samples as a function of heat treatment time, temperature and rate of cooling, absorption spectra and grazing incidence small and wide-angle X-ray scattering measurements were collected (see Methods Sections 3.3.14 and 3.3.15, respectively) Absorption spectra of the samples are shown in Figures 3.20 and 3.21. Figure 3.20 shows the absorption spectra of the 5 different processing conditions, as well as the as spin cast or ‘neat’ PFO film on thin VWR glass. The as spin cast or ‘neat’ PFO films exhibits the greatest absorption maximum at 383 nm and a sharp absorption cutoff at approximately 430 nm, suggesting that it is largely amorphous. Similarly, the PFO film prepared by heating at 280° C followed by rapid quenching on a metal plate to form amorphous or ‘glassy’ resulted in an absorption spectrum very similar to the neat PFO film, exhibiting a maximum in absorbance at 381 nm and a absorption cutoff at 449 nm. These are in good agreement with examples in the literature [131,141]. In contrast, the samples that were heated in the temperature range of the liquid crystalline or ‘nematic crystalline’ phase (120°, 180°, and 200° C) exhibited much broader absorption peaks, with lower absorbance at wavelengths ranging from 382 - 387 nm. Additionally, the absorption tail of these samples did not exhibit a sharp cutoff as did the neat and glassy PFO and continued to absorb at wavelengths >500 nm. These features are characteristic of crystalline film and are in good agreement with the literature [131 ,141].

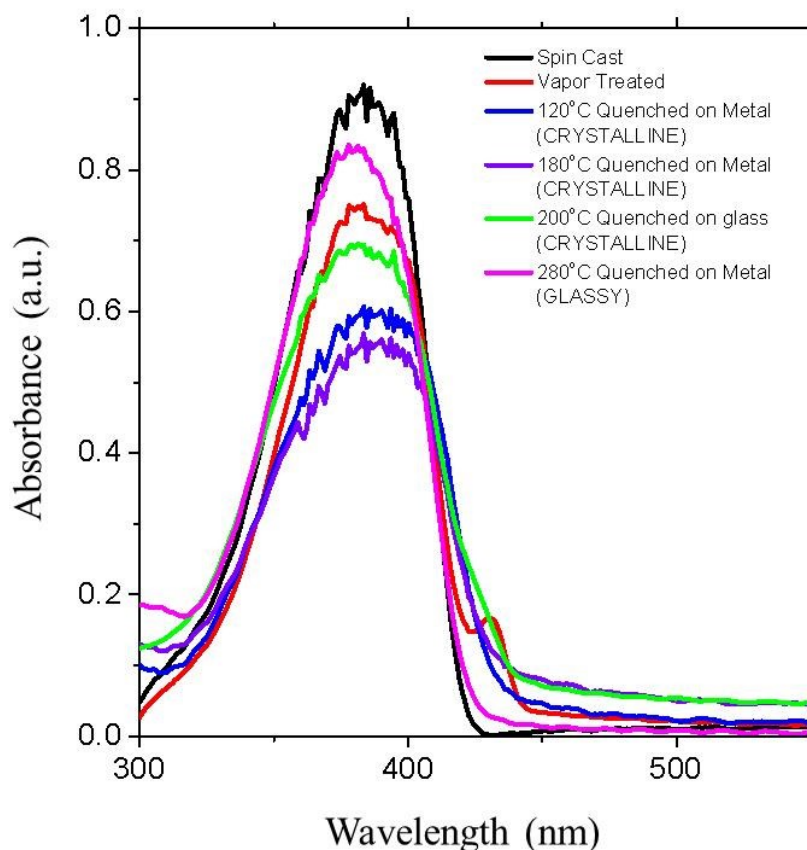


Figure 3.20 Absorption spectra of 100 nm PFO films on VWR glass in as spin cast (neat) form, vapor annealed, heated to 120°, 180°, 200°, and 280° C. Heat treated samples were quenched on glass or metal plates. Color available in electronic copy.

To understand the effect of substrate cooling rate on the resultant crystallinity of the polymer film additional spectra were collected on 100 nm PFO films on thick 1 mm microscope glass that were heat treated at 200° for 1 hour followed by cooling on a glass plate to form the nematic crystalline phase and 280° C for 30 minutes and quenched on metal plate to form the nematic glassy phase (see Fig 3.21). The nematic crystalline sample prepared with the thicker microscope slide glass substrate exhibits a slightly greater absorption maximum broader curve than that produced on the thin VWR glass, suggesting it was slightly more crystalline (see Fig 3.21(a)) [131 ,141]. In contrast, the nematic glassy sample produced on the thicker microscope substrate glass exhibits a similar curve shape and absorbance maximum to the thin VWR glass,

however it exhibits a more pronounced absorption cutoff rather than the broad ‘tail’ exhibited by the film produced on the thin VWR glass (see Fig 3.21(b)). This suggests that the nematic glassy sample formed on the thick microscope slide glass was slightly less amorphous than that produced on the thin VWR glass [131,141]. These differences in the resultant spectra as a function of substrate thickness are as expected, based on the cooling rates that are ideal to form each phase. To produce a fully amorphous sample, a more rapid quench is desirable and a thicker substrate would slow the cooling rate, thereby allowing small crystallites to form. Conversely, a slow cooling rate is desirable for the formation of the nematic crystalline state, so the thicker substrate’s slower cooling rate is advantaged and is perhaps why a slightly broader absorption at all wavelengths is observed. While it is evident that the thicker substrate slightly improves the crystallinity in the PFO film heated at 200° C for 30 minutes, followed by cooling on a glass plate, it was not a significant enough difference to warrant utilizing a different substrate glass. Thus, it was decided that all samples will be prepared using the thin VWR glass substrates.

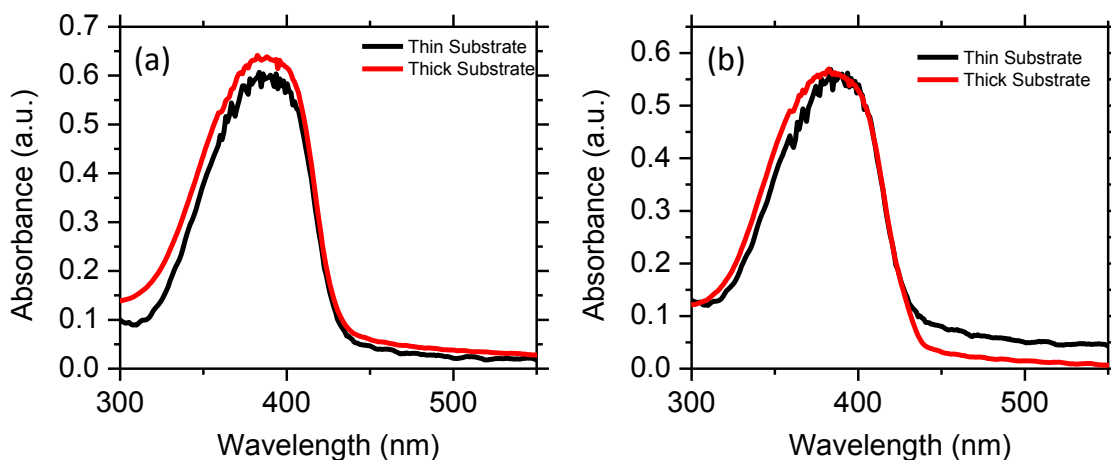


Figure 3.21. Absorption spectra of 100 nm PFO films on thin VWR glass and thick microscope slide glass substrates heated at 200° C for 1 hour and cooled on a glass plate (a), and heated for 280° C for 30 minutes and quenched on a metal plate. Color available in electronic copy.

To further analyze the crystallinity and molecular dipole orientation of the 100 nm PFO films prepared with different processing conditions, a comprehensive set of GISAXS and GIWAXS measurements were taken (see Method Section 3.3.15). Upon review of the collected data, the feature sizes exhibited in these samples was too small to be detected with the GISAXS technique, so only GIWAXS data has been included and analyzed (see Appendix E for all raw GIWAXS profiles). Additionally, while PFO films were prepared on both bare VWR glass and VWR glass substrates coated with 100 nm Ag, only the samples atop Ag were analyzed due to the fact that these most closely resemble the SMI waveguide configuration and that only minor morphological differences were observed from the PFO films atop bare glass and atop Ag.

The first set of GIWAXS measurements were collected on bare VWR glass and VWR glass coated with 100 nm Ag so that their contribution to the GIWAXS profiles of the processed PFO films could be known. The bare glass was completely amorphous and showed a broad reflection at q values ranging from 1.5 to 2.2 (see Appendix E Figs. AE1 and AE2, respectively in). Profiles of VWR glass coated with 100 nm Ag showed two reflections occurring at q values ranging from 2.7 to 3.0 that were present in all other spectra collected on PFO films atop Ag (see Appendix E Fig. AE2). These reflections are characteristic of polycrystalline silver metal.

To determine the degree of crystallinity and molecular dipole orientation of the processed PFO films on 100 nm Ag on VWR glass substrates, line scans in the q_r and q_z directions were extracted from the raw GIWAXS profiles (in Appendix E) collected at incident angles of 0.05° (see Fig. 3.22(a), Fig 3.23(a), Fig. 3.24(a), and Fig. 3.25(a)) and 0.07° (see Fig. 3.22 (b), Fig 3.23(b), Fig. 3.24(b), and Fig. 3.25(b)). The reflections or 'peaks' present in these line scans are characteristic of particular morphological features such as crystallinity, chain orientation and, polymer stacking. These reflections were interpreted by comparing them to known literature values [131,132]. The direction or plane in which these morphological features lie with respect to the sample substrate, are determined by identifying characteristic reflections in the q_r and q_z line.

Reflections observed in the q_r line scan indicate that the given feature(s) lies within the plane of the substrate. In contrast, reflections observed in the q_z line scan indicate that given feature(s) lies out of the plane of the substrate.

Line scans taken from GIWAXS profiles of neat PFO film atop 100 nm Ag on VWR glass collected at incident angles of 0.07° (Fig. 3.22 (a,b)) and 0.09° (Fig. 3.22 (c,d)) both exhibited the characteristic (008) reflection at q of 1.51 \AA^{-1} in the q_r (Fig. 3.22 (a,c)) and q_z (Fig. 3.22 (c,d)) directions. The presence of the 008 reflection indicates that main chains of PFO (c-axis) are oriented WRT to each other and that the sample exhibits only intramolecular order. When comparing the relative intensity of the 008 reflection in the q_r and q_z line scans, it is evident that the q_r line scan exhibits a stronger reflection than the q_z line scan. This suggests that the majority of the intramolecular order is in the plane of the film (i.e., parallel to the substrate).

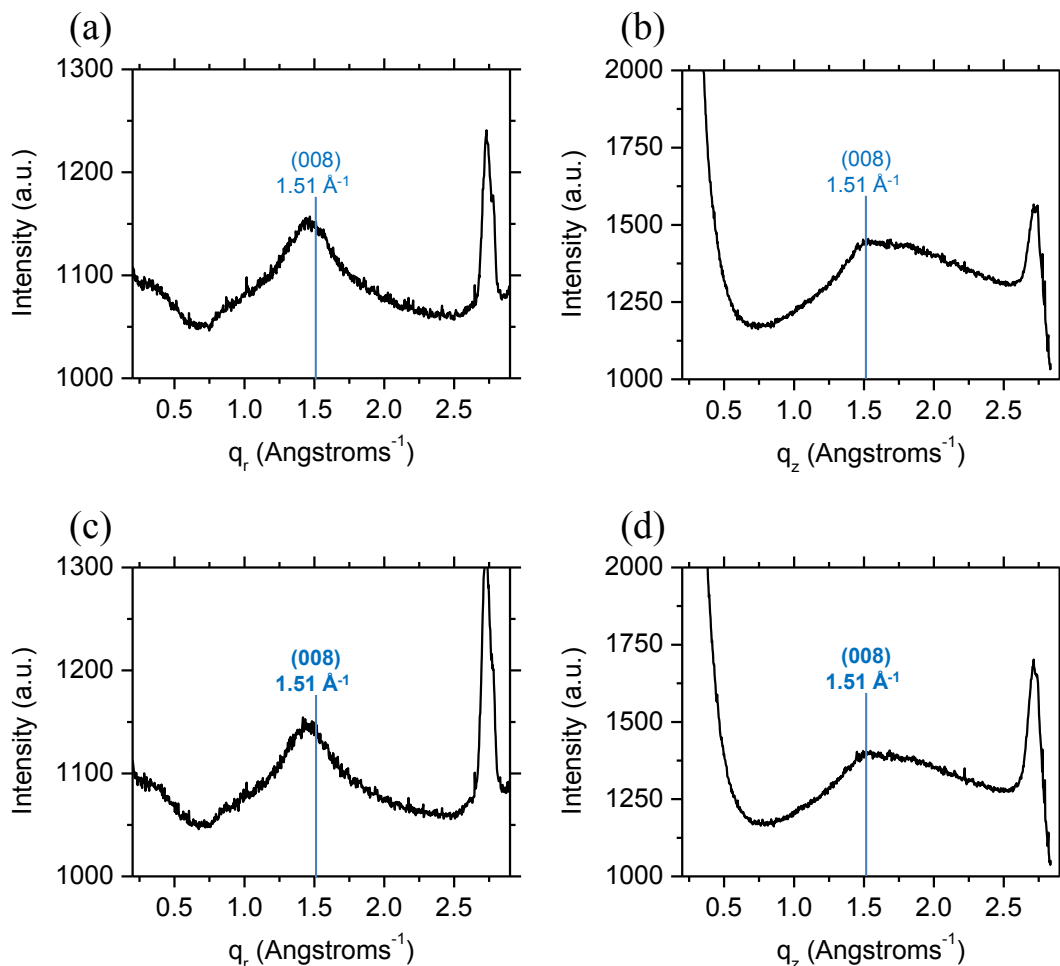


Figure 3.22. Line scans of GIWAXS profiles of neat PFO film atop 100 nm Ag on VWR glass at incident angles of 0.07° (a,b) and 0.09° (c,d) in the q_r (a,c) and q_z (c,d) directions.

Shown in Figure 3.23 are line scans taken from GIWAXS profiles of 100 nm PFO atop 100 nm Ag on VWR glass heated to 120°C and quenched on a metal plate at incident angles of 0.07° (Fig. 3.23 (a,b)) and 0.09° (Fig. 3.23 (c,d)) in the q_r (Fig. 3.23 (a,c)) and q_z (Fig. 3.23 (c,d)) directions. Evidence of both intramolecular (i.e., polymer chain alignment) and intermolecular (polymer crystallites) ordering is evident from both q_r and q_z line scans and both incident angles (of 0.07° and 0.09°). At an incident angle of 0.07° , the q_r line scan exhibits the (060) and (0010) reflections at $q = 1.59$ and 1.91 Å^{-1} , respectively (see Fig. 3.23 (a)), and the q_z line scan exhibits the (020) and (0010) reflections at $q = 0.50$ and 1.91 Å^{-1} , respectively (see Fig. 3.23 (b)). The (060) and (0010) reflection indicate the presence of intramolecular ordering and the (020)

reflection indicates the presence of nanometer length scale crystallites embedded within the amorphous polymer matrix. At the greater incident angle of 0.09° , the q_r line scan exhibits the (002) and (008) reflections at $q = 0.38$ and 1.51 \AA^{-1} , respectively (see Fig. 3.23 (c)), and the q_z line scan exhibits the (020), (006), (060), and the (0010) reflections at $q = 0.50, 1.51, 1.59$, and 1.91 \AA^{-1} , respectively (see Fig. 3.23(b)). The (008), (060), and (0010) indicate intermolecular ordering and the (002) and (020) indicate the presence of small nanometer scale crystallites. Based on these data, it is evident that there is both in-plane and out-of-plane intramolecular polymer chain alignment and intermolecular ordering of the nanometer scale crystallites. However, when comparing the relative intensities of the reflections present in the q_r and q_z line scans, the reflections in the q_r (specifically at $\theta = 0.09^\circ$) for both inter and intramolecular ordering, are more pronounced than that in the q_z line scan. Therefore, it is concluded that there is more in-plane polymer chain alignment and crystallite ordering than out-of-plane alignment.

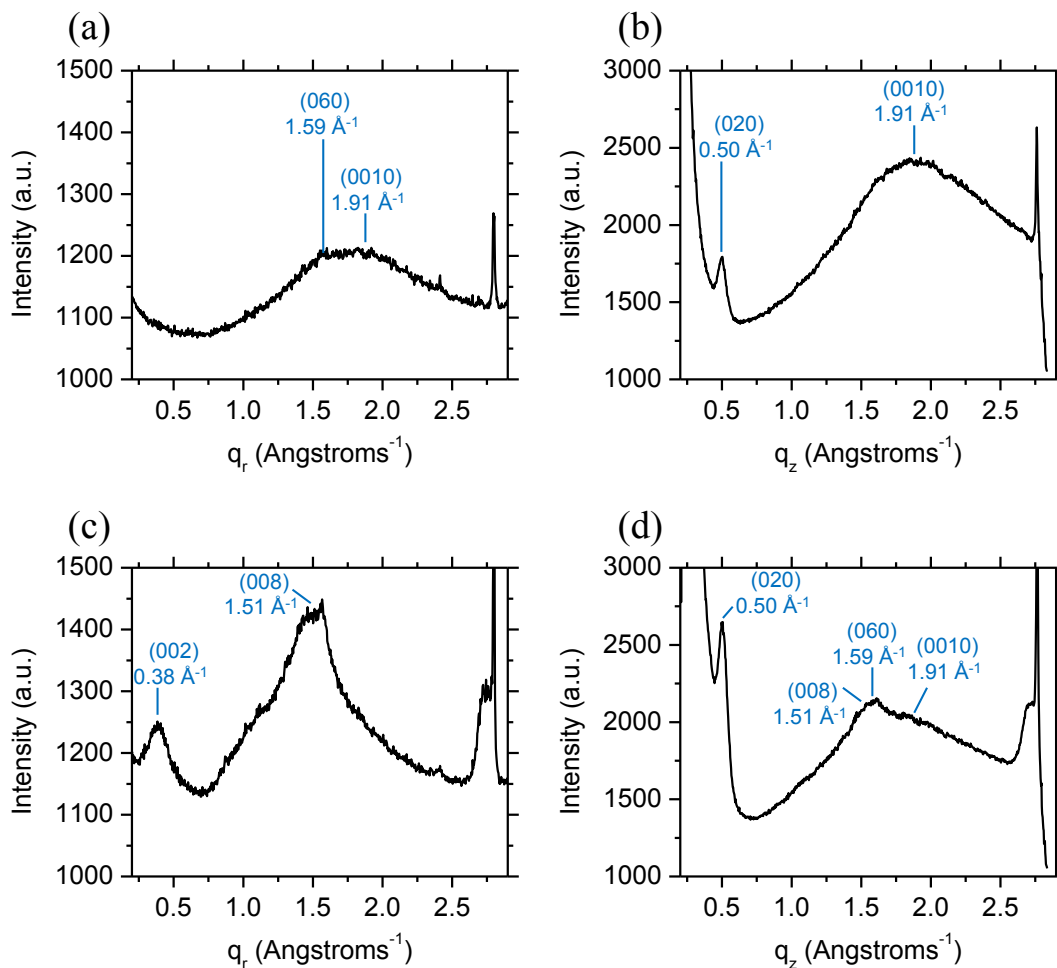


Figure 3.23. Line scans of GIWAXS profiles of PFO film atop 100 nm Ag on VWR glass heat treated at 120° C and quenched on a metal plate at incident angles of 0.07° (a,b) and 0.09° (c,d) in the q_r (a,c) and q_z (c,d) directions.

Similarly to the PFO sample heat treated to 120° C, the 100 nm PFO film on 100 nm Ag on VWR glass heat treated to 180° C and quenched on a metal plate exhibited evidence of both inter and intramolecular ordering at incident angles of 0.07° (Fig. 3.24(a,b)) and 0.09° (Fig. 3.24(c,d)) and in both the q_r (Fig. 3.24 (a,c)) and q_z (Fig. 3.24 (c,d)) line scans. At both incident angles, the q_r line scans exhibit the (002) and (008) reflections at $q = 0.38$ and 1.51 \AA^{-1} , respectively (see Fig. 3.24(a,c)), and the q_z line scans exhibit the (020) and (008) reflections at $q = 0.50$ and 1.51 \AA^{-1} , respectively (see Fig. 3.24(b,d)). The (008) reflection indicates intramolecular

polymer chain alignment and the (002) reflection indicates the presence of small crystallites.

While there is both in-plane and out-of-plane intra and intermolecular ordering, like the sample heat treated at 120° C, the 180° C sample also exhibits more intense and defined reflections in the q_r line than the q_z line scan, indicating that there is more in-plane polymer chain alignment and crystallite ordering than out-of-plane ordering.

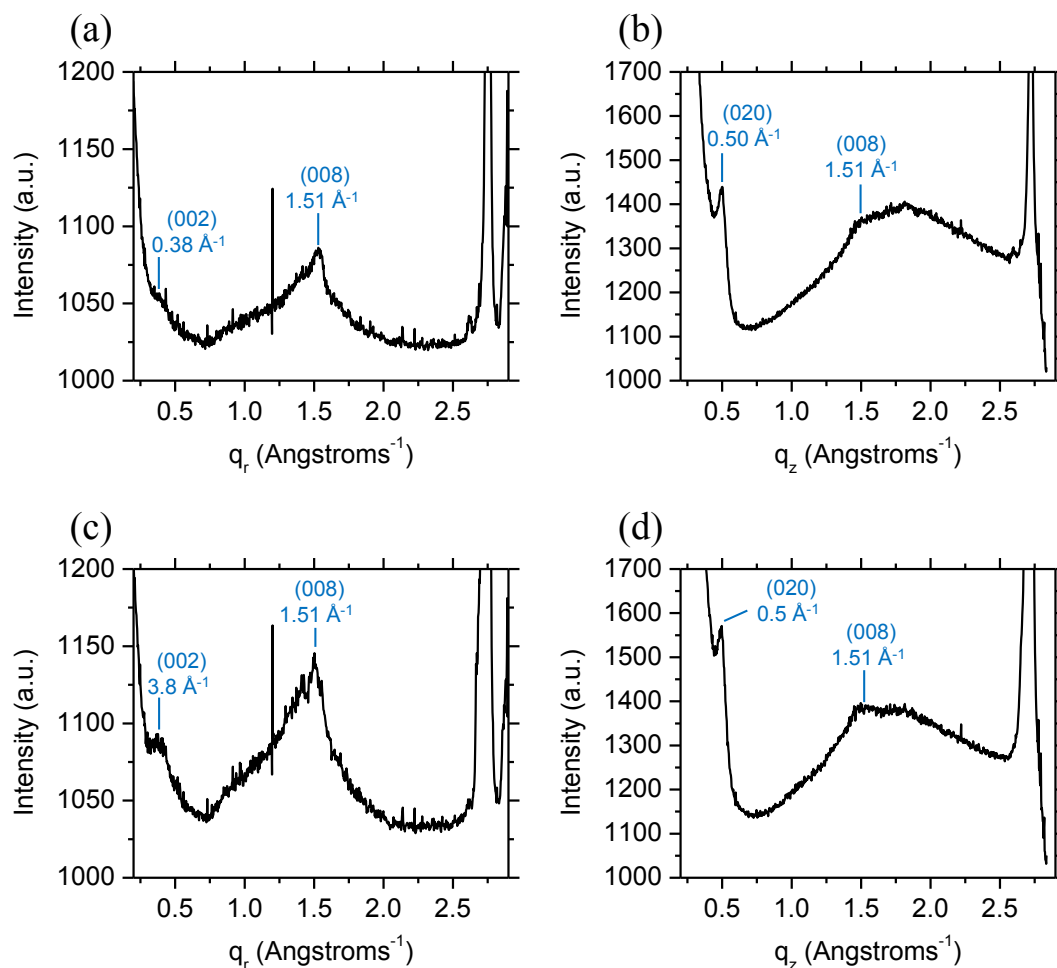


Figure 3.24. Line scans of GIWAXS profiles of PFO film atop 100 nm Ag on VWR glass heat treated at 180° C and quenched on a metal plate at incident angles of 0.07° (a,b) and 0.09° (c,d) in the q_r (a,c) and q_z (b,d) directions.

The third heat treatment within the temperature range liquid crystalline or ‘nematic crystalline’ phase region was carried out by annealing a 100 nm PFO film atop 100 nm Ag on a

VWR glass substrate at 200° C for 1 hour and cooled on a glass plate. The GIWAXS data indicated the presence of both intra and intermolecular ordering in this sample, similar to what was observed in samples heated at 120° and 180° C. The q_r line scans at both 0.07° and 0.09° showed only the (008) reflection at $q = 1.51 \text{ \AA}^{-1}$, respectively, indicating the presence of intramolecular (polymer chain) orientation (see Fig. 3.25(a,b)). The q_z line scans show both the (020) and (008) reflections at $q = 0.50$ and 1.51 \AA^{-1} , respectively, indicating the presence of both nanoscale crystallites and intermolecular ordering (see Fig. 3.25(c,d)). However, it is not evident that there is a preferred direction of alignment.

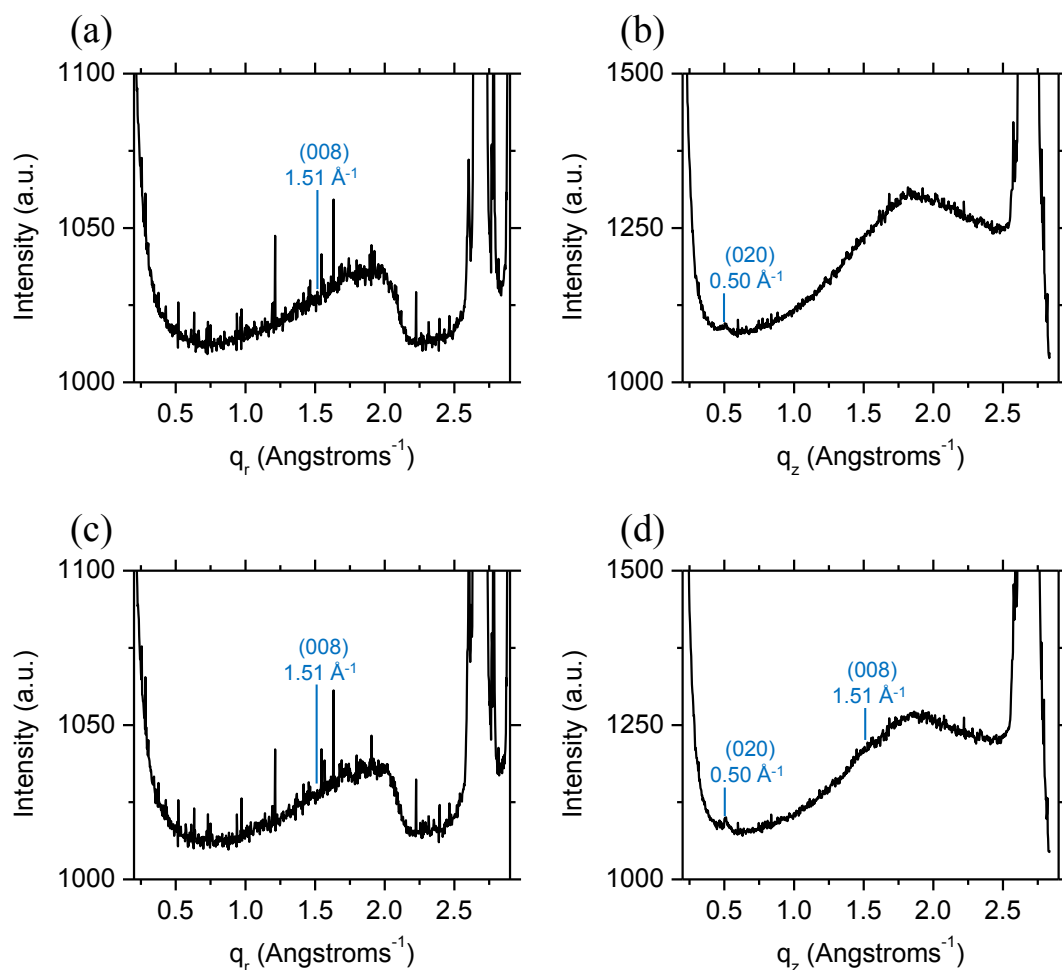


Figure 3.25. Line scans of GIWAXS profiles of PFO film atop 100 nm Ag on VWR glass heat treated at 200° C and quenched on a glass plate at incident angles of 0.07° (a,b) and 0.09° (c,d) in the q_r (a,c) and q_z (c,d) directions.

The final treatment method that was analyzed was prepared by heating a 100 nm PFO film on 100 nm Ag atop VWR glass to 280° C within the nematic glassy phase for 30 minutes followed by quenching on a metal plate. This sample showed no characteristic reflections at any incident angle in either the q_r or q_z directions (see Appendix E Fig. AE12). Therefore, the sample is fully amorphous with roughly equal in-plane and out-of plane molecular dipole orientation.

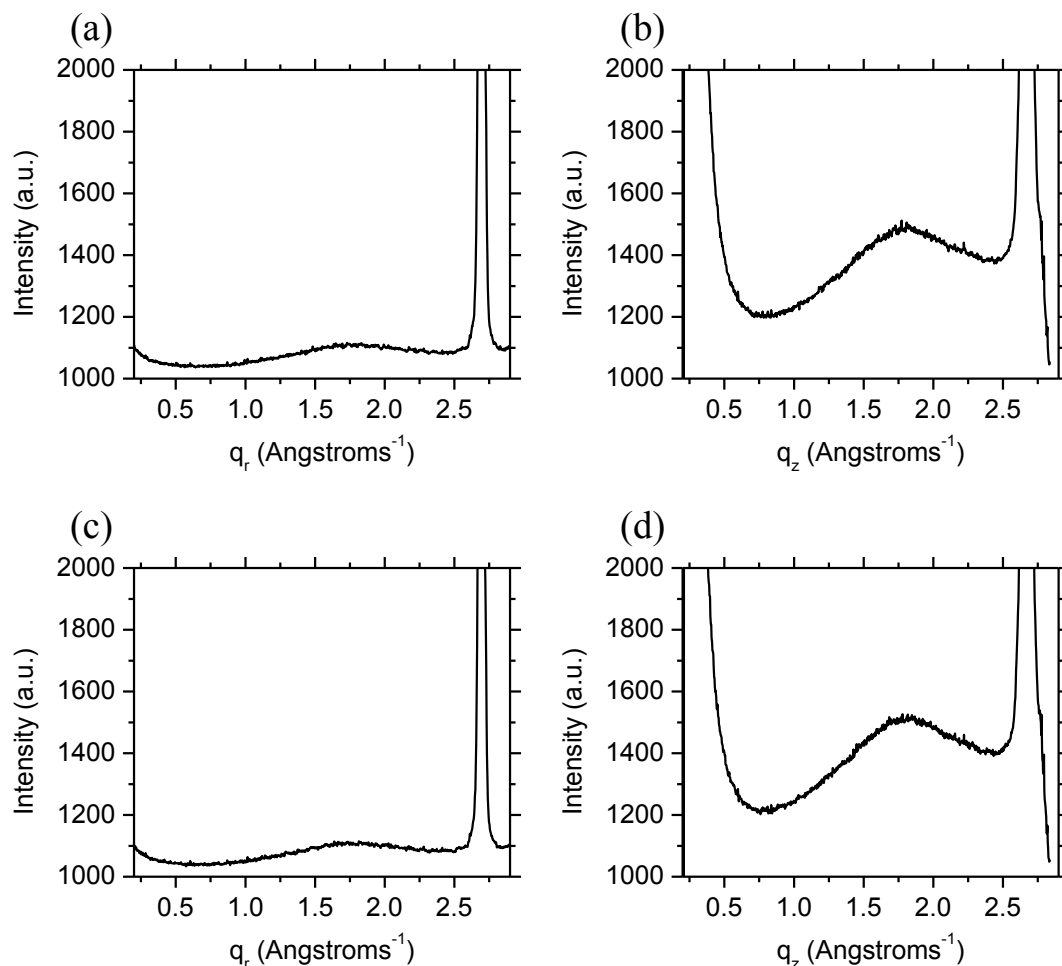


Figure 3.26. Line scans of GIWAXS profiles of PFO film atop 100 nm Ag on VWR glass heat treated at 280° C and quenched on a metal plate at incident angles of 0.07° (a,b) and 0.09° (c,d) in the q_r (a,c)) and q_z (c,d) directions.

3.4.7 Discussion of Molecular Dipole Orientation in PFO Films

As previously described in this chapter as well as the introduction of the thesis, the molecular dipole orientation of the polymer emitter is expected to have a significant impact on the degree of SPP-emitter coupling. Therefore, it was of interest not only to understand the implications of plasmon-emitter coupling as a function of metal film thickness, but also of the PFO molecular dipole orientation with respect to the metal film. Based on GIWAXS characterization of the prepared PFO films, a range of morphologies and molecular ordering was achieved. In the samples that were prepared and characterized, no successful out-of-plane molecular dipole orientation was observed. The as spin cast or 'neat' PFO film exhibited in-plane intramolecular ordering and no crystallinity, the PFO films heated within the nematic crystalline region exhibited largely in-plane intramolecular ordering and the presence of nanometer scale crystallites, and the PFO heated within the nematic glassy region produced a completely amorphous sample with random molecular dipole orientation.

To study SPP-polymer emitter coupling as a function of molecular dipole orientation, amorphous films are desirable because the presence of even small nanometer scale crystallites will increase scattering in the waveguide. In the set of samples prepared and characterized, those prepared by heat treating within the temperature range of the nematic crystalline phase had small crystallites present, and were in turn not considered for further study because of the scattering losses that would be induced due to their crystallinity. Thus, the two samples that were successfully prepared that are suited to study SPP-emitter coupling as a function of molecular dipole orientation are the as spin cast or 'neat' PFO film and the fully amorphous PFO film. As noted, these samples are fully amorphous and the neat PFO has a preferred in-plane orientation, whereas the glassy sample has random orientation. This indicates that the glassy PFO has a greater fraction of out-of-plane molecular dipoles than the neat PFO sample, and in-turn provides a suitable method of studying SPP-emitter coupling as a function of dipole orientation.

While it was beyond the scope of this thesis to fabricate and measure the emissive properties of semiconductor-metal-insulator waveguides with both neat and amorphous ‘glassy’ PFO films, a comprehensive set of measurements was carried out on waveguides with neat PFO and methods to prepare films with randomly oriented molecular dipoles as well semi-crystalline PFO films were developed.

3.5 Conclusions

Theoretical dispersion relations of semiconductor-metal-insulator waveguides presented in Chapter 2 of this thesis showed that by optimizing the Ag metal film thickness in the waveguide, the SPP mode propagation length (L) could be increased (i.e., reducing loss) and the SPP field leakage could simultaneously be increased away from the lossy metal into the semiconductor emitter layer [130]. This in turn was predicted to reduce parasitic loss to tightly bound loss SPP modes at the metal/semiconductor interface. The implications of reducing SPP loss are significant to the design of visible-light-based organic optoelectronic devices driven by metal electrodes.

In this chapter a set of insulator-semiconductor-metal-insulator (ISMI) waveguides were fabricated with neat PFO semiconductor films over a range of Ag metal film thicknesses, and gain spectra of these waveguides were collected at a range of pump power densities. By measuring the emission intensity at the peak wavelength, the ASE threshold, and ASE slope efficiency as a function of metal film thickness, compelling experimental evidence provided validation of the theoretical calculations in Chapter 2 which showed that the most efficient SPP-emitter coupling occurred at a metal film thickness of 45 - 50 nm where the dominant SPP mode(s) exhibited the greatest propagation length (i.e., lowest loss) and greatest field leakage into the semiconductor emitter.

The great disparity in peak emission intensity and ASE threshold exhibited by these samples as a function of metal film thickness further corroborate the theoretical results of Chapter 2. In particular, the work demonstrated that if the metal film thickness of a given light-emitting organic optoelectronic device is not optimized, that parasitic losses to SPP modes may significantly hinder the emissive performance of the device by trapping light energy at the metal/semiconductor interface. The results presented herein showed that if the metal film thickness is optimized and tuned to a thickness of 45 - 50 nm (for this particular ISMI structure) where the dominant SPP mode(s) exhibited low losses and great field leakage, then in-plane parasitic SPP loss can be greatly minimized.

In conjunction with corroborating the theoretical results in Chapter 2 through optical characterization of neat PFO ISMI waveguides, amorphous and semi-crystalline PFO films were fabricated and characterized with GIWAXS measurements. These films with differing molecular ordering may be used in the future to further study polymer semiconductor-SPP coupling as a function of molecular dipole orientation, which is expected to play a critical role in the degree and efficiency of plasmon/polymer interactions.

4 Surface plasmon and photonic mode propagation in gold nanotubes with varying wall thickness

4.1 Abstract

Gold nanotube arrays are synthesized with a range of wall thicknesses (15 to >140 nm) and inner diameters of ~200nm using a hard-template method. A red spectral shift (>0.39 eV) with decreasing wall thickness is observed in dark-field spectra of nanotube arrays and single nanowire/nanotube heterostructures. Finite-difference-time-domain simulations of gold nanotubes with varying wall thickness and inner diameter show that the size regime that were synthesized support propagating surface plasmon modes as well as surface plasmon ring resonances at visible wavelengths (the latter is observed only for excitation directions normal to the nanotube long axis with transverse polarization). The energy of the surface plasmon modes decreases with decreasing wall thickness and is attributed to an increase in mode coupling between propagating modes in the nanotube core and outer surface and the circumference dependence of ring resonances. Surface plasmon mode propagation lengths for thicker-walled tubes increase by a factor of ~2 at longer wavelengths (>700 nm), where ohmic losses in the metal are low, but thinner-walled tubes (30 nm) exhibit a more significant increase in surface plasmon propagation length (by a factor of more than four) at longer wavelengths. Additionally, nanotubes in this size regime support a photonic mode in their core, which does not change in energy with changing wall thickness. However, photonic mode propagation length is found to decrease for optically thin walls less than 60 nm. Finally, correlations are made between the experimentally observed changes in dark-field spectra and the changes in surface plasmon mode properties observed in simulations for the various gold nanotube wall thicknesses, inner diameters, and excitation conditions.

4.2 Introduction

Nanotubes, like nanowires, exhibit desirable properties for a host of applications, including chemical sensing, subwavelength light-emitting diodes, and waveguides due to their anisotropic cylindrical shape — exhibiting nanoscopic diameters but macroscopic lengths [142]. The advantage of metallic nanotubes compared with nanowires, in terms of sensing capability, is their greater surface-area-to-volume ratio and evanescent surface plasmon mode propagation at the metal analyte interface on both the inner and outer tube surfaces [143]. Sensing enhancement as a function of increased surface area-to-volume ratio has been observed previously when comparing solid gold nanospheres to gold nanoshells, with the latter showing a greater wavelength shift per unit change in surrounding refractive index [144,145]. The motivation behind the study of tubular metallic nanostructures in this thesis is to explore and understand surface plasmon tunability, propagation, and confinement in these structures as a function of wall thickness, inner diameter, excitation condition, and incident polarization. This fundamental understanding of surface plasmon tunability in these structures will aid in effectively introducing a gain medium either in the core or as a cladding to study these structures as candidates for subwavelength coherent resonator cavities for nanoscale emitters and as large area array patterned electrodes for visible-light-based optoelectronic devices [146].

The resonant properties of noble metal nanotubes, like nanoshells, can be tuned through control of inner diameter and wall thickness. In the case of gold nanotubes (AuNTs), a pronounced red shift has been observed with decreasing wall thickness (WT) and increasing inner diameter (ID) (for WT ranging from 4–30 nm and ID ranging from 12–30 nm) [113,115,116]. It is noteworthy that, while for tubular and core-shell structures an apparent red spectral shift is observed as a function of decreasing shell thickness, the opposite trend is observed in solid nanoparticle systems (spheres and rods), where a red shift and spectral broadening occur as a

function of increasing size [147]. Therefore, core-shell and tubular systems can be considered unique in their plasmonic response relative to solid geometries.

Prior work on fabrication and optical modeling of AuNT and core-shell structures has been focused on geometries with IDs and WTs much smaller than the wavelength of light (<30 nm) and WT ~ 42 nm [113,115,116]. In that size regime, intrawall electric-field coupling (i.e. coupling between the inner and outer surface of the wall) is strong, and surface plasmon hybridization models can be applied (quasistatic regime) [148,152]. For larger ID structures (ID > 100 nm) where WT is still <50 nm but intrawall coupling is weak, the effects of changing wall thickness are likely to dominate. In that size regime, the structure becomes more comparable to insulator-metal-insulator (IMI) slab waveguides, supporting both propagating surface plasmon polariton (SPP) and photonic modes [116].

In this work, arrays of large 200-nm ID, 2 to 3- μ m-long AuNTs were synthesized in collaboration with Micha Fireman. A large inner diameter was selected such that the nanotube maybe more easily in-filled with a polymer emitter, and also support a photonic mode in the core of the structure. To study the optical properties and SPP mode propagation as a function of wall thickness and excitation direction true color brightfield and darkfield images and scattered-light spectra of both vertical arrays of AuNTs and a single nanowire/nanotube (NW/NT) heterostructure were obtained. Optical measurements of single structures allow for more accurate assessment of the spectral characteristics without inhomogeneous broadening resulting from variance in geometry (e.g. length, diameter, wall thickness) of the synthesized AuNTs.

Simulations carried out by finite-difference-time-domain (FDTD) were conducted to identify and understand the modes supported by AuNTs with different wall thicknesses (varying from 30 to 140 nm) and inner diameters (varying from 15 to 200 nm). These simulations demonstrate that large 200-nm ID AuNTs support three different mode types that depend on excitation direction and polarization: (1) when excitation is incident at the AuNT end, which we refer to as end-on excitation, propagating SPP modes are excited along the length of the nanotube

walls, analogous to that of planar metal films and IMI waveguides [116]. (2) In addition to the propagating SPP mode, a photonic mode is excited in the core of the nanotube. Similarly, for excitation normal to the nanotube long axis (which we refer to as normal excitation) and polarized parallel to the nanotube long axis, both a propagating SPP mode and a photonic mode are also supported. Theoretical propagation length studies for both the SPP and photonic modes were carried out. (3) For excitation normal to the nanotube and polarized transverse to the long axis, surface plasmon ring resonances occur at visible wavelengths. The ring resonances occur radially about the tube surface to form standing waves with electric field patterns that depend on the AuNT's circumference. We relate the modes observed theoretically to those detected experimentally to explain the electromagnetic response of the nanotubes as a function of decreasing wall thickness.

These results demonstrate that nanotubes that support surface plasmons have potential for use as both plasmonic waveguides and nanoscale optical resonators. Additionally, the relatively large inner diameter of the Aunts studied here could facilitate filling of the core with a suitable dye or semiconductor material to introduce gain to the waveguide or cavity. Such waveguides and cavities may be a viable replacement for more conventional surface plasmon waveguide/cavity devices since the SPP field can be excited directly by tapered fiber facets [153-160].

4.3 Methods

4.3.1 Electrodeposition Conditions

To fabricate AuNTs, firstly, a 400-nm-thick nickel film was thermally evaporated onto one side of a nanoporous anodic alumina (AAO) template (200-nm nominal pore diameter, 60- μm -thick, 13-mm total diameter; Anodisc 13, Whatman Inc.) to serve as the working electrode contact to the template pores. The AAO template was then placed in a homemade polyethylene electrodeposition cell. A copper plate and copper tape were used to make electrical contact to the

nickel-coated side of the AAO template when placed in the cell. Epoxy was employed at the edges of the AAO template to ensure that only the exposed pores of the template were in direct contact with the electrolyte and to prevent any leakage of the electrolyte from the electrodeposition cell. The electrodeposition cell was then placed in a beaker with a water level the same height as the electrolyte within the electrodeposition cell to facilitate ultrasonication. An alligator clip connected to a 10-cm length of steel wire immersed in the electrolyte served as the positive counter electrode; using an appropriate retort stand, the tip of the steel wire was submerged in the electrolyte. To electrodeposit sacrificial nickel nanowires, ~5 mL of a nickel plating solution (semi-bright finish; Alfa Aesar) was added to the electrodeposition cell and -1 mA constant current was applied to the working electrode for 2 hours. The entire process was carried out under ultrasonication to ensure that a regular distribution of nanowires was grown across the entire template (Model 2510 Ultrasonic Cleaner, Branson). Scanning electron microscopy (SEM) data revealed that the length of the nickel nanowires ranged from 5 to 10 μm , and diameters corresponded to those of the AAO pores (200-nm nominal pore diameter; ~240-nm average measured diameter). Following a pore-widening step using an 8.5% wt. solution of H_3PO_4 in deionized water (duration of 60, 30, or 15 min.), gold was electrodeposited onto the nickel nanowires using approximately 1 mL of gold plating solution (metal content 25 g/L; Alfa Aesar) and applying -1 mA constant current to the working electrode for 15 to 20 min to form gold coated nickel nanowires. Although electrodepositions were run at a constant applied current of 1mA (6430 subfemtoamp source meter, Keithley Instruments, Inc.), the exact resistance of the deposition area varied from deposition to deposition due to the geometry of the nanoporous alumina template and slight differences in coverage of the insulating epoxy. The most uniform electrodepositions occurred at voltages no greater than 4 volts, often in the range of 3 to 4 volts.

4.3.2 Sample Preparation

In order to prepare samples for SEM imaging and optical characterization, the filled AAO template sample was removed from the electrodeposition cell, mounted on a carbon pad (with nickel working electrode side facing upwards), and subsequently, the nickel working electrode, sacrificial nickel nanowire cores, and AAO were etched. To etch the nickel working electrode, along with the sacrificial nickel nanowire cores, the sample was submerged in a ferric chloride solution (Nickel Etchant, Type 1, Transene Company Inc.) for 1 hr to expose the gold nanotubes embedded in the AAO. To etch the AAO, the sample was submerged in a solution of 3MNaOH for 1 hr. The remaining gold nanotube array was then rinsed with deionized water and allowed to dry prior to characterization.

4.3.3 Scattered-Light Spectroscopy of Gold Nanotubes

A Zeiss Axio Observer Z1 was used to acquire bright-field and dark-field reflected light images and spectra of gold nanotube arrays. Here, 50 \times and 100 \times dark-field objectives were used to collect light from a $\sim 30 \times 60\text{-}\mu\text{m}$ region of a gold nanotube array. A 100-W halogen lamp was used as the light source for bright-field and dark-field microscopy. A darkfield microscope setup was employed to acquire scattered-light spectra of vertically oriented gold nanotube arrays. Under this configuration, unpolarized light from a halogen lamp was directed by an annular reflector and dark-field objective to obliquely illuminate the sample. Only scattered-light was collected by the central path of the reflector/objective and sent to an imaging spectrometer. For single nanowire/nanostructure scattered-light spectroscopy, the nanostructures were dispersed from arrays in methanol (by ultrasonication) and drop deposited onto glass cover slips. The imaging spectrometer was employed to acquire spectra from regions along the length of individual nanowire/nanotube heterostructures with a spatial resolution of $\sim 500\text{ nm}$. All scattered-light spectra were normalized relative to the lamp spectrum.

4.3.4 Electromagnetic Simulations

To identify the modes which can be supported by the nanotubes and understand the nature of their propagation as a function of wall thickness, FDTD simulations of single AuNTs were carried out, with WT of 30, 60, and 140 nm and fixed ID of 200 nm, under broadband (450–850 nm), planewave excitation with FDTD Solutions software (Lumerical Solutions, Inc.). The dispersive dielectric constants of gold used for simulations were taken from the *Handbook of Optical Constants of Solids*, edited by Palik (Academic Press, New York, 1985). A fine mesh size of 5 nm in the radial direction at the metal shell (at least five mesh cells thick) was employed, in order to accurately simulate the optical interaction. A chromium cylinder of 100 nm in length and equivalent inner and outer diameter to the corresponding simulated gold nanotube was placed at the opposite end of the gold nanotube to the plane wave source in order to mitigate back reflection of the propagating surface plasmon mode when extracting surface plasmon propagation length values. Excitation direction and incident polarization were varied by moving the planewave excitation source within the simulation. Theoretical mode spectra were extracted from the FDTD simulations by averaging 10 point spectra collected at equidistantly spaced intervals along both the core and surface of the nanotubes.

To understand the changes in peak surface plasmon mode resonance as a function of the nanotube inner diameter, a set of FDTD simulations were carried out, with single AuNTs with fixed length and wall thickness (WT) of 5 μm and 30 nm, respectively, with varied the inner diameter from 15 to 150 nm (in 15 nm increments), under end-on broadband (450–850 nm), planewave excitation with FDTD Solutions software (Lumerical Solutions, Inc.). The dispersive dielectric constants and simulation parameters were set up identically to the simulations with fixed 200 nm inner diameters, described in the previous paragraph.

4.4 Results and Discussion

Gold nanotube fabrication was carried out by a hard template method, which employed sacrificial nickel nanowires as scaffolds onto which gold was electrochemically deposited. The fabrication steps are illustrated in Fig. 4.1(a) (see Methods). The first step required thermally evaporating 400 nm of nickel onto the back side of a nanoporous anodic alumina (AAO) template to act as the working electrode for subsequent nickel nanowire deposition. The next step exposed the top of the template to a dilute 8.5% wt. solution of H_3PO_4 under ultrasonication for durations of 60, 30, or 15 min in order to widen the template pores. After solvent rinsing, gold was then electrodeposited at -1 mA for 15 to 20 minutes. After gold deposition, the sample was inverted, and the nickel cores and back nickel contact film were etched in a solution of FeCl_3 . Finally, the remaining AAO was removed in NaOH solution. This approach yielded vertically oriented arrays of ~ 108 gold nanotubes over an area of $\sim 30 \text{ mm}^2$.

The scanning electron microscopy (SEM) images in Fig. 4.1 show that the duration of the pore-widening step had a direct effect on wall thickness and, consequently, scattered light spectra of the AuNTs. For longer pore-widening times (60 min), which resulted in an average tube wall thickness of $136 \pm 36 \text{ nm}$ [Fig. 4.1(b)], it is likely that the pores were etched all the way through to the nickel back working electrode contact, and as a result, gold electrodeposition may have occurred at the base of the sacrificial nickel nanowires. For shorter pore-widening times (30 and 15 min), which resulted in average tube wall thicknesses of 55 ± 18 [Fig. 4.1(c)] and $29 \pm 8 \text{ nm}$ [Fig. 4.1(d)], respectively, the gold nanotube ends appeared to taper to very thin wall thicknesses as is evident from the flaky and flexible appearance [Fig. 4.1(d)], suggesting that pore widening did not occur uniformly along the length of the sacrificial nickel nanowires. Scattered-light spectra collected from four different regions of a vertically oriented array of nanotubes exhibited a broad peak at $657 \pm 14 \text{ nm}$ (60-min sample; using a dark-field objective in reflection mode under broadband, unpolarized halogen illumination of the nanotube ends). For the 30-min sample, scattered-light spectra exhibited a peak position of $676 \pm 63 \text{ nm}$. The shortest pore-widening time

(15 min) resulted in the most repeatable spectra with a peak position of 685 ± 2 nm averaged over four different regions of the sample. The standard deviation in the peak position values was attributed to a distribution in the wall thicknesses and gold nanotube diameters across each sample. From this spectral data, it was apparent that the AuNTs preferentially scattered light of longer wavelengths for thinner wall thickness.

To more accurately measure and understand the trend in nanotube resonance spectra with wall thickness (without sampling multiple nanotubes with a distribution of sizes), scattered-light spectra were acquired from an individual nanowire/nanotube (NW/NT) heterostructure (dark-field reflection with broadband, unpolarized halogen illumination normal to the nanotube long axis) formed by over-depositing gold on the sacrificial nickel nanowires. Spectra recorded from the heterostructure at specific points along the structure [denoted by the colored Roman numerals in Fig. 4.2(d)] show that the resonance behavior red shifts from the nanowire to nanotube. Figure 4.2(a) shows a peak maximum for the nanowire end of the heterostructure at 600 nm and a red shift by more than 0.39 eV (140 nm) along the tube region. This shift in plasmon resonance is apparent in the reflected-light brightfield and dark-field true-color images of the heterostructure [Figs. 4.2(b) and 4.2(c), respectively]. Clearly, the tube region (i.e. the lower $2.5 \mu\text{m}$ of the heterostructure) in the bright-field reflected-light image is blue/green in color vs the wire region, which appears yellow. In the dark field image, the tube region scatters red light more effectively than the nanowire region.

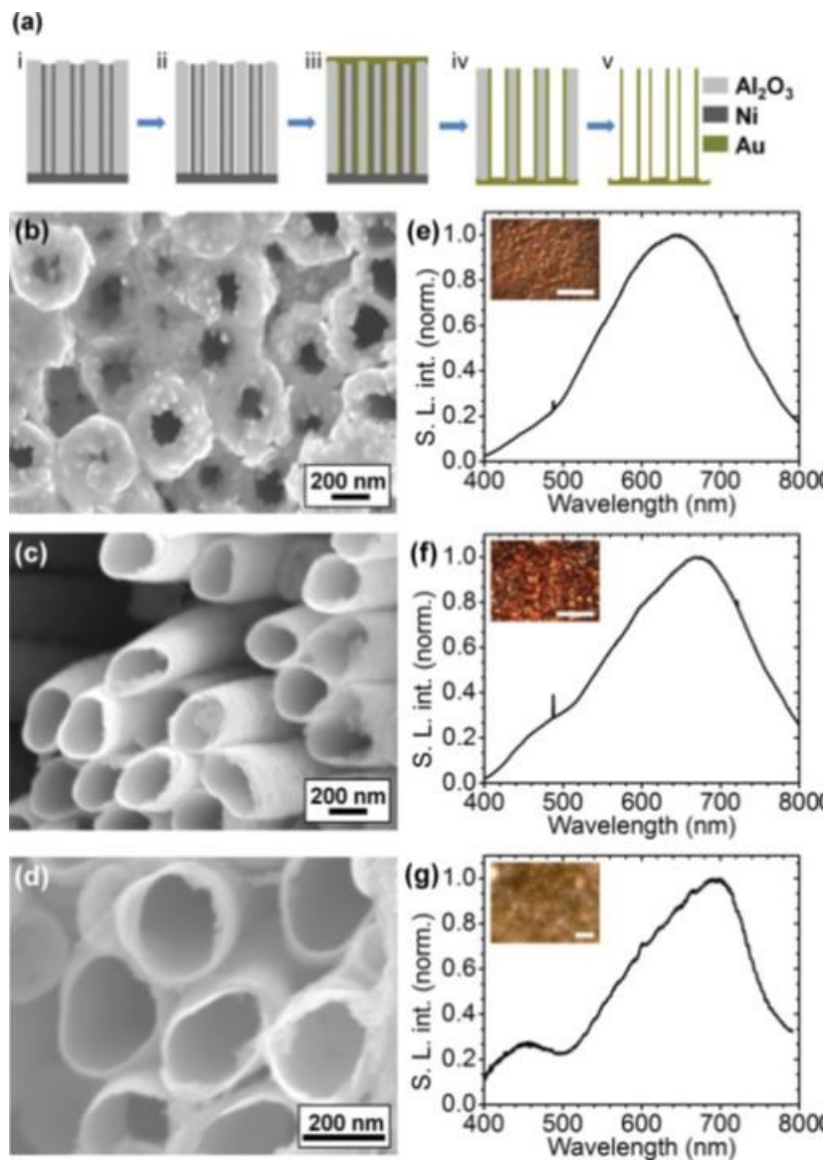


Figure 4.1. (a) Schematic showing the gold nanotube growth process [electrodeposition and pore-widening steps (i), (ii), and (iii) carried out under ultrasonication]. (b)–(d): SEM images of gold nanotubes deposited after AAO pore widening in H₃PO₄ for 60, 30, and 15 minutes, respectively. (e)–(g): Dark-field spectra, using unpolarized, end-on halogen lamp excitation, acquired from the samples imaged in (b)–(d), respectively. Top left corner insets in (e) to (g): True-color dark-field images of the nanotube arrays; scale bars are 25 μ m. Color available in electronic copy.

The change in contrast along the nanotube length in the SEM image of the heterostructure [Fig. 4.2(d)] suggested that the wall thickness of the tube decreased towards the tip, where it became flaky and ultimately discontinuous due to the extreme thinness. Others have reported

similar limitations in the thinness for which continuous gold shells can be fabricated.²⁴ Therefore, the red shift of scattered-light spectra observed along the length of the nanotube section of the heterostructure was attributed to the decreasing wall thickness. These findings corroborate the red shift observed for the three nanotube arrays of different average wall thicknesses (Fig. 4.1).

3-dimensional FDTD simulations of AuNTs were carried out under end-on excitation, to resemble the excitation scheme employed to excite the large area AuNT arrays in the experimental data of Fig. 4.1 (nanotube length = 20 μm in simulations), and under normal excitation conditions in analogy to the excitation scheme used to excite the single NW/NT heterostructure in Fig. 4.2 (nanotube length = 1 μm). For normal excitation, simulations were carried out for both excitation polarization parallel (i.e. axially polarized) and perpendicular (i.e. transversely polarized) to the nanotube long axis, since an unpolarized excitation source was not available. The simulated dimensions were based on average measurements from SEM images of the fabricated AuNT arrays for the three different pore-widening times (see Fig. 4.1). The ID of the grown AuNT arrays varied slightly over the three different etching times, but the ID was held constant in the simulations to more clearly study the relationship between the plasmonic and photonic mode propagation and tube wall thickness.

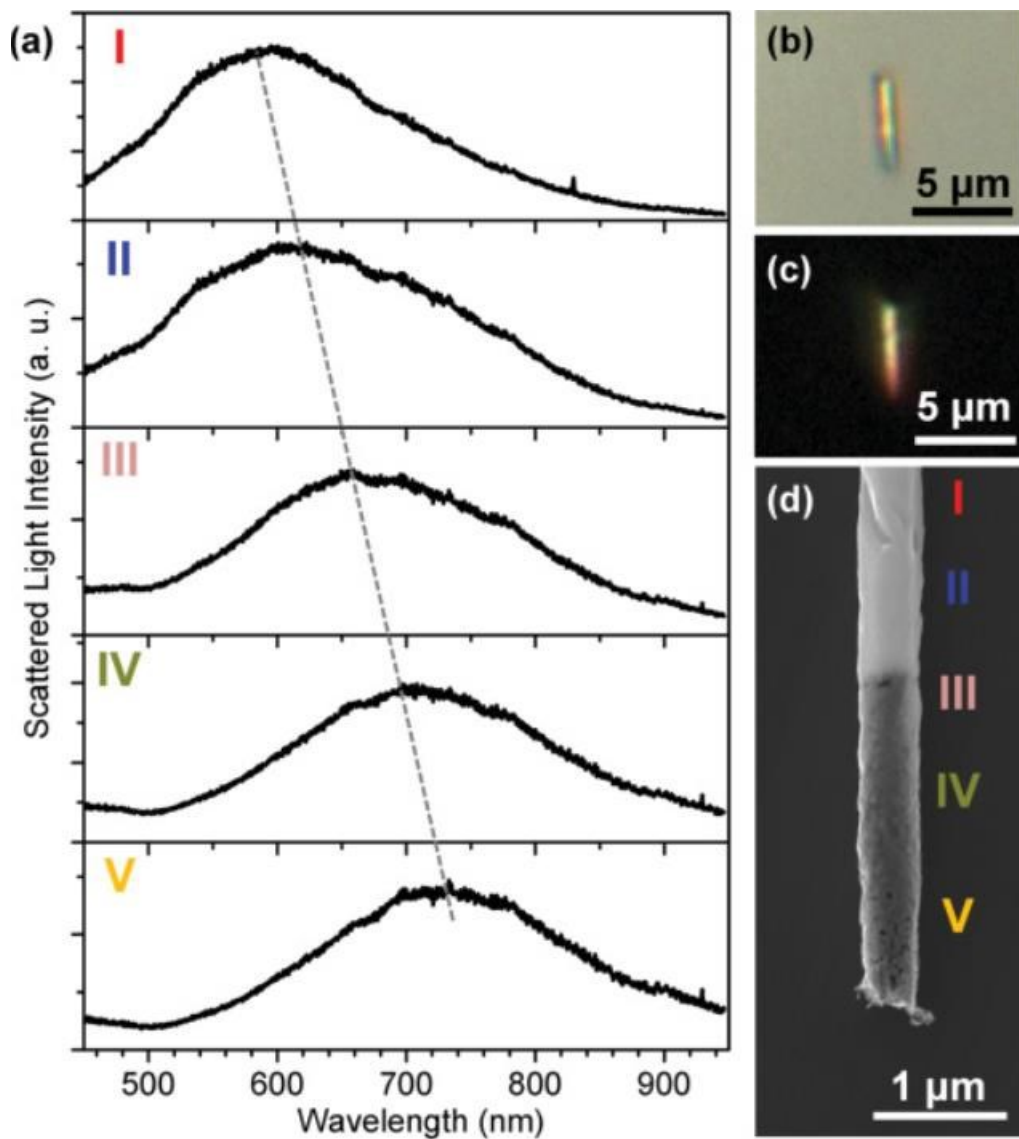


Figure 4.2. (a) Dark-field spectra using unpolarized, normally incident, halogen lamp excitation, acquired along the length of a single, nanotube/nanowire heterostructure [regions where the spectra were acquired from are indicated in with Roman numerals (d)]. Progressing downward along the structure, a red shift in resonance is evident as it becomes more tube-like. (b) Bright-field and (c) dark-field true-color optical images of the heterostructure. (d) SEM image of the NW/NT region of the structure. Color available in electronic copy.

From FDTD data, it was apparent that the AuNTs support both plasmonic and photonic modes in the wavelength range 600–850 nm and most intensely above 660 nm. Electric-field intensity vs wavelength spectra for SPP modes propagating at the AuNT surface [Figs.4. 3(a) and

4.3(b)] and photonic modes in the nanotube core [Figs. 4.3(c) and 4.3(d)] were obtained to determine the wavelength at which the peak electric-field intensity occurred for the two mode types. SPP and photonic mode spectra were produced by averaging 20 points along a line scan 25 nm above the outer surface and along the central axis of the simulated tube, respectively, for both end-on [Figs. 4.3(a) and 4.3(c)] and normal [Figs. 4.3(b) and 4.3(d)] excitation conditions. For the SPP mode, peak electric field intensities (and mode quality factor, $Q = \lambda_{\text{res}}/\Delta\lambda$, where λ_{res} is the resonance wavelength and $\Delta\lambda$ is the full-width-at-half-maximum) occurred at wavelengths of 741, 688, and 678 nm under end-on excitation (Q values of 4, 3, and 3, respectively) and 708, 710, and 580 nm under transversely polarized normal excitation (Q values of 6, 6, and 8, respectively) for AuNTs of 30-, 60-, and 140-nm WT, respectively. For AuNTs under axially polarized normal excitation, a propagating SPP mode and a photonic mode analogous to that observed when excited end-on were observed. Peak electric-field intensities for the simulated photonic mode occurred at wavelengths of 718, 718, and 729 nm under end-on excitation (Q values of 4, 3, and 4, respectively) and 804, 790, and 786 nm under transversely polarized normal excitation (Q values of 10, 11, and 9, respectively) for AuNTs of 30-, 60-, and 140-nm WT, respectively.

From the simulated spectral data, it was apparent that SPP mode spectra exhibited a red spectral shift with decreasing wall thickness, in qualitative agreement with experimentally observed data (see Figs. 4.1 and 4.2). A red shift of 0.16 eV (63 nm) under end-on excitation and 0.39 eV (128 nm) under transversely polarized normal excitation was determined from the simulated data over the studied WT range (140 to 30 nm). The red shift observed in the simulation results for the end-on excited AuNTs is two times greater in magnitude than the shift observed for the fabricated AuNT arrays under end-on excitation [0.08 eV (28 nm)] over the same wall thicknesses range (Fig. 4.1). This disparity in the magnitude of the red shift is attributed to experimental variations in circularity, wall thickness, tube-to-tube distance, and intertube interactions. These factors are expected to cause inhomogeneous broadening of the scattered-light spectra and masking of effects occurring directly due to changes in wall thickness. Additionally,

in the experiment, contributions from both the SPP and photonic modes are likely to contribute to the measured spectra. This finding underlines the importance of developing precise synthesis methods in conjunction with both spectroscopic studies of individual nanostructures and large area arrays to accurately characterize their optical properties.

Figures 4.3(c) and 4.3(d) show that the photonic mode peak electric-field intensity occurred at a nearly fixed wavelength with changing wall thickness. Therefore, it was concluded that the photonic mode does not contribute significantly to the apparent red shift and that the red shift occurs only for surface plasmon modes. Additionally, the large inner diameter suggested that interwall surface plasmon coupling (i.e., coupling between opposite walls of the same nanotube) was negligible. Moreover, the two simulated excitation schemes demonstrated that mode coupling and propagation was strongly dependent on incident excitation angle and polarization direction. These differences can be observed by comparing the radial electric-field intensity profiles for the two excitation schemes [Figs. 4.3(e) and 4.3(f)]. End-on excitation [Fig. 4.3(e)] resulted in a surface plasmon mode on the outer surface of the AuNT, with little change in the shape of the electric-field intensity mode profile. Transversely polarized normal excitation [Fig. 4.3(f)] resulted in radial multipole surface plasmon resonances with electric-field intensity mode profiles that change with circumference, the nature of which will be discussed in the next section. Axially polarized normal excitation exhibited similar electric field profiles to those observed for end-on excitation.

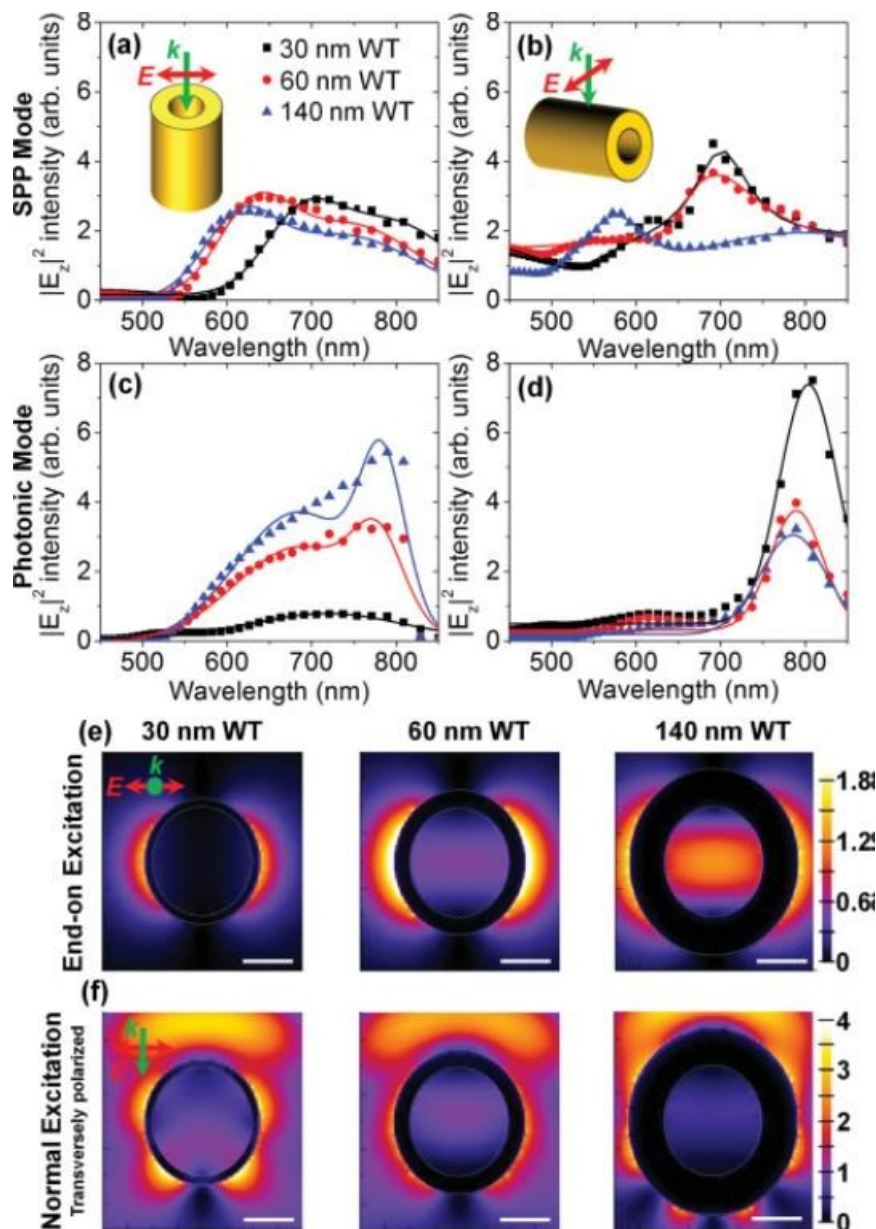


Figure 4.3. Electric-field intensity vs wavelength spectra for (a) and (b) the SPP, and (c) and (d) the photonic modes for (a) and (c) end-on excitation, and (b) and (d) transversely polarized normal excitation (spectra fitted with a double Gaussian). Inset in plots (a) and (b) are schematic representations of the end-on and normal excitation schemes, respectively. Green/gray arrows indicate excitation direction (k) and red/dark gray arrows indicate the polarization direction (E). Radial 2-D electric-field intensity profiles of (simulated AuNTs of 30-, 60-, and 140-nm WT under (e) end-on and (f) transversely polarized normal excitation at wavelengths corresponding to the maximum intensity in the corresponding SPP spectra shown in (a) and (b). Scale bars = 150 nm; color bars in (e) and (f) represent electric-field intensity. Color available in electronic copy.

To study how mode propagation is affected by wall thickness, SPP [Figs. 4.4(a) and 4.4(b)] and photonic [Figs. 4.4(c) and 4.4(d)] mode propagation lengths were extracted from the simulated end-on excited electric-field intensity profiles [Figs. 4.4(e) and 4.4(f); nanotube length = 20 μm]. The propagation length of each mode was extracted by fitting with a single exponential decay function. Under 660 nm excitation, propagation lengths were determined to be 1.1 ± 0.1 , 2.2 ± 0.2 , and 2.0 ± 0.2 μm for the SPP modes and 0.4 ± 0.03 , 1.2 ± 0.1 , and 1.3 ± 0.1 μm for the photonic modes, for wall thicknesses of 30, 60, and 140 nm, respectively [Figs. 4.3(a) and 4.3(c)]. Under 770 nm excitation, propagation lengths increased notably: 4.8 ± 0.7 , 5.1 ± 0.8 , and 4.7 ± 1.6 μm for the SPP modes and 0.7 ± 0.1 , 1.6 ± 0.1 , and 1.7 ± 0.1 μm for the photonic modes for wall thicknesses of 30, 60, and 140 nm, respectively [Figs. 4.3(b) and 4.3(d)].

From these data, it was found that the SPP propagation length of the 30-nm WT AuNT under 660 nm excitation increased by a factor of 4.4 at the longer excitation wavelength (770 nm), whereas the SPP propagation lengths of the 60- and 140-nm WTs only increased by a factor of ~ 2.3 . In the case of the photonic mode, the propagation length increases with increasing wall thickness and longer excitation wavelengths, indicating that mode confinement is dependent on wall thickness. Unlike the change in SPP propagation length, the photonic mode propagation increases more uniformly across the three WTs at the longer wavelength (by factors of 1.75, 1.39, and 1.30 for WTs 30, 60, and 140 nm, respectively).

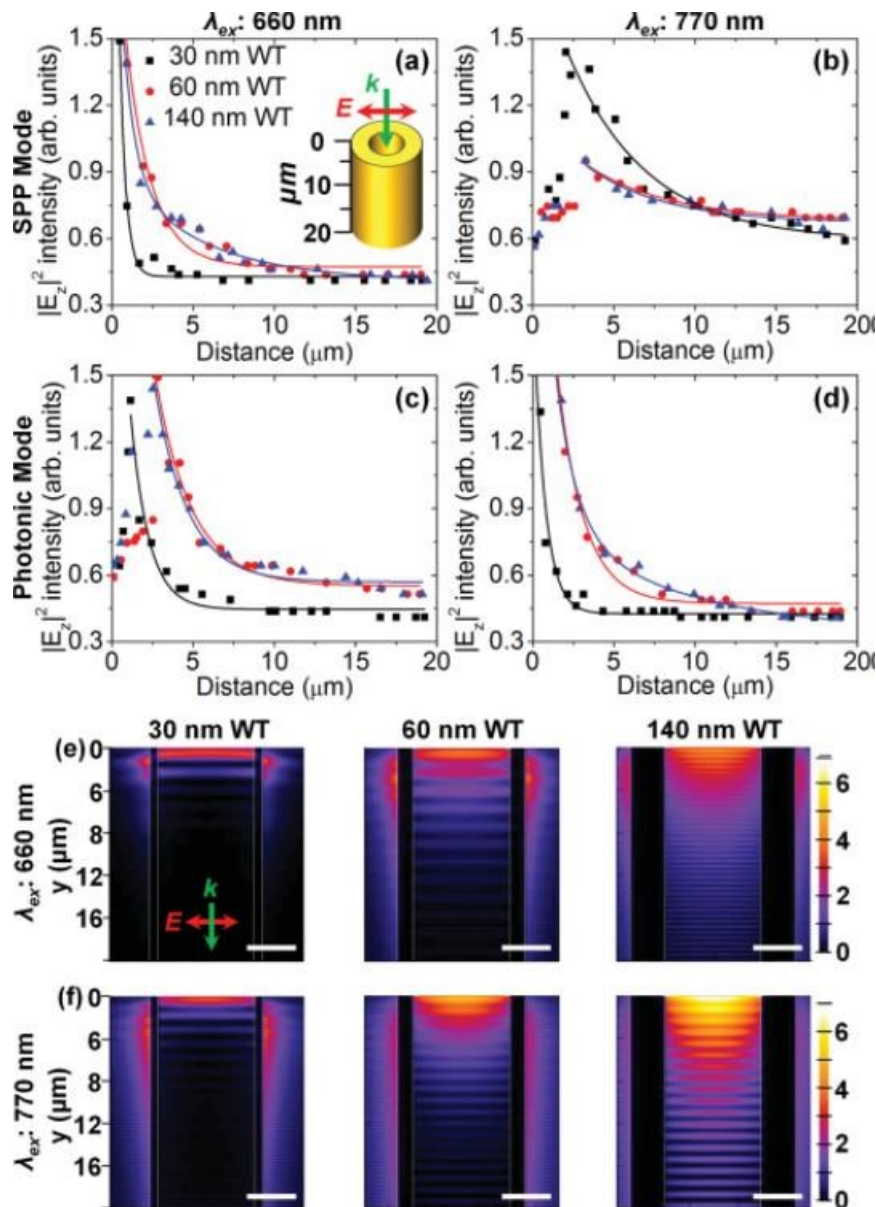


Figure 4.4. Simulated (a) and (b) SPP and (c) and (d) photonic mode decay profiles of single gold nanotubes under end-on excitation with constant 200-nm inner diameter and WT of 30, 60, and 140 nm with an excitation wavelength of (a)–(c) 660 nm and (b)–(d) 770 nm. Axial 2-D electric-field intensity profiles of the tube crosssection under (e) 660 nm and (f) 770 nm end-on excitation (x axis scale bar = 150 nm; color bars represent electric field intensity). Inset in (a) is a schematic of the excitation conditions. Green/gray arrows indicate excitation direction (k) and red/dark gray arrows indicate the polarization direction (E). Color available in electronic copy.

While the experimentally fabricated AuNTs had a fairly constant inner diameter of 200 nm, evidence in the literature suggests that the inner tube diameter also plays a critical role in the resultant surface plasmon mode resonant energy and confinement [115]. Therefore, to design an optimized structure for a given application, the plasmonic response as a function of inner diameter must be accounted for. While it was beyond the scope of this thesis to fabricate nanotubes with varying inner diameter, an additional set of FDTD simulations were conducted to understand how the inner diameter affects the resultant surface plasmon resonant energy. These simulations were carried out on single nanotubes with a fixed wall thickness and length of 5 μm and 30 nm, respectively, and inner diameters ranging from 15-150 nm under end-on excitation. Shown in Figure 4.5(a) and (b) are surface plasmon mode spectra from AuNTs with inner diameters varying from 15 to 150 nm in 15 nm increments.

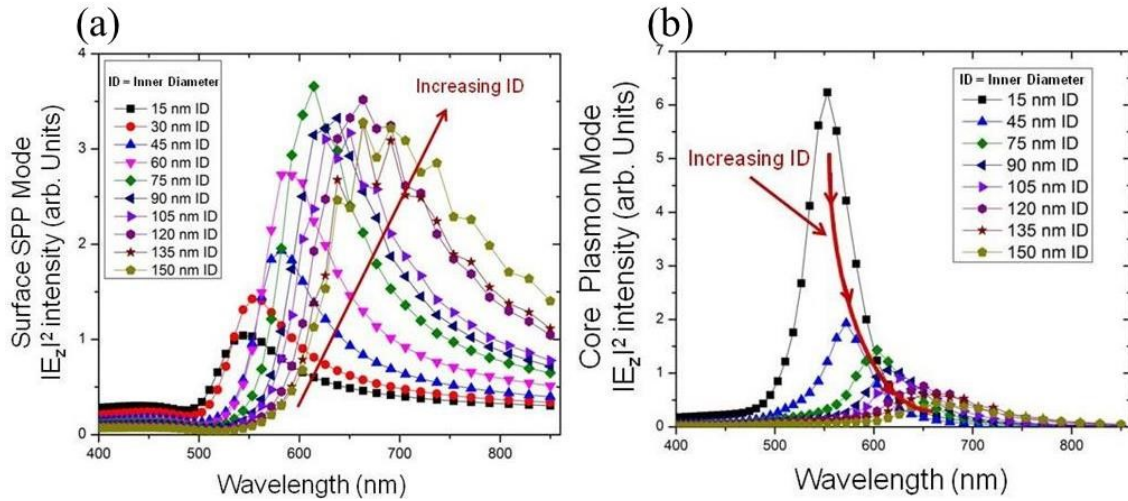


Figure 4.5. FDTD simulated electric-field profiles of the surface plasmon resonances on the surface (a) and in the core (b) of the gold nanotubes with fixed length and wall thickness of 5 μm and 30 nm, respectively, with inner diameters (ID) ranging from 15 nm to 150 nm.

With increasing inner diameter from 15 to 150 nm, a red spectral plasmon resonance shift of 100 nm is observed (Fig. 4.5 (a) and (b)). The surface electric field-intensity (i.e., the

propagating surface plasmon mode intensity) increases as a function of increasing inner diameter to a maximum for a nanotube with inner diameter of 90 nm (Figure 5 (a)). At inner diameters greater than 90 nm, the SPP mode spectra start to broaden and decrease in electric-field intensity. The electric field intensity in the core (i.e., core resonant plasmon mode confinement) was greatest for the smallest, 15 nm inner diameter, and decayed exponentially with increasing inner diameter (Figure 4.5 (b)).

For plasmonic nanoparticles, the geometry dictates the modes that can be supported by the structure and, subsequently, the extinction peaks and spectral widths. Our experimental observations of the apparent red shift in the scattered-light spectra of AuNTs as a function of decreasing wall thicknesses are in qualitative agreement with simulation, in addition to prior literature on metallic tubular and core-shell structures [113,115,146,148]. To further elucidate the results presented here and help attribute the observed experimental red shifts to particular mode types, it is necessary to place the present work in the context of prior work on metallic nanotubes and core-shell systems, which has primarily been concerned with smaller inner-diameter nanostructures.

Initial work towards understanding the fundamental mechanism that gives rise to the apparent red shift as a function of decreasing shell thickness in core-shell structures was conducted by Averitt *et al* [149,163]. By adapting Mie scattering theory, the apparent red shift of gold nanoshells as a function of decreasing shell thickness was attributed purely to classical origins, dictated by the relative thickness of the shell and the core diameter. Broadening of the plasmon peak width was attributed to a reduced effective mean free path of the conduction electrons. It should be noted that the core-shell systems studied by Averitt *et al.* had shell thicknesses below the electron mean free path so electron surface scattering was important [149,150].

The plasmon hybridization model of Prodan *et al.* offered further insight into the plasmonic response of tubular and core-shell nanostructures [142,150]. This model, described as the electromagnetic analogue of molecular orbital theory, can predict the plasmonic responses of complex nanoparticle geometries in terms of a hybridization of plasmon modes arising from more elementary geometries. In particular, the model has been employed to describe the tunability of resonance frequencies in concentric multishell structures as a function of intershell distance, shell thickness, and radius. Subsequently, Moradi built upon the plasmon hybridization model and adapted it specifically to tubular metallic nanostructures with concentric and nonconcentric cores [151,152,164]. In this model, shown schematically in Figure 4.6(a) and (b), the plasmon resonances in metallic nanotubes can be described in terms of a hybridization of plasmon resonances in capillary and wire geometries. This hybridization results in the splitting of the plasmon resonances into a low-energy symmetric mode and a higher-energy antisymmetric mode. As the wall thickness of the nanotube decreases, from thick (Fig. 4.6 (a)) to thin (Fig. 4.6 (b)), the interaction and splitting between the two plasmon modes increases [152]. This results in an effective decrease in energy of the symmetric mode and an increase in energy of the antisymmetric mode for the thinner walled structure (see Fig. 4.6 (b)). This model is valid in a size regime where retardation effects are neglected and so the nanotubes described by the hybridization approach have diameters <40 nm [151,152]. It is important to note that, in this size regime, interwall coupling is strong.

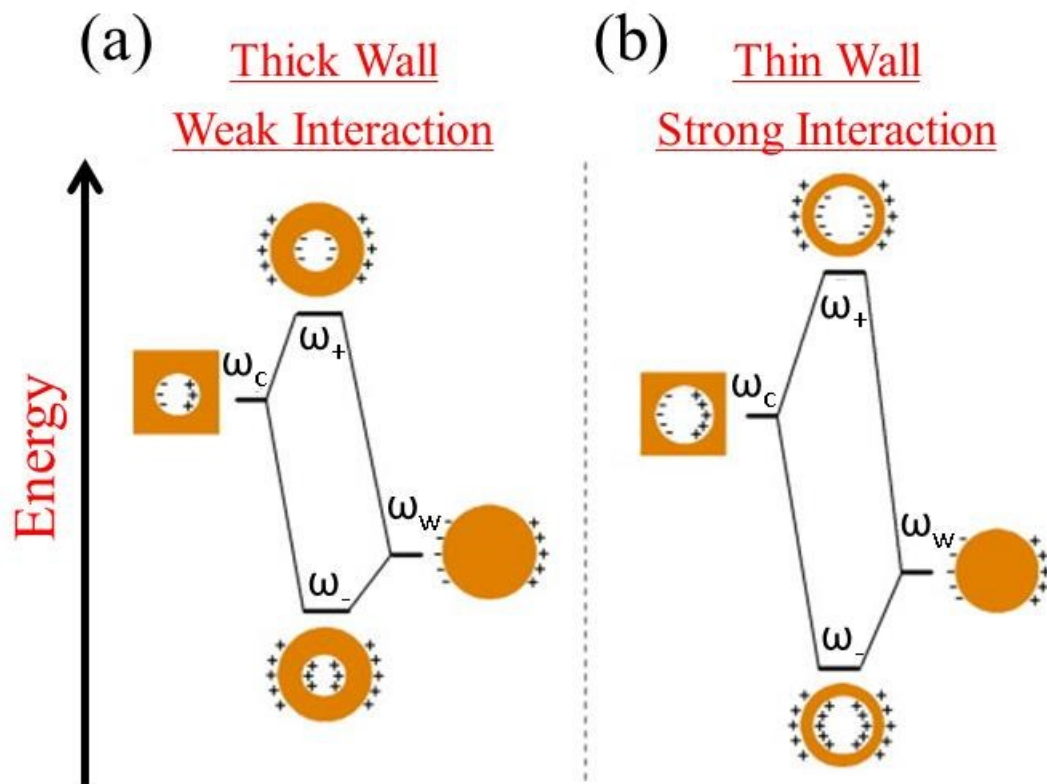


Figure 4.6. Schematic of plasmon hybridization model for tubular metallic nanostructures of thick (a) and thin walls (b), showing the coupling or hybridization between the core mode of a cavity (ω_c) and the surface mode of a wire (ω_w) resulting in two hybridized modes, a lower energy symmetric mode (ω_-) and a higher energy antisymmetric mode (ω_+). Figure adapted from [150,151,163].

The nanotubes described in this paper all have radial dimensions approaching half a wavelength of visible light. Therefore, they are on a much larger length scale than the core-shell and tubular systems studied in the aforementioned works (i.e. <40-nm outer diameter). Thus, these AuNTs do not fall into the size regime where interwall plasmon mode coupling is strong or into the quasistatic size regime where retardation effects can be neglected. However, these large AuNTs do exhibit a characteristic red spectral shift with decreasing WT as observed in the scattered-light spectra of large area arrays (Fig. 4.1) and along the length of the NW/NT heterostructure (Fig. 4.2).

Therefore, we propose that the observed red shift in the experimental scattered-light data with decreasing wall thickness is due to the degree of coupling or hybridization between the core mode and the mode on the nanotube outer surface. As the wall thickness becomes optically thin, the mode in the core becomes leakier, allowing it to interact with the mode on the outer surface. In a variety of systems, ranging from chains of equidistant-spaced metal nanospheres (which exhibit with local surface plasmon modes), to films of metal separated by a dielectric layer IMI waveguides (which exhibit propagating SPP modes), increasing the spatial overlap between modes adjacent to the metal interface increases the degree of mode mixing or coupling, resulting in a red spectral shift in the lower energy mode [81,166-168].

Mode coupling/hybridization in the AuNTs studied here is supported by the simulated SPP mode spectra and propagation length data as follows. While an increase in propagation length of the simulated SPP modes is expected at longer wavelengths for all wall thicknesses (due to reduced ohmic loss in the metal at longer wavelengths), the magnitude of enhancement in SPP mode propagation length at longer wavelengths was notably greater (by a factor of 4.4) for the thinnest WT (30 nm) compared to the thicker cases (60 and 140 nm; propagation length increase of ~ 2.3); see Fig. 4.4. The greater propagation length enhancement for the thinnest AuNT wall thickness strongly suggests that increased coupling or hybridization between the propagating SPP mode on the outer surface of the AuNT and the mode in the core occurs, resulting in a lowering of the SPP mode energy [i.e. a red-shift; see Fig. 4.3(a)] [149,163,165-167].

The theoretically observed red shift with increasing inner diameter is also attributed to a decrease in mode confinement in the core of the structure. When the inner diameter is small (15-30 nm) the confinement is greatest, and in-turn higher energy local or transverse resonances can be supported. As inner diameter is increased (> 90 nm), only lower energy longer wavelength surface plasmon modes can be supported, thus a redshift in the simulated spectra is observed. Such changes in plasmonic resonance with inner diameter have been previously theoretically and experimentally observed and are attributed the difference in confinement within the core of the

structure [115,116]. While AuNTs were not fabricated over a range of inner diameters in this set of experiments, the hard template approach used to synthesize the large 200 nm ID AuNT arrays can be used to fabricate a wide range of inner diameters as well as wall thickness by selecting the appropriate pore size distribution template.

As previously noted, FDTD simulations of AuNTs under transversely polarized normal excitation support radial modes, with quality factors of up to eight at visible wavelengths. These modes are characteristic of ring-type surface plasmon resonances, similar in nature to that observed by Apter *et al.* at ultraviolet wavelengths [116]. While these ring-resonant modes were not explicitly detected in our experiments due to the fact the scattered-light spectra were not conducted under a specific polarization direction, such resonances have been observed in low-aspect-ratio ring-shaped metallic nanostructures with quality factors ranging from 5–10 [116,167–170].

Apter *et al.* developed a nanoring-resonator model to describe high-energy plasmon resonances in tubular metallic nanoshells [116]. The model treats the nanotube as an IMI structure that has been bent into an annular shape, i.e. a ring resonator, and is based on the dispersion relations of surface plasmons on planar IMI structures [116,170]. This model predicts that the red shift in nanotube resonance wavelength is a function of increasing outer nanotube circumference in addition to wall thickness, a point which is not predicted by the hybridization model. Additionally, the ring resonator modes occur when the surface plasmon wavelength (λ_{sp}) matches an integer fraction of the ring's effective perimeter ($P_{eff} = \pi(r_1 + r_2)$ where $r_1 = ID/2$ and $r_2 = r_1 + WT$) and can be calculated with the following equation [116]: $\lambda_{sp} = P_{eff}/m$ (1) where m is the mode of the resonance ($m = 1, 2, \dots$). The calculated λ_{sp} for AuNTs of 30-, 60-, and 140-nm WT with a fixed 200-nm ID are 722 nm ($m = 1$), 816 nm ($m = 1$), and 534 nm ($m = 2$), respectively. These resonance wavelengths for the 30- and 140-nm WT AuNTs are within 8% of the simulated results [Fig. 4.3(b)], and for the 60-nm WT case, the value is within 15% of the simulated data. Therefore, it is highly likely that the large 200-nm ID AuNTs presented in this

paper can support surface plasmon ring-resonances at visible wavelengths, in addition to propagating SPP modes.

4.5 Conclusions

In summary, gold nanotubes were fabricated via electrodeposition and selective pore widening of nanoporous alumina templates. Control over wall thickness was achieved by varying the pore-widening time. Unpolarized scattered-light spectroscopy of large-area gold nanotube arrays in end-on excitation configuration indicated that resonant scattering at visible wavelengths red shifts by 0.08 eV (28 nm) with decreasing nanotube wall thickness from 140 to 30 nm. Unpolarized scattered-light spectra were collected with normal excitation (perpendicular to the long-axis of the structure) along a tapered single nanowire/nanotube heterostructure to more accurately measure the apparent red shift without the inhomogeneous broadening stemming from a distribution of gold nanotube wall thickness in the large area arrays. The redshift measured along the nanowire/nanotube heterostructure was 0.39 eV (100 nm).

Finite-difference-time-domain simulations of gold nanotubes were conducted to understand the relationship between surface plasmon mode propagation and coupling as a function of wall thickness, inner diameter, excitation condition (end-on or normal excitation) and incident polarization (parallel (0°) or perpendicular (90°) to the long axis of the structures). FDTD simulations show red shifts of 0.16 eV (63 nm) with decreasing wall thickness (from 140 to 30 nm) under both end-on and normal excitation with polarization parallel to the long axis of the structure (0°). Under normal excitation with transverse polarization, (i.e., polarization perpendicular to the long axis of the structure (90°)) a more pronounced redshift of 0.39 eV was observed with decreasing wall thickness (from 140 to 30 nm). Through simulations, the trend in the surface plasmon resonance was also studied as a function of increasing inner diameter, and a redshift of 0.34 eV was observed when ID was increased from 15 to 150 nm with a constant 30

nm WT. Additionally, the simulations show that a photonic mode was supported in the core of the large 200 nm inner diameter nanotubes; however, its wavelength did not vary notably with wall thickness. Electric-field intensity profiles showed surface plasmon propagation analogous to insulator-metal-insulator waveguides under end-on and normal excitation polarized parallel (0°) to the long axis of the structure and ring resonator-type modes under normal excitation polarized perpendicular (90°) to the long axis of the structure.

To clearly understand the theoretical and experimentally observed trends surface plasmon mode type and peak resonance as a function of wall thickness and inner diameter under the three different excitation conditions ((i) end on, normal excitation with polarization parallel (0°) (ii) and perpendicular (90°) polarization (iii) with respect to the long axis of the structure) the key findings have been summarized in Table 4.1. Included in Table 4.1 are the findings of this thesis chapter with literature references that corroborate some of the trends which have been previously studied, as well as trends that have not been studied in either the literature or in this thesis. The plasmonic response of both large area nanotube arrays and single nanostructures as a function of wall thickness and inner diameter under end-on excitation have been both theoretically and experimentally studied in this thesis as well as in the literature. The trends in plasmonic response as function of wall thickness and inner diameter are consistent throughout the literature with our findings presented herein, however, the previously studied nanotubes have much small inner diameters and wall thicknesses (<30 nm) than the nanotube studied in this thesis.

Based on extensive literature inquiries, there has been no published theoretical or experimental work that has addressed the plasmonic response of nanotubes under normal excitation or polarized normal excitation. Therefore, the simulations presented in this chapter are the first evidence that tubular metallic nanostructures support ring resonator-type modes under normal excitation with transverse polarization (perpendicular (90°) to the long axis of the structure) and show a red spectral shift with decreasing wall thickness. Additionally, because the

simulated ring resonator modes exhibit much sharper peak resonances and a greater red spectral shift with decreasing wall thickness, this mode type may be of greater utility for both refractive index-based chemical sensing and subwavelength photonic applications. Based on the theoretical evidence of the presence of ring resonator-type modes and their desirable attributes of these mode types, a comprehensive experimental investigation of single gold nanowire/nanotube heterostructures under polarized normal excitation was conducted and presented in Chapter 3 of this thesis.

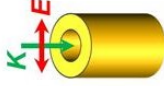
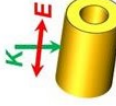

Excitation Condition	Mode type and trend in λ_{SP} with decreasing WT		Mode type and trend in λ_{SP} with increasing WT	
	Theory	Experiment	Theory	Experiment
 End-on	<ul style="list-style-type: none"> Propagating SPPs and photonic mode in core in large 200 nm ID structures, circular SP resonances in small (<30 nm ID structures). 0.16 eV (63 nm) redshift with decreasing WT from 140 to 30 nm (single nanostructure FDTD simulations). Studied in literature [5-8]. 	<ul style="list-style-type: none"> Propagating SPPs in large 200 nm ID structures, circular SP resonances in small (>30 nm ID structures). 0.39 eV (128 nm) redshift with decreasing WT from 140 to 30 nm (from measurements on large area arrays). Studied in literature [5-8]. 	<ul style="list-style-type: none"> Propagating SPPs and photonic mode in core in large ID structures. 0.34 eV (100 nm) redshift with increasing ID from 15 to 150 nm (single nanostructure FDTD simulations). Studied in literature [5-8]. 	<ul style="list-style-type: none"> Not studied in thesis. Addressed previously in the literature: 0.40 eV (160 nm) redshift with increasing ID from 16-24 nm with fixed 11 nm WT [5-8].
 Normal incidence, unpolarized and or parallel Polarization (0°)	<ul style="list-style-type: none"> Propagating SPPs on surface and photonic mode in core in large 200 nm ID structures. 0.16 eV (63 nm) redshift with decreasing WT from 140 to 30 nm (single nanostructure FDTD simulations under polarization parallel to the long axis of the structure (0°)). Not previously studied in the literature. 	<ul style="list-style-type: none"> Propagating SPPs in large 200 nm ID structures. 0.39 eV (128 nm) redshift with decreasing WT from nanowire to tip of tube on single nanostructure with unpolarized excitation. Not previously studied in the literature. 	<p>Not studied in literature or in this thesis.</p>	<p>Not studied in literature or in this thesis.</p>
 Normal incidence, perpendicular polarization (90°)	<ul style="list-style-type: none"> Localized SP resonances (ring-resonator type). 0.39 eV (128 nm) redshift with decreasing WT from 140 to 30 nm (single nanostructure FDTD simulations). Not previously studied in the literature. 	<p>Not previously studied in the literature. Goal: experimentally confirm mode type and trend in λ_{SP} for decreasing WT in thesis Chapter 3.</p>	<p>Not studied in literature or in this thesis.</p>	<p>Not studied in literature or in this thesis.</p>

Table 1. Summary of the theoretical and experimental observed trends surface plasmon mode type and inner diameter under the three different excitation conditions: end on (i), normal excitation with (ii) and perpendicular (iii) with respect to the long axis of the structure).

5 Theoretical and Experimental Study of Surface Plasmon Resonance as a Function of Incident Polarization for Single Gold Nanowire/Nanotube Heterostructures

5.1 Abstract

Theoretical simulations in Chapter 4 of this thesis provide unprecedented evidence that large 200 nm inner diameter gold nanotubes support ring-resonator-type modes under normal incidence, transversely polarized (i.e., electric field polarized at 90° with respect to the nanotube long axis) excitation[171]. Such resonant modes have not been experimentally observed in these structures and are of interest because they exhibit spectrally narrow surface plasmon resonances that are more highly tunable with varying wall thickness. These attributes make them candidates for chemical sensing applications and as tunable resonant cavities for subwavelength active optical applications if in-filled or clad with a suitable light emitting material.

In this chapter, a comprehensive experimental study of gold nanowire/nanotube heterostructures was made to investigate the presence of ring resonator-type surface plasmon modes. Through polarized bright-field and dark-field imaging, and polarized single nanostructure dark-field scattered light spectroscopy, the optical response of these structures was characterized and the first experimental evidence of ring resonator-type surface plasmon modes was observed. It was found that single nanotubes support both a photonic mode in their core and surface plasmon modes on their surface. When polarization was shifted from 0° to 90° with respect to the long axis of the heterostructure, the nanotube ceased to support propagating SPP modes and supported a lower-energy resonant mode characteristic of a ring-resonator-type localized surface plasmon resonance. In addition, the photonic mode in the core of the nanotube was found to

redshift when polarization is varied from 0° to 90° . The nanowire region of the heterostructure did not exhibit a significant change in mode type or energy with varying polarization. This was attributed to the large diameter (> 400 nm), which resulted in the nanowire region effectively acting as a bulk reflector.

5.2 Introduction

As described in Chapter 4 of this thesis, gold nanotubes are attractive structures for use as chemical sensors, subwavelength resonator cavities for coherent light emitters, and other chip-scale optoelectronic circuitry because of their anisotropic geometry and greater surface-area-to-volume-ratio than nanowires [142]. Electromagnetic theory has shown that these structures can support two distinct mode types depending on the polarization of the incident excitation: (i) propagating surface plasmon polariton (SPP) modes along the surface of the structure when incident light is polarized parallel to the nanotube long axis; and (ii) local resonant modes when incident light is polarized transverse to the long axis of the nanotube [142]. The field strength and peak resonant wavelength of the modes can be controlled by tuning wall thickness and inner diameter. Previous experimental studies, including those in Chapter 4 of this thesis have focused on excitation and detection of propagating SPP modes and have observed a red spectral shift with decreasing wall thickness and increasing inner diameter [142,161,172]. However, no studies have experimentally confirmed the presence of localized surface plasmon ring-resonances under normal excitation with varying incident polarization.

Understanding and harnessing local resonant modes supported by tubular metallic nanostructures may lead to the development of superior refractive index-based chemical sensors and the creation of chip-scale plasmonic resonator cavities. The finite-difference-time-domain electromagnetic simulations presented in Chapter 4 of this thesis indicate that large, 200-nm-inner-diameter gold nanotubes (AuNTs) support ring resonator-type localized surface plasmon

resonances under normal excitation with transverse polarization [171]. The work presented in this thesis chapter provides the first experimental evidence indicating the presence of such ring-resonator-type localized surface plasmon modes.

The gold nanowire/nanotube (NW/NT) heterostructures used in this study are comprised of a short NT segment (1.5 - 1.7 μm in length) joined to a long NW tail (4.5 - 7 μm in length). The NW region in these structures is not of primary interest in this study, but provides a suitable basis for comparison of the optical response of a tubular structure to a solid wire of equivalent outer diameter. The NW region is formed as a consequence of the NT synthesis method: electrodeposition of gold occurs both on the sides of the sacrificial nickel nanowires (in the etched space between the nickel nanowires and the nanoporous alumina channels) to form nanotubes and also on top of the nickel nanowires – forming a nanowire connected to the end of the gold nanotube segment within the nanoporous alumina channels (see Methods Section 4, 4.3.1) [171]. While the NW provided a reference with which to compare the optical response of the NT it also confirmed that there was no additional optical contribution from interactions between the NW and NT segments of the heterostructure. Based on the theory presented in Chapter 4, both the NT and NW regions of the heterostructure are long enough such that there should be no significant interaction between the NW and NT regions and in-turn, the optical response of both regions can be independently analyzed without concern of one influencing the other.

In this work, the finite-difference-time-domain simulations presented in Chapter 4 indicating the presence of ring-resonator-type localized surface plasmon modes are experimentally corroborated through a combination of polarized bright-field and dark-field scattered-light microscopy and single-nanostructure spectroscopy of individual gold NW/NT heterostructures [171]. This work was conducted in collaboration with Rutgers undergraduates Emily Esposito and Ryan Belfar. The experimental results show that the optical response of the NW/NT heterostructure varies significantly as a function of incident polarization under normal

incidence excitation. When the polarization incident on the structure is shifted from parallel (0°) to perpendicular (90°) (i.e., transverse) with respect to the long axis of the heterostructure, the mode type shifts from high energy propagating modes to distinct low energy, longer wavelength resonant modes. To provide further insight into these experimental results, additional calculations and full-field electromagnetic simulations were conducted on individual NW and NTs of equivalent dimensions to those experimentally studied. Using the Ring-Resonator Model developed by Apter *et. al* [116] clear evidence was developed that supports the presence of ring-resonator-type localized surface plasmon resonances under 90° polarization.

5.3 Methods

5.3.1 Sample Preparation

To prepare samples of individual nanotubes on both glass and silicon substrates for bright-field/dark-field microscopy and single nanostructure scattered light spectroscopy, 1 cm square silicon and glass substrates were cut using a tungsten carbide scribe. On the cut substrates, a square set of grids were scribed by hand onto the substrates with a tungsten carbide scribe and a ruler. The substrates were then cleaned by sonicating in Sparkleen solution (1g Sparkleen cleaner in 1 L deionized water) in a clean 100 ml beaker for 15 minutes followed by manually scrubbing the surfaces of the substrates with ethanol soaked KimWipes. The substrates were transferred to a clean 100 ml beaker then re-sonicated for 20 minutes in Sparkleen solution followed by rinsing in 3 clean 100 ml beakers filled with deionized water. The substrates were then transferred to a 100 ml beaker filled with a 50/50 mixture of concentrated HCl and ethanol, covered with a watch glass and let set for 20 minutes. The substrates were then carefully rinsed in deionized water and dried using a compressed air gun.

Low concentration dispersions of gold nanotubes synthesized previously (See Chapter 4 Methods sections titled “Electrodeposition Conditions” and Sample preparation”) in a 50/50 mixture of water and ethanol were prepared by sonicating the solution for 15-20 minutes. Small aliquots ranging from 5-10 μL were drop deposited from the sonicated nanotube dispersion onto cleaned glass and silicon substrates. The substrates were placed in covered sample holders and let dry in ambient air for 24 hours.

5.3.2 SEM Analysis of Single AuNW/NT Heterostructure and Image Analysis

Single nanowire/nanotube heterostructures on a silicon substrate were selected and characterized with a Zeiss Sigma FESEM (Carl Zeiss AG, Germany).using the secondary electron detector. The primary gold nanowire/nanotube heterostructure referred to as “tube 1” was imaged at a 0° stage tilt at magnifications of 37 kX, 100 kX, and 200 kX at an acceleration voltage of 5 keV and a working distance of 5.1 mm. The nanowire/nanotube heterostructures were also imaged with a stage tilt angle of 60° to more clearly measure the wall thickness at the tip of the tube. These images were taken at magnifications of 50.6 kX, 100 kX, and 150 kX, at an acceleration voltage of 20 keV and a working distance of 29.6 mm.

From these images, the dimensions of the nanowire/nanotube heterostructure were measured in ImageJ software. ImageJ is free software from NIH and is available for download online [173]. Dimensions were measured by first setting the scale of the image from the FESEM scale bar and using the measuring tool to estimate the length, inner diameter, and wall thickness of the nanowire/nanotube heterostructure.

5.3.3 Polarized Bright-field/Dark-field Imaging of Single Gold Nanotubes

The method used to successfully collect polarized true color bright-field and dark-field images of single NW/NT heterostructures required extensive method development to ensure

minimal depolarization bias from the microscope optics and accurate polarization of the structure. The method development is described herein and the measurements taken to during the optimization process are included in Section F1 of Appendix F. The three major steps in the method development were (i) establishing how best to polarize the incident excitation and collected scattered light, (ii) the determination of the optimal positions of the excitation and collection polarizers in the optical path (to minimize de-polarization bias from the microscope optics and maximize signal throughput to the CMOS CCD camera), and (iii) how to vary the incident polarization without introducing depolarization bias into the image as polarization is varied with respect to the NW/NT heterostructure.

Images were collected with a Nikon Optishot 66 bright-field/dark-field microscope fitted with a halogen lamp and a CMOS CCD camera was used to capture. To establish the optimal polarization conditions to study the plasmonic response of gold nanotubes as a function of incident polarization, images were taken of single gold nanotubes under halogen excitation with a 100X objective with (a) unpolarized excitation and unpolarized collected scattered light, (b) unpolarized excitation with polarized collected scattered light, (c) polarized excitation with unpolarized collected scattered light, and (d) polarized excitation with polarized collected scattered light. For conditions (b)-(d), 1" diameter glass polarizing discs were used for both excitation and collection polarization (see Fig. 1(a) and (b)). When both excitation and collection were polarized, the polarizers were set in-phase WRT to each other. The halogen excitation was polarized by placing one of the polarized glass discs into a filter holder in the path of the halogen light source just after the lens aperture (see Fig. 5.1 (a) and (b)). Collected scattered light was initially polarized by placing a polarized glass disc (identical to that which was used for the polarized excitation) in the path of the beam just prior to the collection lens for the CCD atop the microscope (see Fig. 5.1 (a) and (b)).

In cases (b)-(d), the incident polarization was varied by rotating the polarizing disc(s) in 10 degree increments, and at each increment, an image of a single gold NW/NT heterostructure was collected such that the incident polarized light was varied from parallel to the long axis of the nanotube (0°) to perpendicular to the long axis of the nanotube (90°) (see Fig. 5.1 (a) and (b)). The samples were either placed parallel (position I) or perpendicular (position II) to the x-direction on the microscope stage (see Fig. 5.1(a)-(d)). When sample was placed in position I, the incident polarization was parallel (0°) and perpendicular (90°) with respect to the long axis of the structure in conditions 2 (C2) and 1 (C1) (a,c), respectively. When sample was placed in position II, the incident polarization was parallel (0°) and perpendicular (90°) with respect to the long axis of the structure in conditions 1 (C1) and 2 (C2) (a,c), respectively.

The resultant images showed a clear trend in the optical response as a function of incident polarization, but the background intensity of the images also changed significantly as polarization was shifted. This suggested that at certain angles there was greater depolarization bias from the microscope optics, which reduced the overall signal throughput to the CMOS CCD camera. To test this depolarization bias, the scattered light intensity from a Spectralon® disc was recorded as the polarizers were rotated incrementally from 0° to 90° with respect to the microscope stage (see Fig. 5.1). These measurements showed a significant change in intensity on the microscope CMOS CCD as the polarization was varied, which confirmed that the microscope exhibited a significant amount of polarization bias. This was attributed to the position of the polarizers relative to 45° mirrors in the microscope. Additionally, some of the variation in signal throughput (i.e., depolarization) was introduced by the manual repositioning of the polarizing disc(s), which resulted in the discs not being in phase with each other. Even with the aid of a protractor and other measurement devices, it was difficult to ensure both the excitation and collection polarizers were in-phase with respect to each other when varying their positions in such small (10°) increments.

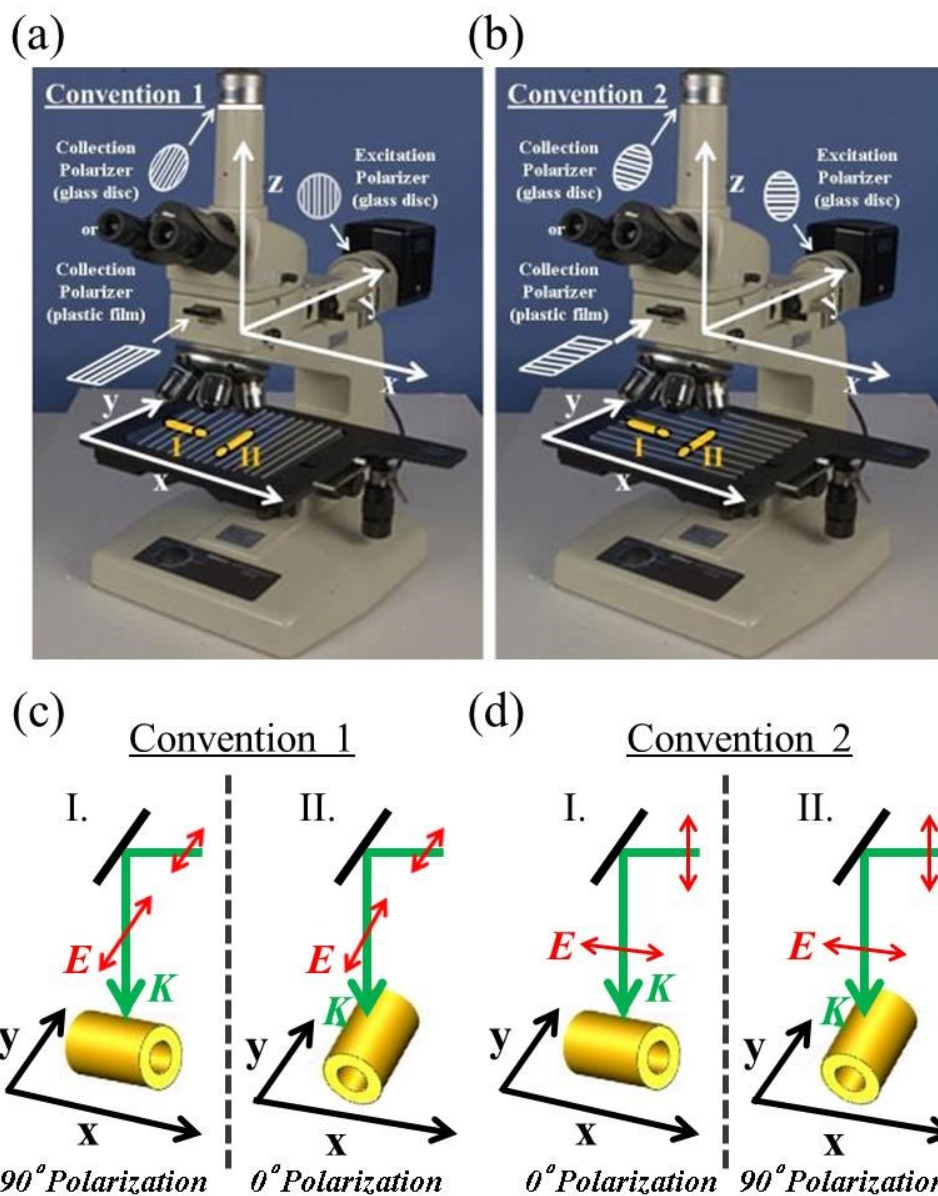


Figure 5.1. Schematics of sample placement and location of the excitation and collection polarizers (a,b), and of the incident polarization on the sample (c,d) in polarization convention 1 (C1) (a,c) where polarization is parallel to the y-axis and convention 2 (C2) (b,d) where polarization is parallel to the x-axis. Samples were oriented parallel (position I) or perpendicular (position II) to the x-direction on the microscope stage. In position I, incident polarization was parallel (0°) and perpendicular (90°) WRT to the long axis of the structure in conditions 2 (C2) and 1 (C1) (a,c), respectively. In position II, incident polarization was parallel (0°) and perpendicular (90°) WRT to the long axis of the structure in conditions 1 (C1) and 2 (C2) (a,c), respectively. Color available in electronic copy.

While these measurements showed that placement of the polarizers in the optical path of the microscope will require optimization, they showed that whether polarization was parallel or perpendicular to the long axis of the NW/NT heterostructure, the same trends in the plasmonic response were observed regardless if single excitation or collection polarization, or dual excitation and collection polarization were used. However, the dual polarization case made the trend more evident because it minimized depolarization through the microscope excitation and collection optics.

To improve the phase alignment between the excitation and collection polarizer, the polarized glass disc in the collection path was replaced with a rectangular piece of polarized film that was slipped into the filter holder slot just above the microscope objective lens (see Fig 5.1(a) and (b)). The excitation was polarized in the same fashion as the previous measurement technique polarized, with a glass disc that was placed directly in the optical path in front of the halogen light source aperture in a filter holder (see Fig 5.1(a) and (b)). Using the rectangular polarizing film strip instead of circular glass disc for the collection polarization helped ensure that the excitation and collection polarizers were in-phase and allowed for more accurate determinations of the amount of inherent bias/depolarization taking place due in the microscope due to the optics.

Once it was ensured that the excitation and collection polarizer could be easily and reproducibly set in phase with respect to each other, the next critical step in refining the polarized bright-field and dark-field imaging (and later dark-field scattered light spectroscopy) was the determination of the optimal position of the excitation and collection polarizers WRT to the microscope stage to minimize depolarization bias from the microscope optics (and in turn maximize signal throughput loss). To establish the optimal position of the polarizers which minimized depolarization bias and maximized signal throughput, bright-field spectra were collected of blank glass in polarization conditions 1 (C1) (see Fig. 5.2 (a,c)) and 2 (C2) (see Fig.5.2(b,c)) in dual excitation and collection polarization (Fig. 5.2(a)-(c)) and with the collection

polarizer only (Fig. 5.2(d)). Spectra were collected by outcoupling the resultant microscope image out the back of the instrument where it was directed to an Andor 303is imaging. For this experiment, the CMOS CCD could have been used to compare the relative signal throughput as a function of polarizer position relative to the microscope stage, but the spectrometer provided a more accurate and facile means of doing so.

The first set of measurements employed dual polarization of both the excitation and collection in conditions 1 (C1) and 2 (C2) using a glass disc for the excitation polarizer and a plastic film for the collection polarizer (see Fig. 5.1(a)-(c)). For both conditions 1 (C1) and 2 (C2), the excitation polarizer was varied $+10^\circ$ clockwise and counterclockwise from the 0 position where they are truly in phase to determine if there was any significant depolarization emanating from the microscope optics (see Fig. 5.2(a)-(c)). It was observed for the C1 condition that the most intense signal was observed when the polarizers were geometrically in phase WRT to each other (see Fig. 5.2(a) and (c)). In contrast, for the C2 condition a slightly more intense signal was observed when the excitation polarizer was rotated 10° clockwise WRT to the collection polarizer (see Fig. 5.2(b) and (c)). This suggests a slight depolarization from the microscope optics in the C2 condition. However, when comparing the overall throughput (i.e., intensity) from C1 to C2 under dual polarization, the C2 condition has a throughput over 4x greater than C1 (see Fig. 5.2(c)). Therefore, it was concluded that C2 polarization condition was the optimal case to use due to the significantly greater throughput.

To further verify that the C2 polarization convention exhibits a significantly higher throughput and potentially isolate the location and cause of the depolarization in the optical path, another set of spectra were collected on blank glass using polarized collection only in both C1 and C2 conditions (see Fig. 5.2(d)). The resultant spectra captured under collection polarization-only also show increased in throughput in the C2 condition by a factor of approximately 6 (Fig. 5.2(d)). This is in agreement with the dual polarized spectra in which the C2 condition yields a

higher throughput by a factor of 4 (see Fig. 5.2(c)). Based on these findings, it suggests that a significant fraction of the microscope depolarization is due to the 45° mirror that directs the excitation down into the objective. Based on these findings, the optimized technique used to collect the polarized true color bright-field and dark-field utilized dual excitation and collection polarizers fixed in condition 2 (C2) to maximize throughput and minimize polarization bias.

While it was shown that depolarization bias can be minimized by setting the polarizers in condition 2 (C2), if the incident polarization on the NW/NT heterostructure is to be varied, it cannot be done by rotating the polarizers, or the resultant signal throughput will vary across the measurement set. The solution to this problem was to fix, or 'lock' the excitation and collection polarizers in convention 2 (C2), where there is the least amount of depolarization bias was observed and physically rotate the sample itself such that the incident polarization was varied relative to the long axis of the NW/NT heterostructure. This was achieved by mounting the sample on a rotating micrometer stage that was affixed to the microscope stage. Incident polarization angle relative to the long axis of the NW/NT heterostructure was varied (from position (I) to (II), in Figs. 5.1(a) and 1(b)) by rotating the micrometer stage, re-centering the region of interest in the field of view and collecting an image. The challenge of having to rotate the sample to vary incident polarization was that with every rotation, the microscope stage needed to be carefully repositioned and the objective re-focused to bring the structure was back into the field of view. This process was achieved with ease after practice and was aided by marking the sample with a clear grid system carefully and creating an image map of the sample under varying magnifications.

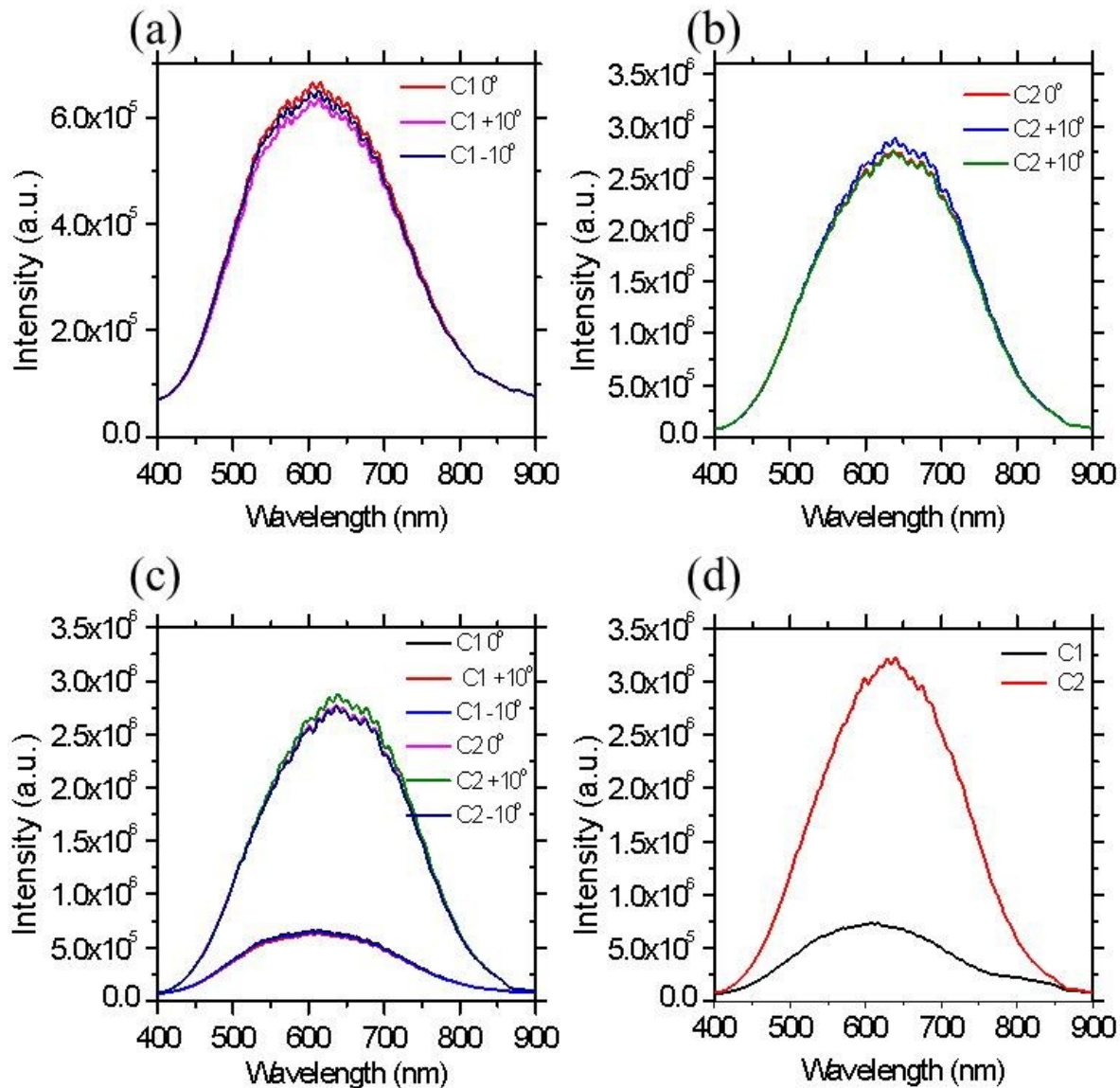


Figure 5.2. Spectra on blank glass with polarized excitation and collection in C1 (a) and C2 (b) polarization conditions with excitation polarizer (i) in phase with the collection polarizer, (ii) 10° clockwise WRT to the collection polarizer and (iii) 10° counterclockwise WRT to the excitation polarizer. (c) Compilation of spectra in (a) and (b) illustrating the 4X increase in signal throughput of the C2 polarization condition relative to C1. Shown in (d) are spectra on blank glass with polarized collection only in C1 and C2 polarization conditions showing a 6X increase signal throughput of the C2 polarization condition relative to C1. Color available in electronic copy.

In summary, the optimal method for collecting polarized true color bright-field and dark-field images of the NW/NT heterostructure employed the use of dual excitation and collection

polarization, using a glass disc to polarize the excitation and plastic film to polarize the collected scattered light. Both polarizers were set in-phase in condition 2 (C2) and the sample was rotated on a micrometer stage to vary the incident polarization. To make accurate comparisons of the bright-field and dark-field images under varying polarization angles, they were collected using the same exposure times and gain settings.

5.3.4 Polarized Bright-field/Dark-field Image RGB and Grayscale Intensity Analysis

To gain a qualitative understanding of the peak resonant frequencies of the surface plasmon modes supported by gold nanotubes as a function of incident polarization, a red-green-blue (RGB) pixel analysis was conducted at various points along the true color bright-field and dark-field images of singly NW/NT heterostructures. This RGB pixel analysis was conducted with ImageJ software. The preliminary method used for this analysis was conducted by opening the desired image in ImageJ software, selecting a circular region with an approximate diameter of the nanotube at the tip, center, and end of the nanowire/nanotube heterostructure (see Fig. 5.3). The selected regions were analyzed by selecting the “Analyze” tab, followed by “Tools” and finally, by selecting “Color Histogram”, which outputs the percentage of red, green, and blue pixels in the selected region. It was found that this method was not optimal because the sampling region was too large and was biased by the background. Measurements taken with this un-optimized procedure are presented in Section F1. of Appendix F.

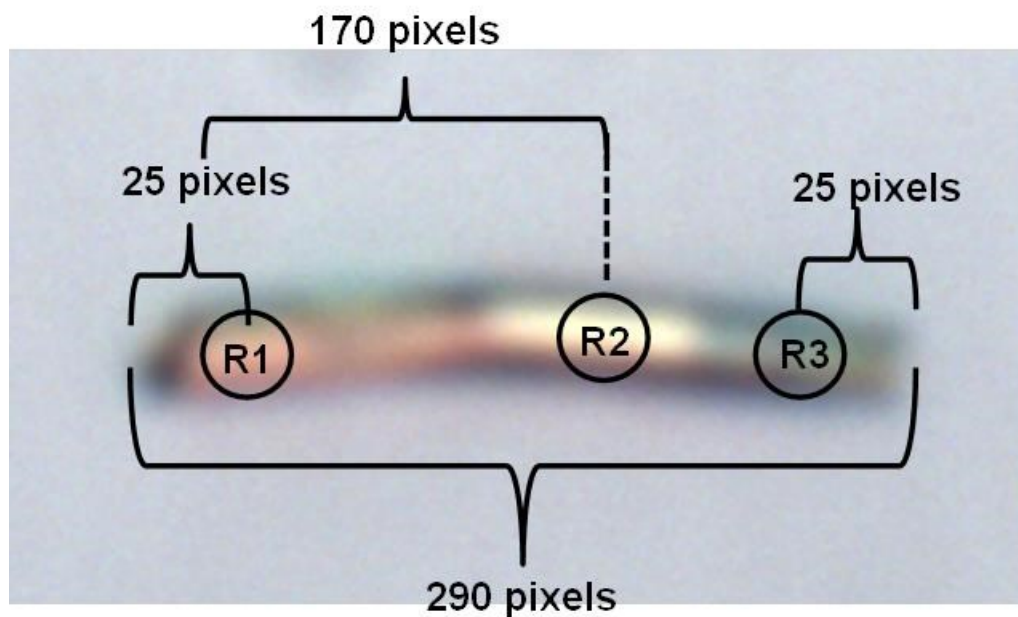


Figure 5.3. True color bright-field image of a NW/NT heterostructure “tube 1” with marked regions where RGB and grayscale analysis were conducted: (R1) broken wire region, (R2) un-damaged wire region, and (R3) tube region. Color available in electronic copy.

An optimized analysis was conducted by measuring a smaller 15 x 15 pixel square in the nanowire and nanotube regions of the heterostructure (see Fig. 5.4). This smaller sample reduces error from pixels at the interface of the heterostructure and the image background.



Figure. 5.4. True color bright-field image of nanowire/nanotube heterostructure “tube 1” with 15 x 15 pixel blue boxes indicating the regions where the RGB and grayscale analysis were collected. Color available in electronic copy.

To further corroborate that any measured change in the percentage of red, green, and blue pixels in the analysis of the nanowire/nanotube heterostructures manifested from the plasmonic response of the nanostructure as a function of incident polarization, an RGB analysis was conducted on the background of each true color bright-field and dark-field image (see Fig. 5.4). The percentage of red, green, and blue pixels in the background surrounding the tube was calculated from a featureless 15 x 15 pixel region in each image using the “Color Histogram” function.

In conjunction with the RGB analysis, some of the bright-field and dark-field images were turned into 16-bit grayscale images and an intensity analysis was conducted by using a line scan through the length of the center of the nanowire/nanotube heterostructures to understand how the SPP mode intensity along the structure changes with incident polarization. Grayscale intensity analysis was conducted by opening the true-color image in ImageJ software and converting it to a 16-bit grayscale image by selecting the “Image” tab, followed by “Type”, and then clicking on “16-bit.” Once this was complete, the selected regions were analyzed by selecting the “Analyze” tab, followed by “Tools” and finally, by selecting “Histogram”, which outputs the grayscale intensity.

5.3.5 Polarized Dark-field Scattered Light Single Nanostructure Spectroscopy of Single NW/NT Heterostructures

Polarized single nanostructure dark-field scattered light spectroscopy was conducted on individual NW/NT heterostructures to more fundamentally elucidate the plasmonic response as a function of incident polarization. As with the polarized bright-field/dark-field imaging, successfully collecting the polarized dark-field scattered light spectra of single NW/NT heterostructures required extensive method development to optimize the process. Data sets that were collected in this process of optimization are presented in the Appendix of this chapter.

Spectra were collected on both the NW and NT regions of individual gold NW/NT heterostructures with the same microscope (Nikon Optishot 66) and similar procedures used for the bright-field and dark-field imaging. However instead of directing the signal to the CMOS CCD mounted atop the microscope, it was directed out the back of the microscope passed through a reverse Galilean beam expander to narrow the beam and routed to an Andor 303is imaging spectrometer through a series of three carefully aligned mirrors and focused with a 100 mm achromatic doublet onto the spectrometer CCD (see Fig. 5.5).

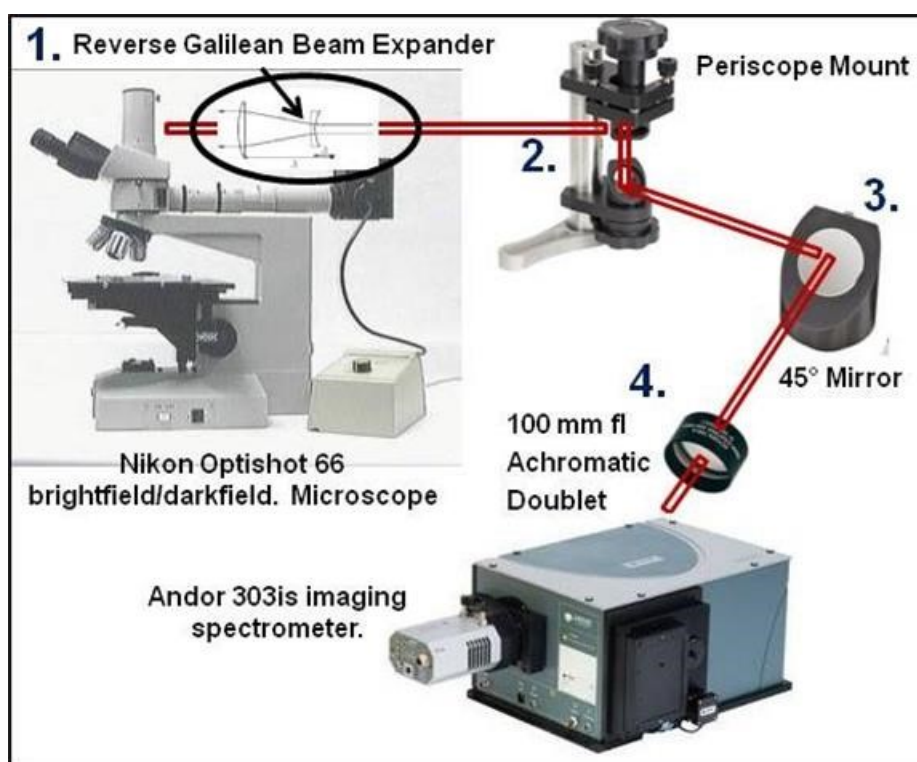


Figure 5.5. Schematic of the bright-field/dark-field microscope integrated with an imaging spectrometer. (1) Out-coupled light from the back of the microscope is reduced in diameter with a reverse Galilean beam expander. (2) The light then travels down a periscope mount to a (3) 45 degree mirror and through a (4) 100 mm focal length achromatic doublet onto the Andor 303is imaging spectrometer. Color available in electronic copy.

Spectra were by setting the microscope to dark-field mode, projecting an image of the structure onto to spectrometer CCD and selectively binning the region of interest within the 200 μm input slits of the spectrometer by assigning a rectangular region of pixels on the spectrometer

CCD. To set the sample in the desired position, fine adjustments of the microscope stage were made. For very minor adjustments of sample position on the spectrometer CCD, the third mirror, (just prior to the spectrometer) was adjusted to shift the projected image into the desired position (see Fig. 5.5). All spectra were collected using grating 1 (150 lines/mm) in imaging mode with custom binning, with exposure times ranging from 1 to 2 seconds with up to 60 acquisitions to ensure a high signal to noise ratio. In conjunction, the sample was imaged with the spectrometer CCD prior to every spectrum collected to ensure the proper region of the sample was being analyzed.

To ensure that there was minimal depolarization bias; spectra were collected with (i) unpolarized excitation, (ii) polarized collection only, and (iii) in-phase dual polarized excitation and collection. As in the bright-field/dark-field imaging, a glass disc was used to polarize the excitation path and a plastic film was used to polarize the collected scattered light. The polarizers were set in either conditions 1 (C1) or 2 (C2), such that the polarization was either parallel to the x- or y-direction on the microscope stage (see Fig. 5.1). So, for example, to set the incident polarization on the heterostructure to 0° when polarization is set to condition 1, (where light is polarized parallel to the y-axis of the microscope stage), the long axis of the structure must be aligned parallel to the y-direction of the microscope stage. In contrast, to set the incident polarization on the heterostructure to 0° when polarization is set to condition 2, (where light is polarized parallel to the x-axis of the microscope stage), the long axis of the structure must be aligned parallel to the x-direction of the microscope stage. Measurements in both polarization conventions 1 and 2 were made to establish which convention resulted in the least amount of polarization bias and to establish repeatability of the measurements. Like in the case of the bright-field/dark-field imaging, condition 2 (C2) resulted in the greatest signal throughput. Therefore, the optimized polarized spectra presented in the results and discussion section were collected by fixing the polarizers in condition 2 (C2) and physically rotating the sample stage to vary the

incident polarization, such that the structure was either parallel to the x- or y-direction of the microscope stage.

To accurately measure the optical response of the nanowire and nanotube regions of the NW/NT heterostructure as a function of incident polarization, the exact position along the heterostructure and size of the area being from where the spectrum is captured must be consistent throughout the entire measurement set. Spectra collected from regions on the sample of dissimilar size or at varying positions may bias the spectral response and in-turn skew or mask the true plasmonic response of the heterostructure as a function of incident polarization. The consequences of collecting spectra from dissimilar regions are shown and described in section F2. in Appendix F.

To ensure that spectra are collected from the same region of equal sampling area on the structure, the long axis of the heterostructure must be positioned perfectly parallel to either the x- or y-direction of the spectrometer input slits, (which corresponds to the x- and y-directions of the microscope stage). This is due to the fact that only a rectangular region can be selected or 'binned' on the spectrometer CCD, and if the heterostructure is not positioned at angles other between 0° and 90° WRT to the spectrometer input slits, the dimensions of the region being analyzed will not be of equal. Therefore, spectra were not collected over a range of angles (as was done with the polarized bright-field and dark-field imaging), but only at incident polarizations of 0° and 90° . Additionally, if the structure is not truly parallel or perpendicular to the microscope stage, the incident polarization will not be truly parallel or perpendicular to the long axis of the heterostructure, thus biasing the measurement. To ensure that the sample was properly aligned and that same region of interest was maintained throughout a measurement set, images were collected prior to the acquisition of each spectrum with the spectrometer CCD with the input slits in the full open position and when closed to $200\text{ }\mu\text{m}$.

Raw dark-field scattered light single nanostructure spectra were corrected for contributions from (i) scattered light from the substrate, (ii) ambient or stray light within the lab, and (iii) from the lamp background by collecting the three additional spectra with the same acquisition parameters as used for the experimental measurements and inputting them into Equation 1:

$$\frac{\text{raw AuNT spectrum} - \text{blank substrate background spectrum}}{\text{Spectralon® background} - \text{ambient room background}} \quad (1)$$

where the “blank substrate background spectrum” is a spectrum collected on the same substrate as the sample but in a region without any nanostructures in the field of view to correct for any scattered light from the substrate, the “Spectralon background” is a spectrum taken of a piece of Spectralon® to correct for the lamp background, and the “ambient room background” is a spectrum collected with halogen light source on the microscope turned off to correct for ambient or stray light within the lab.

5.3.6 FDTD Simulations of Single Gold NW and NTs of Representative Geometries of the “tube 1” NW/NT heterostructure

Finite-difference-time-domain (FDTD) simulations of single gold NTs and NWs of equivalent geometries to the nanowire/nanotube heterostructure “tube 1” were conducted with and without a silicon substrate under normal incidence at both parallel (0°) and perpendicular (90°) polarizations. The gold NT and NW structures were simulated using the dispersive dielectric constants from the *Handbook of Optical Constants of Solids*, and the silicon substrate was simulated using optical constants from Palik. For all NT and NW simulations, a fine 2 nm mesh was used throughout the simulation space in order to accurately simulate the optical interaction. To minimize edge effects both the NT and NW structures were extended through the simulation

boundaries. The NT had inner and outer radii of 176.5 nm and 214.5, respectively and a length of 100 nm. The NW had a radius of 236.5 nm and a length of 100 nm. For simulations with a silicon substrate, the substrate was 480 nm in thickness and extended through the simulation boundaries. Electric and magnetic field monitors as well as electric-field movie monitors were placed at the center of tube to provide a cross-sectional profile as well as a monitor that bisected the structure in the plane perpendicular to the \vec{k} of the excitation source. The electric and magnetic field monitors were used to extract line scans of the plasmonic response from both the surface and core of the NT and from the surfaces of the NW. The movie monitors provided a readily interpretable overview of how the plasmonic response evolved and decayed upon plane wave excitation. Theoretical mode spectra were extracted from the FDTD simulations by averaging 10 spectra collected at equidistantly spaced intervals along both the core and surface of the nanotubes.

5.4 Results and Discussion

As described in the Methods section, considerable effort went into optimizing the techniques used to collect accurate polarized bright-field and dark-field images and polarized dark-field scattered light spectra of the nanowire and nanotube regions of the gold NW/NT heterostructures. Numerous measurement sets were collected for different gold NW/NT heterostructures during the optimization of these procedures. While these data provide some qualitative insight into the plasmonic response of these structures as a function of incident polarization, their true value is the insight that they offer into how these measurement techniques were developed, tested, and optimized. It is for these reasons that they are included in the Appendix F. The results presented in this Results and Discussion section are were collected on a single gold NW/NT heterostructure with the optimized methods described previously.

5.4.1 FESEM Analysis of a Single Gold NW/NT Heterostructure

For the purpose of this study a representative single gold NW/NT heterostructure was selected and carefully imaged in a FESEM to characterize its physical structure so that its plasmonic response could be correlated to its dimensions to gain a clear fundamental understanding of mode character as a function of incident polarization. For the purpose of clarity, the single nanowire/nanotube heterostructure shall be referred to as “tube 1”.

Shown in Figs. 5.6(a) - (f) are FESEM micrographs of tube 1 at a 0° stage tilt at a working distance of 5.1 mm at magnifications of 37 kX, 100 kX, and 200 kX at an acceleration voltage of 5 keV (Fig. 5.6(a)-(f)), and with a stage tilt angle of 60° at a working distance of 29.6 mm at magnifications of 50.6 kX, 100 kX, and 150 kX, at 20 keV (Figs. 5.6(d)-(f)). Images taken with the 60° stage tilt were collected to more clearly observe the wall thickness at the tip of the tube.

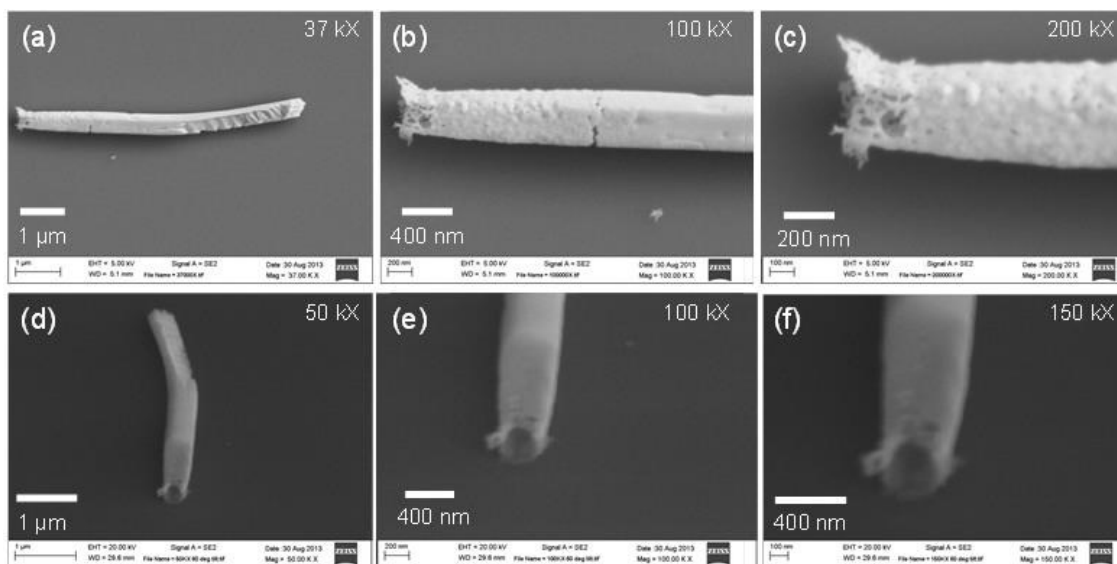


Figure 5.6. FESEM micrographs of gold NW/NT heterostructure “tube 1” taken on a flat stage (a-c) and at a tilt angle of 60° (d-f) at (a) 37 kX, (b, e) 100 kX, (c) 200 kX, (d) 50 kX, and (f) 150 kX.

From the FESEM micrographs the tube portion of the heterostructure can be identified by its darker appearance (see Fig. 5.6(d)-(f)), indicating a thinner structure due to less electron

density than the solid wire region. Additionally, the tube region has a greater surface roughness than the longer nanowire region. It is also noteworthy that the tube region is slightly tapered from where it is joined to the nanowire to the tip, where it becomes flaky and discontinuous.

Furthermore, it is evident that the tube is not truly cylindrical. These geometrical variations are expected to influence the plasmonic response of the structure, relative to the 'perfect' structures simulated in Chapter 2. Therefore, some discrepancies in the peak resonant wavelength and spectra width of the modes were expected between theory and experiment. However, the NW region served as a useful reference with which to compare the response of the NT region.

Additionally, the change in polarization response was the primary trend of interest for identifying ring-resonator localized surface plasmon resonances, rather than an absolute correlation between theory and experiment.

From ImageJ analysis of the FESEM micrographs taken with a flat stage it was determined that the gold NW/NT heterostructure is $6.29\text{ }\mu\text{m}$ in overall length, with a NT region of $1.63\text{ }\mu\text{m}$ in length and a NW region of $4.66\text{ }\mu\text{m}$ in length. The diameter of the NT region was 475 nm where it meets the wire and tapers to 382 nm at the tip. The NW region at its thickest point was 471 nm . From the FESEM micrographs taken with a stage tilt angle of 60° (see Fig. 5.6(d)-(f)), the wall thickness, inner diameter and outer diameter were measured by averaging twenty measurements collected along the perimeter of the NT face and correcting for the tilt angle. The NT wall thickness was found to be of $48 \pm 8\text{ nm}$, with an outer diameter of 300 nm , thus the inner radius was 102 nm and the outer radius is 150 nm .

5.4.2 Polarized True Color Bright-field and Dark-field Images and Analysis of Single NW/NT Heterostructures

Having established an optimized method for collecting polarized bright-field and dark-field images of single NW/NT heterostructures, a set true color bright-field and dark-field images of gold NW/NT heterostructure “tube 1” were collected under dual excitation and collection polarization varying from 0° to 90° with respect to the long axis of the structure in 10° increments (see Fig. 5.7). In this optimized method, the excitation polarizer (glass disc) and collection polarizer (plastic film) were fixed in the C2 condition (see Fig.5.1) and the incident polarization was varied by carefully rotating the sample in 10° increments on a micrometer stage mounted to the microscope stage (see Methods Section 5.3.3) By rotating the sample, experimental polarization bias of the measurement system is minimized as the polarization incident on the sample is varied.

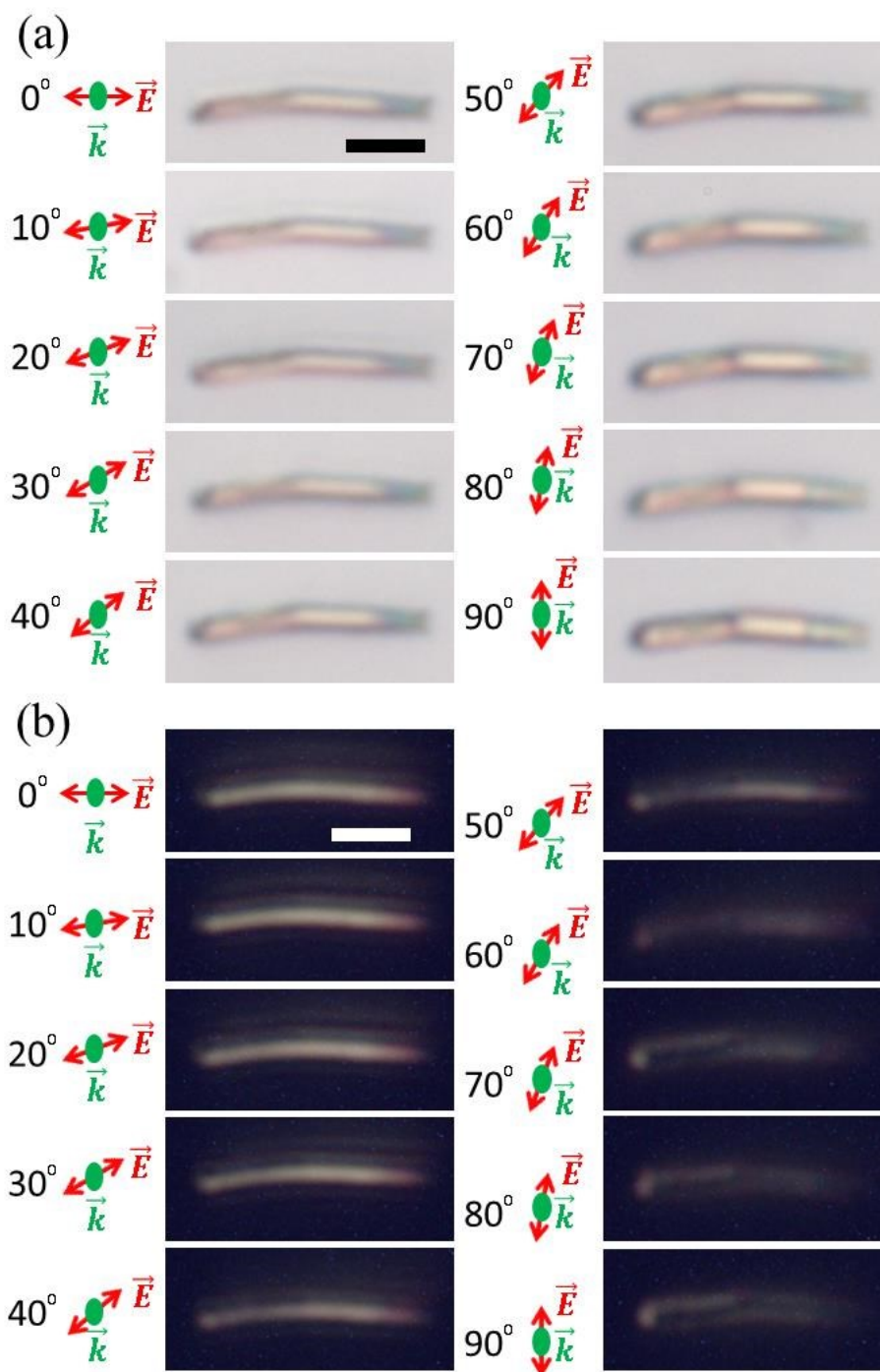


Figure 5.7. True color bright-field (a) and dark-field (b) images of gold NW/NT heterostructure "tube 1" for polarizations ranging from 0° to 90° in 10° increments with both excitation and collection polarizers fixed in the C2 condition and varying polarization by rotating the sample. Beside each image is a schematic of the excitation direction and polarization, where \vec{k} denotes the excitation propagation direction and \vec{E} denotes polarization of the electric field. All scale bars = 2 μm . Color available in electronic copy.

color, the un-damaged wire region was golden yellow, and the damaged/cleaved wire region was red in color. In contrast, the dark-field images exhibited significant changes in the scattered-light response of the gold NW/NT heterostructure (see Fig. 5.7). At 0° polarization, the “tube 1” gold NW/NT heterostructure exhibited a strong scattering along the entire length of the structure, with the wire region being bright gold/yellow in color, while the tube region was red. As the polarization incident on the structure was varied towards 90° , the scattering in the core of the structure, especially the tube region diminishes. Only a faint shadow or halo is visible around the perimeter of the structure while the core appears dark like the substrate. This suggests that as the polarization was shifted from 0° to 90° , the peak resonant energy of the structure is either red-shifted to a value beyond the spectral range of the CCD camera, and or that there is increased mode coupling to the substrate, which may result in the structure appearing transparent.

To more empirically understand the changes in the plasmonic response as a function of incident polarization an analysis of the percentage of red (R), green (G), and blue (B) pixels was conducted on both the NT and NW regions of true-color bright-field and dark-field images of the “tube 1” gold NW/NT heterostructure (see Fig. 5.8). In this analysis the percentages of R, G, and B pixels were determined as a function of incident polarization on blank regions of each image to establish background values (see Fig. 5.8(a) and (b)) for both the bright-field and dark-field images, respectively, and for both the NT (see Fig. 5.8(c) and (d)) and NT (see Fig. 5.8(e) and (f))

regions of the heterostructure (see Appendix F Section F1 for supporting measurements).

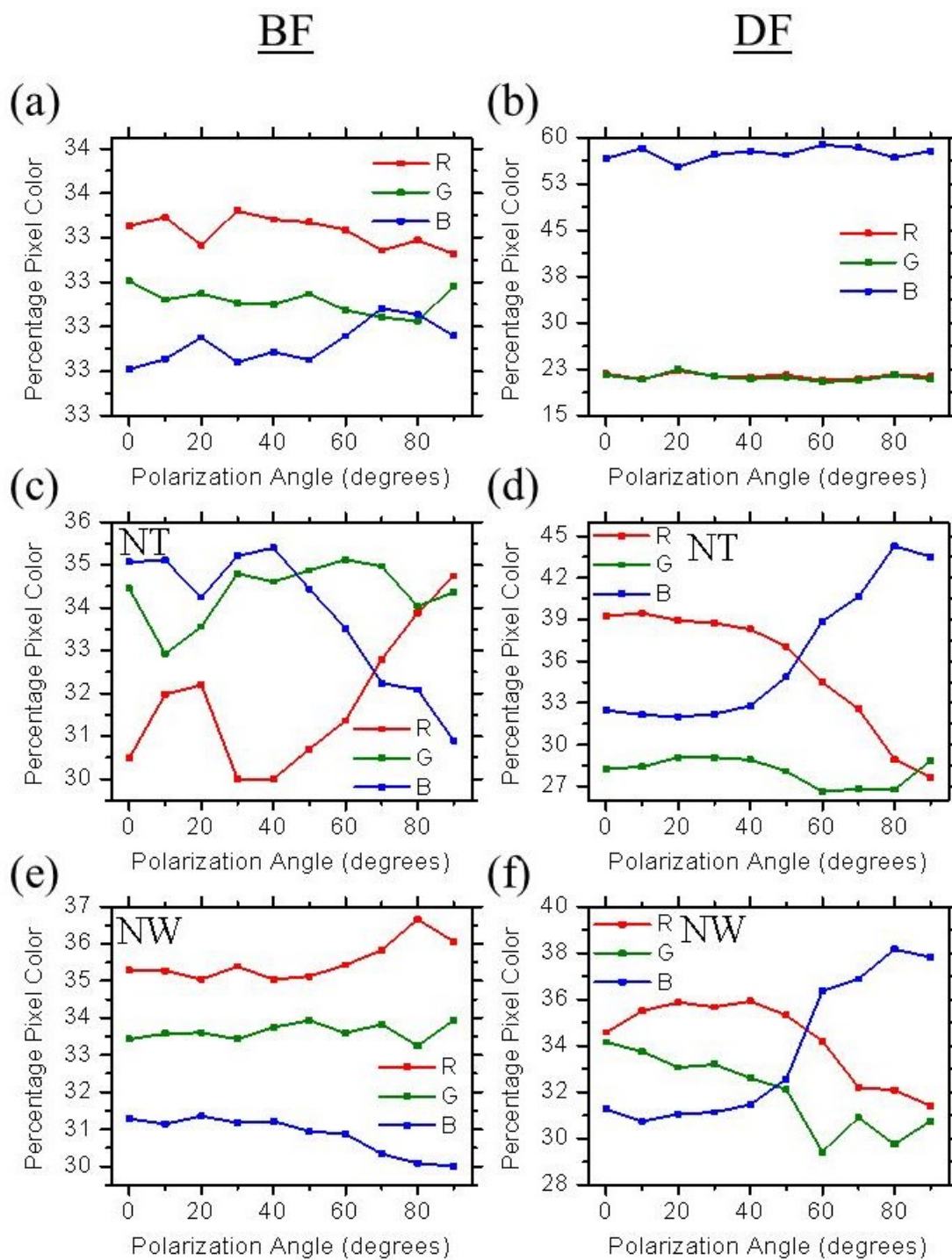


Figure 5.8 Percentages of red (R), green (G), and blue (B) pixels on a blank region of (a) & (b) shown in Fig. 5.7 (a,b) on the (c,d) nanotube region and (e,f) nanowire region of NW/NT heterostructure “tube 1” under as a function of incident polarization under bright-field (a,c,e) and dark-field (b,d,f) illumination. Color available in electronic copy.

The RGB analysis of the background or blank portion of each image as a function of incident polarization established a baseline value of the percentages of R, G, and B pixels in each image (see Fig. 5.8 (a) and (b)) and helped to interpret the resulting changes in the RGB pixel percentages in the NW and NT regions of the heterostructure. In both the bright-field and dark-field image sets, the background RGB pixel percentages remained constant as a function of polarization. In the bright-field image the percentage of R, G, and B pixels were virtually identical, all ranging from 33.1% to 33.6% from 0° to 90° polarization. This suggests that there was no bias in the background scattering with shifting polarization. In the dark-field images, the percentage of R, G, and B pixels remained roughly constant ranging (20 -22.5% for R and G, and 55 - 60% for B), but the percentage of blue pixels was significantly greater for all polarization angles. The greater percentage of blue pixels may be attributed to increased Rayleigh/Mie scattering cross-section as a function of decreasing wavelength.

The RGB analysis of the bright-field images of the nanotube region images (see Figs. 5.8(c)) shows a 5% increase in the percentage of r pixels from 30% to 35% with an accompanying decrease in the percentage of b pixels of similar magnitude (5%) from 35% to 30.5% on going from 0° to 90° polarization with respect to the long axis of the heterostructure. The increased in the percentage of R pixels with simultaneous decrease in the percentage of B pixels suggested that as polarization is varied from 0° to 90° , the mode energy decreases to a longer wavelength resonance. The G pixels percentage in the bright-field images of the nanotube region show no clear trend with polarization. The dark-field images of the nanotube region show slight decrease in the percentages of R and G pixels (<4%) and a significant increase in the percentage of B pixels (>10%) when polarization is varied from 0° to 90° (see Figs 5.8(d)). The decreases in the R and G pixel percentages and significant increase in the percentage of B pixels suggests a significant spectral shift to a longer, lower energy modes, which may be redshifted beyond the CCD camera detection limit. Such a significant red spectral shift along the length of

the NT heterostructure may also suggest the presence of localized surface plasmon modes, which are expected to couple more effectively to the substrate. Again, such effective substrate coupling may manifest the structure being more transparent in the appearance, as more of the mode energy is dissipated into the substrate.

The significant increase in the percentage of B pixels is attributed to the high percentage of B pixels in the background of the dark-field images (evident in Fig. 5.8(b)), which contributes more significantly to the image analysis as the NW/NT heterostructure became more transparent in appearance (see Fig. 5.7(b)). This background contribution is likely to have biased the results of the image analysis shown in Figure 5.8(b) and (d) at incident polarization angles greater than 60° , however it clearly demonstrates the significant change in the heterostructure's mode character.

The RGB analysis of the NW region (see Fig 5.8(e) and (f)) under bright-field illumination reveals minimal change in the percentage of all RGB components, with R pixels ranging from 35% - 36.5%, G pixels ranging from 33% - 34%, and B pixels ranging from 30% - 31%. In dark-field, the NW region shows slight decrease ($<5\%$) in the R and G percentages and a slight increase in the percentage of B pixels (6%). The decrease in R and G pixels is attributed to the change in mode character from a propagating SPP mode to a local resonant mode which couples to the substrate more effectively. The increase in the B pixels may be in part due to the increased contribution from the background as the structure becomes more transparent with increasing polarization, but may also be attributed to increased mode coupling and or the structure acting as a bulk reflector. Comparing the NW and NT, it is clear that they both exhibit similar behavior in the dark-field RGB analysis. However, the bright-field image analysis suggests that the NW may blueshift, unlike the NT, which appears to redshift. Moreover, it is likely that due to the lack of NIR sensitivity of the CCD used in this image analysis, that an

accurate understanding of the plasmonic response was gleaned from this true-color bright-field and dark-field image analysis.

In summary, the polarized -dependent true-color bright-field and dark-field images, and subsequent RGB analysis provide clear evidence that the optical response of NW and NT regions of NW/NT heterostructures changes significantly with incident polarization. At 0° polarization the NT region supports higher energy modes and as the polarization is shifted to 90° the mode energy and in-turn peak resonant wavelength redshifts. In contrast, the NW region exhibits a slight blueshift as the polarization is varied from 0 to 90, which may be attributed to the NW acting as a bulk reflector or changes in how it couples to the substrate.

5.4.3 Polarized Dark-field Scattered-Light Single Nanostructure Spectroscopy of Single Gold NW/NT Heterostructures

While a qualitative understanding of the optical response of gold NW/NT heterostructures was gleaned from polarized true color bright-field and dark-field imaging, clearer insight was gained by collecting polarized dark-field, scattered-light spectra of the NW and NT regions under 0° and 90° incident polarization. As with the polarized bright-field/dark-field imaging and analysis, there was considerable evolution in the method for collection of polarized scattered-light spectra of these structures. The spectra collected from numerous gold NW/NT heterostructures during this method optimization process are included in the Appendix of this chapter.

Optimized dark-field scattered light spectra of the nanowire and nanotube regions of the “tube 1” heterostructure were collected with dual excitation and collection polarization under the C2 condition (see Methods Section 5.3.5). The incident polarization was varied from 0° to 90° by physically rotating the sample on the microscope stage, as before. Dual polarization was used to

minimize bias from the microscope optics and polarization C2 was used to maximize signal throughput condition (see Appendix F). However, the most critical improvement made in this measurement set was ensuring that the structure was positioned truly parallel and perpendicular to the x-direction of the microscope stage (see Fig. 5.9), such that when the image of the heterostructure was projected onto the spectrometer CCD, it was truly parallel (see Fig. 5.9(a)) and perpendicular (see Fig. 5.9(b) and (c)) to the spectrometer input slits (see Appendix F Section F1). This made it possible to spatially select or ‘bin’ the region interest on either the NW (see Fig. 5.9(a) and (c)) or the NT (see Fig. 5.9(a) and (b)) on the gold NW/NT heterostructure with virtually identical sampling volume when it was rotated on the microscope stage. Additionally, having the structure truly parallel and perpendicular to the x-direction of the microscope stage ensured that the incident polarization was truly parallel (0°) or perpendicular (90°) to the long axis of the structure.

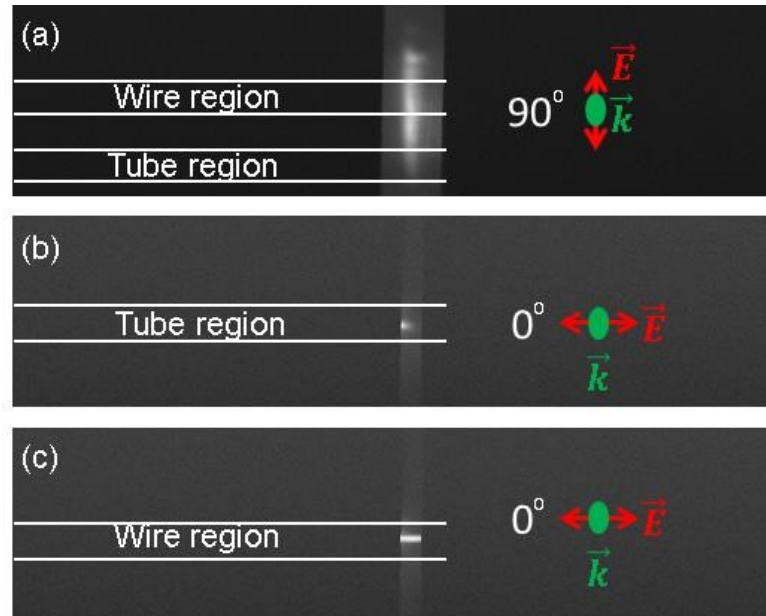


Figure 5.9. Spectrometer CCD images of gold NW/NT heterostructure “tube 1” when parallel (a) and perpendicular (b,c) to the spectrometer input slits with bounded regions schematically depicting the areas from which spectra of the nanowire (a,c) and nanotube (a,b) regions of the heterostructure were collected. Beside each image is a schematic of the excitation direction and polarization, where \vec{k} denotes the excitation propagation direction and \vec{E} denotes polarization of the electric field. Incident polarization with respect to the long axis of the structure is 90° in (a) and 0° in (b,c).

Dark-field spectra of the NW and NT regions of heterostructure “tube 1” under 0° to 90° incident polarization are shown in Figure 5.10(a) and (b), respectively. The NT region exhibited a significant red spectral shift of 97 nm (0.26 eV) from 623 nm at to 720 nm as the incident polarization was shifted from 0° to 90° (see Fig. 5.10(a)). The NW region exhibits a blue spectral shift of 87 nm (0.21 eV) from 756 nm to 669 nm as the incident polarization is shifted from 0° to 90° (see Fig. 5.10 (b)). These trends are in qualitative agreement with the RGB image analysis presented earlier in this section as well as the other sets of un-optimized spectra collected of “tube 2” presented Section F1 of Appendix F.

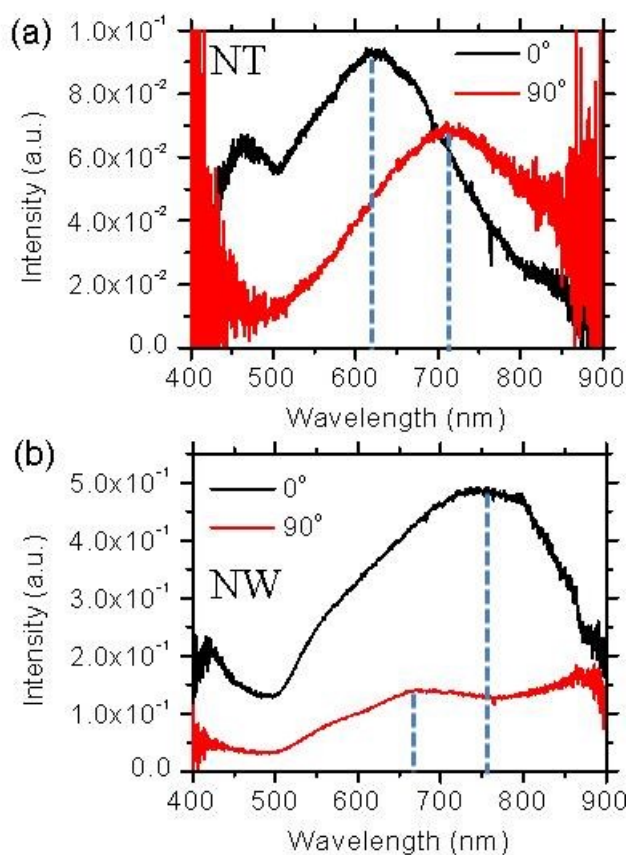


Figure 5.10. Dark-field scattered light spectra of the NT (a) and NW (b) regions of gold NW/NT heterostructure “tube 1” for 0° and 90° polarization with respect to the long axis of the structure (dual excitation and collection polarization in the C2 condition was employed). Color available in electronic copy.

5.4.4 Computational and Theoretical Analysis of the Plasmonic Response of Single Gold NW/NT Heterostructures as a Function of Incident Polarization

To fundamentally understand and de-convolute the photonic and plasmonic response of the NW/NT heterostructures an analytical analysis coupled with comprehensive theoretical simulations were conducted. Evidence that the tube region of the heterostructure supported ring-resonator-type localized surface plasmon resonances under 90° incident polarization was found when the spectral response of the NT region of “tube 1” was compared to the analytical nanoring-resonator model developed Apter *et. al* [115], as well as earlier simulations presented in Chapter 4 and additional simulations presented in this section.

The analytical nanoring-resonator model developed by Apter *et. al* was used to describe high-energy plasmon resonances in tubular metallic nanoshells and treated the nanoshells as insulator-metal-insulator (IMI) structures that has been bent into an annular shape, i.e., a ring resonator [116]. It was based on the dispersion relations of surface plasmons on planar insulator-metal-insulator (IMI) structures and predicted a red spectral shift of the ring resonance wavelength is a function of increasing outer circumference, in addition to wall thickness, a point which was not predicted by the hybridization model of Prodan *et al.* [149]. As discussed in Chapter 4, based on the model by Apter *et al.* the ring resonator modes occur when the surface plasmon wavelength (λ_{sp}) matches an integer fraction of the ring's effective perimeter ($P_{eff} = \pi(r_1 + r_2)$ where $r_1 = ID/2$ and $r_2 = r_1 + WT$) and can be calculated with the following equation [14]: $\lambda_{sp} = P_{eff}/m$ (1) where m is the mode of the resonance ($m = 1, 2, \dots$).

Based on the measured dimensions of “tube 1” (see Results and Discussion section titled “FESEM Analysis of a Single Gold Nanowire/Nanotube Heterostructure”), the calculated lowest order (where $m = 1$ ring-resonance for the structure occurred at 791 nm. The experimentally measured peak scattered light wavelength of “tube 1” under 90° incident polarization was 720 nm, which was within 9% of the calculated value. This was a good qualitative agreement between

theory and experiment considering that “tube 1” was not cylindrical, it was tapered, and the tip of the tube was discontinuous (as observed in the FESEM micrographs of “tube 1” in Fig. 5)). Additionally, it is likely that “tube 1” exhibited variations in wall thickness from the tip of the tube to where it met the nanowire region. Such dimensional variations will alter the plasmonic response relative to a tube or ring with a uniform wall thickness and inner diameter, and one that is truly cylindrical.

Finite-difference-time-domain (FDTD) electromagnetic simulations of a single gold NW and NT with representative dimensions to the NW and NT regions of the “tube 1” gold NW/NT heterostructure were conducted to characterize the optical response of a ‘perfect’ representative structure of “tube 1” without the geometrical variations and defects that the actual “tube 1” NW/NT heterostructure exhibited. FESEM analysis revealed that the NT region of the “tube 1” heterostructure had an average outer diameter of 428.5 nm with wall thickness of 48 ± 8 nm, and the NW region had an average outer diameter of 471 nm. The simulated NT was taken to have inner and outer diameter of 429 nm and wall thickness of 38.5 nm, respectively. The simulated NW had an outer diameter of 472.28 nm. Simulations were conducted of both individual NW and NT structures in air and on top of a silicon substrate in air. They were carried out with normal incidence plane wave excitation with 0° and 90° polarizations.

From the NT simulations, spectra of the magnitude of the total unpolarized electric field intensity versus wavelength were extracted from the surface (see Fig. 5.11(a,b) and core (see Fig. 5.11 (c,d)) of the NTs with and without a silicon substrate under both 0° (see Fig. 5.11 (a,c)) and 90° (see Fig. 5.11 (b,d)) incident polarization. Under 0° incident polarization, the core mode of the NT with and without a silicon substrate showed peak resonant wavelengths of 561.3 nm and 566.7 nm, respectively (see Fig. 5.11 (a)). Under 90° polarization, the core mode of the NT with and without a silicon substrate redshifted to a single peak resonant wavelength of 753.2 nm (see Fig. 5.11 (b)). The surface mode under 0° polarization exhibited peak resonant wavelengths of

556.1 nm and 566.7 nm, respectively (see Fig. 5.11 (c)). Under 90° polarization, the surface modes exhibited a doublet peak, instead of a single Gaussian resonance, and redshifted to peak resonant wavelengths of 601.0 nm and 607.1 nm (see Fig. 5.11 (d)).

Comparing the magnitudes of the red spectral shift of the NT core mode, upon varying incident polarization from 0° to 90° with and without a silicon substrate, redshifts of 191.9 nm and 186.5 nm were observed, respectively (see Fig. 5.11 (a,b)). In contrast, the red shift of the NT surface mode upon varying incident polarization from 0° to 90° with and without a silicon substrate exhibited much smaller redshifts of 45 nm and 40.4 nm, respectively (see Fig. 5.11 (c,d)). It is likely that the core mode of the NT was a photonic mode due to the large inner diameter, which was far too large for inter-wall surface plasmon mode coupling. Therefore, these simulated results suggested that the experimentally measured redshift in the NT portion of “tube 1” was largely a result of the change in energy of the photonic mode in the core.

The simulated results of the NT surface mode suggested that it could be attributed to a surface plasmon and that the redshift observed when polarization was varied from 0° to 90° , indicated that the mode type dramatically changed from a propagating SPP (as observed previously in Chapter 4) to a lower energy, localized surface plasmon resonance. This redshift under 90° polarization was consistent with the Ring Resonator Model [116]. However, there was not good agreement between the simulated values of the surface mode resonance under 90° polarization and both the experimentally measured resonance under 90° polarization and the calculated ring-resonance wavelength for this NT using the Ring Resonator Model [116]. The Ring Resonator model predicted a peak resonant wavelength of 791 nm for the structure, which was in reasonable agreement with the experimentally measured wavelength (720 nm), whereas the simulated value predicted surface plasmon mode energies ranging from 601.0 – 607.2 nm.

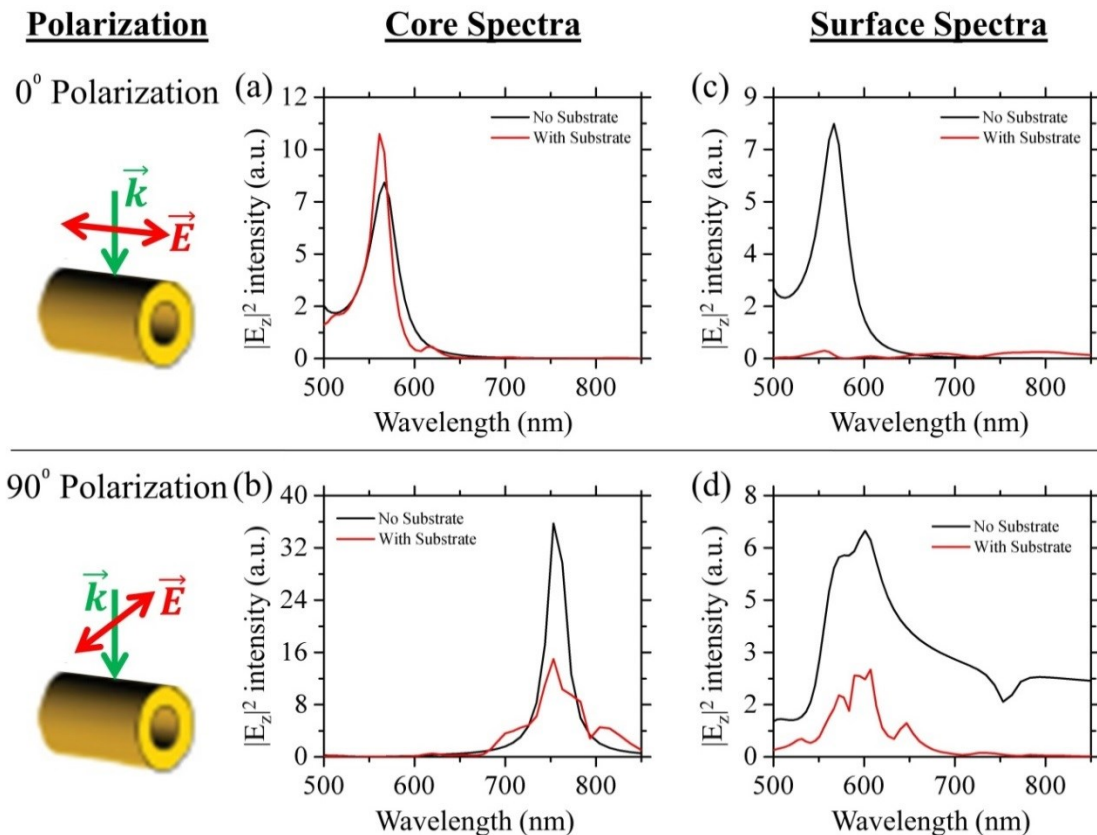


Figure 5.11. Simulated NT resonant spectra extracted from NT core (a,b) and NT surface (c,d) spectra under parallel (0°) (a,c) and perpendicularly (90°) polarized (b,d) under normal incidence broadband plane wave excitation. Inset at left are schematic representations of the normal incidence excitation conditions with 0° and 90° polarization. Color available in electronic copy.

While the simulated magnitude of NT surface plasmon resonance redshift with varying polarization from 0° to 90° did not correlate well with the calculated redshifted peak resonance of the Ring Resonator Model (or the experimentally measured value), the simulated cross-sectional (see Fig. 5.12(a-d) and Fig. 5.13(a-d)) and radial (see Fig. 5.12(e-h) and Fig. 5.13(e-h)) 2-D electric-field intensity profiles plotted at the peak resonant wavelengths of the core (see Fig. 5.12) and surface (see Fig. 5.13) modes of the NT under 0° and 90° polarization provided clear evidence that the NT supported a ring-resonator-type localized surface plasmon resonance under 90° polarization.

Figure 5.12 shows the cross-sectional (see Fig. 5.12(a-d)) and radial (see Fig. 5.12(e-h)) 2-D electric-field intensity profiles of the NT plotted at the peak resonant wavelengths of the NT core mode under 0° and 90° polarization (see Fig. 5.12(a,b,e,f) and Fig. 5.12(c,d,f,h), respectively), with and without a silicon substrate (see Fig. 5.12(b,d,f,h) and Fig. 5.12(a,c,e,g), respectively). The resonance shift of the core mode with varying polarization was discussed previously; however, from these profiles, it was clear that the core modes were primarily photonic in nature and existed under both 0° and 90° polarization. This was attributed to the large inner diameter of the structure (>400 nm), which is too large for inter-wall surface plasmon coupling to occur).

Figure 5.13 shows the cross-sectional (see Fig. 5.13(a-d)) and radial (see Fig. 5.13(e-h)) 2-D electric-field intensity profiles of the NT plotted at the peak resonant wavelengths of the NT surface mode under 0° and 90° polarization (see Fig. 5.13(a,b,e,f) and Fig. 5.13(c,d,f,h), respectively), with and without a silicon substrate (see Fig. 5.13(b,d,f,h) and Fig. 5.13(a,c,e,g), respectively). The resonance shift of the surface mode with varying polarization was discussed previously; however, these profiles clearly illustrated that a distinct localized surface plasmon resonance appeared only under 90° polarization without the presence of a photonic mode in the core. This surface plasmon resonance under 90° polarization was characteristic of a ring-resonator-type mode with nodal points around the ring's (or in this case, the NT's) effective perimeter. While at 0° polarization, it was expected that the NT surface would support a propagating SPP mode. This was observed and studied in Chapter 4. However, because the edges of the NTs extended beyond the simulation boundary, it may have prevented the direct excitation of the propagating SPP mode under 0° polarization.

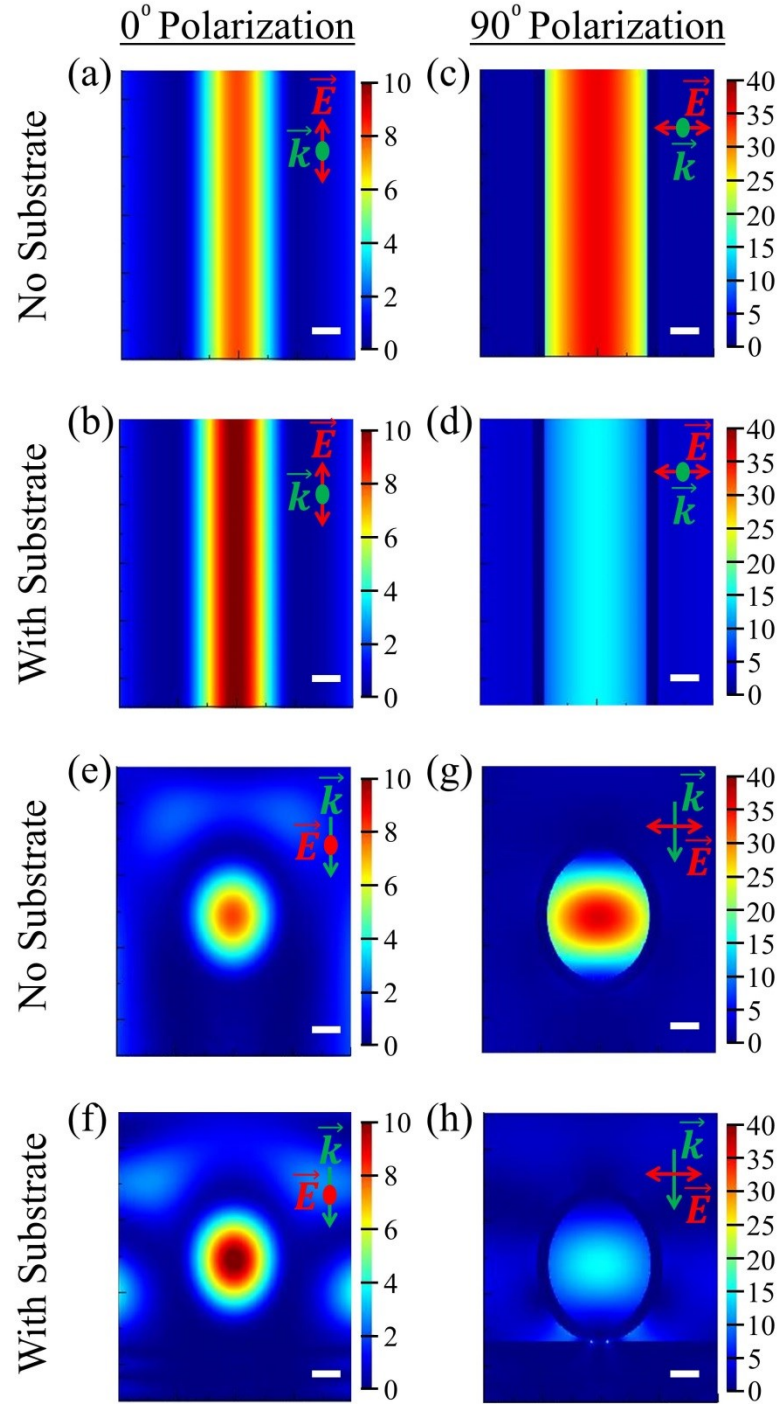


Figure 5.12 Cross-sectional (a-d), and radial (e-h), 2-D electric-field intensity profiles plotted of the NT at the peak resonant wavelengths of the core mode under 0° (a,b,e,f), and 90° (c,d,f,h) incident polarization, with (b,d,f,h) and without (a,c,e,g) a silicon substrate.

The inset in each profile is a schematic of the excitation direction and polarization, where \vec{k} denotes the excitation propagation direction and \vec{E} denotes the polarization of the electric field. All scale bars = 100 nm. Color available in electronic copy.

In conjunction with the trends in core and surface mode wavelengths as a function of polarization, the presence of a silicon substrate in the simulation significantly decreased the relative mode intensity from simulations without a substrate, especially under 90° polarization. This was evident in the core and surface mode spectra (see Fig. 5.11), where three out of the four plots showed that the simulations with a silicon substrate exhibited peaks of significantly lower intensity compared to those from simulations without a substrate. The exception to this trend was the case of the core mode under 0° polarization with the presence of a substrate which may be due to interference effects between the core mode and reflected electric fields from the substrate. This difference in relative mode intensity was also evident in the 2D cross-sectional and radial electric field profiles plotted at the peak resonance energy of the core (see Fig. 5.12(b,d,f,h) and Fig. 5.12(a,c,e,g), respectively) and the surface (Fig. 5.13(b,d,f,h) and Fig. 5.13(a,c,e,g), respectively) modes. From these profiles, the magnitude of the electric field intensity (indicated by the color-bar scale) showed a significant decrease in the presence of the silicon substrate, most significantly under 90° polarization. This increased mode coupling to the substrate, in conjunction with the red spectral shift of both the core and surface modes as polarization was varied from 0° to 90° were the likely reasons why the NW/NT heterostructure structure appeared transparent in the true-color dark-field scattered-light images (see Fig. 5.7) under 90° polarization.

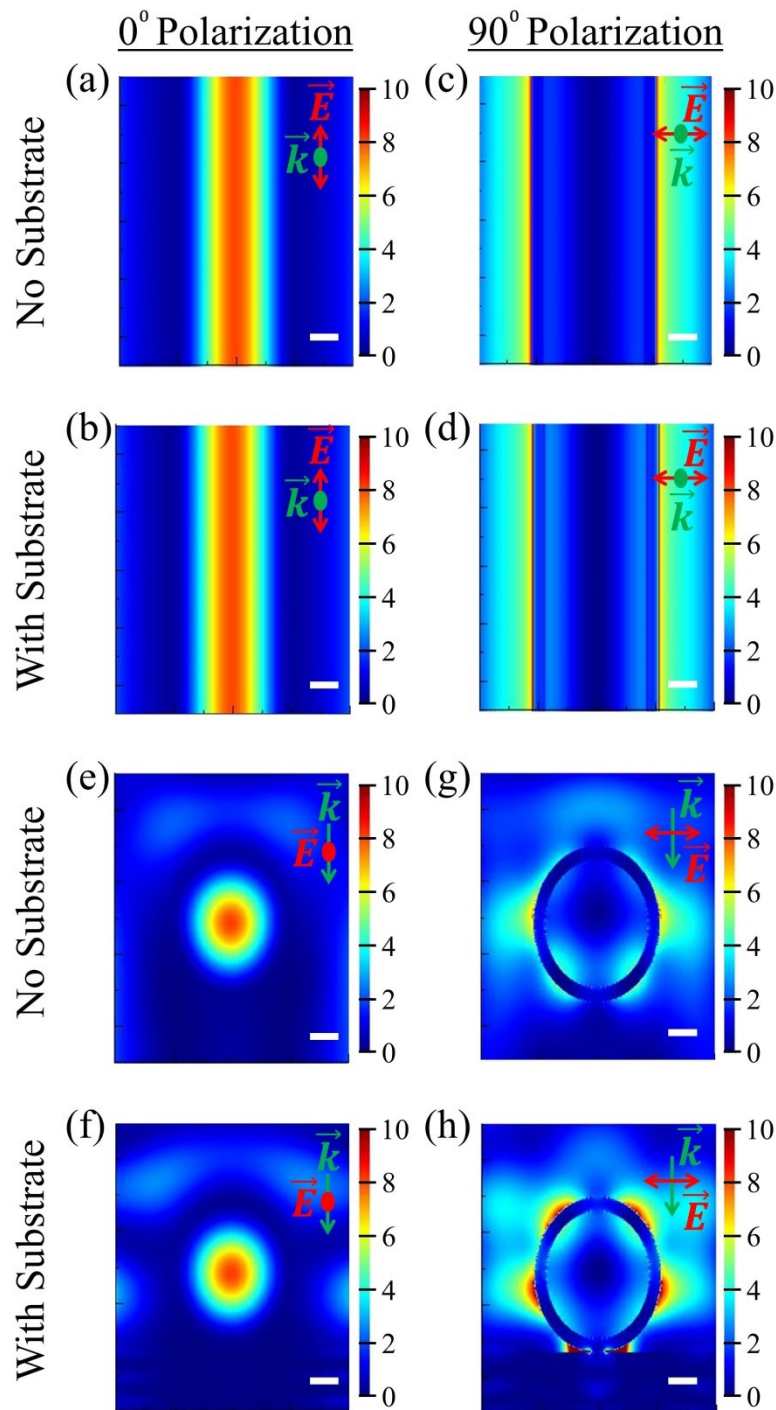


Figure 5.13 Cross-sectional (a-d), and radial (e-h), 2-D electric-field intensity profiles plotted of the AuNT at the peak resonant wavelengths of the surface mode under 0° (a,b,e,f), and 90° (c,d,f,h) polarization, with (b,d,f,h) and without (a,c,e,g) a silicon substrate. The inset in each profile is a schematic of the excitation direction and polarization, where \vec{k} denotes the excitation propagation direction and \vec{E} denotes polarization of the electric field. All scale bars = 100 nm. Color available in electronic copy.

Additional simulations of single NW structures with geometry representative of the NW region of the fabricated “tube 1” gold NW/NT heterostructure were also conducted under 0° and 90° incident polarizations. As there was not a cavity or core, as in the case of the NT, only a surface mode was analyzed. As a function of varying incident polarization from 0° to 90° no change in the NW surface mode spectrum was observed without a substrate (see Fig. 5.14), indicating that the NW acted as a bulk reflector. This behavior was likely due to the fact that the NW had a radius of >400 nm, which was significantly greater than the optical thickness of Au metal. Therefore, it was expected that the experimentally observed blueshift in the NW region of the “tube 1” NW/NT heterostructure was likely due to a substrate coupling effect, which will be explored further in the future through additional simulations.

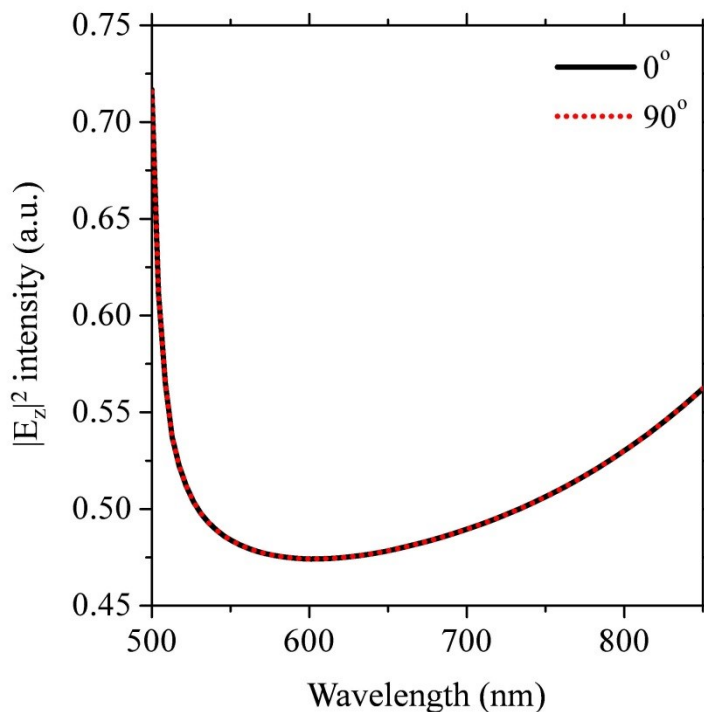


Figure 5.14. Simulated surface mode spectra of the NW without the presence of a silicon substrate under parallel (0°) and perpendicularly (90°) polarized normal incidence broadband plane wave excitation.

5.5 Conclusion

The optical response of both the NW and NT regions of single gold NW/NT heterostructures was elucidated through collection and analysis of polarized true-color bright-field and dark-field images, polarized single-nanostructure dark-field scattered light spectroscopy, and comprehensive full-field electromagnetic simulations. RGB and grayscale analysis of the polarized true-color bright-field and dark-field images showed that as incident polarization was varied from 0° to 90° , the structure became transparent in appearance, suggesting a spectral shift to lower energy, longer wavelength modes and increased mode coupling to the silicon substrate. These changes suggested that the longer wavelength scattered light under 90° polarization may be a result of localized resonant modes rather than propagating modes.

Polarized single nanostructure dark-field scattered light spectroscopy further elucidated this change in optical response with varying polarization and revealed that the scattered light spectra of the NT region redshifted by 0.26 eV (97 nm) from 0° to 90° incident polarization and the wire region blueshifted by 0.21 eV (87 nm), indicating that the tube region supported a lower energy, longer wavelength local resonance. Such lower energy modes are characteristic of localized surface plasmon resonances.

To more fundamentally understand the optical response of the NW and NT portions of the NW/NT heterostructures, full-field-electromagnetic simulations of individual NWs and NTs (with dimensions comparable to those of the fabricated structures that were characterized experimentally) were carried out under 0° and 90° incident polarizations, with and without the presence of a silicon substrate. These simulations provided clearest clear understanding of the experimentally observed spectral response of both the NW and NT. The simulations revealed that NTs supported both a photonic mode in the core and a surface mode, which redshifted on going from 0° to 90° polarization. With the presence of a silicon substrate, the photonic mode in the core and the surface mode redshift by 0.56 eV and 0.13 eV, respectively, when polarization was varied

from 0° to 90° . Therefore, the simulations indicated that the experimentally measured red spectral shift in the dark-field spectrum of the NT region resulted primarily from a decrease in the photonic mode energy upon polarization being varied from 0° to 90° . Additionally, the simulations provided compelling evidence that NTs can support ring-resonator-type surface plasmon modes. The NW simulations revealed that there was negligible change in the optical response of the structure with varying incident polarization. The experimentally observed blueshift was attributed to surface coupling. As described previously, this will be further investigated in the future through additional simulations.

To further de-convolute the photonic and surface plasmon modes it is proposed that additional simulations could be carried out to probe the far-field scattered field only. The simulations presented in Chapter 4 and in this chapter were designed to probe the total near-field response of the structures. However, by simulating only the scattered field using a “total-field-scattered-field” simulation, it is expected that only the surface plasmon modes would be detected. This simulation approach may provide a more direct comparison with the measured dark-field scattered-light spectra.

The ability to tune the photonic and plasmonic response as a function of geometry (inner diameter, wall thickness, and length), as well as varying incident polarization make these NW/NT heterostructures candidates for applications as resonator cavities for coherent subwavelength emitters as well as tunable low-loss metal electrodes. In fundamentally elucidating the optical response of these tubular metallic nanostructures, a structure can be optimized and tuned for a specific application. Through this theoretical and experimental study, the first evidence that a nanotube of this size (~ 400 nm outer diameter) can support ring-resonator-type localized surface plasmon modes has been presented. These resonant modes may have utility in numerous subwavelength optoelectronic applications as well as chemical or refractive index sensing.

6 Summary and Future Work

6.1 Preface

This chapter is intended to provide both a summary of the work presented in Chapters 2-5 of this thesis and a roadmap for future research based on this work. It has been broken down into two sections, one covering the planar thin film semiconductor-metal-insulator (SMI) waveguides presented in Chapters 2 and 3, and the other covering the tubular metallic nanostructures presented in Chapters 4 and 5.

6.2 Planar Thin-Film Semiconductor-Metal-Insulator Waveguides

In Chapter 2, a comprehensive set of dispersion relations were solved for a planar asymmetric F8BT-Ag-SiO₂ (SMI) waveguide over a range of metal film thicknesses, and for three dielectric constant conditions. These solutions provided the basis for the experimental study presented in Chapter 3. Unlike the majority of dispersion relations presented in the literature, the set that were solved included those where all three layers of the waveguide were treated as “real” materials, i.e., with complex dielectric constants. While this was more computationally intensive it allowed dispersion relations of the SMI waveguide to be solved under representative conditions of steady state and stimulated emission regimes of the F8BT emitter and accurately accounted for absorption loss in all three layers of the waveguide.

The solutions of these dispersion relations demonstrated that by tuning metal film thickness, and the emission regime of the organic semiconductor, a significant fraction of surface plasmon polariton mode amplitude could be leaked into the active semiconductor layer, thereby decreasing the amount of optical energy trapped by the metal. At visible wavelengths, mode leakage increased by factors of up to 3.8 and 88 by tuning metal film thickness and by addition of gain, respectively. This enhanced SPP field leakage and increased propagation length may lead to

the ability to mitigate surface plasmon losses at metallic electrodes in organic optoelectronic devices such as OLEDs and organic lasers, thereby increasing the light outcoupling efficiency.

Chapter 3 provided experimental corroboration of the theoretical results presented in Chapter 2 through the fabrication and optical characterization of a set of glass/PFO/Ag/glass ISMI waveguides with varying Ag metal film thickness. Excitation pump power-dependent emission spectra of these waveguides were collected over a range of pump power densities and their resulting emission intensity, FWHM, ASE threshold, slope efficiency, and peak emission wavelength were studied as a function of Ag film thickness. These experimental results provided corroboration of the theoretically predicted trend in the efficiency of semiconductor-SPP coupling as a function of metal film thickness. It was experimentally observed that the ISMI waveguide which exhibited the greatest emission intensity, lowest ASE threshold and greatest slope efficiency had an Ag metal film thickness of 45 nm, which correlated very well with the theoretically predicted Ag film thickness of 47 nm for which SPP mode propagation length and penetration depth were at a maximum.

While there was good agreement between theory and experiment, the dispersion relations presented in Chapter 2 were solved for the organic semiconducting polymer F8BT, not PFO, which was used in the experimental work (PFO was chosen for the experiments due to limitations in the available laser pump excitation wavelengths). In the future, it is of importance to solve the set for the exact polymer used in the experimental work. However, it is expected that the results would be quite similar because of the similar optical constants of the two polymers.

An additional considerations for future experimental validation of the theoretical results presented in Chapter 2 is a more comprehensive characterization of the layers comprising the ISMI waveguides. Starting with the Ag metal film, accurate thickness and roughness measurements should be carried out over the range of Ag metal film thicknesses used in the ISMI waveguides. Knowing the thickness and roughness may aid in making a clearer correlation to the

theoretical results and potentially account for additional losses in the fabricated structures due to defects and/or discontinuities in the films. Surface roughness is a key consideration, especially if the studied range of metal film thickness was expanded to films < 35 nm, which may become discontinuous and exhibit ‘islands’ of metal, which may alter the plasmonic response. Polymer layer thickness and roughness is also a consideration that must be taken into account. While absorption spectra show that the spin cast layers of neat PFO are uniform, the edges of the samples, where the pump power-dependent waveguide emission spectra were collected exhibited significantly different relative intensities. This suggested that there was a distribution of thickness of the polymer film covering the glass substrate, or the polymer film was damaged during the polishing process; either of which could significantly bias the measurement.

However, in total, three sets of ISMI waveguides were fabricated and measured over the course of this thesis and the overall trend in their emissive properties was clear in all three sample sets. Some of the disparities between the sample sets could manifest from non-uniformity of the polymer thin film or sample edge defects caused during polishing. Additionally, the fabrication of the ISMI waveguides required bonding of the glass superstrate to the PFO thin film that was spin cast onto the Ag metal film. The bonding process, which was conducted manually, entailed depositing a small (unmeasured) quantity of Norland Optical Adhesive (NOA-63) onto the PFO film followed by pressing the glass superstrate onto the drop of adhesive such that it covered the entire PFO film. The epoxy thin film was then cured by exposure to UV light. While the refractive index of the epoxy was very similar to the glass superstrate, the layer thickness, uniformity, and range across the entire sample set was not known. Additionally, it was not known if the manual pressure applied during the bonding process altered or damaged the PFO and Ag thin films. Therefore, in future related experiments, it may be important to investigate the epoxy layer thickness and uniformity, as well as to collect emission spectra of SMI waveguides without the use of a glass superstrate. The latter would be challenging because organic semiconducting

polymers photo-oxidize in air and can be damaged by the highly focused laser pump source used in the collection of waveguide emission measurements. Furthermore, the theoretical dispersion relations presented in Chapter 2 suggested that the SPP leakage can extend to distances much greater than the 100 nm PFO emitter film thickness - distances in excess of 74 μm . Therefore, gain spectra collected from true SMI waveguides (without a bonded superstrate layer) may vary significantly due to changes in reflection and interference within the SMI layer stack.

In conjunction with improved ISMI waveguide characterization, the next and perhaps more challenging step is the fabrication and optical characterization of ISMI waveguides with polymer films with different molecular dipole orientations. In Chapter 3, a considerable effort was made to determine the molecular dipole orientation of PFO films processed in different ways in order to develop PFO films with different molecular dipole orientation. Extensive characterization of PFO films processed with different techniques was carried out through GISWAXS measurements made at Brookhaven National Lab. Many of the PFO thin films that were prepared exhibited the presence of small (nanometer scale) polymer crystallites, which may induce scattering and be undesirable for applications in a waveguides. However, the as-spin-cast or 'neat' PFO film exhibited no crystallinity but had a large percentage of the molecular dipoles in an in-plane orientation. Additionally, a completely amorphous PFO film with equal in- and out-of-plane molecular dipole orientation was prepared and characterized. Chapter 3 presented the experimental results of ISMI waveguides prepared with neat PFO films with preferential in-plane molecular orientation, and the next logical step would be to fabricate a matching set of waveguides with completely amorphous PFO films.

Comparing the neat PFO to the amorphous PFO, it is expected that the neat films would couple less effectively to SPP modes due to the fact that molecular dipoles oriented parallel to the plane of the polymer-metal interface are expected to be damped by their own image on the metal surface [31,106]. In contrast, the amorphous films, which have a higher percentage of out-of-

plane-oriented molecular dipole emitters, are expected to couple more effectively to SPP modes because dipoles oriented perpendicularly to the plane are expected to directly couple to SPP modes. While it is premature to speculate on the outcome of how varying the molecular dipole orientation of the polymer film will affect the emissive properties of the ISMI waveguides, it is an important set of experiments to conduct to fundamentally understand how to optimize and tune SPP-polymer emitter coupling.

However, fabrication of ISMI waveguides with amorphous PFO films also presents new fabrication challenges, not faced with the as-spin-cast 'neat' PFO. The basic fabrication method of the neat PFO ISMI waveguide entailed the thermal evaporation of the Ag metal film onto a glass substrate followed by spin casting the PFO film atop the Ag metal and epoxy bonding the glass superstrate onto the PFO layer. To produce the amorphous PFO, the film had to be heat treated in an inert atmosphere at temperatures in excess of 280° C. Consequently, if the PFO film was deposited onto the Ag metal thin film and heat treated, it is likely that at 280° C the Ag metal film roughness would increase due to the difference in surface energies between the Ag and glass substrate. This may be especially problematic for thin Ag metal films (< 35 nm), which could rapidly become discontinuous if heat treated. Increased metal roughness and discontinuities in the metal films may significantly alter the emissive properties of the waveguide and alter the SPP-polymer emitter coupling that occurs at the metal-semiconductor interface.

Alternate paths to produce ISMI waveguides with amorphous PFO films have been considered, however, there are other pitfalls that may be encountered. The secondary path that has been considered is spin casting of the polymer thin film on the bare glass superstrate, followed by heat treatment to produce the amorphous film. The Ag metal film would then be thermally evaporated directly onto the amorphous PFO thin film followed by epoxy bonding of the glass substrate onto the Ag metal film. The concerns posed with this fabrication path are (i) the metal film roughness, which may be impaired by the heat treated polymer film, and (ii) the

epoxy layer would be between the Ag metal film and the glass substrate, not the glass superstrate and the PFO film as in the case of the neat PFO ISMI waveguides studied in Chapter 2. Both key concerns could influence the emissive properties of the waveguides and also make it difficult to make a valid comparison to the previously studied neat PFO ISMI waveguides. However, a neat PFO sample could be prepared in an analogous fashion to make a comparison. Therefore, an optimal fabrication method for the amorphous PFO ISMI waveguides will have to be developed and the validity of comparing them to the previously studied neat PFO ISMI waveguides must be assessed.

Beyond the exploration of different polymer molecular dipole orientations, to fully understand if plasmon-polymer emitter coupling is a benefit or a hindrance to the optical performance of optoelectronic devices, it is suggested to fabricate additional sets of such ISMI waveguides with other semiconducting light-emitting polymers with either emission that directly overlaps with the SPP mode energies supported by the device or emission far from the SPP mode energies. This may shed further insight into how to effectively build devices for different applications where SPP coupling is either desired or needs to be completely mitigated. Moreover, this may provide further insight into whether direct coupling to SPP modes provides a benefit to the device performance.

To further understand the SPP propagation and mode leakage as a function of metal film thickness, molecular dipole orientation, and polymer emission energy overlap with the SPP mode energies, additional measurement techniques should be investigated. As described in the Introduction section of Chapter 3, the optical characterization of ISMI waveguides via collection of gain measurements provides only indirect evidence of the interactions taking place between the semiconductor emitter and the SPPs. Therefore, to more directly measure and characterize the plasmonic response, polarized gain spectra could be collected, where both the excitation and emission polarizations of the waveguide are controlled and analyzed. However, this would

require alternative excitation geometry to what was used for the gain spectra presented in Chapter 2, where excitation was incident on the sample normal to the plane of the waveguide. One solution would be to end-fire couple the laser pump source into the waveguide such that the excitation direction is parallel to the plane of the waveguide; however, this may require that the sample be of much smaller geometries such that there is sufficient outcoupled edge emission from the opposite end of the waveguide from which it is excited. It would also be of great value, albeit challenging, to more directly measure and observe the SPP mode propagation through the use of a Kretschman- or Otto-type coupling apparatus, where a direct and tangible metric of SPP propagation length could be made.

6.3 Tubular metallic Nanostructures

In Chapter 4, large-area arrays of gold nanotubes were synthesized via electrodeposition and selective pore widening of nanoporous alumina templates with large (~ 200 nm) inner diameter and varying wall thickness (30 to 140 nm) and optically characterized as a function of wall thickness. Both large-area arrays as well as single nanowire/nanotube heterostructures were studied via true-color bright-field and dark-field image analysis and dark-field scattered light spectroscopy. Unpolarized scattered-light spectroscopy of large-area gold nanotube arrays in end-on excitation configuration indicated that resonant scattering at visible wavelengths red shifts by 0.08 eV (28 nm) with decreasing nanotube wall thickness from 140 to 30 nm. Unpolarized scattered-light spectra were collected with normal excitation (perpendicular to the long-axis of the structure) along a tapered single nanowire/nanotube heterostructure to more accurately measure the apparent red shift without in-homogenous broadening arising from a distribution of nanotube wall thickness in the large area arrays. The redshift measured along the nanowire/nanotube heterostructure was 0.39 eV (100 nm).

Full-field 3-dimensional electromagnetic simulations were carried out on single nanotubes of varying wall thickness and inner diameter to more fundamentally understand the plasmonic response as a function of decreasing wall thickness and inner diameter. Simulations show that at the large size regime (inner diameter ~ 200 nm) that were synthesized supported propagating surface plasmon modes as well as surface plasmon ring resonances at visible wavelengths (the latter is observed only for excitation directions normal to the nanotube long axis with transverse polarization). The energy of the surface plasmon modes decreased with decreasing wall thickness and was attributed to an increased in mode coupling between propagating modes in the nanotube core and outer surface and the circumference dependence of ring resonances. Surface plasmon mode propagation lengths for thicker-walled tubes increased by a factor of ~ 2 at longer wavelengths (> 700 nm), where ohmic losses in the metal are low, but thinner-walled tubes (30 nm) exhibited a more significant increase in surface plasmon propagation length (by a factor of more than four) at longer wavelengths. Additionally, nanotubes in this size regime support a photonic mode in their core, which did not change in energy with changing wall thickness. However, photonic mode propagation length was found to decrease for optically thin walls less than 60 nm. Finally, correlations were made between the experimentally observed changes in dark-field spectra and the changes in surface plasmon mode properties observed in simulations for the various gold nanotube wall thicknesses, inner diameters, and excitation conditions.

One key aspect that this body of work did not account for were additional plasmonic phenomena potentially occurring in large-area arrays of densely packed nanotubes. It is expected that if the nanotubes in a large-area array are in sufficiently close proximity to each other (< 30 nm), additional coupled SP resonances or SPPs will occur within the gap between the tubes. Such resonances may further enhance the plasmonic response of the nanotube arrays and in-turn alter the peak resonant intensities and energies that were measured compared to those for single nanostructures. Considering that the large-area arrays of AuNTs were fabricated with an

electrochemical growth process in porous anodic alumina templates with non-periodic pores, it is currently unclear what the actual distribution in spacing between adjacent nanotubes is. These distances merit further study if these large-area arrays of tubular metallic nanostructure are to be used as patterned electrodes because optimizing the array may allow further tailoring of the overall plasmonic response.

Geometrical variation in nanotube wall thickness and inner diameter has been shown to cause inhomogeneous broadening of the plasmonic response of the large-area arrays. Furthermore SEM micrographs collected of individual nanotubes showed that the nanotubes were relatively tapered and that the ends of the nanotubes were often jagged, flaky, and discontinuous. The simulations of single nanotubes that were carried out were of structures with a fixed inner diameter and were perfectly cylindrical. Therefore, the simulations did not account for the taper, non-cylindrical shape, and or other nanotube structural defects. While there was good qualitative agreement between theory and experiment, such structural variations may induce increased loss or alter the plasmonic response of both individual nanotubes and large-area arrays of nanotubes. Additionally, based upon the synthesis method, the nanotubes were expected to be polycrystalline, which may have resulted in increased surface roughness and or defects, and, in turn, have reduced the actual SPP propagation length and coherence. In the thesis, no comprehensive study was made on the effect of surface roughness or morphology of the metal on the dark-field spectra.

In conjunction with the need to further understanding the plasmonic response of the large area arrays and the geometrical non-uniformities of these metallic nanotubes, Chapter 4 did not experimentally address the plasmonic response of tubular metallic nanotubes with varying inner diameter. However, simulations presented in Chapter 4 do provide evidence that agrees with the current literature in that there is a high degree of tunability of the plasmonic response by varying inner diameter. The majority of published experimental studies characterized metal nanotube

structures with significantly smaller inner diameters (<30 nm) compared to those in this work (~ 200 nm). Therefore, there may be utility in fabricating additional arrays of nanotubes with intermediate inner diameters ($30 \text{ nm} < \text{ID} < 200 \text{ nm}$) beyond the quasi-static regime to understand how the resonance changes with increasing inner diameter. Furthermore, in this intermediate range of inner diameters, it is expected that as the ID increases, the tube will be able to support a photonic mode in the core at a given inner diameter, similar to what was observed in the simulations of large 200-nm-ID AuNTs presented in Chapter 4. Further experimental studies of AuNTs with inner diameters above and below the photonic mode cut-off may be useful to further understand the utility of these structures as patterned electrodes for visible-light-based optoelectronics to improve light outcoupling efficiency.

Chapter 5 presented a comprehensive theoretical and experimental study of gold nanowire/nanotube heterostructures to investigate the presence of ring resonator-type surface plasmon modes. Through polarized bright-field and dark-field imaging, and polarized single nanostructure dark-field scattered light spectroscopy, the optical response of these structures was characterized and the first experimental evidence that these large 200 nm inner diameter gold nanotubes support ring resonator-type surface plasmon modes was observed under normal incidence with polarization perpendicular to the long axis of the structure (90°). It was found that single nanotubes support both a photonic mode in their core and surface plasmon modes on their surface under both parallel (0°) and perpendicular (90°) polarization. When polarization was shifted from 0° to 90° with respect to the long axis of the heterostructure, the nanotube ceased to support propagating SPP modes and supported a lower-energy resonant mode characteristic of a ring-resonator-type localized surface plasmon resonance. In addition, the photonic mode in the core of the nanotube was found to redshift when polarization is varied from 0° to 90° . The nanowire region of the heterostructure did not exhibit a significant change in mode type or energy

with varying polarization. This was attributed to the large diameter (> 400 nm), which resulted in the nanowire region effectively acting as a bulk reflector.

With the knowledge of how to tune the nanotube geometry (WT and ID) to provide a specific resonant energy (Chapter 4), and the ability to control the surface plasmon resonant type (Chapter 5), the groundwork has been laid to explore the viability of using individual nanotubes as plasmonic or optical resonator cavities. To do so, it is proposed to either in-fill the core or clad the surface of a nanotube with an organic semiconducting light-emitting polymer. Such a structure could be designed to act as plasmonic resonator cavity, analogous to that used in a conventional light laser to provide stimulated emission of surface plasmons, towards the development of a subwavelength plasmonic laser, or “SPASER” (Surface Plasmon Amplification by the Stimulated Emission of Radiation). Additionally, if the nanotube geometry is tuned to exhibit leaky propagating SPP modes, it may provide a means of mediating efficient/low-loss excitonic energy transfer across the semiconductor-metal interface.

Practical fabrication routes for the creation of polymer in-filled or clad tubular metallic nanostructures have not been researched in detail, however, some preliminary paths have been considered. The most facile means of preparing nanotubes in-filled with a polymer is to grow a large-area array of metallic nanotubes and leave the nanotubes within the anodic alumina template in which they were electrochemically grown. Then, a layer of polymer could be deposited on top of the template containing the nanotubes via spin-casting, drop-casting, or simply placing a thick film on top of template. Then by heating the template and polymer film, and applying pressure to the top surface, the melted polymer may wick into the cores of the nanotubes. Other proposed techniques include submerging a free-standing large-area array of nanotubes (without the alumina template) in a dilute solution of the polymer emitter and through solvent evaporation a cladding on the inner and outer surfaces of the tubes may be formed. Alternatively, the nanotubes could be liberated from the template (as described in Chapter 5) and

placed in solution, where a precipitation or co-precipitation technique could be utilized to discretely encapsulate and or in-fill individual nanotubes with a semiconductor material. In a similar fashion to the gain spectra of ISMI waveguides presented in Chapter 3, such measurements could be collected from large-area arrays or solutions of clad/in-filled metallic nanotubes of varying geometry and the resultant emission could provide further insight into plasmon-polymer emitter coupling. Single nanostructure spectroscopy could also be conducted (as done in Chapter 3) to measure the plasmonic response of individual clad/in-filled nanotubes as a function of excitation geometry and polarization. Such optical measurements collected on clad/in-filled large-area arrays or discrete metallic nanotubes may also provide further evidence that large inner-diameter nanotubes can be regarded as ‘rolled-up’ IMI-type waveguides and may exhibit a similar trend in plasmonic response as a function of metal film thickness as the planar asymmetric SMI or ISMI waveguides.

Appendix A.

Appendix A is broken into two sections A1 and A2. A1 presents the Mathematica Code used to reproduce N_{eff} and L for Burton and Cassidy Asymmetric Silica-Gold-Silica IMI Waveguide and section A2 presents the Mathematica Code used to Solve Dispersion Relations for a F8BT/Ag/SiO₂.

A1. Mathematica Code used to reproduce N_{eff} and L for Burton and Cassidy Asymmetric Silica-Gold-Silica IMI Waveguide

The code in lines 1-8 takes in the real and imaginary parts of the wavevector plus all of the parameters to find the absolute value of the homogenous function (kmode). The function kplot[kr,ki] is used to calculate values of the homogenous equation for the standard inputs for the empirical dielectric constants for the cover material ϵ_0 , the silver film ϵ_1 and the silica substrate ϵ_2 under 1.3 μm excitation. Metal film thickness is fixed at 20 nm. The substrate and cover are taken to be purely real, with $n_{cover} = 1.46$ and $n_{silica} = 1.044$.

Ln[1] = apow2[k_,k0_,e_] := k^2 - k0^2 * e

Ln[2] = k0[λ_] := 2 * Pi / (λ * 10^-9)

Ln[3] = apos[asqrd_] := Sqrt[asqrd]

Ln[4] = aneg[asqrd_] := -Sqrt[asqrd]

Ln[5] = kmode[kr_,ki_,e0_,e1_,e2_, λ_,t_] := Simplify[Abs[((apos[apow2[kr + I* ki,k0[λ],e1]]*e2)/(apos[apow2[kr + I* ki,k0[λ],e2]]*e1)) + ((apos[apow2[kr + I* ki,k0[λ],e1]]*e0 + apos[apow2[kr + I* ki,k0[λ],e0]]*e1) + (apos[apow2[kr + I* ki,k0[λ],e1]]*e0 - apos[apow2[kr + I* ki,k0[λ],e0]]*e1)*e-2*apos[apow2[kr + I* ki,k0[λ],e1]]*t*10^-9)/((apos[apow2[kr + I* ki,k0[λ],e1]]*e0 + apos[apow2[kr + I* ki,k0[λ],e0]]*e1) - (apos[apow2[kr + I* ki,k0[λ],e1]]*e0 - apos[apow2[kr + I* ki,k0[λ],e0]]*e1)*e-2*apos[apow2[kr + I* ki,k0[λ],e1]]*t*10^-9)]]

Ln[6] = e0 = 1.46^2; e1 = -72.1 + 2.3*I; e2 = 2.13; λ1 = 1300; t1 = 20;

Ln[7] = kplot[kr_,ki_] := kmode[kr,ki,e0,e1,e2,λ1,t1]

Ln[8] = kneff[neff_,lexp_]:=kmode[k0[λ1]*neff,10^(-lexp),e0,e1,e2,λ1,t1]

Lines 9 outputs the global minimum for the standard values given in line 6. Lines 10 and 11 calculate the effective mode index by using the free-space wavevector and calculate the exponent of the propagation length.

Ln[9] = sol=Quiet@NMinimize[kmode[kr,ki,e0,e1,e2,λ1,t1],{kr,ki},
WorkingPrecision→80,MaxIterations→2500] $\frac{\text{sol}[[2]][[1,2]]}{k0[\lambda 1]} \square \text{Log}[10, \frac{1}{\text{sol}[[2]][[2,2]]}]$

Ln[10] = FindMinimum[{kmode[kr,ki,e0,e1,e2,λ1,t1]},{kr, 7060366.997, 7080666.519},
{ki, 5,10000}], stepsize = 2.5;

Ln[11] = FindMinimum[{kmode[kr,ki,e0,e1,e2,λ1,t1]},{
kr,7.060366997`*^6,7.080666519`*^6}, {ki,5,10000}]

Because the decay constants (α 's) are defined only in terms of their squares, the sign is not specified. This allows different mode solutions to be found for positive and negative α 's. Two distinct solutions were found for $\alpha_0, \alpha_1, \alpha_2 > 0$, the antisymmetric bound mode and the symmetric bound mode, which correspond to bound solutions decaying into the substrate and cover. One solution, the antisymmetric leaky mode is found when $\alpha_0 < 0, \alpha_1, \alpha_2 > 0$ and one solution, the symmetric leaky mode is found for $\alpha_2 < 0, \alpha_0, \alpha_1 > 0$. To solve for all four distinct solutions for this structure, different initial conditions and boundary conditions were used. No modes were found for a 'doubly leaky case when $\alpha_0, \alpha_1 < 0$.

Antisymmetric Bound Mode

There are two bound modes found when $\alpha_0, \alpha_1, \alpha_2 > 0$. The antisymmetric bound mode is found by minimizing the solutions as done in lines 9-11 and then appropriately bounding the solution ($k'' < 2.5, k'' > 1.482$, line 15). Lines 12-15 takes the real and imaginary parts of the effective wavevector and calculates the effective mode index and log of the imaginary part

(which is equal to the propagation length L) over a range of metal film thickness (5-100 nm). Lines 16 and 17 generate tables of the real and imaginary parts of k . Lines 18 and 19 generate the plots of n_{eff} versus metal film thickness and $\text{Log}(L)$ (m) versus metal film thickness, respectively.

Ln[12] = stepsize = 2.5;

Ln[13] = tstart = 20;

Ln[14] = tend = 100;

Ln[15] = kthick = {}; Do[sol = Quiet@NMinimize[{kmode[kr, ki, e0, e1, e2, λ 1, t],
kr < 2.5*k0[λ 1], kr > 1.482*k0[λ 1]}, {kr, ki}, WorkingPrecision → 100, MaxIterations → 5000];
AppendTo[kthick, sol], {t, tstart, tend, stepsize}];

Ln[16] = kthicklist = Table[{tstart + stepsize(t-1), kthick[[t, 2]][[1, 2]]/k0[λ 1]}, {t, 1,
Length[kthick]}]

Ln[17] = kthickimaglist = Table[{tstart + stepsize(t-1), Log[10, 1/kthick[[t, 2]][[2, 2]]]}, {t, 1,
Length[kthick]}];

Ln[18] = ListLinePlot[kthicklist, PlotRange → {1.4, 1.6}] ListLinePlot[kthickimaglist, PlotRange
→ {-7, 0}]

Ln[19] = ListLinePlot[kthickimaglist, PlotRange → {-7, 0}]

Symmetric Bound Mode

The symmetric bound mode is the second of the two mode solutions found when $\alpha_0, \alpha_1, \alpha_2 > 0$. It is solved identically to the antisymmetric bound mode. The solution is minimized (lines 9-11) and then appropriately bounded in line 15. In this case, the bounds are set to $k' < 1.47$ and $k' > 1.40$ and line 15 becomes:

Ln[15] = kthick = {}; Do[sol = Quiet@NMinimize[{kmode[kr, ki, e0, e1, e2, λ 1, t], kr > 1.4*k0[λ 1],
kr < 1.47*k0[λ 1]}, {kr, ki}, WorkingPrecision → 100, MaxIterations → 3000];
AppendTo[kthick, sol], {t, tstart, tend, stepsize}];

Antisymmetric Leaky Mode

The antisymmetric leaky mode is solved when $\alpha_0 < 0$ and $\alpha_l, \alpha_2 > 0$. Lines 2 and 3 were written to allow interchangeability of the sign of the decay constants in the main dispersion relation equation (7.1.1), which is line 5 of this code. In this case α_0 is set to a negative value and line 5 is modified to reflect this sign change accordingly:

```
Ln[5] = kmode[kr_,ki_,ε0_,ε1_,ε2_,λ_,t_] := Simplify[Abs[((apos[apow2[kr + I*
ki,k0[λ],ε1]]*ε2)/(apos[apow2[kr + I* ki,k0[λ],ε2]]*ε1))+((apos[apow2[kr + I*
ki,k0[λ],ε1]]*ε0+aneg[apow2[kr + I* ki,k0[λ],ε0]]*ε1)+(apos[apow2[kr + I* ki,k0[λ],ε1]]*ε0-
aneg[apow2[kr + I* ki,k0[λ],ε0]]*ε1)*e-2*apos[apow2[kr + I* ki,k0[λ],ε1]]*t*10^-
9)/((apos[apow2[kr + I* ki,k0[λ],ε1]]*ε0+aneg[apow2[kr + I* ki,k0[λ],ε0]]*ε1)-
(apos[apow2[kr + I* ki,k0[λ],ε1]]*ε0-aneg[apow2[kr + I* ki,k0[λ],ε0]]*ε1)*e-
2*apos[apow2[kr + I* ki,k0[λ],ε1]]*t*10^-9))]
```

No boundary conditions are required to solve for the antisymmetric leaky mode, thus the boundary conditions in line 15 are removed and it is written as:

```
Ln[15] = kthicklist = Table[{tstart + stepsize(t-1), kthick[[t,2]][[1,2]]/k0[λ1]}, {t, 1,
Length[kthick]}];
```

Symmetric Leaky Mode

The symmetric leaky mode is solved when $\alpha_2 < 0$ and $\alpha_0, \alpha_l > 0$. As noted in the discussion of the antisymmetric leaky mode solution, lines 2 and 3 were written to allow interchangeability of the sign of the decay constants in the main dispersion relation equation (7.1.1), which is line 5 of this calculation. In this case α_2 is set to a negative value and line 5 is modified to reflect this sign change accordingly:

```
Ln[5] = kmode[kr_,ki_,ε0_,ε1_,ε2_,λ_,t_] := Simplify[Abs[((apos[apow2[kr + I*
ki,k0[λ],ε1]]*ε2)/(aneg[apow2[kr + I* ki,k0[λ],ε2]]*ε1))+((apos[apow2[kr + I*
ki,k0[λ],ε1]]*ε0+apos[apow2[kr + I* ki,k0[λ],ε0]]*ε1)+(apos[apow2[kr + I* ki,k0[λ],ε1]]*ε0-
apos[apow2[kr + I* ki,k0[λ],ε0]]*ε1)*e-2*apos[apow2[kr + I* ki,k0[λ],ε1]]*t*10^-
9)/((apos[apow2[kr + I* ki,k0[λ],ε1]]*ε0+apos[apow2[kr + I* ki,k0[λ],ε0]]*ε1)-
```

```
(apos[apow2[kr + I* ki,k0[λ],ε1]]*ε0-apos[apow2[kr + I* ki,k0[λ],ε0]]*ε1)*e-  
2*apos[apow2[kr + I* ki,k0[λ],ε1]]*t*10^-9)]
```

Boundary conditions were required to solve for the symmetric leaky mode. In this case, the bounds are set to $k' < 1.461$, $k' > 1.455$ and $ki > 0$ and line 15 was modified accordingly:

```
Ln[15] =kthick={}; Do[sol = Quiet@NMinimize[{kmode[kr,ki,e0,e1,e2,λ1,t],kr>1.455*k0[λ1],  
kr<1.461*k0[λ1],ki>=0},{kr,ki},WorkingPrecision → 100, MaxIterations→5000];  
AppendTo[kthick,sol],{t,tstart,tend,stepsize}];
```

A2. Mathematica Code used to Solve Dispersion Relations for a F8BT/Ag/SiO₂

Dispersion relations (Eqs. 1-4 in 2.3.1) for the three dielectric constant cases (PRSS, CSS, and CG) were solved iteratively in Mathematica using an N-minimize[®] function and setting boundary conditions for the real part of the complex surface plasmon polariton wavevector, k' . The code in Lines 1-8 takes in the real and imaginary parts of the complex plasmon polariton wavevector, k , plus all of the parameters to find the absolute value of the homogenous function (kmode). The function kplot[kr,ki] is used to calculate values of the homogenous equation for the standard inputs for the empirical dielectric constants for ϵ_0 (ϵ_{SiO_2} , substrate), ϵ_1 (ϵ_{Ag} , film) and ϵ_2 (ϵ_{F8BT} , cover). ϵ_{Ag} was fixed for the three dispersion relation conditions but ϵ_{SiO_2} and ϵ_{F8BT} varied for the three dispersion relation conditions (see Appendix B. Table 1). Excitation wavelength was fixed at 576 nm and initial metal film thickness was fixed at 20 nm.

```
Ln[1] = apow2[k_,k0_,ε_]:=k^2-k0^2*ε
```

```
Ln[2] = k0[λ_]:=2*Pi/(λ*10^-9)
```

```
Ln[3] = apos[asqrd_]:=Sqrt[asqrd]
```

```
Ln[4] = aneg[asqrd_]:=-Sqrt[asqrd]
```

Ln[5] = kmode[kr_,ki_,e0_,e1_,e2_,λ_,t_]:= Simplify[Abs[((apos[apow2[kr + I*
ki,k0[λ],e1]]*e2)/(apos[apow2[kr+I*ki,k0[λ],e2]]*e1))+((apos[apow2[kr+I*
ki,k0[λ],e1]]*e0+apos[apow2[kr+ I* ki,k0[λ],e0]]*e1)+(apos[apow2[kr + I* ki,k0[λ],e1]]*e0-
apos[apow2[kr+I*ki,k0[λ],e0]]*e1)*e-2*apos[apow2[kr+I*ki,k0[λ],e1]]*t*10^-
9)/((apos[apow2[kr+I* ki,k0[λ],e1]]*e0+apos[apow2[kr + I* ki,k0[λ],e0]]*e1)-(apos[apow2[kr
+I*ki,k0[λ],e1]]*e0-apos[apow2[kr+I*ki,k0[λ],e0]]*e1)*e-2*apos[apow2[kr + I*
ki,k0[λ],e1]]*t*10^-9))]]

Ln[6] = e0 = 2.13; e1 = -12.5681 + i0.854591 *I; e2 = 3.6446; λ1=576; t1= 20;

Ln[7] = kplot[kr_,ki_]:=kmode[kr,ki,e0,e1,e2,λ1,t1]

Ln[8] = kneff[neff_,lexp_]:=kmode[k0[λ1]*neff,10^(-lexp),e0,e1,e2,λ1,t1]

Table AA1 ε values for the substrate (SiO₂) and cover (F8BT) media for the three dispersion relation conditions.

	ε_{SiO_2}	ε_{F8BT}
PRSS	2.13	3.6446
CSS	2.13+0.0015i	3.6446+0.2358i
CG	2.13+0.0015i	3.6446-0.00083i

To solve for all four distinct mode solutions for this structure, either the positive or negative roots of α are selected for the desired condition from Lines 2 and 4 and inputted accordingly into Line 5 to solve for a particular mode. The solution step size and metal film thickness range over which the solution is to be solved for are inputted (Lines 9-11). For these solutions, a fixed step size of 1 nm was used and solutions were searched for over a range of 5-100 nm (Lines 10 and 11). Line 12 takes the real and imaginary parts of the complex surface plasmon polariton wavevector, k , and calculates the effective mode index and Log of $1/k^i$ (which is equal to the propagation length, L) over a range of metal film thickness (5-100 nm). Lines 13 and 14 generate tables of the real and imaginary parts of the complex surface plasmon polariton wavevector.

Ln[9] = stepsize = 1;

```

Ln[10] = tstart = 5;

Ln[11] = tend = 100;

Ln[12] = kthick = {}; Do[sol = Quiet@NMinimize [{kmode[kr,ki,e0,e1,e2, $\lambda$ 1,t],
Kr>A*k0[ $\lambda$ 1],kr<B*k0[ $\lambda$ 1]}, {kr,ki}, WorkingPrecision  $\rightarrow$  100, MaxIterations $\rightarrow$ 5000];
AppendTo[kthick,sol], {t,tstart,tend,stepsize}];

Ln[13] = kthicklist = Table[{tstart + stepsize(t-1), kthick[[t,2]][[1,2]]/k0[ $\lambda$ 1]}, {t, 1,
Length[kthick]}];

Ln[14] = kthickimaglist = Table[{tstart + stepsize(t-1), Log[10,1/kthick[[t,2]][[2,2]]]}, {t, 1,
Length[kthick]}];

```

The most critical step in the finding physically reasonable mode solutions are the k_r boundary conditions (denoted by “A” and “B” in Line 12 of code). For a given mode, multiple distinct boundary conditions may be required over the 5-100 nm metal film thickness range of interest. Appendix Table 2 summarizes the boundary conditions used to solve for the four distinct modes (SB, SL, AB, and AL) for the three dispersion relation conditions (PRSS, CSS, and CG).

Table AA2. Boundary conditions (*A* and *B*) for the real part of the complex surface plasmon polariton wavevector, k_r , at specific metal film thickness ranges (t_{start} to t_{end}) for the four mode solutions (SB, SL, AB, and AL) for the three dispersion relation conditions (PRSS, CSS, and CG). Metal film thicknesses are entered into Lines 10 and 11 and boundary conditions (*A* and *B*) are entered into Line 12 of the code.

Dispersion Relation Condition/ Mode Symmetry	t_{start} (nm)	t_{end} (nm)	<i>A</i> (lower k_r bound)	<i>B</i> (upper k_r bound)
PRSS/SB	5	100	1.59	1.67
PRSS/SL	5	15	1.25	1.9
PRSS/SL	15	47	1.56	1.9

PRSS/SL	47	100	1.599	1.9
PRSS/AB	5	100	2	10
PRSS/AL	5	100	1.4	3.5
CSS/SB	12	18	1.49	1.6
CSS/SB	18	27	1.5	1.579
CSS/SB	25	42	1.53	1.597
CSS/SB	42	100	1.591	1.62
CSS/SL	5	15	1.25	1.9
CSS/SL	15	45	1.56	1.9
CSS/SL	45	100	1.599	1.9
CSS/AB	5	100	1.8	7
CSS/AL	5	100	1.4	2.9
CG/SB	5	20	1.613	1.65385
CG/SB	20	100	1.5999	1.65383
CG/SL	5	20	1.27	1.7
CG/SL	20	50	1.51	1.7
CG/SL	50	85	1.59	1.619
CG/SL	85	100	1.5999	1.619
CG/AB	5	100	1.8	7
CG/AL	5	100	1.4	2.9

Appendix B

Background on Gain and Loss Measurements via VSL and SES Techniques

Gain coefficients were measured using a widely utilized technique called the Variable Stripe Length Method (VSL) that is based on the one-dimensional amplifier model [174-175]. The VSL method was first introduced in the 1970's and is a favorable method to extract optical gain coefficients in thin films of materials ranging from conjugated polymers to inorganic materials, such as Eu-doped GaN thin films [91,174-178]. This method is widely employed because it requires no special sample preparation and both transparent and opaque samples can be measured. All that is required is the sample be planar and have an edge that is suitable to collect the emission from. In addition, the basic principle of the technique is extremely simple.

In the VSL method, the sample is optically excited by an intense pulsed laser beam that is focused into a narrow with a cylindrical and projected onto the sample, perpendicular to the surface of the sample. The excitation stripe length (l) (or (t) in some of the literature) is varied by a gate or slit with a micrometer. An amplified spontaneous emission (ASE) signal with intensity, I_{ASE} , is collected from the edge of the sample, focused, filtered with a long-pass filter and analyzed by a spectrometer (see Fig AB1 for a schematic of the VSL method) [178].¹⁷⁷ At high laser excitation pump power densities ($> 1\text{mW/cm}^2$) with low pulse repetition rates ($<20\text{ Hz}$), as l is increased, a population inversion occurs in the emitter and the partially coherent ASE signal intensity should grow exponentially. The increase in ASE intensity with increasing stripe length l is described in a first approximation by a one-dimensional optical amplifier model [174,175]. The one dimensional amplifier is a good approximation for VSL measurements applied to planar active waveguides when the gain coefficient is high. The optical pumping geometry realizes a geometry very similar to the one found in gain-guided electrically driven stripe semiconductor lasers which are widely used in photonics. Here, the lateral mode confinement is realized by

confining the inverted region, i.e., the gain region, to a narrow stripe by spatial confinement of the injected current. The limits of the one-dimensional amplifier model are evident when the gain coefficient is low (a few cm^{-1}).

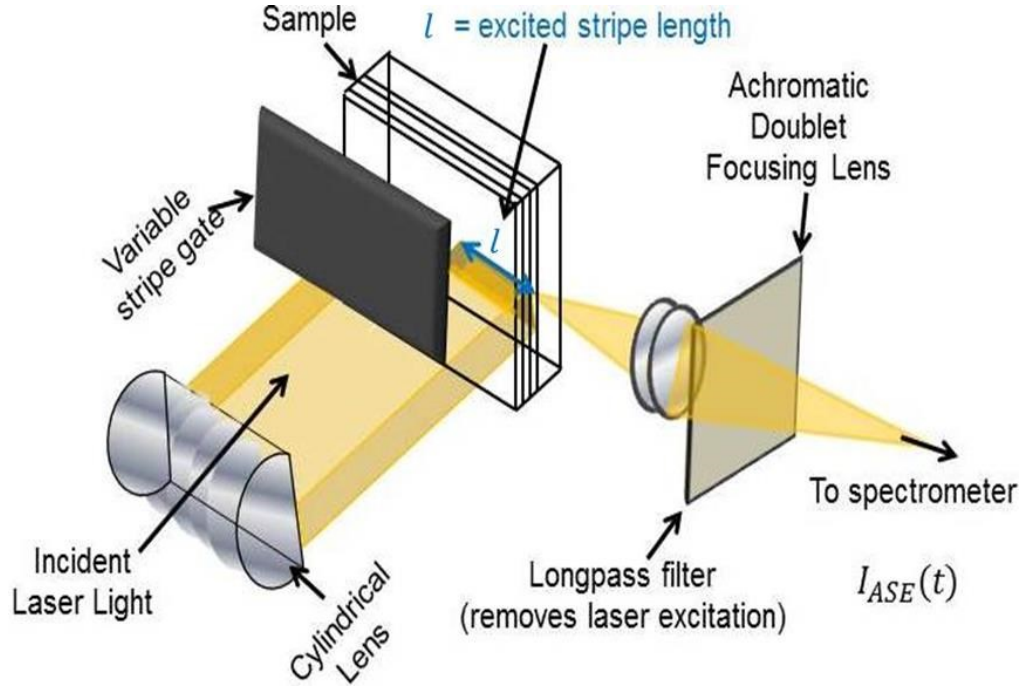


Figure AB1. Schematic of the variable stripe length method (VSL). The amplified spontaneous emission is collected from the edge of the sample as a function of excitation stripe length, t . Color available in electronic copy.

In the one-dimensional amplifier model with excitation cross-sectional area, S , and length L , a propagation intensity equation can be written for the (amplified) spontaneous [174,175]

$$\frac{dI}{dt} = (\Gamma g_m - \alpha)I + (A_{sp}N^* \times h\nu)[\Omega(t)/4\pi] \quad (\text{AB.E1})$$

where g_m is the gain of the material, Γ is the confinement factor of the waveguide structure, α is the propagation loss coefficient, A_{sp} is the spontaneous emission rate, N^* is the excited state population density and $h\nu$ is the energy of the emitted photon, and I is the optical intensity produced by a uniformly pumped stripe. $\Omega(t)$ is the solid angle subtended by the exit amplifier

face (see Figs. AB1 and AB2). On the right hand side of the equation, the term $\Omega(z)/4\pi$ is the fraction of spontaneous emission from element dt that propagates along the amplification axis.

Only under specific conditions can the equation for ASE intensity at the exit face of the amplifier be analytically integrated. The majority of the ASE emission arises from the emitting element near $t = L$, which experiences the largest single pass gain, it is assumed that $\Omega(t) \cong \Omega = S/L^2$ (see Figure AB2). More generally, the stripe length (t) dependence of $\Omega(t)$ strongly affects the collection efficiency of the ASE signal. Thus, the condition that $\Omega(t) \cong \Omega$ corresponds to the assumption of constant collection efficiency. This hypothesis is satisfied for optical fibers and two-dimensional waveguides but not fulfilled in the case of planar waveguides where the modes spread in the waveguide plane. Inhomogeneities in the measured ASE signal intensity may also arise due to an inappropriate selection of the numerical aperture and depth of focus of the collection optics used in the experiments, or as a result of partial collection of surface light emission (i.e., non-guided light) [174,175].

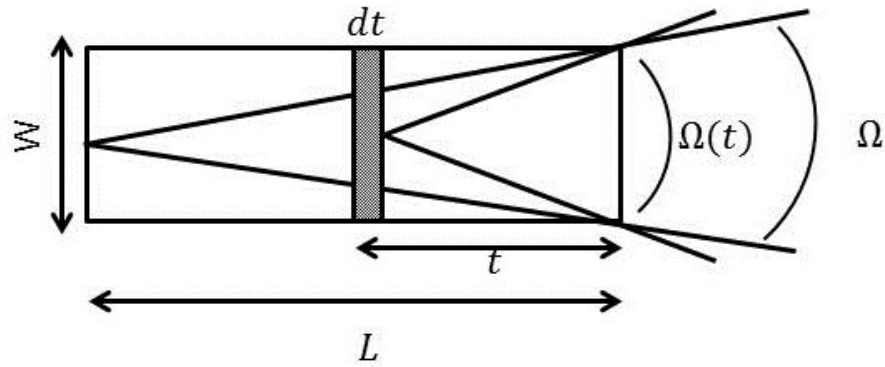


Figure AB2. Schematic of the excited stripe on the surface of the planar waveguide. L is the total length of the amplifier, t excitation stripe length projected on the sample surface, dt is the change in excitation stripe length, $\Omega(t)$ is the solid angle defined by the exit facet of the waveguide and the of the excitation stripe edge on the sample surface. $\Omega(t) = \Omega$ when $t = L$ [174,175].

In addition to the primary assumption of the one-dimensional amplifier model, which is stripe-length independent light collection efficiency, there is an additional assumption made: a

constant gain coefficient along the amplifier axis. Under certain circumstances, a spatial dependence in the gain coefficient is observed. This is typically related to gain saturation problems or when a non-homogeneous laser excitation pump intensity profile is used. So, in summary, the second general hypothesis is referred to as the “homogeneity of the gain and pump intensity over the whole excitation stripe length t ”[178]. The analytical form of the propagation intensity equation for spontaneous emission is:

$$I_{ASE}(t) = \frac{J_{sp}(\Omega)}{g_{mod}} (e^{g_{mod} \times z} - 1), \quad (\text{AB.E2})$$

where

$$J_{sp}(\Omega) = \left(\frac{A_{SP} h \nu \Omega N^*}{4\pi} \right) \quad (\text{AB.E3})$$

is the spontaneous emission intensity emitted with the solid angle Ω and g_{mod} is the net modal gain of the material, $g_{mod} = \Gamma g_m - \alpha$.

The assumptions necessary to make VSL measurements of SMI waveguides that will be studied, i.e.: (1) assume uniform collection angle and (2) assume homogeneous pump power across the excitation stripe length and uniform gain across the excitation stripe length will now be considered. To ensure uniform collection angle, we consider that the stripe width is on the order of 0.2 mm and its overall length does not exceed 2 mm. Thus, the longest stripe length has an ASE exit cone angle of 5.71° . With a 100 mm focal length achromatic doublet with a collection angle, θ , of 7.25° , it is expected that all the light over the range of stripe lengths will be easily collected. With regards to uniform gain along the excitation stripe, optical absorption measurements will be taken along the film to ensure uniformity of the gain medium. Uniformity in the excitation stripe has been maximized by using a high quality laser and only utilizing the central portion of the strip formed with the cylindrical lens. If this becomes an issue as

measurements proceed, a laser beam diffuser optic will be added before the sample to ensure uniform excitation.

To measure optical propagation loss coefficient, a variation of the VSL method is used called shifting excitation spot method (SES) [112,174,178]. This method, schematically represented in Figure AB3, uses a small stripe excitation area, whose lateral position can be shifted with respect to the sample edge. The resultant emission is collected from the sample edge similar to that in the VSL method. Since the emitted light travels along a region which is not photo-excited, the collected intensity as a function of the distance between the edge of the excitation stripe and the physical edge of the waveguide is characterized by an exponential attenuation law (Equation AB.E4). In the simple case of collimated optical beams (like in optical fibers) the intensity decay follows the exponential Beer–Lambert law. Since the optical mode remains collimated while propagating, the collection efficiency is independent of the exciting stripe position thus allowing for an easy measurement of the propagation loss coefficient, α . In the case of a planar waveguide, the optical mode has an angular spread in the waveguide plane which depends on the exciting stripe distance from the edge of the waveguide. The optical loss value can be determined through the relation between output intensity and distance from the edge given by:

$$I = I_0 e^{-\alpha x} \quad (\text{AB.E4})$$

where I_0 is the intensity generated at the edge of the excitation stripe, α (cm^{-2}) is the propagation loss coefficient (i.e., the net modal loss) and x (cm) is the distance between the sample edge and the excitation stripe.

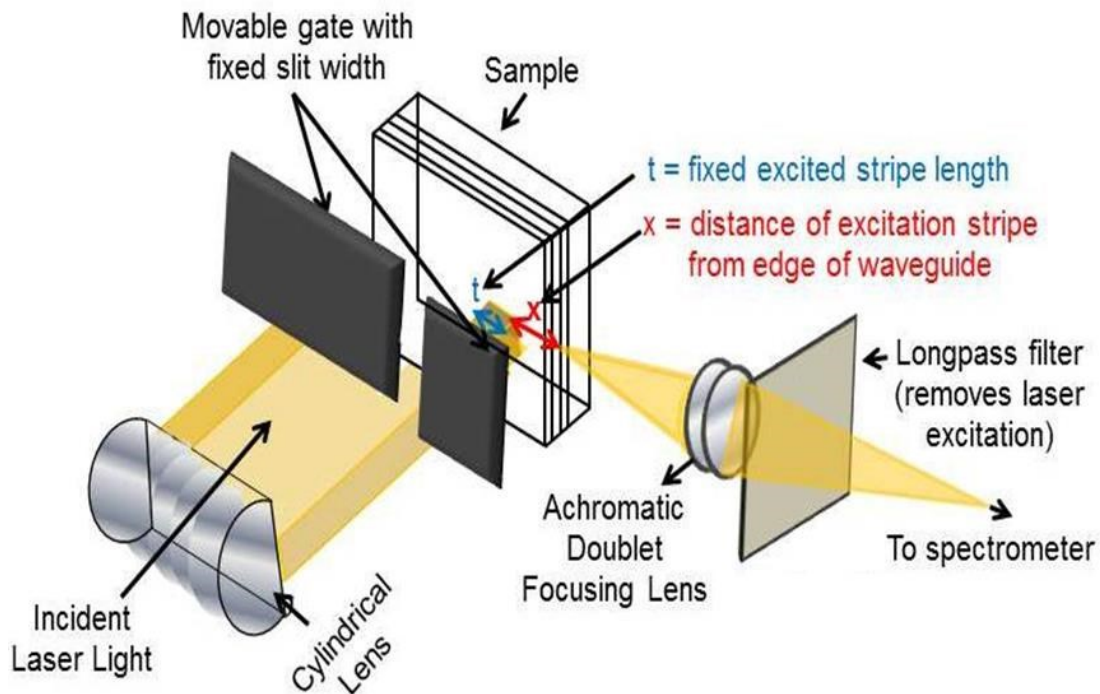


Figure AB3. Schematic of shifting excitation spot technique (SES). t is the excitation stripe length (which is fixed) and x is distance of the stripe from the edge of the waveguide. Color available in electronic copy.

Appendix C

Preliminary Unpolarized and Polarized Pump Power Dependent Emission Spectra of ISI and ISMI Waveguides

Pump power emission spectra of neat PFO ISI and ISMI waveguides fabricated with Ag metal film thicknesses of 0, 35, 50, 65, and 100 nm were collected at two excitation pump power densities (0.64 and 0.835 W/cm^2), using a 2 mm excitation stripe length fixed at the edge of the SMI waveguide. Emission spectra of a waveguide with neat PFO only (i.e. the 0 nm thickness case) were collected to serve as a reference to compare the waveguides with Ag metal to understand how the resultant PFO emission changes as a function of metal film thickness (see Fig. AC1(a) and (b)). Spectra of PFO-only waveguides exhibited peak emission wavelengths of 453 and 451 nm at power densities of 0.64 and 0.835 W/cm^2 , respectively. At the higher 0.835 W/cm^2 power density, the emission intensity increases by a factor of 40X and the FWHM narrows by 59% from 7.09 nm to 4.25 nm. This suggests that the ASE threshold for the PFO-only waveguide is at the power density of 0.835 W/cm^2 or between 0.64 and 0.835 W/cm^2 . Figure AC1(c) and (d) show the gain spectra at the same two power densities of the SMI waveguides with metal film thicknesses of 35, 50, 65, and 100 nm. Plots of the peak emission wavelength, maximum emission intensity, and FWHM as a function of Ag film thickness were generated to aid in a careful analysis of these spectra (see Fig. AC2)

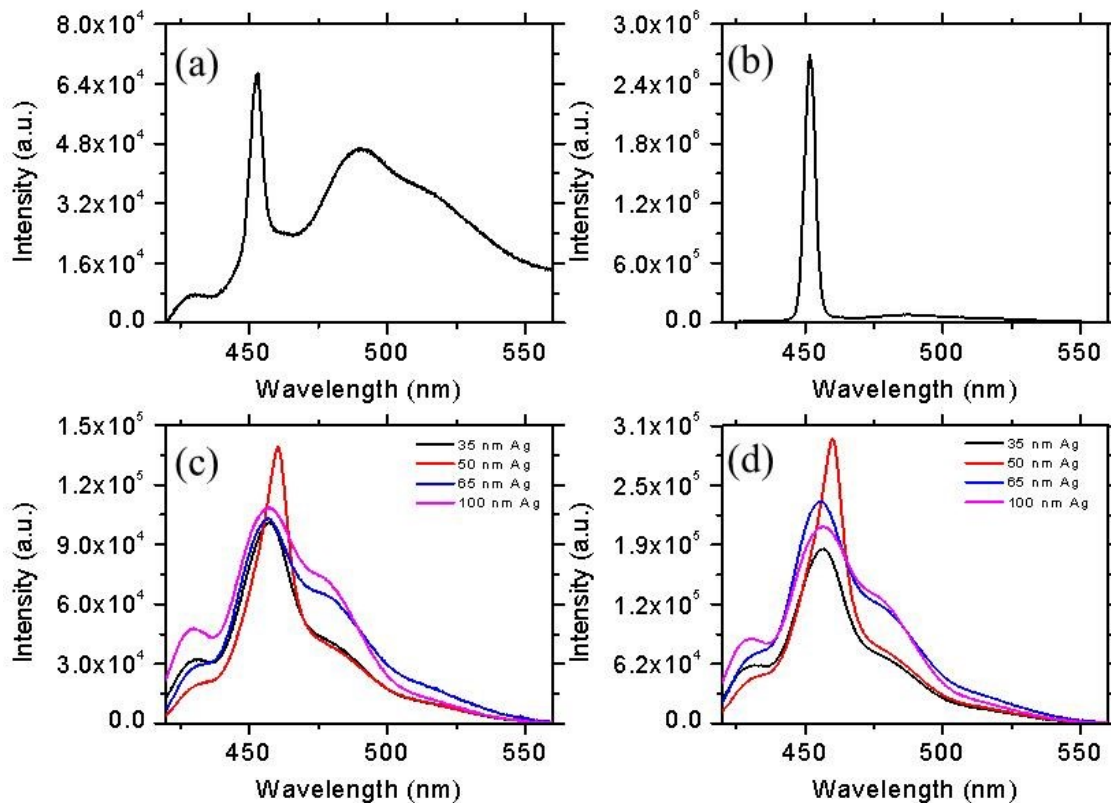


Figure AC1. Gain spectra of a PFO-only ISI waveguide (a,b) and ISMI waveguides with metal film thicknesses of 35, 50, 65, and 100 nm (c,d) under 355 nm excitation with power densities of 0.64 W/cm^2 (a,c) and 0.835 W/cm^2 (b,d). Color available in electronic copy.

Comparing the peak emission wavelengths of the neat PFO-only waveguide gain spectra to the Ag metal containing ISMI waveguides, it shows that the Ag metal containing SMI waveguides produce emissions that are redshifted by 3-9 nm (depending on Ag film thickness) at both power densities, relative to the PFO-only case (see Fig. AC2(a)). As the Ag metal film thickness is varied, the SMI waveguides with 35, 65, and 100 nm Ag film exhibit peak emission wavelengths between 455 and 456 nm for both power densities (see Fig. AC2(a)). However, the peak emission wavelength from the 50 nm Ag film waveguide is 460 nm for both power densities, which is redshifted by 4 - 5 nm relative to all other cases (see Fig. AC2 (a)).

Peak or maximum emission intensity as a function of metal film was also plotted (see Fig. AC2 (b)). The PFO-only waveguide was excluded from these plots and presented separately because the resultant emission intensity was significantly greater than all of the Ag film containing SMI waveguides. For the spectra collected at a power density of 0.835 W/cm^2 , the emission from the PFO-only waveguide was nearly an order of magnitude greater than that of most strongly emitting Ag film containing SMI waveguide. This suggests that a significant fraction of the resultant PFO emission has coupled to SPP modes on the Ag metal film, and or there is loss incurred due to the metal's non-negligible imaginary component of its complex dielectric constant. Looking at the trend in peak emission intensity as a function of Ag metal film thickness, as Ag film thickness is increased from 35 to 50 nm, the emission intensity increases by 137% and 148% at power densities of 0.64 and 0.835 W/cm^2 , respectively (see Fig. AC2 (b)). When metal film thickness is increased beyond 50 nm to 65 nm and then 100 nm, the overall emission intensity decreases by 77.6% and 148% at power densities of 0.64 and 0.835 W/cm^2 , respectively (see Fig. AC2 (b)).

The trend observed in the FWHM of the gain spectra at both power densities mirrored that which was observed in the maximum emission intensity as a function of metal film thickness. The PFO-only waveguides, which exhibited the greatest emission intensity, also exhibit the narrowest FWHM of 7.09 and 4.35 nm at power densities of 0.64 and 0.835 W/cm^2 , respectively (see Fig. AC2 (c)). The gain spectra of the SMI waveguides with Ag film thicknesses of 35, 50, 65, and 100 nm exhibited FWHM of 25.88, 15.78, 43.71, and 46.09 at a power density 0.54 W/cm^2 and FWHM of 24.71, 18.09, 37.92, and 43.58 nm at a power density of 0.835 W/cm^2 . Looking at this trend, it is observed that the FWHM narrows, or decreases from the 35 nm to the 50 nm Ag film case to a minimum, followed by a subsequent broadening with increasing metal film thicknesses of 65 and 100 nm. Thus, the 50 nm Ag film case, which exhibited the peak emission intensity, also exhibits the narrowest FWHM.

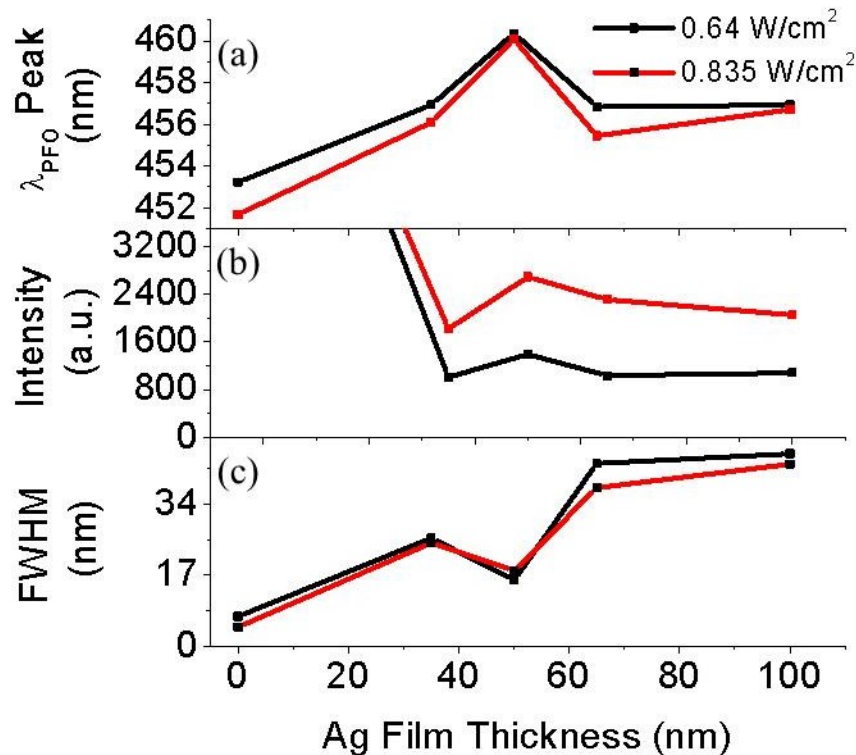


Figure AC2. Peak emission wavelength (a), peak emission intensity (b), and FWHM (c) of PFO-only waveguides (0 nm Ag) and SMI waveguides with Ag film thicknesses of 35, 50, 65, and 100 nm under power densities of 0.64 and 0.835 W/cm². The plot of emission intensity (c) was scaled to show trend in the Ag metal containing SMI waveguides only.

Two identical sets of measurements to those in Fig AC1(a)-(d) were collected simultaneously with the same two power densities (0.64 and 0.835 W/cm²) and sample set, with polarized outcoupled edge emission (see Fig. AC3 and Methods Section 3.3.9). Spectra were collected when collection polarization was set parallel (0°) (see Fig. AC3(a) and Fig. AC4 (a) and (b)) and perpendicular (90°) (see Fig. AC3 (b) and Fig. AC4(c) and (d)) WRT to the plane of the waveguide. These measurements were collected to potentially isolate the photonic waveguide mode(s) and the SPP mode(s) for future studies as a function of incident power, stripe length, metal film thickness, and polymer dipole orientation.

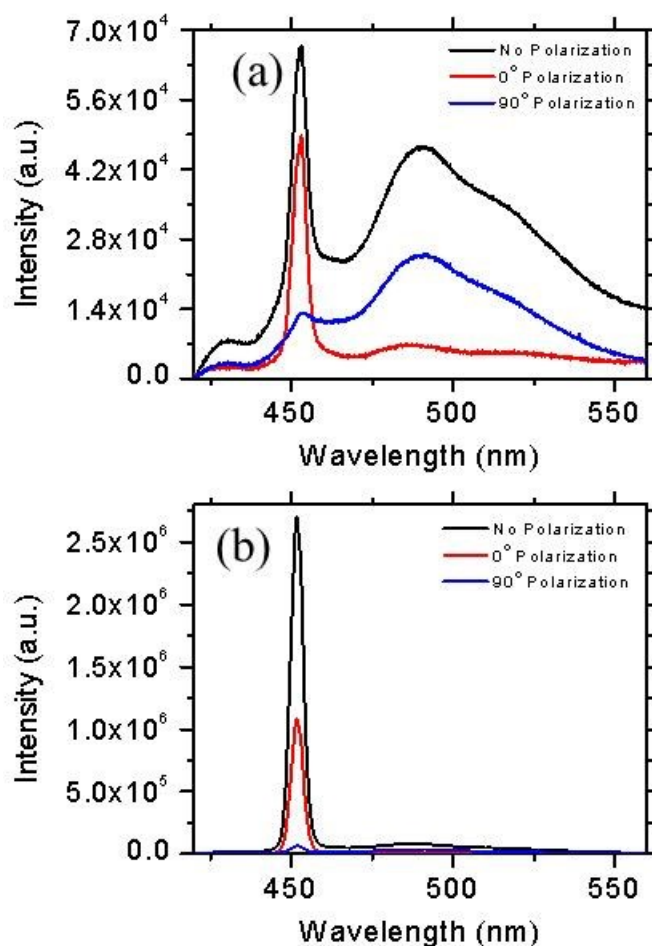


Figure AC3. Gain spectra of a neat PFO-only waveguide with unpolarized emission, emission polarized parallel (0°) and perpendicular (90°) to the plane of the waveguide excited with power densities of 0.64 W/cm² (a) and 0.835 W/cm² (b). Color available in electronic copy.

The polarized gain spectra collected from the neat PFO-only waveguide are shown in Fig. Y and plotted against the unpolarized spectra shown previously in Fig. AC3. At the lower power density of 0.64 W/cm² the PFO is within the steady state emission regime and more clearly illustrates the difference when the outcoupled edge emission from the waveguide is polarized (see Fig. AC3(a)). When the polarization is parallel (0°) to the plane of the waveguide, the emission is less intense due to the fact that the polarizer will attenuate some of the signal, however the profile is very similar in shape to that of the unpolarized gain spectrum. In contrast, when

polarization is perpendicular (90°) to the plane of the waveguide the primary PFO emission centered at 452 nm is nearly extinct, while the peak at 490 nm is still present. This trend is also observed for the gain spectra collected with the higher power density of 0.835 W/cm^2 when the PFO is undergoing ASE (see Fig. AC3(b)). This shows that the majority of the photonic mode is polarized in the plane of the substrate.

The polarized gain spectra of the Ag metal containing SMI waveguides exhibit identical behavior to the PFO-only waveguide at both the of 0.64 W/cm^2 (see Fig. AC4(a,b)) and 0.835 W/cm^2 (see Fig. AC4(c,d)). Under polarization parallel (0°) to the plane of the waveguide (Fig. AC4(a) and (c)), the resultant spectra are virtually identical to the unpolarized spectra in Fig. AC1. When polarization is perpendicular (90°) to the plane of the waveguide, the primary 450-455 nm emission is virtually extinct and also the longer wavelength 490 nm emission is also significantly reduced (see Fig. AC4(c) and (b)). Thus, like in the case of the PFO-only waveguide, the photonic mode is polarized in the plane of the waveguide and there appears to be no significant changes in the behavior of the waveguide when the thin Ag metal film is introduced to the structure.

Additionally, the resultant gain spectra under both polarizations show nearly identical trends in peak emission wavelength, maximum emission intensity and FWHM as a function of Ag film thickness as the unpolarized spectra shown in Fig. AC5. Plots of the peak emission wavelength of the Ag metal containing SMI waveguides with unpolarized emission, and emission polarized parallel (0°) and perpendicular (90°) to the plane of the waveguide are shown in Fig AC5(a)-(c) under both 0.64 and 0.835 W/cm^2 power densities. They all show a redshift with increasing metal film thickness with maxima for the SMI waveguide with a 50 nm metal film thickness. Plots of the relative emission intensity and FWHM of the Ag metal containing SMI waveguides with unpolarized emission, and emission polarized parallel (0°) and perpendicular

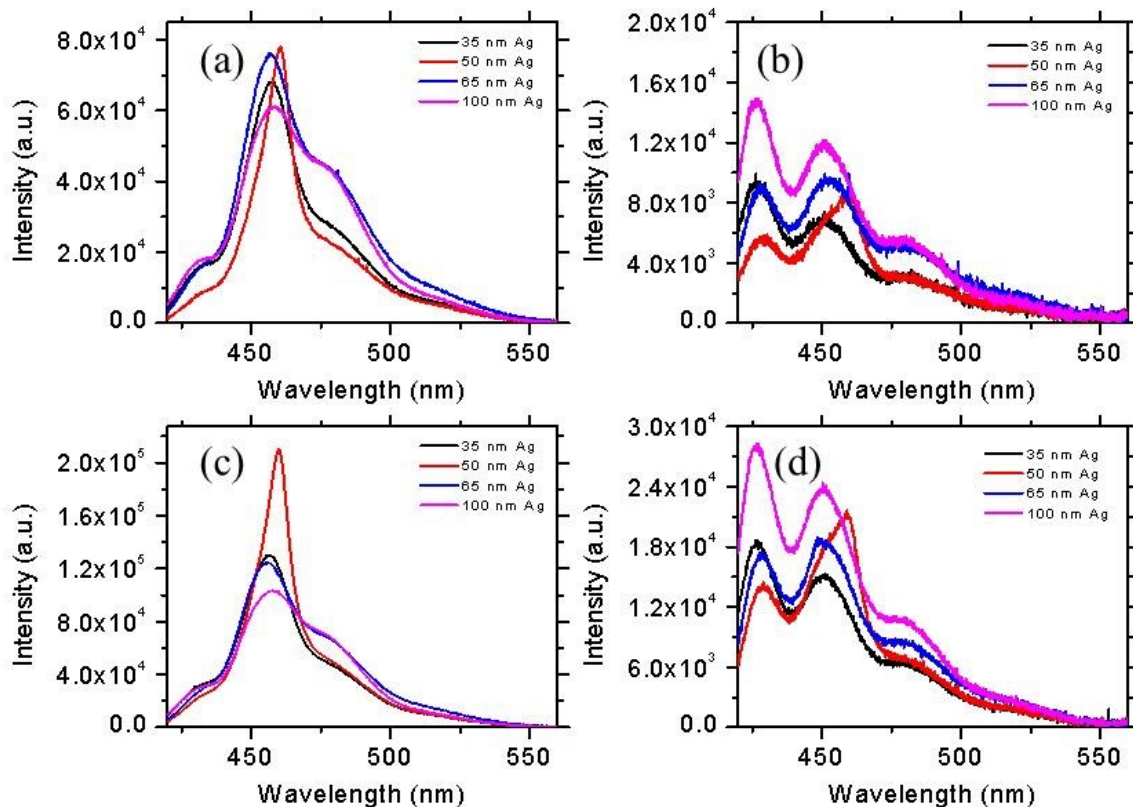


Figure AC4. Gain spectra of a neat PFO SMI waveguide Ag film thicknesses of 35, 50, 65, and 100 nm excited with power densities of 0.64 W/cm^2 (a,b) and 0.835 W/cm^2 (c,d) with emission polarized parallel (0°) (a,c) and perpendicular (90°) (b,d) to the plane of the waveguide. Color available in electronic copy.

(90°) to the plane of the waveguide are shown in Fig AC5 (d)-(f) under both 0.64 and 0.835 W/cm^2 power densities. The trend in the maximum emission intensity is virtually identical for both power densities and for unpolarized and polarized emission; showing a maximum in emission intensity for the waveguide with a 50 nm Ag film thickness and a decrease in emission intensity with either increasing or decreasing metal film thickness. The trend in the FWHM for both power densities and for unpolarized and polarized emission is also virtually identical to the unpolarized case (see Fig. AC5 (g)-(i)); showing a minima in the FWHM for the SMI waveguide with a 50 nm Ag film thickness with significant broadening as metal film thickness is increased. The only deviation from the trend in FWHM was for the SMI waveguide with 100 nm Ag film

thickness under 0.835 W/cm^2 with 90° polarization. In this case, the FWHM was narrower than expected and is attributed to an experimental error.

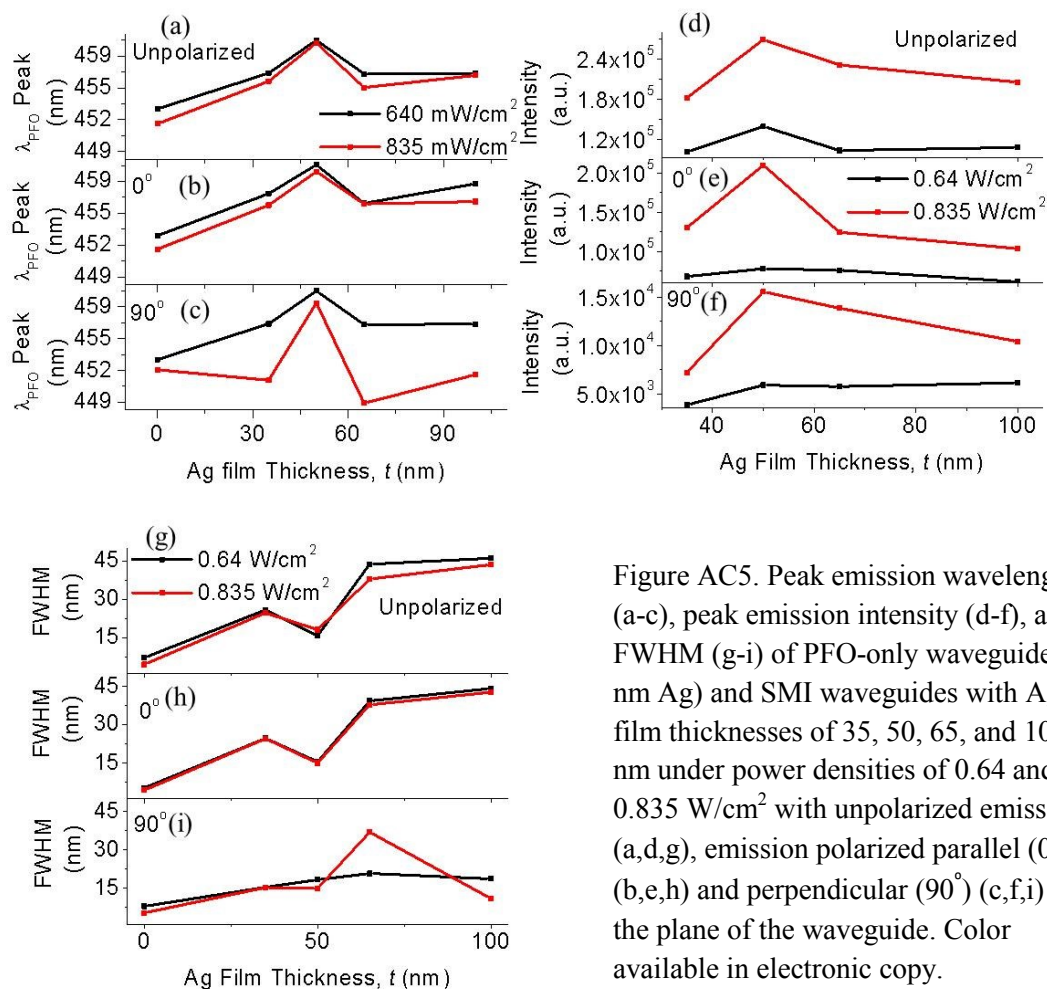


Figure AC5. Peak emission wavelength (a-c), peak emission intensity (d-f), and FWHM (g-i) of PFO-only waveguides (0 nm Ag) and SMI waveguides with Ag film thicknesses of 35, 50, 65, and 100 nm under power densities of 0.64 and 0.835 W/cm^2 with unpolarized emission (a,d,g), emission polarized parallel (0°) (b,e,h) and perpendicular (90°) (c,f,i) to the plane of the waveguide. Color available in electronic copy.

While there is a clear trend in peak emission wavelength, relative intensity, and FWHM as a function of metal film thickness, there was concern as to the reproducibility and reliability of these measurements, specifically based on how the outcoupled edge emission was collected and analyzed. As described in the methods section, the outcoupled edge emission was focused and a spot was projected onto the spectrometer CCD. For these measurements, the focused spot was in

excess of $4500\ \mu\text{m}$. However, the spectra were collected from a narrow $250\ \mu\text{m}$ diameter region which was selected by traversing the position of the spot using the focusing optics such that the desired region was aligned with the spectrometer input slits. This process of imaging and spectrum acquisition is represented in Figure AC6, for a neat PFO SMI waveguide with a $50\ \text{nm}$ Ag film thickness. Figure AC6 (a) shows an image of the focused outcoupled edge emission, with the spectrometer slits fully open and the $250\ \mu\text{m}$ diameter region where the spectra (shown in Fig. AC6(b)) were collected marked in red. The spectra were collected from the interface of the dark and bright regions in Fig. AC6 (a), which is the interface between the Ag metal and the brightly emitting PFO.

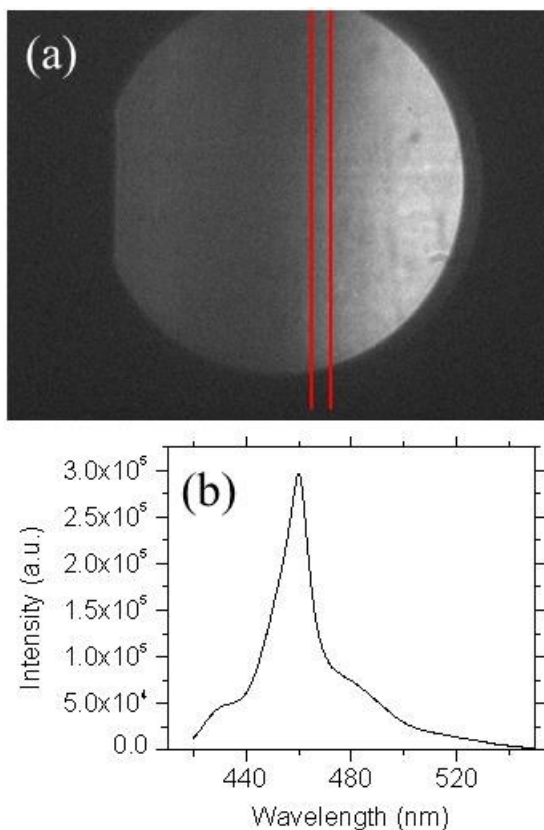


Figure AC6 (a) Spectrometer CCD image of the outcoupled edge emission from a neat PFO SMI waveguide with $50\ \text{nm}$ Ag film thickness focused to a $4500\ \mu\text{m}$ diameter spot and (b) corresponding spectrum of outcoupled edge emission. Vertical red lines in (a) denote the $250\ \mu\text{m}$ diameter region where spectrum in (b) was collected.

There are several pitfalls to this method of collecting spectra from SMI waveguides, namely reproducibility. It is highly unlikely that the same slice of the interface region will be selected from sample to sample. Additionally, different regions within the spot from a single sample may result in significantly different emission profiles. Such significant changes may arise because the energy transfer between the metal film and molecular dipole emitters will change as a function of distance from the Ag metal film. For example, at the interface, there will be significant quenching of the polymer dipoles, at greater distances from the metal film there will be a region that effectively couples to SPP modes, followed by regions with minimal coupling. Additionally, theory has shown that the SPP modes leak significantly into both the polymer cover and silica substrate, and in turn the mode energy will be distributed over wide regions in the waveguide. Therefore, by selecting a very specific region to collect a representative spectrum from may skew or mask the true behavior of the waveguide emission as a function of metal film thickness.

To test the position dependence of the resultant gain spectrum and optimize this measurement technique, spectra were collected from four 250 μm diameter regions on from a single spot incident on the spectrometer CCD using a neat PFO SMI waveguide with a 50 nm Ag film thickness (see Fig. AC7). Images of the four regions are shown in Fig AC7(a) with the corresponding spectra in Fig AC7 (b). An analysis of the peak emission wavelength and intensity, and FWHM was conducted in Fig. AC7(c) shows significant changes in the emission intensity and FWHM as a function of the position. The peak wavelength ranges from 457 to 461 nm over the four spectra, however, the peak emission intensity increases by over 300% from position 1 to position 4 on the sample. This is accompanied by a 230% increase or broadening in the FWHM from 21 to 49 nm from position 1 to 4. This high degree in variability from position to position on the sample strongly suggests that a refined measurement technique must be developed to ensure that an accurate measurement of the entire emission from the waveguide is measured.

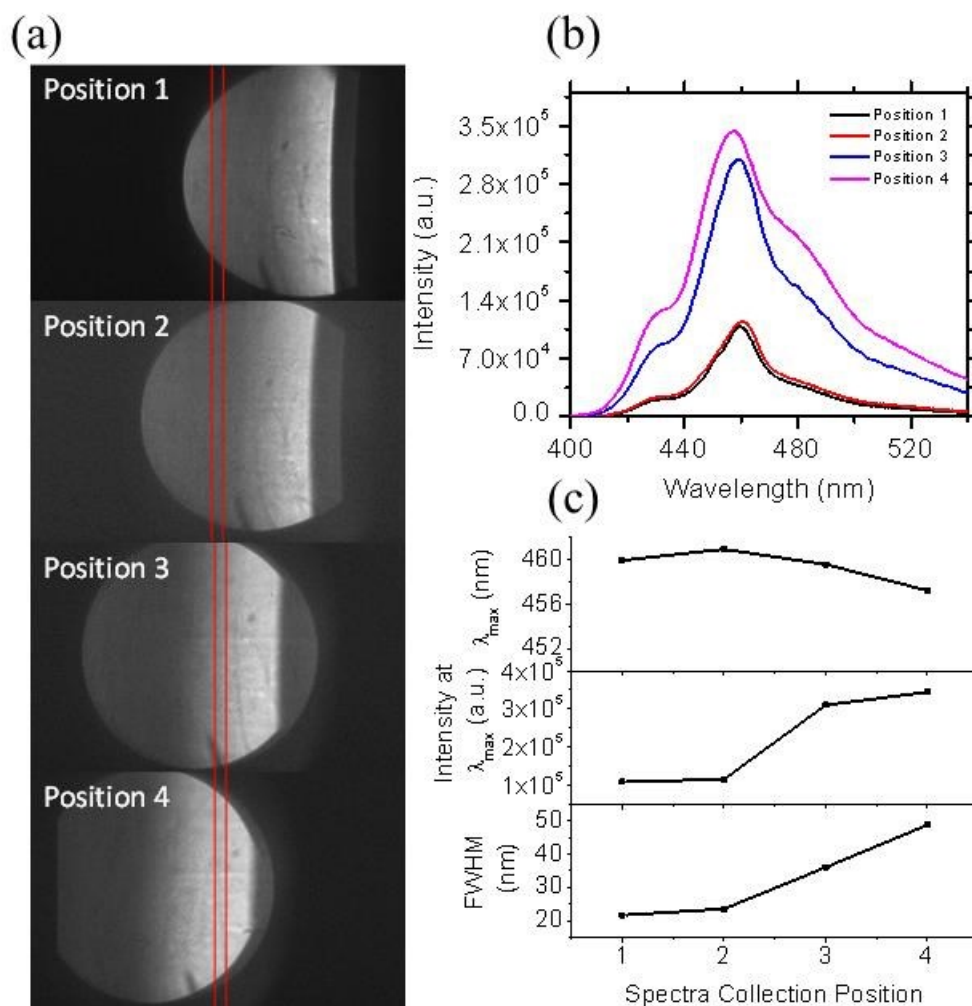


Figure AC7. (a) Images of the outcoupled edge emission from a neat PFO SMI waveguide with 50 nm Ag film thickness. Regions bounded in red are where gain spectra shown in (b) were collected. (c) Analysis of peak emission wavelength, maximum emission intensity and FWHM of spectra in (b). Color available in electronic copy.

To accurately and reproducibly measure the outcoupled edge emission from the SMI waveguides, the focusing optics between the edge of the sample were manipulated to reduce the original 4500 μm diameter spot (Fig.AC8(a)) incident on the spectrometer CCD by 5.6X to <800 μm (see Fig AC8(b)). This reduced spot size allowed a significantly larger percentage of the total emission to be analyzed when the input slits were narrowed to 250 μm to collect a spectrum ((see

Fig AC8(c)), thereby increasing the accuracy of the measurement and decreasing variability in from sample to sample.

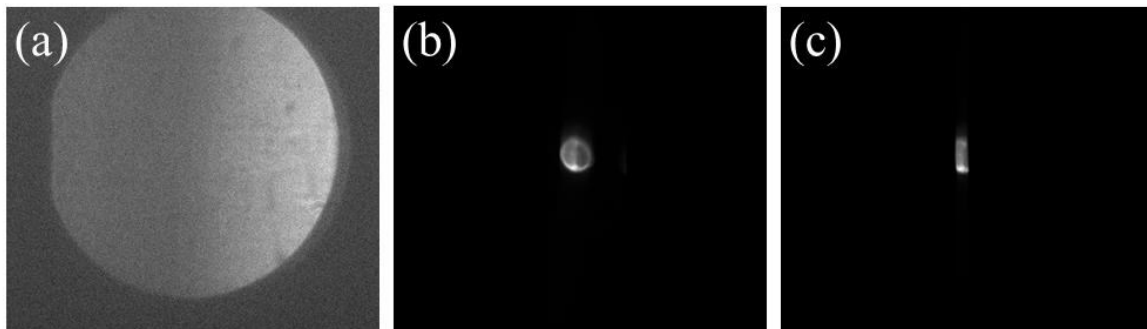


Figure AC8. Spectrometer CCD images of the outcoupled edge emission from a neat PFO SMI waveguide with 50 nm Ag film thickness focused to a 4500 μm diameter spot (a) and an 800 μm diameter spot (b) with the spectrometer input aperture slits fully open (a,b) and closed to 250 μm in diameter (c).

After the spot size was reduced to 800 μm in diameter, a new set of unpolarized gain spectra were collected from a neat PFO only waveguide, and Ag metal containing SMI waveguides with film thicknesses of 35, 50, 65, and 100 nm under a power density of 0.64 W/cm^2 (see Fig. AC9). Each gain spectrum is plotted separately in Fig. AC9(a)-(e) on an emission intensity scale (y-axis) appropriate for each spectrum and also together in a single plot in Fig.AC1(f) on the same y-axis scale accurately show the difference in the resultant emission intensity as a function of metal film thickness. Plots of the peak emission wavelength, maximum emission intensity, and FWHM as functions of Ag film thickness are shown in Fig. AC10 (a)-(c), respectively, to visually represent the changes in the resultant emission spectra.

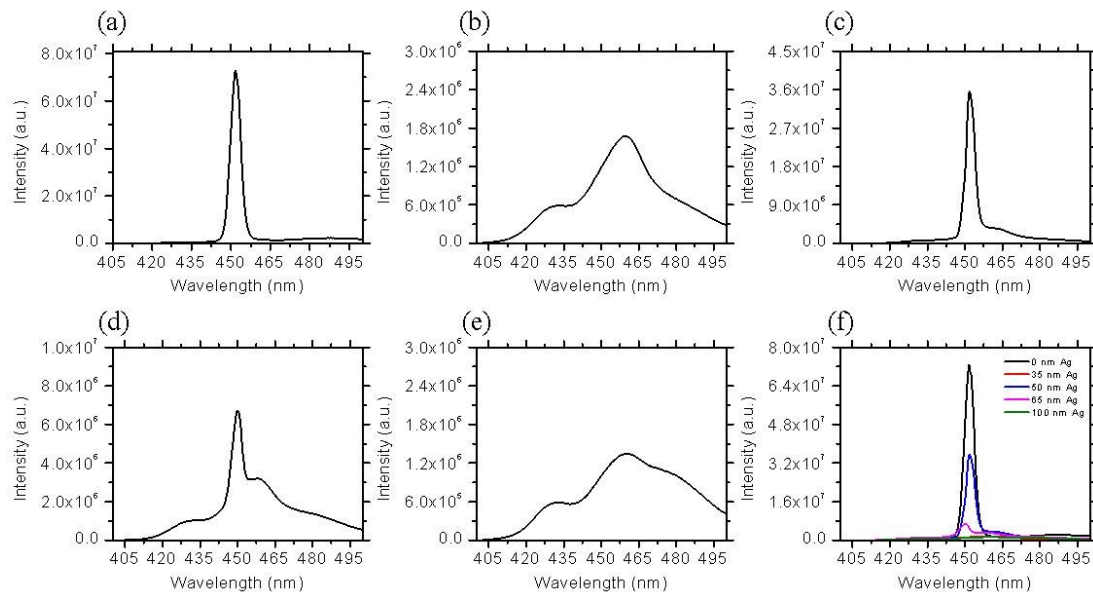


Figure AC9. Gain spectra of a PFO-only waveguide (a) and SMI waveguides with metal film thicknesses of 35 (b), 50 (c), 65 (d), and 100 nm (d), under 355 nm excitation with a power density of 0.64 W/cm^2 . Shown in (f) is a compilation plot of spectra shown in (a)–(e).

The peak emission wavelengths of the new set of measurements show a slightly different trend than in the previous gain spectra collected with a large incident spot size, however the range of values was virtually identical. The peak wavelengths recorded were: 451.75 nm, 459.64 nm, 451.79 nm, 449.83 nm, and 460.33 for waveguides with Ag metal film thicknesses of 0 (PFO-only), 35, 50, 65, and 100 nm, respectively. In the previous measurement sets made with a large spot size, the SMI waveguide with a 50 nm Ag film thickness resulted in the most redshifted emission relative to the PFO only waveguide. In contrast, these measurements show that the peak emission wavelength of the 50 nm Ag SMI waveguide is virtually identical to that of the PFO only waveguide.

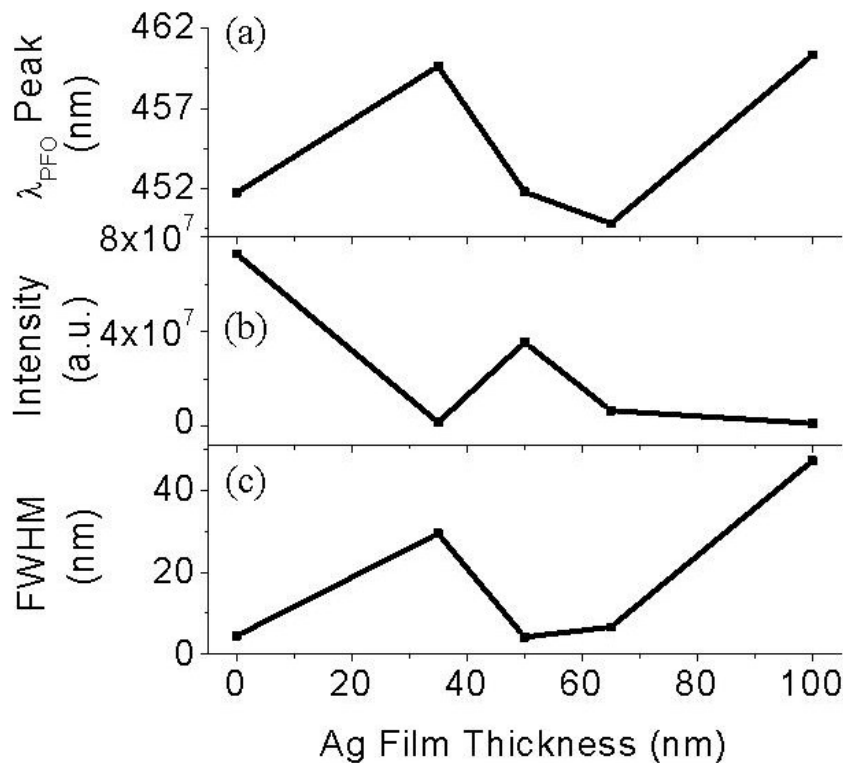


Figure AC10. Peak emission wavelength (a), peak emission intensity (b), and FWHM (c) of waveguides with Ag film thicknesses of: 0 (PFO only), 35, 50, 65, and 100 nm under a power density of 0.64 W/cm² as a function of metal film thickness.

The trend in maximum emission intensity for the gain measurements collected with the small 800 μm diameter spot is identical to that observed from the spectra collected with the large 4500 μm diameter spot (see Fig. AC9(b)). The PFO-only waveguide (0 nm Ag film thickness) exhibited the greatest emission intensity of all waveguides, with an emission that was approximately 100% greater than the most brightly emitting waveguide containing a metal film (i.e., the 50 nm Ag film case). When comparing the trend in maximum emission intensity within the Ag film containing waveguide, the trend is also identical to that observed previously; the emission intensity increases with increasing film thickness from 35 nm to 50 nm, where it reaches a maximum, followed by a sharp decrease in intensity with increasing film thickness.

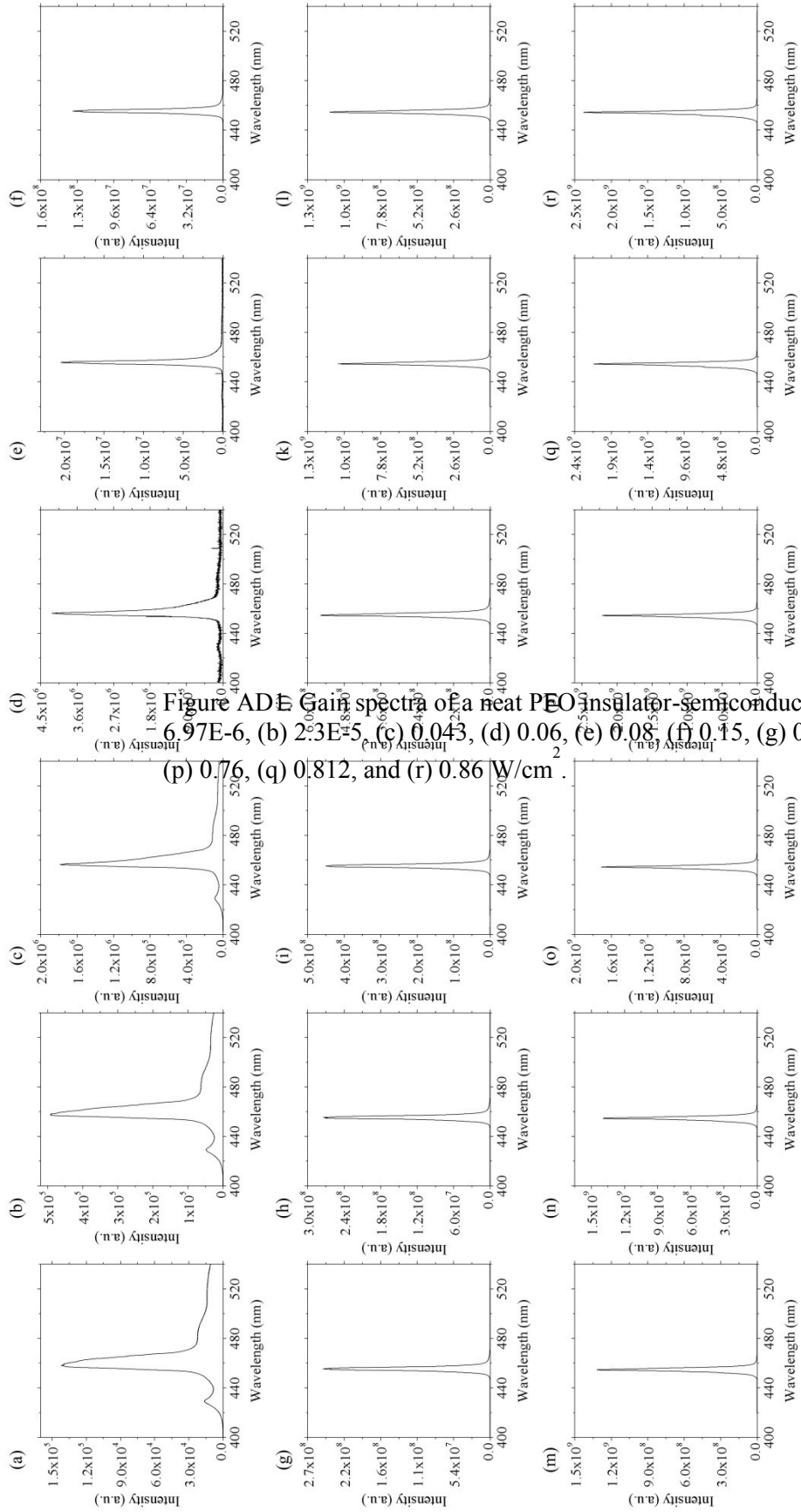
The trend in FWHM is also identical to that observed from the spectra collected with the large 4500 μm diameter spot (see Fig. AC9(c), however the values merit close attention. As a function of metal film thickness, the calculated FWHM values are: 4.484 nm, 29.49 nm, 4.21 nm, 6.59 nm, and 47.28 nm for waveguides with Ag metal film thicknesses of 0 (PFO-only), 35, 50, 65, and 100 nm, respectively. Thus, as metal film thickness increases from 35 nm to 50 nm the FWHM narrows, followed by significant broadening with increasing metal film thickness. As expected, the PFO-only (0 nm Ag) waveguide exhibited a narrow FWHM; however, the 50 nm Ag SMI waveguide exhibits a slightly narrower FWHM value than the PFO-only waveguide. Based on spectral resolution limitation of the 250 μm input slit or spectrometer gratings, these values may for all intense purposes be considered equal.

Appendix D

Spectra of Pump Power Dependent Emission Spectra of neat PFO ISI and ISMI

Waveguides

Figures are laid out in landscape format on the following pages in this section.



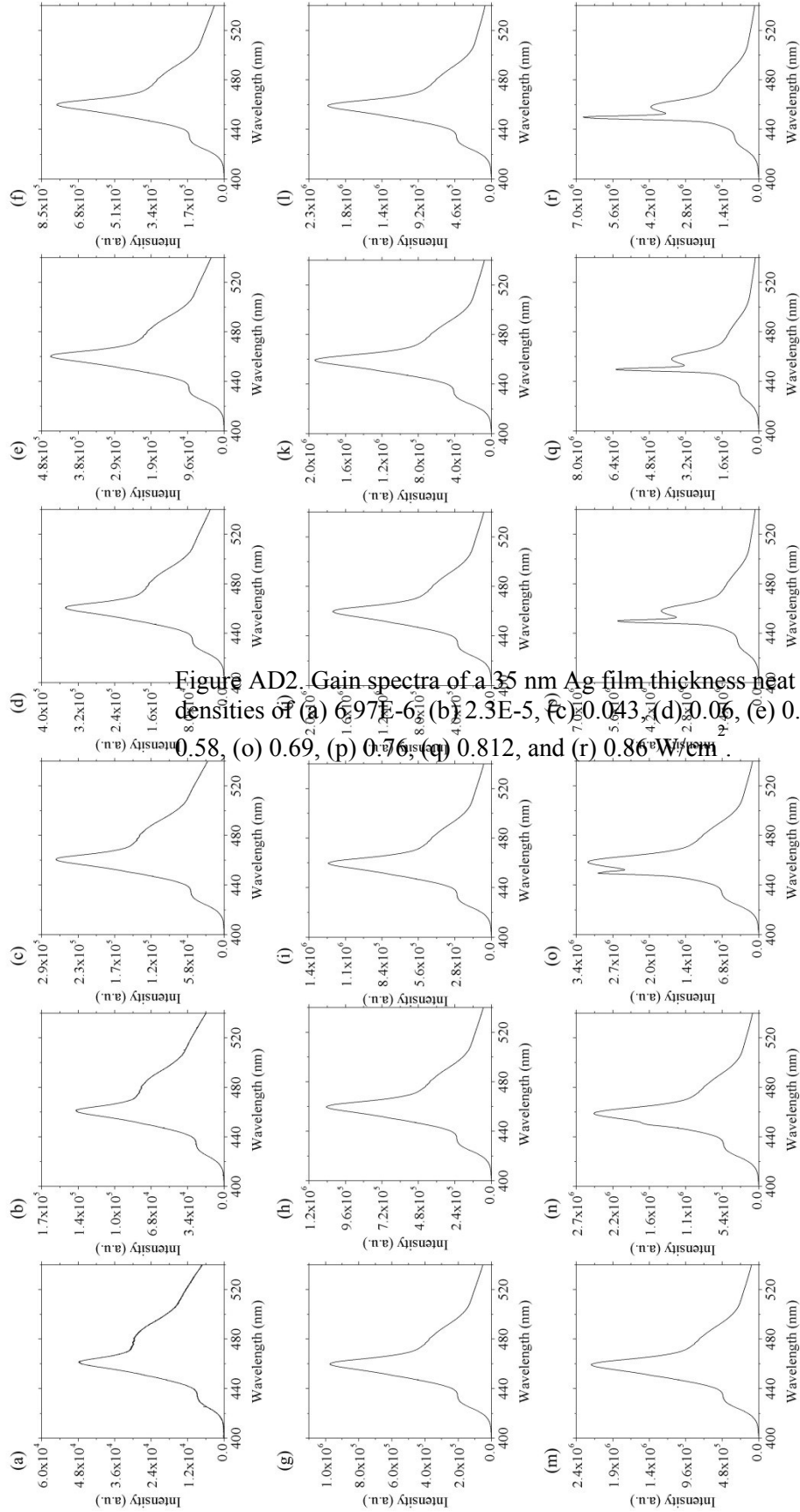
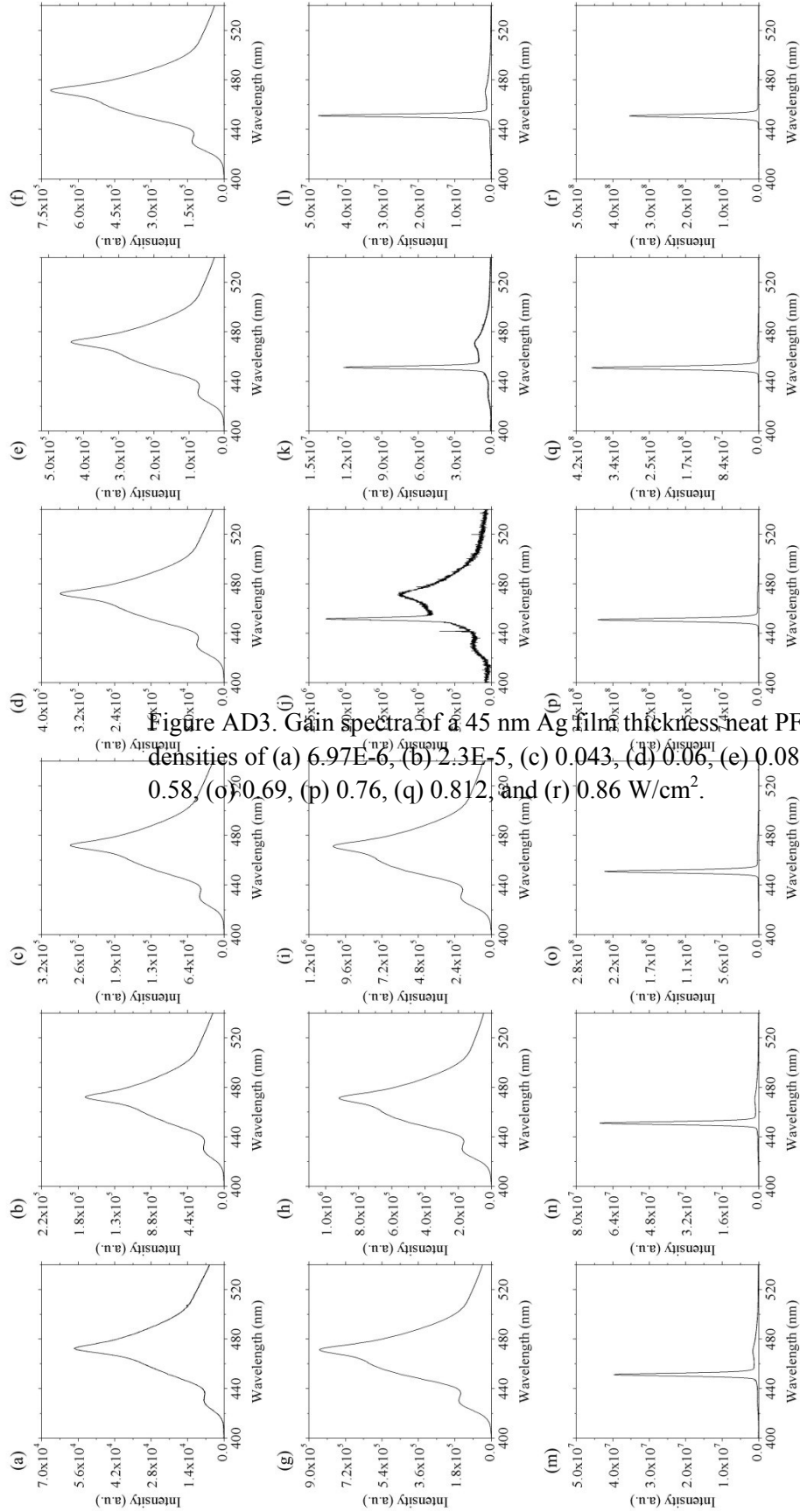


Figure AD2. Gain spectra of a 35 nm Ag film thickness at PFO insulator-semiconductor-metal densities of (a) 0.07, (b) 0.08, (c) 0.09, (d) 0.10, (e) 0.11, (f) 0.12, (g) 0.13, (h) 0.14, (i) 0.15, (j) 0.16, (k) 0.17, (l) 0.18, (m) 0.19, (n) 0.20, (o) 0.21, (p) 0.22, (q) 0.23, (r) 0.24.



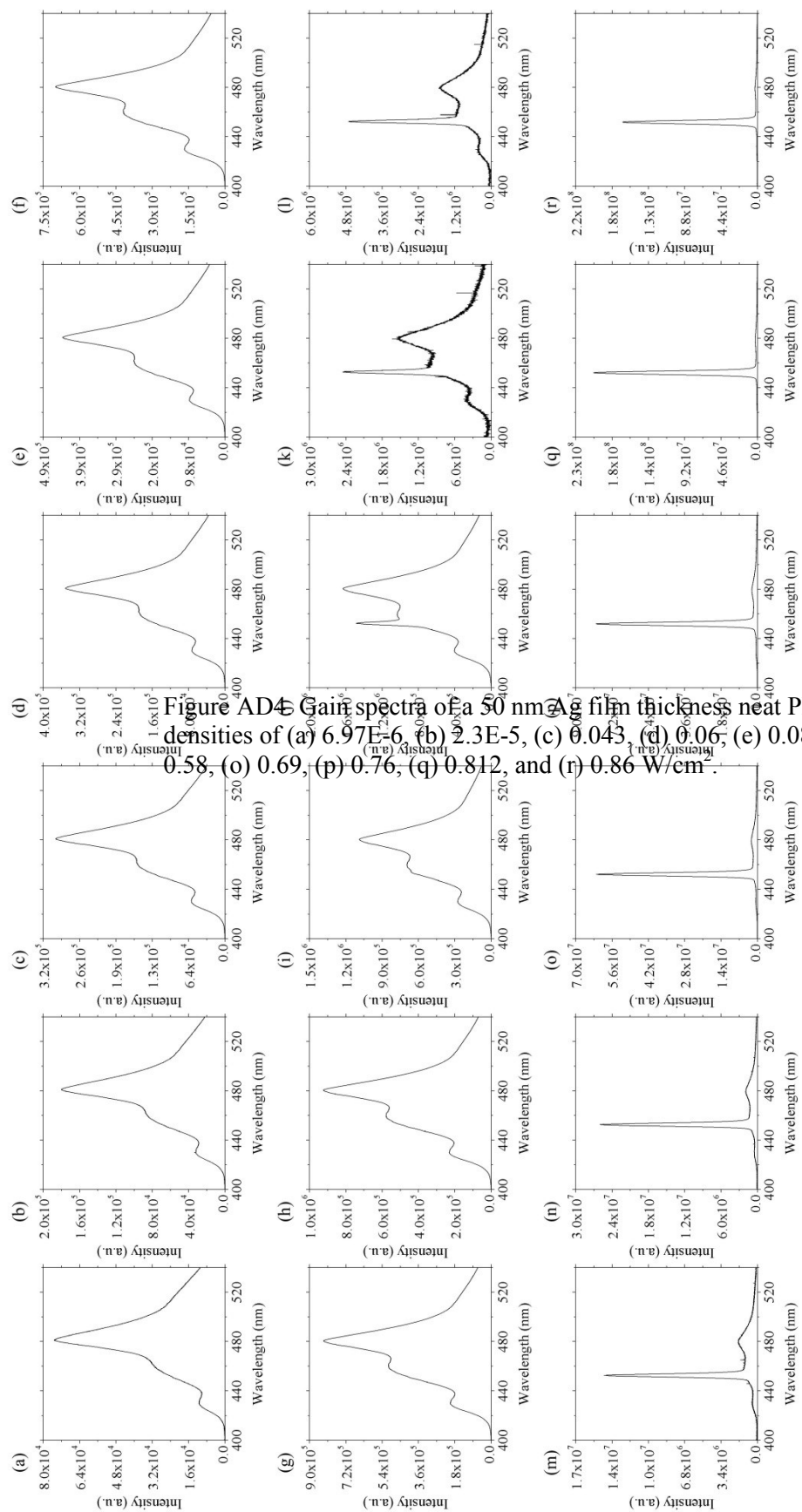
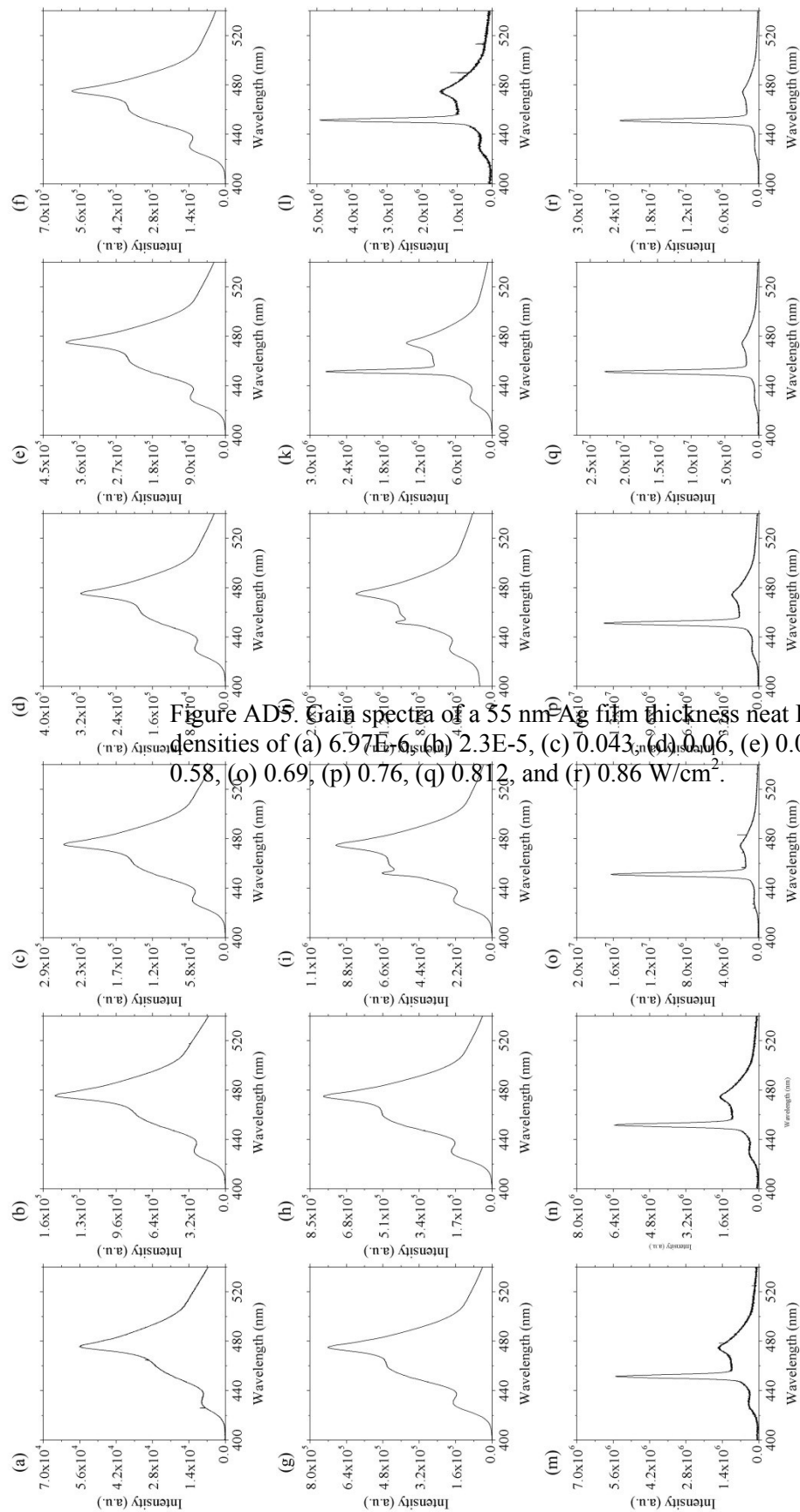
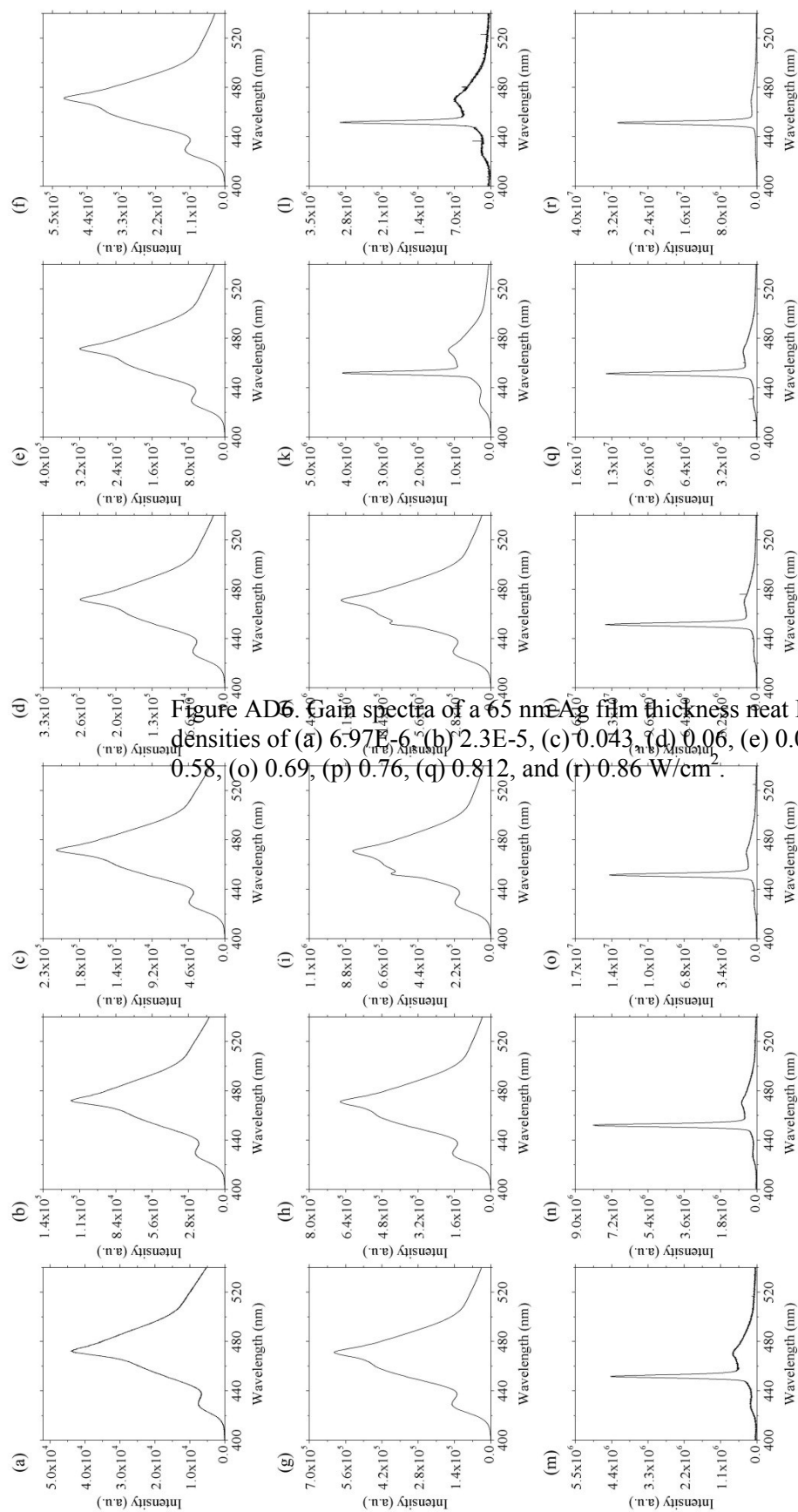
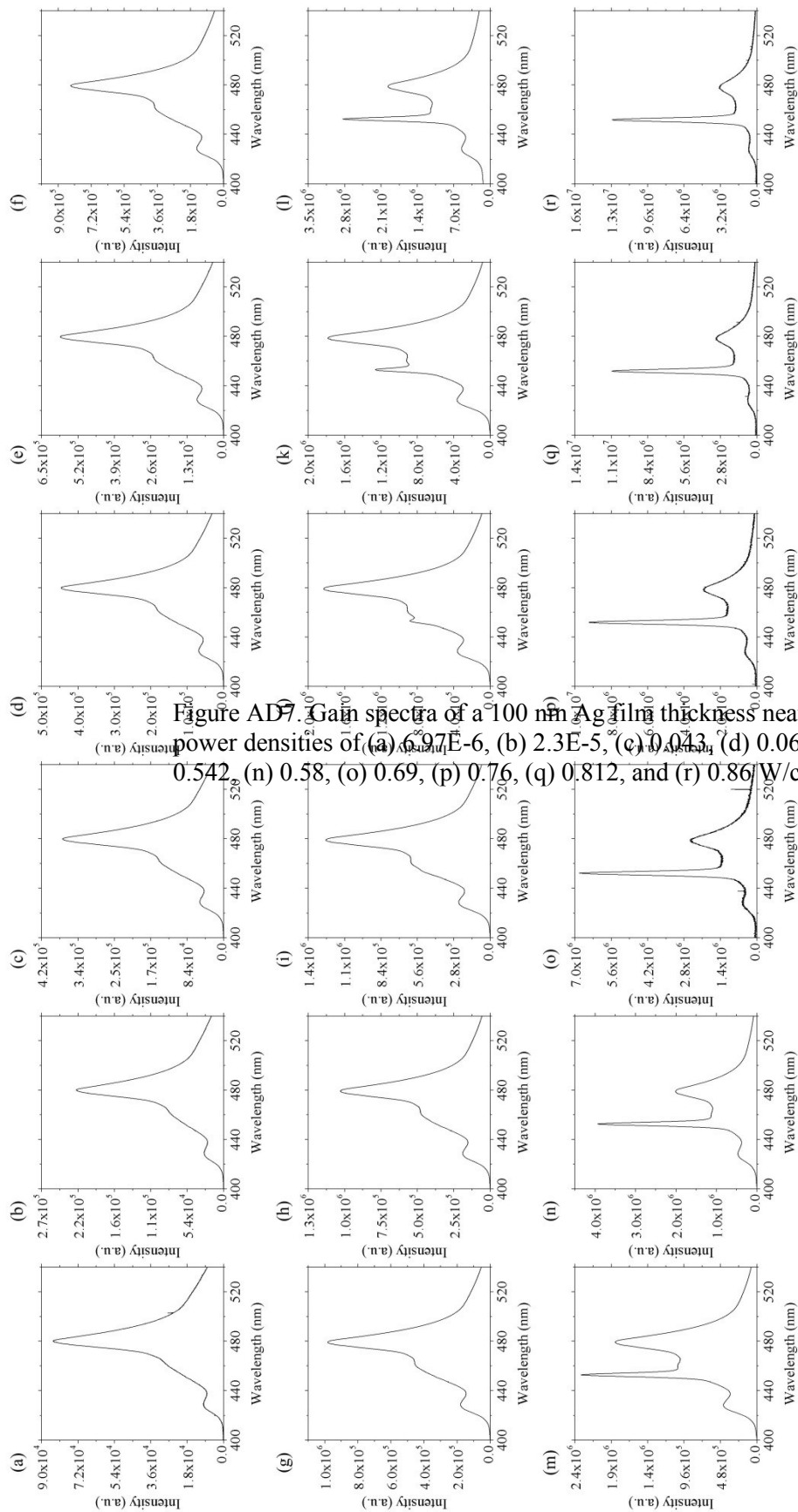


Figure AD4: Gain spectra of a 50 nm Ag film thickness at PFO insulator-semiconductor-metal interface for various laser intensities of (a) 6.97×10^{-6} , (b) 2.3×10^{-5} , (c) 0.043, (d) 0.06, (e) 0.08, (f) 0.15, (g) 0.21, (h) 0.25, (i) 0.29, (j) 0.32, (k) 0.35, (l) 0.38, (m) 0.41, (n) 0.44, (o) 0.47, (p) 0.5, (q) 0.53, (r) 0.56, (s) 0.59, (t) 0.62, (u) 0.65, (v) 0.68, (w) 0.71, (x) 0.74, (y) 0.77, (z) 0.8, (aa) 0.83, (ab) 0.86, (ac) 0.89, (ad) 0.92, (ae) 0.95, (af) 0.98, (ag) 1.01, (ah) 1.04, (ai) 1.07, (aj) 1.1, (ak) 1.13, (al) 1.16, (am) 1.19, (an) 1.22, (ao) 1.25, (ap) 1.28, (aq) 1.31, (ar) 1.34, (as) 1.37, (at) 1.4, (au) 1.43, (av) 1.46, (aw) 1.49, (ax) 1.52, (ay) 1.55, (az) 1.58, (ba) 1.61, (bb) 1.64, (bc) 1.67, (bd) 1.7, (be) 1.73, (bf) 1.76, (bg) 1.79, (bh) 1.82, (bi) 1.85, (bj) 1.88, (bk) 1.91, (bl) 1.94, (bm) 1.97, (bn) 2.0, (bo) 2.03, (bp) 2.06, (bq) 2.09, (br) 2.12, (bs) 2.15, (bt) 2.18, (bu) 2.21, (bv) 2.24, (bw) 2.27, (bx) 2.3, (by) 2.33, (bz) 2.36, (ca) 2.39, (cb) 2.42, (cc) 2.45, (cd) 2.48, (ce) 2.51, (cf) 2.54, (cg) 2.57, (ch) 2.6, (ci) 2.63, (cj) 2.66, (ck) 2.69, (cl) 2.72, (cm) 2.75, (cn) 2.78, (co) 2.81, (cp) 2.84, (cq) 2.87, (cr) 2.9, (cs) 2.93, (ct) 2.96, (cu) 2.99, (cv) 3.02, (cw) 3.05, (cx) 3.08, (cy) 3.11, (cz) 3.14, (da) 3.17, (db) 3.2, (dc) 3.23, (dd) 3.26, (de) 3.29, (df) 3.32, (dg) 3.35, (dh) 3.38, (di) 3.41, (dj) 3.44, (dk) 3.47, (dl) 3.5, (dm) 3.53, (dn) 3.56, (do) 3.59, (dp) 3.62, (dq) 3.65, (dr) 3.68, (ds) 3.71, (dt) 3.74, (du) 3.77, (dv) 3.8, (dw) 3.83, (dx) 3.86, (dy) 3.89, (dz) 3.92, (ea) 3.95, (eb) 3.98, (ec) 4.01, (ed) 4.04, (ee) 4.07, (ef) 4.1, (eg) 4.13, (eh) 4.16, (ei) 4.19, (ej) 4.22, (ek) 4.25, (el) 4.28, (em) 4.31, (en) 4.34, (eo) 4.37, (ep) 4.4, (eq) 4.43, (er) 4.46, (es) 4.49, (et) 4.52, (eu) 4.55, (ev) 4.58, (ew) 4.61, (ex) 4.64, (ey) 4.67, (ez) 4.7, (fa) 4.73, (fb) 4.76, (fc) 4.79, (fd) 4.82, (fe) 4.85, (ff) 4.88, (fg) 4.91, (fh) 4.94, (fi) 4.97, (fj) 5.0, (fk) 5.03, (fl) 5.06, (fm) 5.09, (fn) 5.12, (fo) 5.15, (fp) 5.18, (fq) 5.21, (fr) 5.24, (fs) 5.27, (ft) 5.3, (fu) 5.33, (fv) 5.36, (fw) 5.39, (fx) 5.42, (fy) 5.45, (fz) 5.48, (ga) 5.51, (gb) 5.54, (gc) 5.57, (gd) 5.6, (ge) 5.63, (gf) 5.66, (gg) 5.69, (gh) 5.72, (gi) 5.75, (gj) 5.78, (gk) 5.81, (gl) 5.84, (gm) 5.87, (gn) 5.9, (go) 5.93, (gp) 5.96, (gq) 5.99, (gr) 6.02, (gs) 6.05, (gt) 6.08, (gu) 6.11, (gv) 6.14, (gw) 6.17, (gx) 6.2, (gy) 6.23, (gz) 6.26, (ha) 6.29, (hb) 6.32, (hc) 6.35, (hd) 6.38, (he) 6.41, (hf) 6.44, (hg) 6.47, (hh) 6.5, (hi) 6.53, (hj) 6.56, (hk) 6.59, (hl) 6.62, (hm) 6.65, (hn) 6.68, (ho) 6.71, (hp) 6.74, (hq) 6.77, (hr) 6.8, (hs) 6.83, (ht) 6.86, (hu) 6.89, (hv) 6.92, (hw) 6.95, (hx) 6.98, (hy) 7.01, (hz) 7.04, (ia) 7.07, (ib) 7.1, (ic) 7.13, (id) 7.16, (ie) 7.19, (if) 7.22, (ig) 7.25, (ih) 7.28, (ii) 7.31, (ij) 7.34, (ik) 7.37, (il) 7.4, (im) 7.43, (in) 7.46, (io) 7.49, (ip) 7.52, (iq) 7.55, (ir) 7.58, (is) 7.61, (it) 7.64, (iu) 7.67, (iv) 7.7, (iw) 7.73, (ix) 7.76, (iy) 7.79, (iz) 7.82, (ja) 7.85, (jb) 7.88, (jc) 7.91, (jd) 7.94, (je) 7.97, (jf) 8.0, (jg) 8.03, (jh) 8.06, (ji) 8.09, (jj) 8.12, (jk) 8.15, (jl) 8.18, (jm) 8.21, (jn) 8.24, (jo) 8.27, (jp) 8.3, (jq) 8.33, (jr) 8.36, (js) 8.39, (jt) 8.42, (ju) 8.45, (jv) 8.48, (jw) 8.51, (jx) 8.54, (jy) 8.57, (jz) 8.6, (ka) 8.63, (kb) 8.66, (kc) 8.69, (kd) 8.72, (ke) 8.75, (kf) 8.78, (kg) 8.81, (kh) 8.84, (ki) 8.87, (kj) 8.9, (kk) 8.93, (kl) 8.96, (km) 8.99, (kn) 9.02, (ko) 9.05, (kp) 9.08, (kq) 9.11, (kr) 9.14, (ks) 9.17, (kt) 9.2, (ku) 9.23, (kv) 9.26, (kw) 9.29, (kx) 9.32, (ky) 9.35, (kz) 9.38, (la) 9.41, (lb) 9.44, (lc) 9.47, (ld) 9.5, (le) 9.53, (lf) 9.56, (lg) 9.59, (lh) 9.62, (li) 9.65, (lj) 9.68, (lk) 9.71, (ll) 9.74, (lm) 9.77, (ln) 9.8, (lo) 9.83, (lp) 9.86, (lq) 9.89, (lr) 9.92, (ls) 9.95, (lt) 9.98, (lu) 10.01, (lv) 10.04, (lw) 10.07, (lx) 10.1, (ly) 10.13, (lz) 10.16, (ma) 10.19, (mb) 10.22, (mc) 10.25, (md) 10.28, (me) 10.31, (mf) 10.34, (mg) 10.37, (mh) 10.4, (mi) 10.43, (mj) 10.46, (mk) 10.49, (ml) 10.52, (mn) 10.55, (mo) 10.58, (mp) 10.61, (mq) 10.64, (mr) 10.67, (ms) 10.7, (mt) 10.73, (mu) 10.76, (mv) 10.79, (mw) 10.82, (mx) 10.85, (my) 10.88, (mz) 10.91, (na) 10.94, (nb) 10.97, (nc) 11.0, (nd) 11.03, (ne) 11.06, (nf) 11.09, (ng) 11.12, (nh) 11.15, (ni) 11.18, (nj) 11.21, (nk) 11.24, (nl) 11.27, (nm) 11.3, (nn) 11.33, (no) 11.36, (np) 11.39, (nq) 11.42, (nr) 11.45, (ns) 11.48, (nt) 11.51, (nu) 11.54, (nv) 11.57, (nw) 11.6, (nx) 11.63, (ny) 11.66, (nz) 11.69, (oa) 11.72, (ob) 11.75, (oc) 11.78, (od) 11.81, (oe) 11.84, (of) 11.87, (og) 11.9, (oh) 11.93, (oi) 11.96, (oj) 11.99, (ok) 12.02, (ol) 12.05, (om) 12.08, (on) 12.11, (oo) 12.14, (op) 12.17, (oq) 12.2, (or) 12.23, (os) 12.26, (ot) 12.29, (ou) 12.32, (ov) 12.35, (ow) 12.38, (ox) 12.41, (oy) 12.44, (oz) 12.47, (pa) 12.5, (pb) 12.53, (pc) 12.56, (pd) 12.59, (pe) 12.62, (pf) 12.65, (pg) 12.68, (ph) 12.71, (pi) 12.74, (pj) 12.77, (pk) 12.8, (pl) 12.83, (pm) 12.86, (pn) 12.89, (po) 12.92, (pp) 12.95, (pq) 12.98, (pr) 13.01, (ps) 13.04, (pt) 13.07, (pu) 13.1, (pv) 13.13, (pw) 13.16, (px) 13.19, (py) 13.22, (pz) 13.25, (qa) 13.28, (qb) 13.31, (qc) 13.34, (qd) 13.37, (qe) 13.4, (qf) 13.43, (qg) 13.46, (qh) 13.49, (qi) 13.52, (qj) 13.55, (qk) 13.58, (ql) 13.61, (qm) 13.64, (qn) 13.67, (qo) 13.7, (qp) 13.73, (qq) 13.76, (qr) 13.79, (qs) 13.82, (qt) 13.85, (qu) 13.88, (qv) 13.91, (qw) 13.94, (qx) 13.97, (qy) 14.0, (qz) 14.03, (ra) 14.06, (rb) 14.09, (rc) 14.12, (rd) 14.15, (re) 14.18, (rf) 14.21, (rg) 14.24, (rh) 14.27, (ri) 14.3, (rj) 14.33, (rk) 14.36, (rl) 14.39, (rm) 14.42, (rn) 14.45, (ro) 14.48, (rp) 14.51, (rq) 14.54, (rr) 14.57, (rs) 14.6, (rt) 14.63, (ru) 14.66, (rv) 14.69, (rw) 14.72, (rx) 14.75, (ry) 14.78, (rz) 14.81, (sa) 14.84, (sb) 14.87, (sc) 14.9, (sd) 14.93, (se) 14.96, (sf) 14.99, (sg) 15.02, (sh) 15.05, (si) 15.08, (sj) 15.11, (sk) 15.14, (sl) 15.17, (sm) 15.2, (sn) 15.23, (so) 15.26, (sp) 15.29, (sq) 15.32, (sr) 15.35, (ss) 15.38, (st) 15.41, (su) 15.44, (sv) 15.47, (sw) 15.5, (sx) 15.53, (sy) 15.56, (sz) 15.59, (ta) 15.62, (tb) 15.65, (tc) 15.68, (td) 15.71, (te) 15.74, (tf) 15.77, (tg) 15.8, (th) 15.83, (ti) 15.86, (tj) 15.89, (tk) 15.92, (tl) 15.95, (tm) 15.98, (tn) 16.01, (to) 16.04, (tp) 16.07, (tq) 16.1, (tr) 16.13, (ts) 16.16, (tt) 16.19, (tu) 16.22, (tv) 16.25, (tw) 16.28, (tx) 16.31, (ty) 16.34, (tz) 16.37, (ua) 16.4, (ub) 16.43, (uc) 16.46, (ud) 16.49, (ue) 16.52, (uf) 16.55, (ug) 16.58, (uh) 16.61, (ui) 16.64, (uj) 16.67, (uk) 16.7, (ul) 16.73, (um) 16.76, (un) 16.79, (uo) 16.82, (up) 16.85, (uq) 16.88, (ur) 16.91, (us) 16.94, (ut) 16.97, (uu) 17.0, (uv) 17.03, (uw) 17.06, (ux) 17.09, (uy) 17.12, (uz) 17.15, (va) 17.18, (vb) 17.21, (vc) 17.24, (vd) 17.27, (ve) 17.3, (vf) 17.33, (vg) 17.36, (vh) 17.39, (vi) 17.42, (vj) 17.45, (vk) 17.48, (vl) 17.51, (vm) 17.54, (vn) 17.57, (vo) 17.6, (vp) 17.63, (vq) 17.66, (vr) 17.69, (vs) 17.72, (vt) 17.75, (vu) 17.78, (vv) 17.81, (vw) 17.84, (vx) 17.87, (vy) 17.9, (vz) 17.93, (wa) 17.96, (wb) 17.99, (wc) 18.02, (wd) 18.05, (we) 18.08, (wf) 18.11, (wg) 18.14, (wh) 18.17, (wi) 18.2, (wj) 18.23, (wk) 18.26, (wl) 18.29, (wm) 18.32, (wn) 18.35, (wo) 18.38, (wp) 18.41, (wq) 18.44, (wr) 18.47, (ws) 18.5, (wt) 18.53, (wu) 18.56, (wv) 18.59, (ww) 18.62, (wx) 18.65, (wy) 18.68, (wz) 18.71, (xa) 18.74, (xb) 18.77, (xc) 18.8, (xd) 18.83, (xe) 18.86, (xf) 18.89, (xg) 18.92, (xh) 18.95, (xi) 18.98, (xj) 19.01, (xk) 19.04, (xl) 19.07, (xm) 19.1, (xn) 19.13, (xo) 19.16, (xp) 19.19, (xq) 19.22, (xr) 19.25, (xs) 19.28, (xt) 19.31, (xu) 19.34, (xv) 19.37, (xw) 19.4, (xx) 19.43, (xy) 19.46, (xz) 19.49, (ya) 19.52, (yb) 19.55, (yc) 19.58, (yd) 19.61, (ye) 19.64, (yf) 19.67, (yg) 19.7, (yh) 19.73, (yi) 19.76, (yj) 19.79, (yk) 19.82, (yl) 19.85, (ym) 19.88, (yn) 19.91, (yo) 19.94, (yp) 19.97, (yq) 20.0, (yr) 20.03, (ys) 20.06, (yt) 20.09, (yu) 20.12, (yv) 20.15, (yw) 20.18, (yx) 20.21, (yy) 20.24, (yz) 20.27, (za) 20.3, (zb) 20.33, (zc) 20.36, (zd) 20.39, (ze) 20.42, (zf) 20.45, (zg) 20.48, (zh) 20.51, (zi) 20.54, (zj) 20.57, (zk) 20.6, (zl) 20.63, (zm) 20.66, (zn) 20.69, (zo) 20.72, (zp) 20.75, (zq) 20.78, (zr) 20.81, (zs) 20.84, (zt) 20.87, (zu) 20.9, (zv) 20.93, (zw) 20.96, (zx) 20.99, (zy) 21.02, (zz) 21.05, (aa) 21.08, (ab) 21.11, (ac) 21.14, (ad) 21.17, (ae) 21.2, (af) 21.23, (ag) 21.26, (ah) 21.29, (ai) 21.32, (aj) 21.35, (ak) 21.38, (al) 21.41, (am) 21.44, (an) 21.47, (ao) 21.5, (ap) 21.53, (aq) 21.56, (ar) 21.59, (as) 21.62, (at) 21.65, (au) 21.68, (av) 21.71, (aw) 21.74, (ax) 21.77, (ay) 21.8, (az) 21.83, (ba) 21.86, (bb) 21.89, (bc) 21.92, (bd) 21.95, (be) 21.98, (bf) 22.01, (bg) 22.04, (bh) 22.07, (bi) 22.1, (bj) 22.13, (bk) 22.16, (bl) 22.19, (bm) 22.22, (bn) 22.25, (bo) 22.28, (bp) 22.31, (bq) 22.34, (br) 22.37, (bs) 22.4, (bt) 22.43, (bu) 22.46, (bv) 22.49, (bw) 22.52, (bx) 22.55, (by) 22.58, (bz) 22.61, (ca) 22.64, (cb) 22.67, (cc) 22.7, (cd) 22.73, (ce) 22.76, (cf) 22.79, (cg) 22.82, (ch) 22.85, (ci) 22.88, (cj) 22.91, (ck) 22.94, (cl) 22.97, (cm) 23.0, (cn) 23.03, (co) 23.06, (cp) 23.09, (cq) 23.12, (cr) 23.15, (cs) 23.18, (ct) 23.21, (cu) 23.24, (cv) 23.27, (cw) 23.3, (cx) 23.33, (cy) 23.36, (cz) 23.39, (da) 23.42, (db) 23.45, (dc) 23.48, (dd) 23.51, (de) 23.54, (df) 23.57, (dg) 23.6, (dh) 23.63, (di) 23.66, (dj) 23.69, (dk) 23.72, (dl) 23.75, (dm) 23.78, (dn) 23.81, (do) 23.84, (dp) 23.87, (dq) 23.9, (dr) 23.93, (ds) 23.96, (dt) 23.99, (du) 24.02, (dv) 24.05, (dw) 24.08, (dx) 24.11, (dy) 24.14, (dz) 24.17, (ea) 24.2, (eb) 24.23, (ec) 24.26, (ed) 24.29, (ee) 24.32, (ef) 24.35, (eg) 24.38, (eh) 24.41, (ei) 24.44, (ej) 24.47, (ek) 24.5, (el) 24.53, (em) 24.56, (en) 24.59, (eo) 24.62, (ep) 24.65, (eq) 24.68, (er) 24.71, (es) 24.74, (et) 24.77, (eu) 24.8, (ev) 24.83, (ew) 24.86, (ex) 24.89, (ey) 24.92, (ez) 24.95, (fa) 24.98, (fb) 25.01, (fc) 25.04, (fd) 25.07, (fe) 25.1, (ff) 25.13, (fg) 25.16, (fh) 25.19, (fi) 25.22, (fj) 25.25, (fk) 25.28, (fl) 25.31, (fm) 25.34, (fn) 25.37, (fo) 25.4, (fp) 25.43, (fq) 25.46, (fr) 25.49, (fs) 25.52, (ft) 25.55, (fu) 25.58, (fv) 25.61, (fw) 25.64, (fx) 25.67, (fy) 25.7, (fz) 25.73, (ga) 25.76, (gb) 25.79, (gc) 25.82, (gd) 25.85, (ge) 25.88, (gf) 25.91, (gg) 25.94, (gh) 25.97, (gi) 26.0, (gj) 26.03, (gk) 26.06, (gl) 26.09, (gm) 26.12, (gn) 26.15, (go) 26.18, (gp) 26.21, (gq) 26.24, (gr) 26.27, (gs) 26.3, (gt) 26.33, (gu) 26.36, (gv) 26.39, (gw) 26.42, (gx) 26.45, (gy) 26.48, (gz) 26.51, (ha) 26.54, (hb) 26.57, (hc) 26.6, (hd) 26.63, (he) 26.66, (hf) 26.69, (hg) 26.72, (hh) 26.75, (hi) 26.78, (hj) 26.81, (hk) 26.84, (hl) 26.87, (hm) 26.9, (hn) 26.93, (ho) 26.96, (hp) 26.99, (hq) 27.02, (hr) 27.05, (hs) 27.08, (ht) 27.11, (hu) 27.14, (hv) 27.17, (hw) 27.2, (hx) 27.23, (hy) 27.26, (hz) 27.29, (ia) 27.32, (ib) 27.35, (ic) 27.38, (id) 27.41, (ie) 27.44, (if) 27.47, (ig) 27.5, (ih) 27.53, (ii) 27.56, (ij) 27.59, (ik) 27.62, (il) 27.65, (im) 27.68, (in) 27.71, (io) 27.74, (ip) 27.77, (iq) 27.8, (ir) 27.83, (is) 27.86, (it) 27.89, (iu) 27.92, (iv) 27.95, (iw) 27.98, (ix) 28.01, (iy) 28.04, (iz) 28.07, (ja) 28.1, (jb) 28.13, (jc) 28.16, (jd) 28.19, (je) 28.22, (jf) 28.25, (jg) 28.28, (jh) 28.31, (ji) 28.34, (jj) 28.37, (jk) 28.4, (jl) 28.43, (jm) 28.46, (jn) 28.49, (jo) 28.52, (jp) 28.55, (jq) 28.58, (jr) 28.61, (js) 28.64, (jt) 28.67, (ju) 28.7, (jv) 28.73, (jw) 28.76, (jx) 28.79, (jy) 28.82, (jz) 28.85, (ka) 28.88, (kb) 28.91, (kc) 28.94, (kd) 28.97, (ke) 29.0, (kf) 29.03, (kg) 29.06, (kh) 29.09, (ki) 29.12, (kj) 29.15, (kl) 29.18, (km) 29.21, (kn) 29.24, (ko) 29.27, (kp) 29.3, (kq) 29.33, (kr) 29.36, (ks) 29.39, (kt) 29.42, (ku) 29.45, (kv) 29.48, (kw) 29.51, (kx) 29.54, (ky) 29.57, (kz) 29.6, (la) 29.63, (lb) 29.66, (lc) 29.69, (ld) 29.72, (le) 29.75, (lf) 29.78, (lg) 29.81, (lh) 29.84, (li) 29.87, (lj) 29.9, (lk) 29.93, (lm) 29.96, (ln) 29.99, (lo) 30.02, (lp) 30.05, (lq) 30.08, (lr) 30.11, (ls) 30.14, (lt) 30.17, (lu) 30.2, (lv) 30.23, (lw) 30.26, (lx) 30.29, (ly) 30.32, (lz) 30.35, (ma) 30.38, (mb) 30.41, (mc) 30.44, (md) 30.47, (me) 30.5, (mf) 30.53, (mg) 30.56, (mh) 30.59, (mi) 30.62, (mj) 30.65, (mk) 30.68, (ml) 30.71, (mn) 30.74, (mo) 30.77, (mp) 30.8, (mq) 30.83, (mr) 30.86, (ms) 30.89, (mt) 30.92, (mu) 30.95, (mv) 30.98, (mw) 31.01, (mx) 31.04, (my) 31.07, (mz) 31.1, (na) 31.13, (nb) 31.16, (nc) 31.19, (nd) 31.22, (ne) 31.25, (nf) 31.28, (ng) 31.31, (nh) 31.34, (ni) 31.37, (nj) 31.4, (nk) 31.43, (nl) 31.46, (nm) 31.49, (nn) 31.52, (no) 31.55, (np) 31.58, (nq) 31.61, (nr) 31.64, (ns) 31.67, (nt) 31.7, (nu) 31.73, (nv) 31.76, (nw) 31.79, (nx) 31.82, (ny) 31.85, (nz) 31.88, (oa) 31.91, (ob) 31.94, (oc) 31.97, (od) 32.0, (oe) 32.03, (of) 32.06, (og) 32.09, (oh) 32.12, (oi) 32.15, (oj) 32.18, (ok) 32.21, (ol) 32.24, (om) 32.27, (on) 32.3, (oo) 32.33, (op) 32.36, (oq) 32.39, (or) 32.42, (os) 32.45, (ot) 32.48, (ou) 32.51, (ov) 32.54, (ow) 32.57, (ox) 32.6, (oy) 32.63, (oz) 32.66, (pa) 32.69, (pb) 32.72, (pc) 32.75, (pd) 32.78, (pe) 32.81, (pf) 32.84, (pg) 32.87, (ph) 32.9, (pi) 32.93, (pj) 32.96, (pk) 32.99, (pl) 33.02, (pm) 33.05, (pn) 33.08, (po) 33.11, (pp) 33.14, (pq) 33.17, (pr) 33.2, (ps) 33.23, (pt) 33.26, (pu) 33.29, (pv) 33.32, (pw) 33.35, (px) 33.38, (py) 33.41, (pz) 33.44, (qa) 33.47, (qb) 33.5, (qc) 33.53, (qd) 33.56, (qe) 33.59, (qf) 33.62, (qg) 33.65, (qh) 33.68, (qi) 33.71, (qj) 33.74, (qk) 33.77, (ql) 33.8, (qm) 33.83, (qn) 33.86, (qo) 33.89, (qp) 33.92, (qq) 33.95, (qr) 33.98, (qs) 34.01, (qt) 34.04, (qu) 34.07, (qv) 34.1, (qw) 34.13, (qx) 34.16, (qy) 34.19, (qz) 34.22, (ra) 34.25, (rb) 34.28, (rc) 34.31, (rd) 34.34, (re) 34.37, (rf) 34.4, (rg) 34.43, (rh) 34.46, (ri) 34.49, (rj) 34.52, (rk) 34.55, (rl) 34.58, (rm) 34.61, (rn) 34.64, (ro) 34.67, (rp) 34.7, (rq) 34.73, (rr) 34.76, (rs) 34.79, (rt) 34.82, (ru) 34.85, (rv) 34.88, (rw) 34.91, (rx) 34.94, (ry) 34.97, (rz) 35.0, (sa) 35.03, (sb) 35.06, (sc) 35.09, (sd) 35.12, (se) 35.15, (sf) 35.18, (sg) 35.21, (sh) 35.24, (si) 35.27, (sj) 35.3, (sk) 35.33, (sl) 35.36, (sm) 35.39, (sn) 35.42, (so) 35.45, (sp) 35.48, (sq) 35.51, (sr) 35.54, (ss) 35.57, (st) 35.6, (su) 35.63, (sv) 35.66, (sw) 35.69, (sx) 35.72, (sy) 35.75, (sz) 35.78, (ta) 35.81, (tb) 35.84, (tc) 35.87, (td) 35.9, (te) 35.93, (tf) 35.96, (tg) 35.99, (th) 36.02, (ti) 36.05, (tj) 36.08, (tk) 36.11, (tl) 36.14, (tm) 36.17, (tn) 36.2, (to) 36.23, (tp) 36.26, (tq) 36.29, (tr) 36.32, (ts) 36.35, (tu) 36.38, (tv) 36.41, (tw) 36.44, (tx) 36.47, (ty) 36.5, (tz) 36.53, (ua) 36.56, (ub) 36.59, (uc) 36.62, (ud) 36.65, (ue) 36.68, (uf) 36.71, (ug) 36.74, (uh) 36.77, (ui) 36.8, (uj) 36.83, (uk







Appendix E

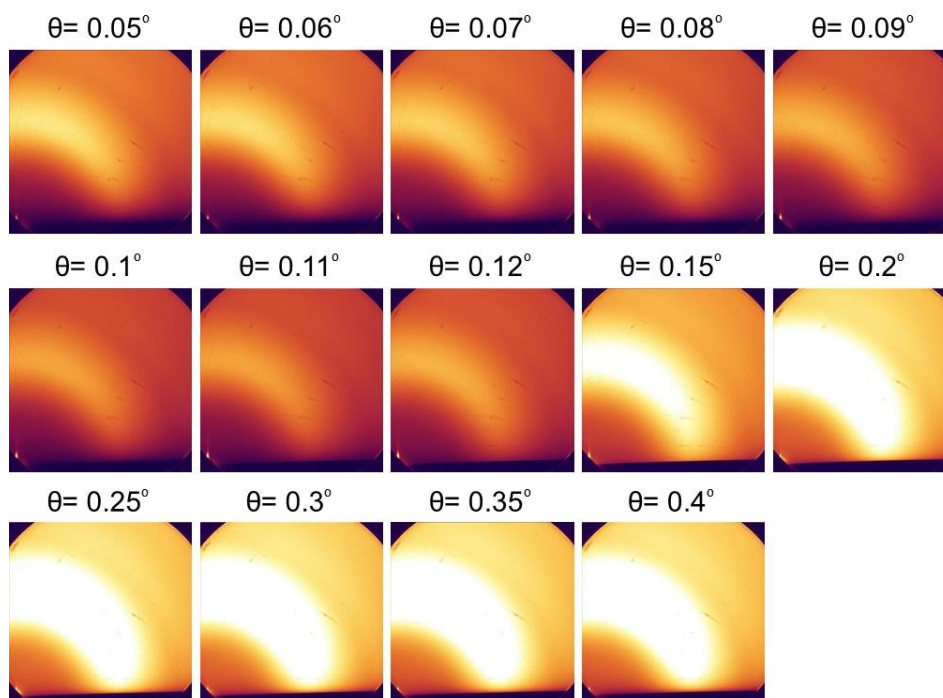


Figure AE.1 GIWAXS profiles of bare VWR glass collected at incident angles ranging from 0.05° to 0.4° . Color available in electronic copy.

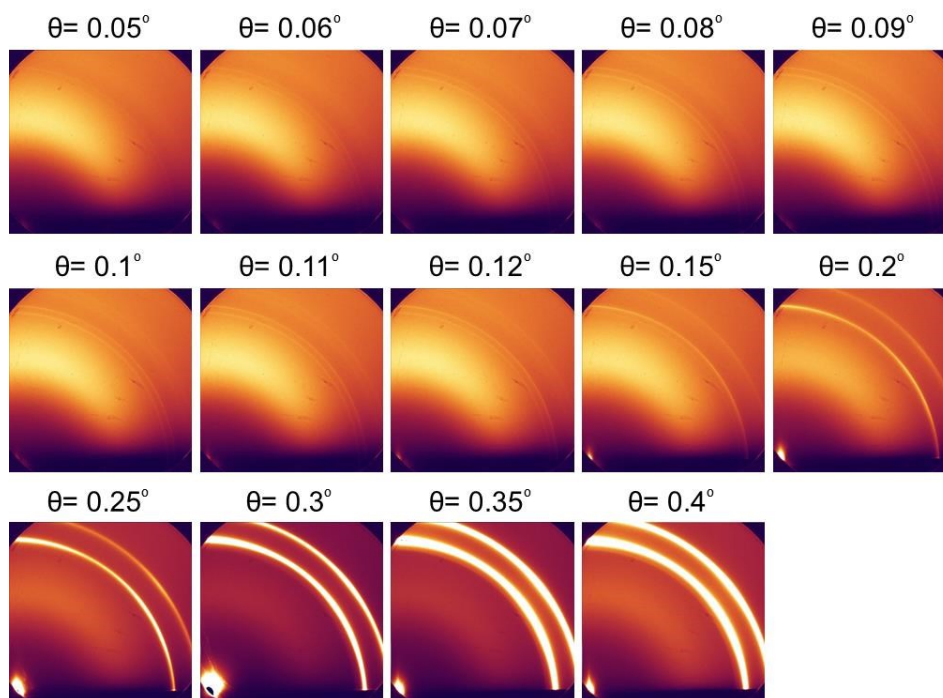


Figure AE.2. GIWAXS profiles of 100 nm Ag on VWR glass collected at incident angles ranging from 0.05° to 0.4° . Color available in electronic copy.

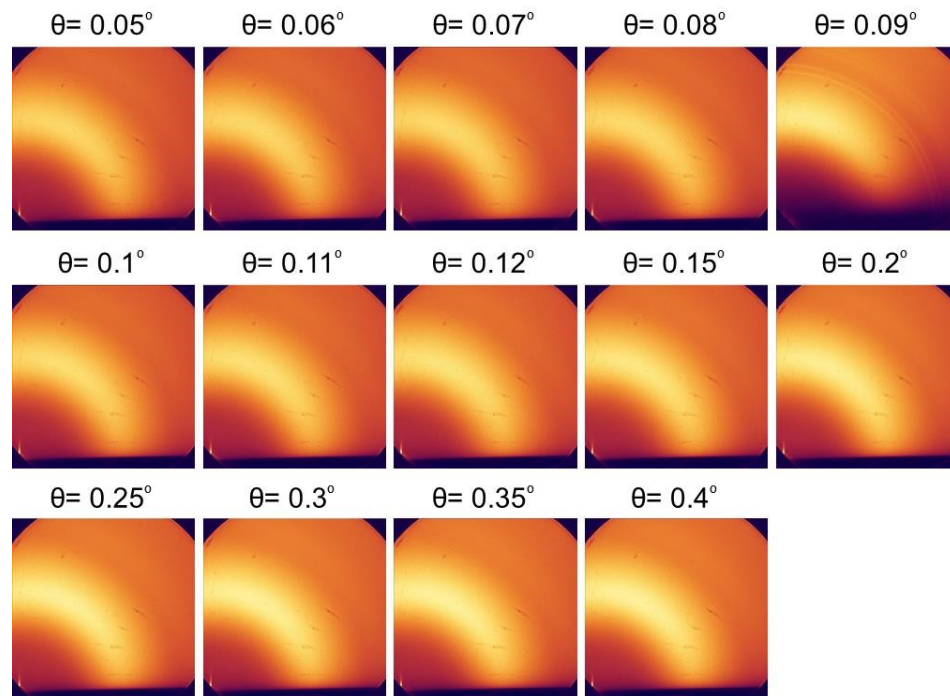


Figure AE3. GIWAXS profiles of 100 nm neat PFO on bare VWR glass collected at incident angles ranging from 0.05° to 0.4° . Color available in electronic copy.

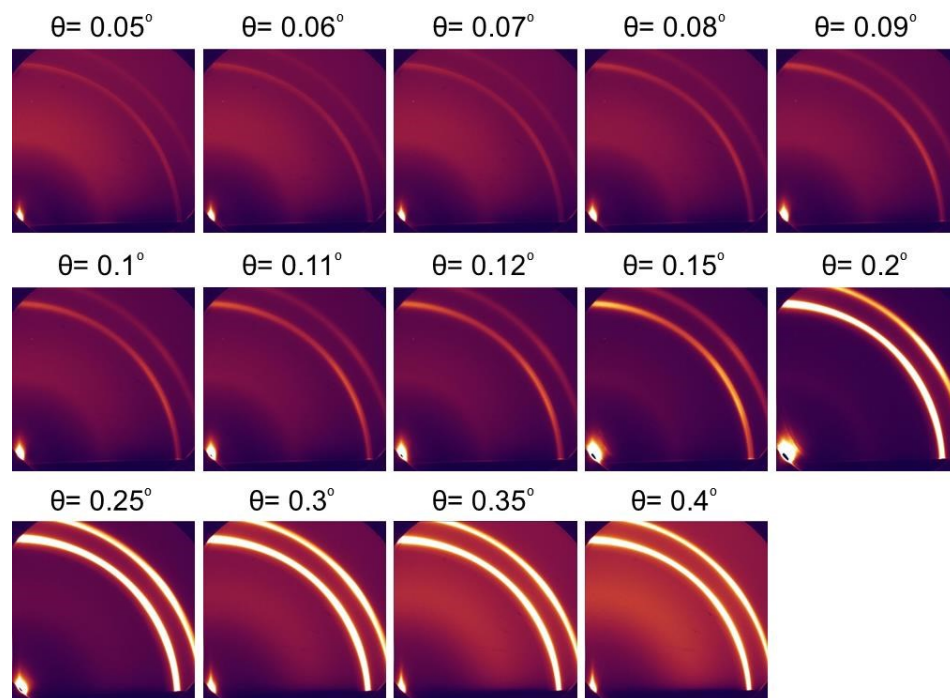


Figure AE4. GIWAXS profiles of 100 nm neat PFO atop 100 nm Ag on VWR glass collected at incident angles ranging from 0.05° to 0.4° . Color available in electronic copy.

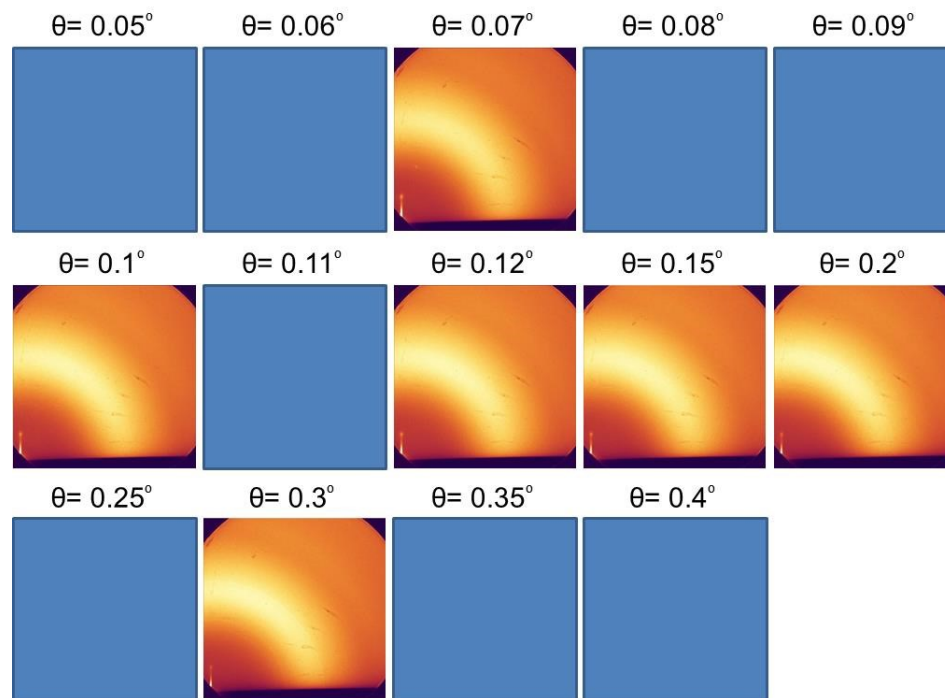


Figure AE5. GIWAXS profiles of 100 nm PFO on bare VWR glass heat treated at 120° C for 30 minutes and quenched on a metal plate collected at incident angles ranging from 0.05° to 0.4°. Color available in electronic copy.

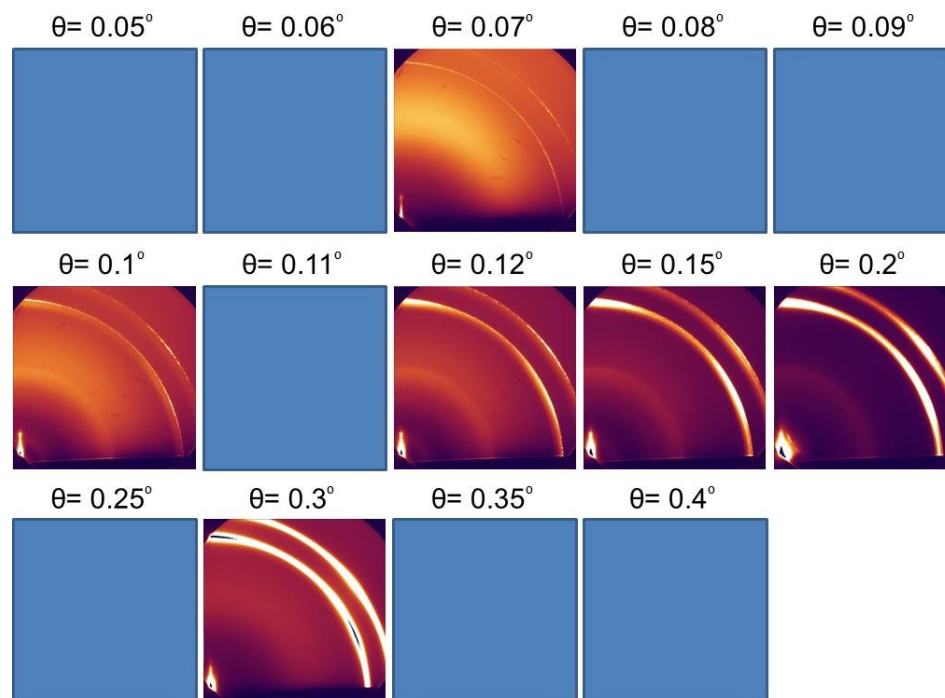


Figure AE6. GIWAXS profiles of 100 nm PFO atop 100 nm Ag on VWR glass heat treated at 120° C for 30 minutes and quenched on a metal plate collected at incident angles ranging from 0.05° to 0.4°. Color available in electronic copy.

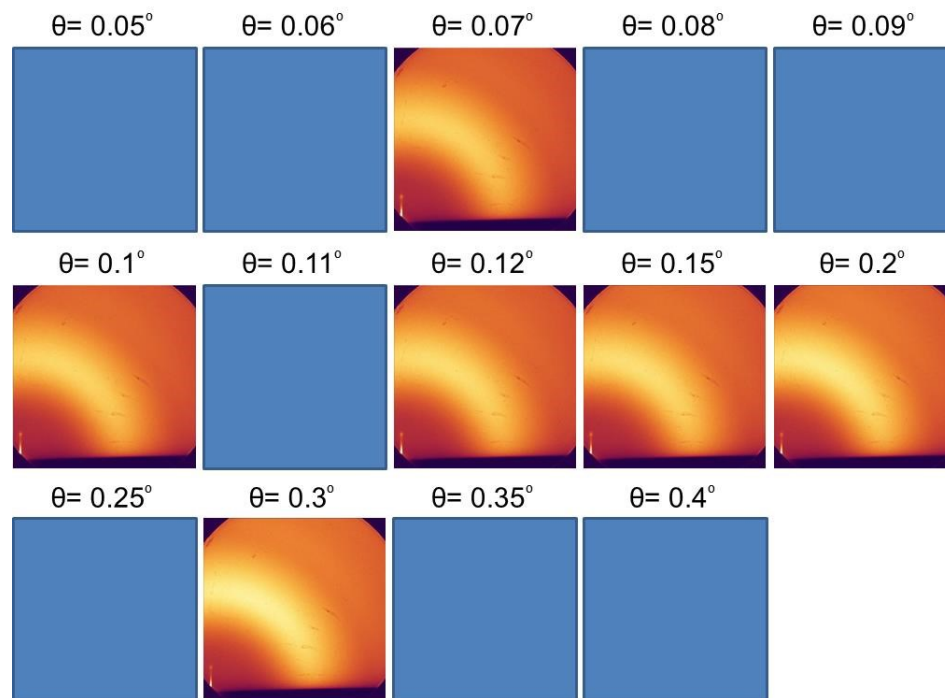


Figure AE7. GIWAXS profiles of 100 nm PFO on bare VWR glass heat treated at 180° C for 30 minutes and quenched on a metal plate collected at incident angles ranging from 0.05° to 0.4°. Color available in electronic copy.

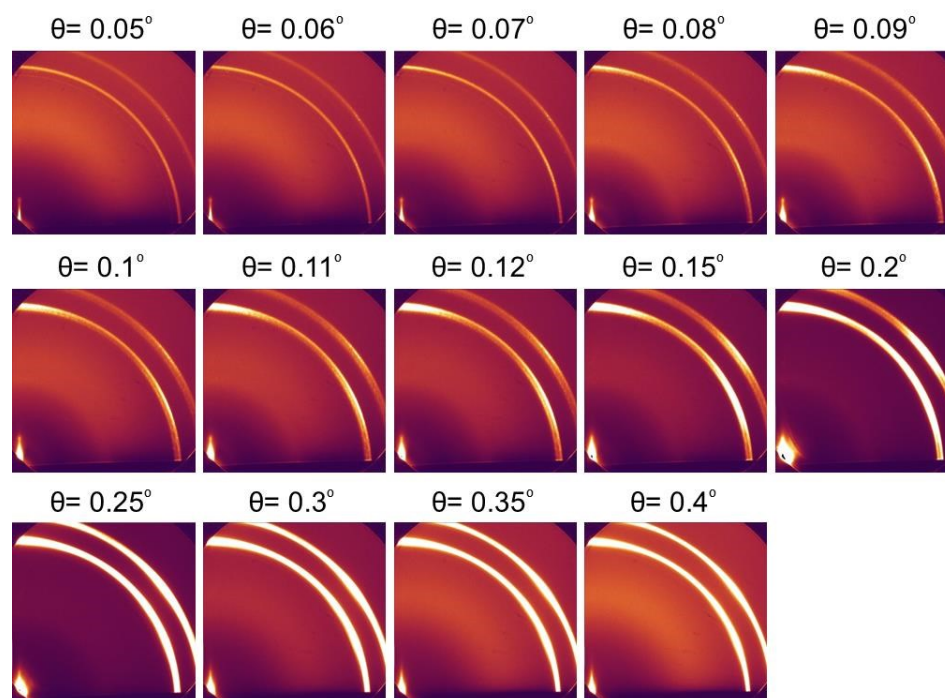


Figure AE8. GIWAXS profiles of 100 nm PFO atop 100 nm Ag on VWR glass heat treated at 180° C for 30 minutes and quenched on a metal plate collected at incident angles ranging from 0.05° to 0.4°. Color available in electronic copy.

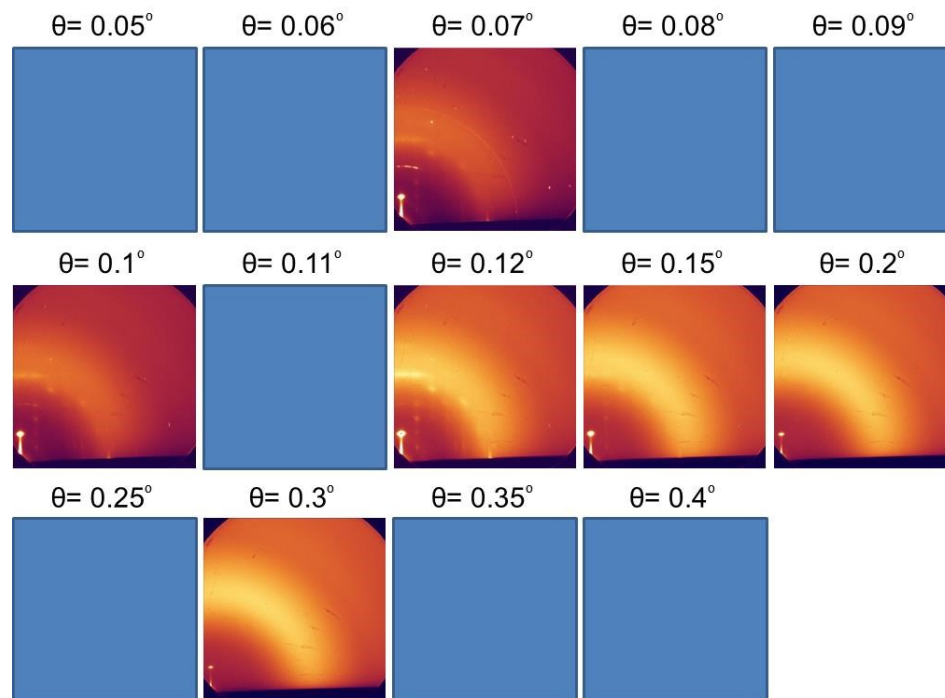


Figure AE9. GIWAXS profiles of 100 nm PFO on bare VWR glass heat treated at 200° C for 60 minutes and cooled on a glass plate collected at incident angles ranging from 0.05° to 0.4°. Color available in electronic copy.

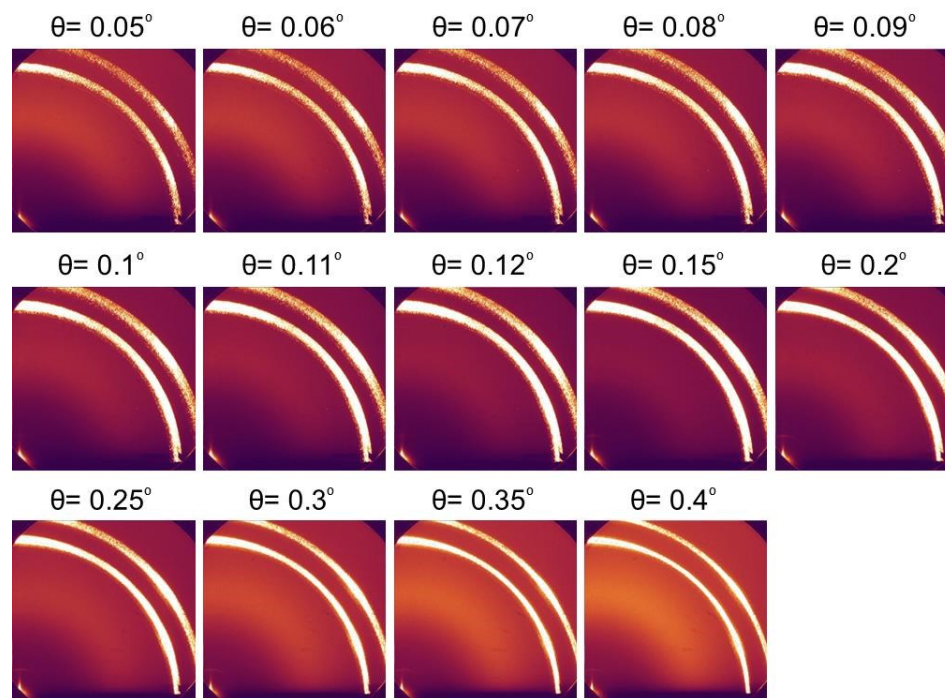


Figure AE10. GIWAXS profiles of 100 nm PFO atop 100 nm Ag on VWR glass heat treated at 200° C for 60 minutes and cooled on a glass plate collected at incident angles ranging from 0.05° to 0.4°. Color available in electronic copy.

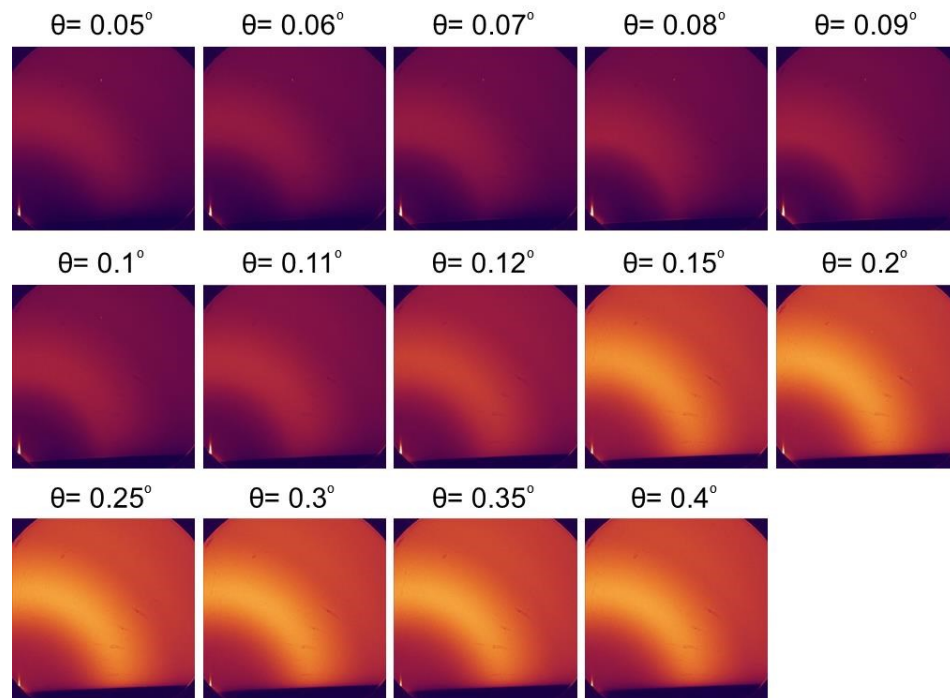


Figure AE11. GIWAXS profiles of 100 nm PFO on bare VWR glass heat treated at 280° C for 30 minutes and quenched on a metal plate collected at incident angles ranging from 0.05° to 0.4°. Color available in electronic copy.

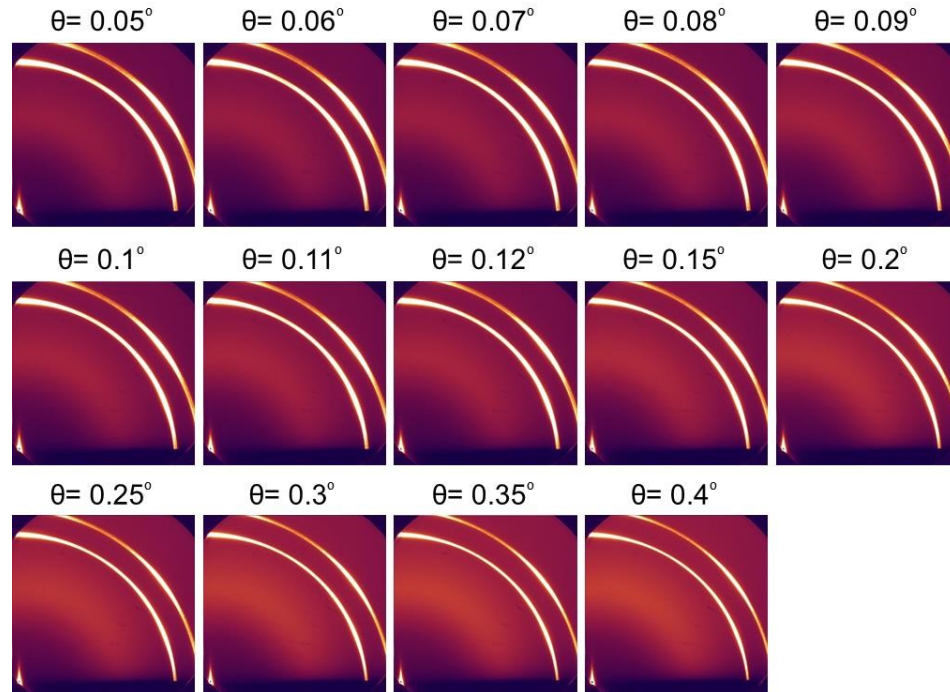


Figure AE12. GIWAXS profiles of 100 nm PFO atop 100 nm Ag on VWR glass heat treated at 280° C for 30 minutes and quenched on a metal plate collected at incident angles ranging from 0.05° to 0.4°. Color available in electronic copy.

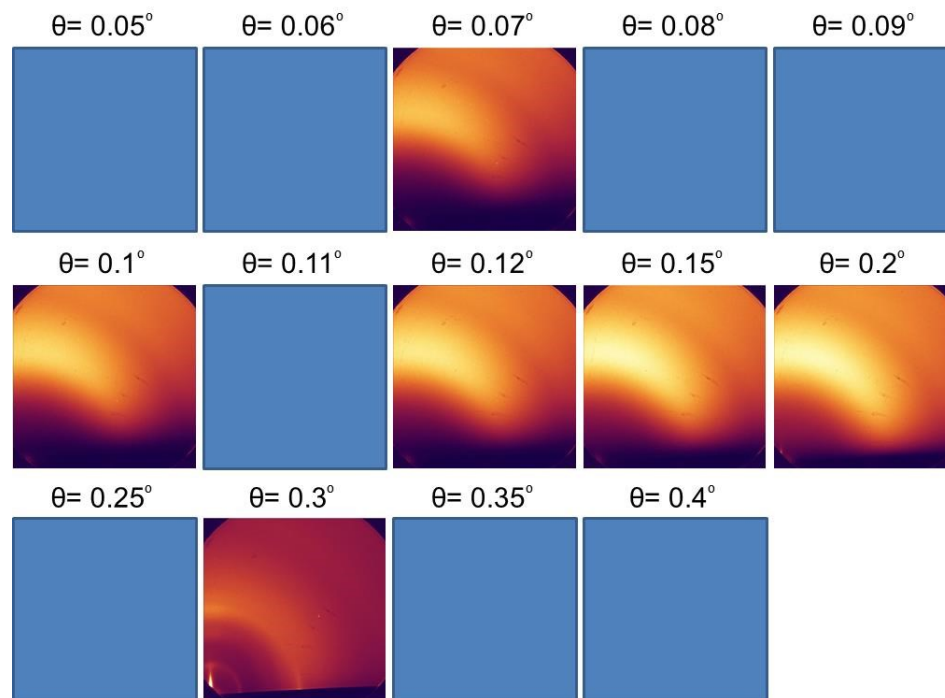


Figure AE13. GIWAXS profiles of 100 nm PFO on bare VWR glass vapor annealed in toluene vapor for 60 minutes collected at incident angles ranging from 0.05° to 0.4° . Color available in electronic copy.

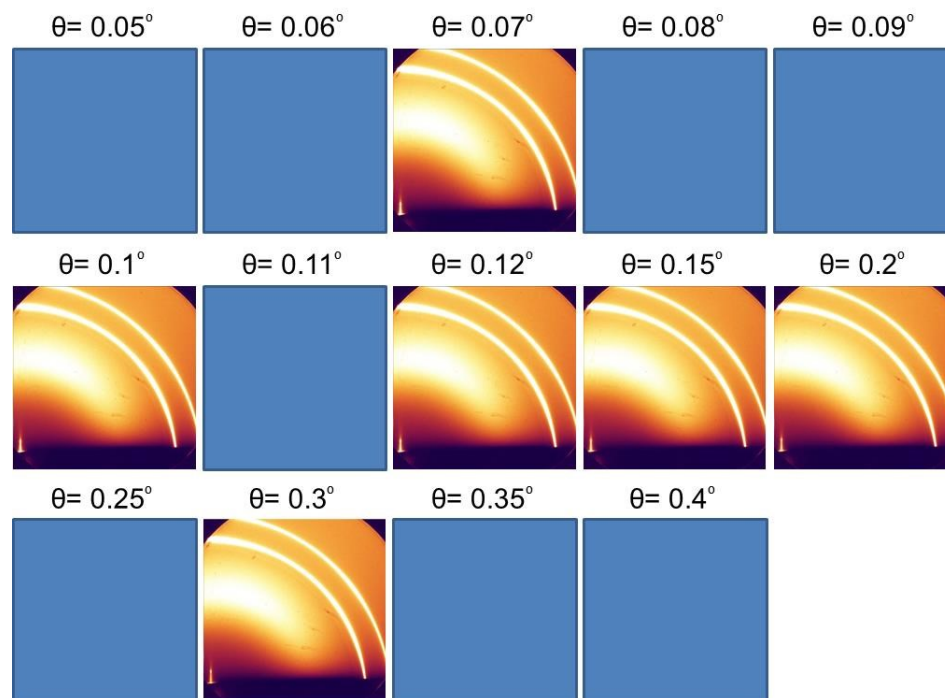


Figure AE14. GIWAXS profiles of 100 nm PFO atop 100 nm Ag on VWR glass vapor annealed in toluene vapor for 60 minutes collected at incident angles ranging from 0.05° to 0.4° . Color available in electronic copy.

Appendix F

F1. Polarized True Color Bright-field and Dark-field Images and Analysis of Single NW/NT Heterostructures Collected during Method Optimization

Presented in this section are multiple sets of true color bright-field/dark-field images and RGB pixel analyses of individual gold NW/NT heterostructures on silicon substrates that were collected as a function of incident polarization. These data were collected during the optimization of the polarized imaging method and provide the basis for how the technique was refined. The majority of these data were collected on “tube 1”, which was carefully characterized by FESEM analysis.

The first set of true color bright-field and dark-field polarized images presented in Fig. AF1 were taken by positioning the “tube 1” NW/NT heterostructure on the microscope stage parallel to the x-direction (see Fig. AF1) and varying both the excitation and collection polarizers (both polarized glass discs in phase WRT to each other) in 10° increments from Convention 1 (where the polarization is parallel to the y-direction, see Fig. AF1(a) and(b)) to Convention 2 (where the polarization is parallel to the x-direction, see Fig. AF1(c) and (d)) such that the polarization incident on the heterostructure is varied from perpendicular to the long axis of the structure (90°) to parallel to the long axis of the structure (0°). As noted in the methods section of this chapter, by rotating the polarizing discs instead of the sample, there is polarization bias introduced from the microscope optics from Convention 1 to 2 (see Figs AF1(a)-(d)), however these images were included for a more complete overview of the experimental work and still provides a qualitative understanding of the plasmonic response of the heterostructure as a function of incident polarization.

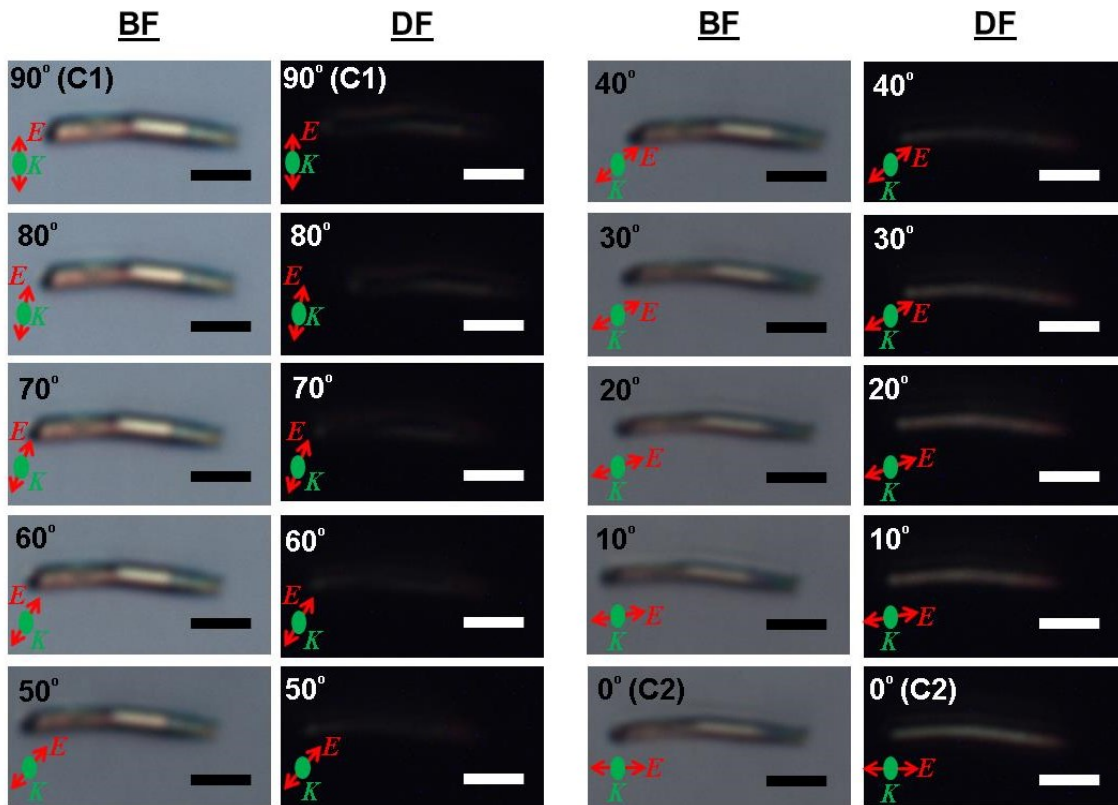


Figure AF1. True color bright-field and dark-field images of gold NW/NT heterostructure “tube 1” under in-phase excitation and collection polarization varied in 10° increments from 90° WRT to the long axis of the heterostructure (Condition 1) to 0° WRT to the long axis of the heterostructure. Inset in all images are schematics of the excitation direction and incident polarization, where \vec{k} denotes the excitation propagation direction and \vec{E} denotes polarization of the electric field. All scale bars = 200 μm . Color available in electronic copy.

Upon visual inspection of the polarized true color bright-field and dark-field images in Fig. AF1, it is evident from the dark-field image that as polarization is shifted from 0° to 90° WRT to the long axis of the heterostructure that the scattered light intensity diminishes and there is little scattered light emanating from center or core of the structure. Additionally, in the images approaching 90° polarization WRT to the long axis of the heterostructure, a shadow or halo is evident around the perimeter of the structure and the tapered tip (tube region). This suggests that as the polarization is varied, the modes couple more energy to the substrate. Additionally, the dark halo and transparency in the core of the heterostructure under polarization perpendicular to the long axis of the structure (90°) also suggests that there is increased mode coupling to the

substrate. In contrast, there is little visual evidence of change in the optical response of the heterostructure as a function of incident polarization from the true color bright-field images. However, it is evident that as the polarization is varied from C1 to C2 that the overall bright-field images, specifically the image backgrounds are not as bright. This is attributed to the polarization bias from the microscope optics, which reduces the signal throughput to the microscope CCD camera. Because of the incident polarization bias (and in-turn reduced signal throughput introduced by shifting the polarizing discs) and the fact that the dark-field images in Fig. AF1 were underexposed, the percentage of red, green, and blue pixels and grayscale intensity analysis were not conducted for this initial image set of “tube 1” shown in Fig. AF1.

An identical set of images was collected with the same method on a second gold NW/NT heterostructure termed “tube 2” (see Fig. AF2). A RGB and grayscale intensity analysis was conducted on the NT region of the dark-field images because the image quality was good and the analysis provided a solid qualitative trend in the optical response of the NT as a function of incident polarization. As in the previous set of images collected of “tube 1”, in this set of images, the gold NW/NT heterostructure was set parallel to the y-direction on the microscope stage (see Fig. 5.1 in Section 5.3.3) and both the excitation and collection polarization polarized glass discs were shifted (both in phase) from C1 to C2 (see Fig. 5.1 in Section 5.3.3) in 10 degree increments such that the incident polarization was varied from 0° to 90° WRT to the long axis of the nanowire/nanotube heterostructure. Additionally, these polarization measurements were repeated with the collection polarizer only and again with the excitation polarizer only. This aided in confirming that the origin of the observed shift intensity and RGB percentages came from the plasmonic response of the heterostructure, not the microscope bias or additional artifacts from the use of dual excitation and collection polarization. These measurements were also flawed because of polarization bias introduced by rotating the polarizers and the fact that the tube was not positioned perfectly parallel to the y-axis for the bright-field images.

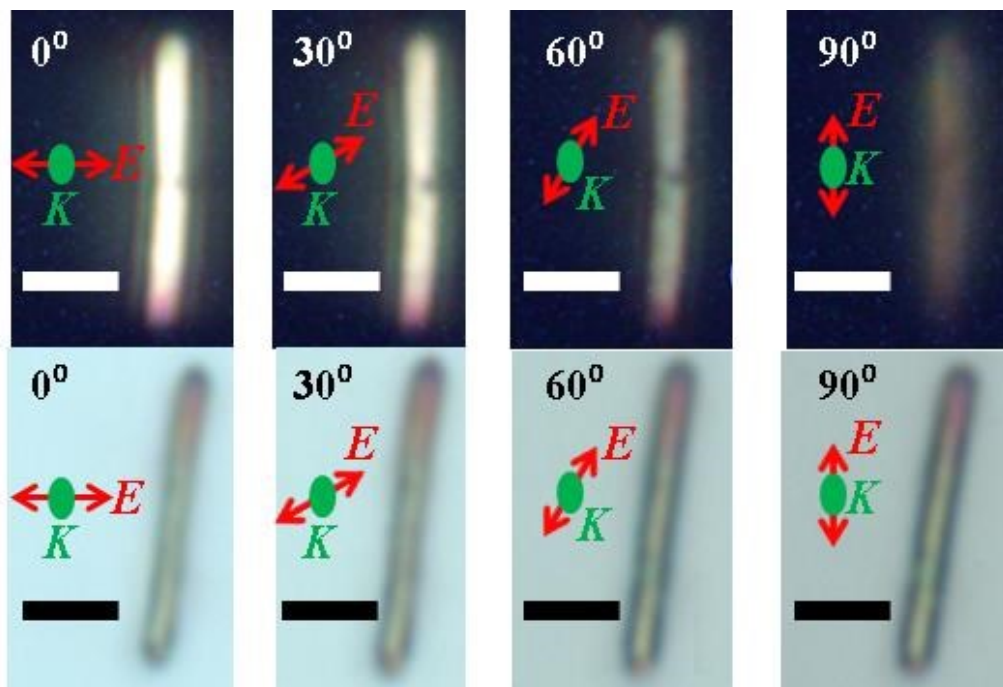


Figure AF2. True color bright-field and dark-field images of a gold NW/NT heterostructure “tube 2” under in-phase excitation and collection polarization varied in 10° increments from 90° WRT to the long axis of the heterostructure (Condition 1) to 0° WRT to the long axis of the heterostructure (images taken at 10° , 20° , 40° , 50° , 60° , and 70° polarization are not shown). Inset in all images are schematics of the excitation direction and polarization, where \vec{k} denotes the excitation propagation direction and \vec{E} denotes polarization of the electric field. All scale bars = $2\ \mu\text{m}$. Color available in electronic copy.

RGB and grayscale analysis (see Fig. AF3) conducted on the dark-field images tube region of the “tube 2” heterostructure shown in Fig. AF2 was conducted in accordance with the original procedure and large sampling area (see Methods Section 5.3.4). Again, as noted, this is not the optimal method polarization method and it is not the optimal RGB/grayscale analysis sampling method due to the fact that the large sampling area includes pixels at the perimeter or edge of the heterostructure. Nonetheless, a qualitative understanding of the optical response as a function of incident polarization was gleaned from this analysis.

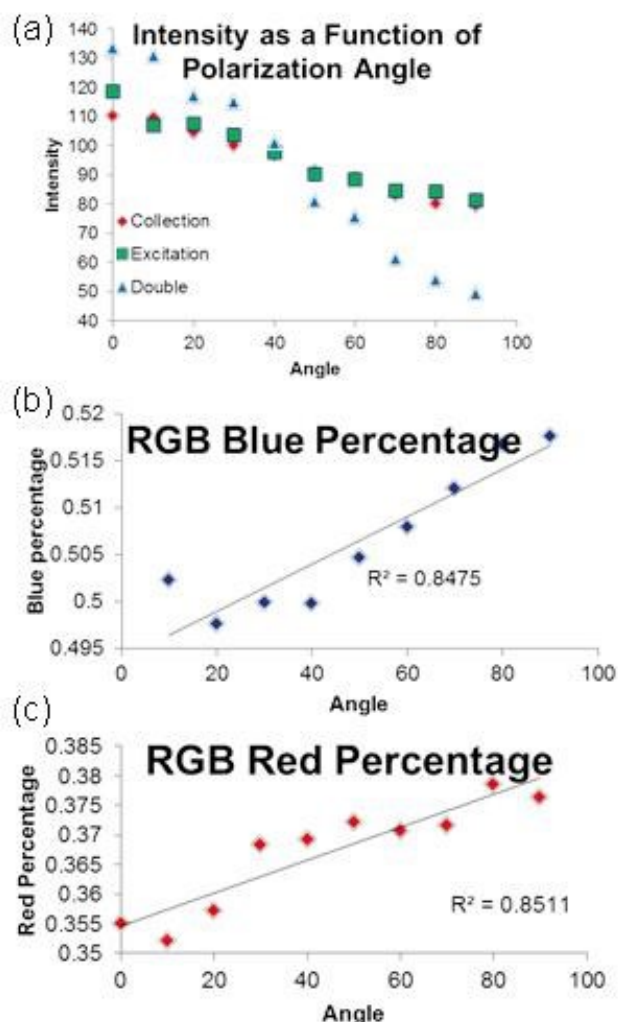


Figure AF3. (a) Grayscale intensity analysis of the dark-field images of the NT region of gold nanowire/nanotube heterostructure “tube 2” under (i) collection polarization only, (ii) excitation polarization only, and (iii) dual excitation and polarization from 0° to 90° WRT to the long axis of the heterostructure, (b) percentage blue and (c) percentage red pixels of the tube region of darkfield images under dual polarization from 0° to 90° WRT to the long axis of the heterostructure. Green pixel analysis (not shown) was inconclusive.

The grayscale analysis of the all three polarization conditions (under (i) collection polarization only, (ii) excitation polarization only, and (iii) dual excitation and polarization from 0° to 90° WRT to the long axis of the heterostructure) showed a decrease in intensity when polarization shifted from 0° to 90° (see Fig. AF3 (a)). This corroborates the visually observed change in the plasmonic response with incident polarization (see Figs AF1 and AF2), where the

tube and wire regions were scattering intensely under 0° polarization and became transparent as the polarization approached 90° . Additionally, the grayscale intensity analysis (see Fig. AF3(a)), under the three different polarization conditions showed the same trend regardless of the polarization condition thereby suggesting that the resultant change in intensity emanates from the nanostructure and not an artifact from the polarizers. However, it should be noted that the most significant change in intensity with change in polarization was observed for the dual excitation/collection polarization configuration. This is attributed to the fact that some of the intensity decrease may be masked by de-polarized light in the single polarization cases (where either the excitation or collection paths were polarized). It is for these reasons that the optimized measurements were collected with dual excitation and collection polarization.

The RGB analysis in Fig. AF3 shows an increase in the percentage of B and R pixels when polarization is shifted from 0° to 90° WRT to the long axis of the heterostructure. The analysis of G pixels showed an insignificant change with changes in polarization. When ascribing significance to the observed increase in R and B pixel percentages with changing polarization, it is important to note that the background of the image contains a significant percentage of B pixels (this is discussed in detail in section 5.4.2) and that the nanowire/nanotube heterostructure becomes more transparent when polarization is shifted from 0° to 90° . Therefore, it is believed that the increasing percentage of B pixels is largely due to the background and increased transparency of the heterostructure, not from changes in the optical response. In contrast, the percentage change in R pixels is significant and is attributed to the change in the optical response of the NW/NT heterostructure, suggesting that as the polarization approaches 90° , the structure supports lower energy, longer wavelength modes, in contrast to the higher energy modes supported along entire length of the structure under 0° polarization.

To further corroborate that the differences in the RGB and grayscale analysis of the polarized images in Figs. AF2 are due to a change in optical response from gold NW/NT

heterostructure and not from artifacts induced by the use of dual excitation/collection polarization or polarization bias, another set of bright-field and dark-field images of “tube 1” were collected with (i) no polarizers in the excitation or collection path (see Figs. AF4(a) and (b)), (ii) dual excitation and collection polarizers (see Figs. AF4 (c), (d), (g), and (h)), and (iii) and the collection polarizer only (see Figs. AF4(e), (f), (i), and (g)) at 0° and 90° WRT to the long axis of the heterostructure. For this set of images, a rectangular piece of polarized film was utilized for the collection polarizer to ensure minimal polarization bias with respect to the excitation polarizer (glass disc) (see Fig.5.1 in 5.3.3). Additionally, the collection polarizer was placed in the filter slot directly above the microscope objective instead atop the collection lens below the microscope CMOS CCD, which reduces alignment error with respect to the excitation polarizer (placed directly after the halogen light source) (see Fig.5.1 in 5.3.3). For these images, “Tube 1” was placed on the stage parallel to the x-direction and the polarization was set to either 0° or 90° by rotating the polarizers from C2 to C1 (see Fig.5.1 in 5.3.3 and Fig AF3).

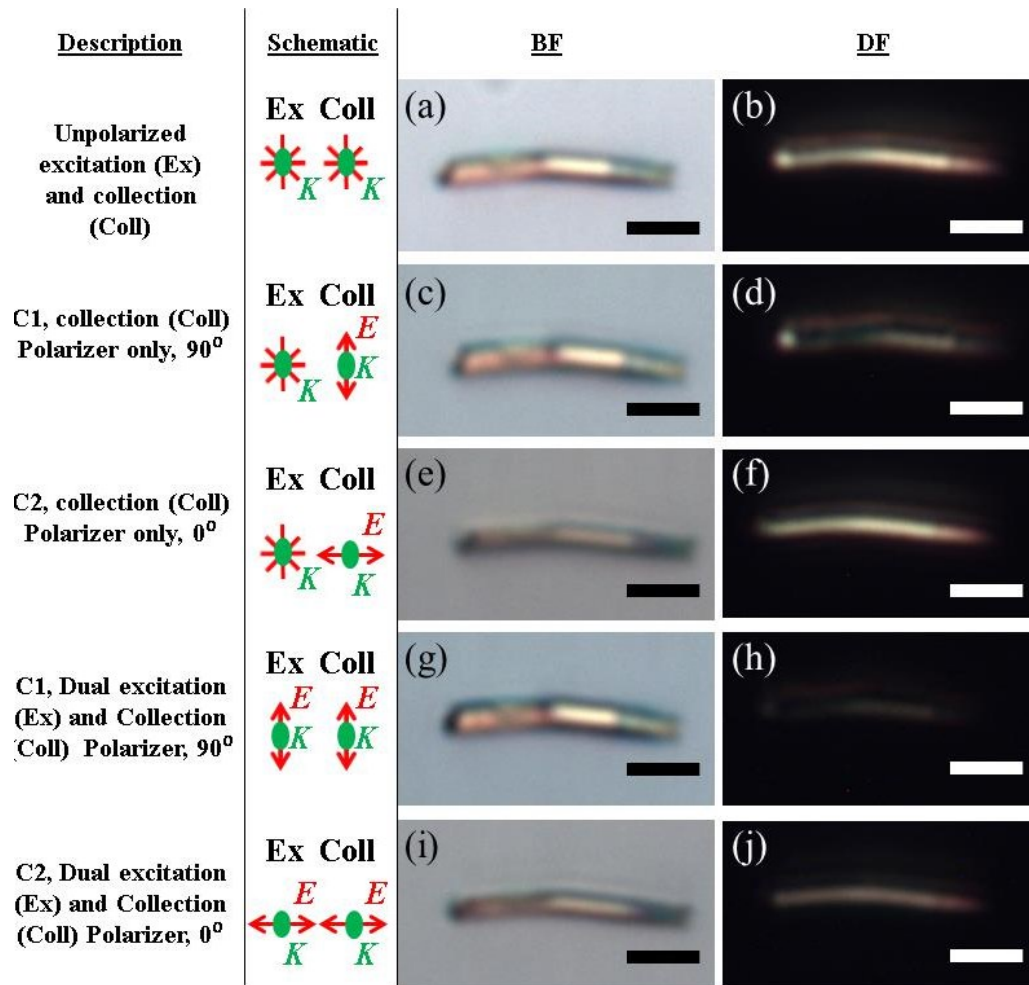


Figure AF4. True color bright-field (a,c,e,g,i) and dark-field (b,d,f,h,j) images of gold NW/NT heterostructure “tube 1” under (a,b) unpolarized excitation and collection, (c,d,g,h) polarized excitation and collection (dual), and (e,f,i,j) polarized collection only at 0° polarization (c-f) and 90° polarization (g-j) with respect to the long axis of the heterostructure. Beside all images are schematics of the excitation direction and polarization, where \vec{k} denotes the excitation propagation direction and \vec{E} denotes polarization of the electric field. All scale bars = 2 μm . Color available in electronic copy.

The bright-field images in Figure AF4 show the tube region is blue in color, the undamaged wire region is a bright golden yellow, and the cleaved/damaged wire region is red in color. The dark-field images in Figure AF4 show that under unpolarized excitation, the heterostructure scatters brightly along the entire length of the structure, with the tube region being bright red in color and the wire region is a golden yellow (see Figs. AF4 (a) and AF4 (b)). This

uniform scattering along the length of the structure is also observed in both the collection polarizer only and dual polarizer cases under 0° polarization. This suggests that the dominant mode under both unpolarized normal excitation and normal excitation with polarization parallel to the long axis of the structure (0°) are propagating modes, which are supported along the length of the structure. In contrast, under 90° polarization for both the collection polarizer only and dual polarizer cases, the heterostructure appears to be largely transparent, with a shadow or halo along the edges and a tube region that still scatters red light. This suggests that the dominant mode or modes under normal excitation with transverse 90° polarization couples to the substrate are much lower energy, characteristic of localized surface plasmon resonances. Most significantly, these polarized images show that the optical response is consistent under unpolarized excitation with only polarized collection and under both polarized excitation and collection (dual polarization). While it is evident that the intensity of the dual polarized images is less intense than those under collection polarization only, this is attributed to increased attenuation due to the second polarizer, which reduces the overall excitation source throughput.

F2. Polarized Dark-field Scattered-Light Single Nanostructure Spectroscopy of Single Gold NW/NT Heterostructures Collected during Method Optimization

The preliminary set of spectra was collected from “tube 2”, and the optimized set was taken on “tube 1”, which is presented in the Results and Discussion section of Chapter 5.” Spectra and corresponding images of “tube 2” captured with the spectrometer CCD were collected under: (i) unpolarized excitation and collection at 0° and 90° with respect to the x-direction of the microscope stage, (ii) polarized collection only at 0° and 90° WRT to the long axis of the structure in both polarization conditions 1 and 2, and (iii) dual excitation and collection polarization at 0° and 90° with respect to the long axis of the structure in both polarization conditions 1 (C1) and 2

(C2) (see Methods section titled “Polarized Dark-field Scattered-Light Single Nanostructure Spectroscopy of Single NW/NT heterostructures” for measurement details).

For all measurements described in the previous paragraph and Methods section titled “Polarized Dark-field Scattered-Light Single Nanostructure Spectroscopy of Individual NW/NT Heterostructures”), the entire “tube 2” heterostructure was imaged with the spectrometer CCD (with input aperture slits fully open) (see Fig. AF5(a)-(e) and Fig. AF5 (p)-(t)) to ensure that the image plane of the structure was clearly focused onto the spectrometer CCD. Additionally, prior the collection of each spectrum, an image of the region from which the spectrum was collected was captured using the narrowed 200 μm input slits used to collect the spectrum (see Fig. AF5(f)-(o) and Fig. AF5 (u)-(dd)). These images aided in ensuring that that the spectra were taken from same region and sampling volume as the structure is rotated on the microscope stage.

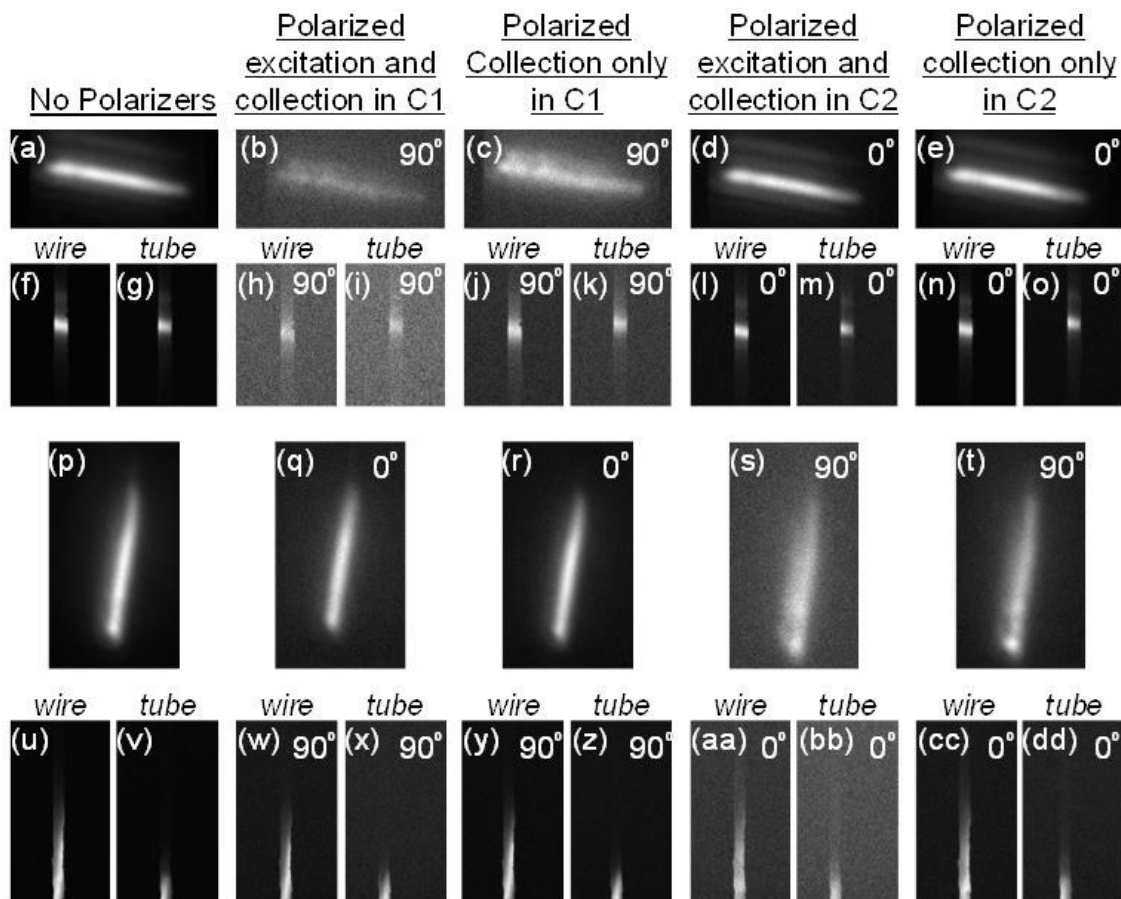


Figure AF5. Spectrometer CCD images of gold NW/NT heterostructure “tube 2” in full view (a-e, and p-t, of the nanowire (f,h,j,l,n,u,w,y,aa,cc) and nanotube (g,i,k,m,o,v,x,z,bb,dd) regions only (where spectra were collected) when the long axis of the structure was parallel (a-o) and perpendicular (p-dd) to the x-direction of the microscope stage under: (i) unpolarized excitation and collection (a,f,g,p,u,v), (ii) polarization in condition 1 (C1) with both excitation and collection polarization (b,h,i,q,w,x) and with collection polarization only (c,j,k,r,y,z) and (iii) polarization in condition 2 (C2) with both excitation and collection polarization (d,l,m,s,aa,bb) and with collection polarization only (e,n,o,t,cc,dd). Resultant polarization incident on the structure is denoted in the top right corner of each image.

From the images in Figure AF5 it is evident that as polarization is shifted from 0° to 90° WRT to the long axis of the heterostructure, the high energy mode(s) cease to be supported and the scattered light response is much less intense across the length of the structure. This is analogous to what is observed in the polarized true-color dark-field images taken with the

microscope CMOS CCD. Additionally, these images show the intrinsic problem with this measurement set, which is that the heterostructure is not situated perfectly parallel or perpendicular to the x-direction on the microscope stage and in-turn not being perfectly parallel or perpendicular on the spectrometer input slits (see Fig. AF5(a)-(o) and (p)-(t)). This results in the incident polarization not being truly parallel or perpendicular to the long axis of the heterostructure and more importantly, it results in different sampling volumes collected by the spectrometer when the structure is parallel (Fig. 15(a)-(o)) and perpendicular (Fig. 15(p)-(dd)) to the x-direction of the microscope stage.

The problem of collecting dissimilar sampling areas is less severe for the NT region than the NW region of the heterostructure, because only the tip of the structure is being analyzed, which was easier to accurately position within the slits of the spectrometer (regardless if the structure is parallel or perpendicular to the x-direction of the microscope stage) (see Fig. AF5(g,l,k,m,n,o,v,x,z,bb,dd)). Because the sampling volume and relative position of the nanotube remain roughly constant as the sample is rotated, it was valid to compare spectra taken of the tube region at varying incident polarization and in-turn make observations about the plasmonic response of the structure as a function of incident polarization. In contrast, when spectra are collected from the NW region at the center of the heterostructure (see Fig. AF5(f,h,j,l,n,u,w,y,aa,cc)) the sampling region was much larger when the structure was perpendicular to the x-direction of the microscope stage (see Fig. AF5(u,w,y,aa,cc)) than when it was parallel to the x-direction of the microscope stage (see Fig. AF5(f,h,j,l,n)). Due to the significant differences in sampling region and area, the spectra of the NW region were too dissimilar to make a valid assessment of the plasmonic response as a function of incident polarization.

The consequence of collecting spectra from dissimilar sampling regions is clearly illustrated by the unpolarized spectra of the nanowire region of the NW/NT heterostructure “tube

2'' collected when the long axis of the heterostructure was parallel (0°) and perpendicular (90°) to the x-direction of the microscope stage (see Fig. AF6). The spectrum of the wire region collected when the structure was parallel (0°) to the x-direction of the microscope stage exhibited a maximum at 638 nm, whereas the perpendicular (90°) case exhibited a red-shifted maximum at approximately 661 nm with much greater peak intensity. This confirms that there are significant differences in sampling area and volume of the spectra taken on the NW regions when the structure is parallel (0°) versus perpendicular (90°) to the x-direction of the microscope (as previously observed from the discussion of the images in Figure AF5(f,h,j,l,n,u,w,y,aa,cc)).

In contrast, the unpolarized spectra of the NT region taken when the structure is both parallel (0°) and perpendicular (90°) to the x-direction of the microscope stage exhibit an identical 635 nm peak resonance and only slightly different peak scattered light intensities. The difference in intensity may be due to differences in signal throughput from the microscope optics as the sample is rotated and perhaps a slightly different sampling area. This demonstrates that if the measurements are taken from a similar region, the plasmonic response should be identical in shape and regardless if the structure is parallel (0°) or perpendicular (90°) to the x-direction of the microscope stage. Thus, for the ensuing measurements presented in Figures AF7 and AF8, the plasmonic response of the NT region as a function of incident polarization may be considered reliable, but the plasmonic response of the NW region is biased by dissimilar sampling area under the two different incident polarizations (0° and 90°).

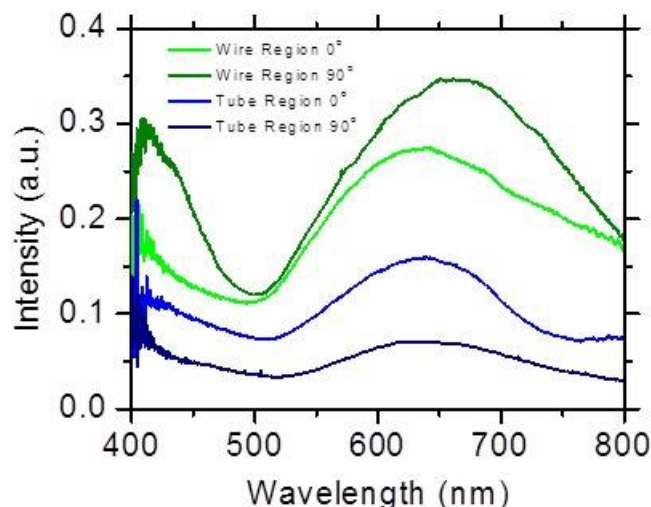


Figure AF6. Unpolarized dark-field scattered light spectra of the NW and NT regions of heterostructure “tube 2” when parallel (0°) and perpendicular (90°) WRT to the x-direction of the microscope stage. Color available in electronic copy.

Polarized dark-field scattered light spectra of the nanotube region of heterostructure “tube 1” were collected when the incident polarization was both 0° and 90° WRT to the long axis of the heterostructure with collection polarization only (shown in Figures AF7(a) and (b)) and with dual excitation and collection polarization (shown in Figure AF7(c) and (d)). Spectra were taken in both C1 (Fig AF7(a) and (c)) or C2 (Fig. AF7 (b) and (d)) polarization conventions to establish which resulted in the least amount of polarization bias and maximal throughput (see Fig. 1 and Methods section titled “Polarized Dark-field Scattered-Light Single Nanostructure Spectroscopy of Single AuNTs” for measurement details). Incident polarization was varied from 0° to 90° by physically rotating the sample such that it was either parallel or perpendicular to the x-direction of the microscope stage depending on the polarization condition (C1 or C2) the microscope was set in.

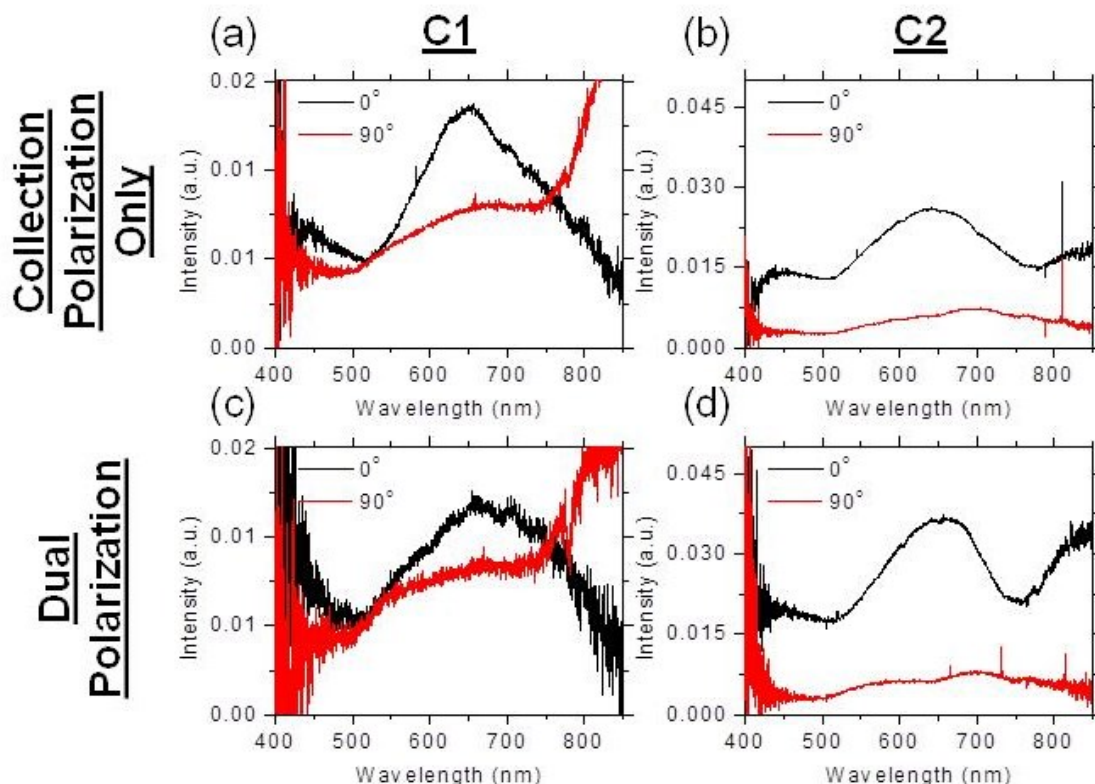


Figure AF7. Dark-field scattered light spectra of the tube region of gold nanowire/nanotube heterostructure “tube 2” under 0° and 90° incident polarization with: collection polarization only (a,b) and dual excitation and collection polarization (c,d) with polarization set in condition 1 (C1) (a,c) and polarization set in condition 2 (C2) (b,d). Color available in electronic copy.

The spectra of the NT region of the “tube 2” heterostructure show a uniform optical response in both conventions 1 (C1) and 2 (C2) with either single or dual polarization (see Fig. AF7). While the throughput is greater when the single collection polarizer is used, it indicates that an accurate assessment of the optical response was made as polarization was varied from 0° to 90° . This further confirms that the sampling area and volume was consistent as the sample was rotated on the microscope stage. At a 0° incident polarization, the maxima in the scattered light spectra of the NT region are: 650 nm in C1 and 645 nm in C2 for collection polarization only (see Fig. AF7(a,b)) and 654 nm in C1 and 652 nm in C2 for dual excitation and collection polarization (see Fig. AF7(c,d)). At a 90° incident polarization, the maxima in the scattered light spectra of the

NT region are: 684 nm in C1 and 692 nm in C2 for collection polarization only, and 677 nm in C1 and 694 nm in C2 for dual excitation and collection polarization. Thus, there is an overall red spectral shift in the NT region when incident polarization is shifted from 0° to 90° WRT to the long axis of the heterostructure. The magnitude of the red spectral shift when polarization is shifted from 0° to 90° is 34 nm for C1 and 52 nm for C2 with collection polarization only, and 23 nm for C1 and 45 nm for C2 for dual excitation and collection polarization. In conjunction with the red spectral at 90° incident polarization, the resultant scattered light spectra are significantly less intense, suggesting the absence of a higher energy propagating surface modes and only the presence of a lower-energy, longer wavelength resonant modes, which couple to the substrate more effectively.

As noted previously, the polarized spectra of the NW region of the “tube 2” heterostructure are likely to be unreliable due to the significant differences in the sampling region when the tube is parallel and perpendicular to the x-direction of the microscope stage. However, these data are summarized and shown in Figure AF8. At a 0° incident polarization, the maxima in the scattered light spectra of the wire region are: 704 nm in C1 and 710 nm in C2 for collection polarization only (see Fig. AF8(a,b)) and 744 nm in C1 and 702 nm in C2 for dual excitation and collection polarization (see Fig. AF8 (c,d)). At a 90° incident polarization, the maxima in the scattered light spectra of the NW region are: 625 nm in C1 and 704 nm in C2 for collection polarization only, and 621 nm in C1 and 681 nm in C2 for dual excitation and collection polarization. Thus, there is an overall blue spectral shift in the NW region when incident polarization is shifted from 0° to 90° WRT to the long axis of the heterostructure. The magnitude of the blue spectral shift when polarization is shifted from 0° to 90° is 79 nm for C1 and 6 nm for C2 with collection polarization only, and 123 nm for C1 and 21 nm for C2 for dual excitation and collection polarization. Similarly to the nanotube case, under 90° incident polarization, the resultant scattered light spectra of the nanowire region are significantly less intense. However, the

measured blueshift may indicate a higher order mode under 90° incident polarization, but due to the aforementioned issues with these spectra, it cannot be definitively confirmed.

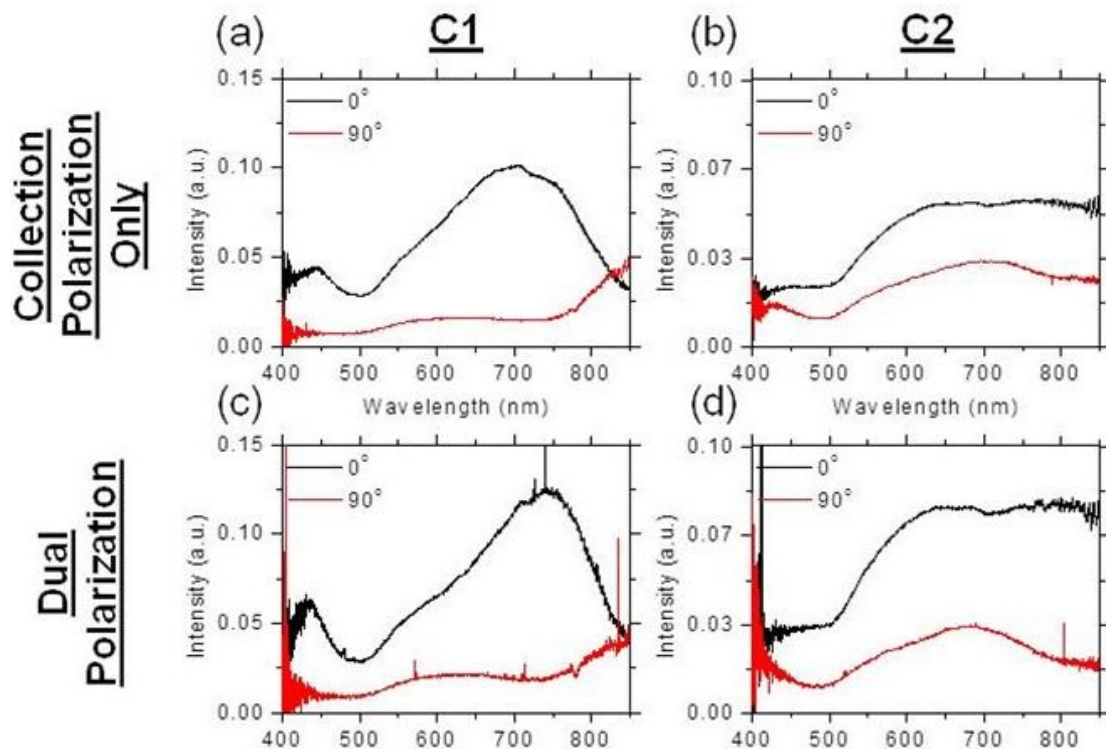


Figure AF8. Dark-field scattered light spectra of the NW region of gold NW/NT heterostructure “tube 2” under 0° and 90° incident polarization with: collection polarization only (a,b) and dual excitation and collection polarization (c,d) with polarization set in condition 1 (C1) (a,c) and polarization set in condition 2 (C2) (b,d). Color available in electronic copy.

In summary, the measurements from gold NW/NT heterostructure “tube 2” shows that when polarization is shifted from 0° to 90° WRT to the long axis of the heterostructure, the scattering response of both the NT and NW regions becomes less intense, suggesting the structure no longer supports higher energy propagating modes under 90° polarization. As the incident polarization is varied from 0° to 90° , the NT region red shifts by an average value of 38.5 nm and the NW region blueshifts by an average value of 57 nm from. These data suggests that under 90° polarization the NT region supports lower energy longer wavelength resonant modes and, the

wire region supports a higher energy resonant mode. These measurements also provide insight into how the optimized measurement techniques were developed and the important parameters for accurately measuring the plasmonic responses of the nanowire and nanotube regions of these heterostructures.

When comparing polarization condition (C1 and C2) and the merits of using single or dual polarization, it is evident that condition 2 (C2) has an overall higher throughput than condition 1 (C1) for both single and dual polarization (this is clearly evident in the spectra taken of the NT region (see Fig. AF5). This suggests that there is less polarization bias in C2 than C1, and in-turn C2 is the optimal polarization configuration to measure the plasmonic response of the gold nanowire/nanotube heterostructures with this experimental setup. When deciding whether to utilize single collection polarization only or dual excitation and collection polarization, there are pros and cons to both. The collection polarization only configuration has higher overall throughput than the dual polarization configuration because there is only one polarizer in the system that attenuates light. However, the majority of the spectra in Figures AF6 and AF7 under the dual polarization configuration exhibit much sharper spectral peaks than those with collection polarization only. This suggests that the optimized spectra should be collected with dual excitation and collection polarization so as to increase the accuracy of measuring the plasmonic response of the structure. Lastly, these measurements must be collected when the NW/NT heterostructure is truly parallel or perpendicular to the x-direction of the microscope stage and spectrometer input slits to ensure that the same region of the sample is analyzed when the structure is rotated on the microscope stage to vary the incident polarization.

Bibliography

1. A. De Luca, M. P. Grzelczk, I. Pastoriza-Santos, L. M. Liz-Marza, M. La deda, M. Striccoli, G. Strangi, "Dispersed and encapsulated gain medium in plasmonic nanoparticles : a multipronged approach to mitigate optical losses," *ACS Nano*, **5**, [7], 5823 (2011).
2. M. C. Gather, K. Meerholz, N. Danz, K. Leosson, "Net optical gain in a plasmonic waveguide embedded in a fluorescent polymer," *Nat. Photon.* **4**, 457 (2010).
3. B. J. Scholz, J. Frischeisen, A. Jager, D. S. Setz, T. C. G. Reusch, and W. Brütting, "Extraction of surface plasmons in light-emitting diodes via high-index coupling," *Opt. Express* **20**(S2), A205-A112 (2012).
4. L. H. Smith, J. A. E. Wasey, and W. L. Barnes, "Light outcoupling efficiency of top-emitting organic light-emitting diodes," *Appl. Phys. Lett.* **84**(16), 2986-2988 (2004).
5. S. Nowy, B. C. Krummacher, J. Frischeisen, N. A. Reinke, and W. Brütting, "Light extraction and optical loss mechanisms in organic light-emitting diodes: influence of the emitter quantum efficiency," *J. Appl. Phys.* **104**, 123109-123109-9 (2008).
6. B. Koo, S. Kim, and J-L. Lee, "Indium-tin-oxide free transparent electrodes using a plasmon frequency conversion layer," *J. Mater. Chem. C* **1**, 246-252 (2013).
7. M. Ariu, et al., *J. Phys.: Condens. Matter*, **14**, 9975-9986 (2002).
8. K. Asada, et al., *Jap. J. Appl. Phys.*, 2006, **45**, L247-L249. (2010).
9. F. C. Krebs, et al., *Nanoscale*, **2**, 873-886 (2010).
10. F. Hide, et al., *Sci.* **273**, 1833 (1996).
11. S. Moynihan, D. Iacopino, D. M. O'Carroll, H. Doyle, D. A. Tanner, G. Redmond, "Emission colour tuning in semiconducting polymer Nanotubes by energy transfer to organo-lanthanide dopants," *Adv. Mater.* **19**, 2474 (2007).
12. A. Polman, *Plasmonics applied*, *Science* **322**, 868 (2008).
13. E. Ozbay, "Plasmonics: Merging photonics and electronics at nanoscale dimensions," *Science* **311**, 189 (2006).
14. G. P. Agrawal, *Fiber-optic communication systems*, Wiley, New York, 2002.
15. I. P. Kaminow, T. Li, A. E. Willner, *P. Optical Fiber Telecommunications V B: Systems and Networks*, Academic press Elsevier, Burlington MA 2008.
16. W. Wei, C. M. Lieber, *Nat Mater*, **6** [11], 841, 2007.
17. T.W. Ebbesen, C. Genet, and S. I. Bozhevolnyi, "Surface plasmon circuitry," *Phys. Today* **61**, 44 (2008).
18. W. L. Barnes, A. Dereux, and T. W. Ebbesen, "Surface plasmon subwavelength optics," *Nature* **424**, 824 (2003).
19. <http://www.nanovip.com/page/2>
20. <http://www.fugal.comfiber.html>
21. S. Lal, S. Link, and N. J. Halas, "Nano-optics from sensing to waveguiding", *Nature Photon.* **1**, 641 (2007).
22. S. A. Maier, *Plasmonics: Fundamentals and applications*, Springer (2007).
23. H. J. Queisser, "Photovoltaic conversion at reduced dimensions," *Physica E: Low-dimensional Systems and Nanostructures* **14**, 1 (2002).
24. J. Bellessa, C. Bonnand, J. C. Plenet, J. Mugnier, "Strong coupling between surface plasmons and excitons in an organic semiconductor," *Phys. Rev. Lett.*, **93**, [3], 036404-1 (2004).
25. E. M. Purcell, "Spontaneous emission probabilities at radio frequencies," *Phys. Rev.* **69**, 681 (1946).
26. D.E. Chang, A. S. Sørensen, P. R. Hemmer, and M. D. Lukin, "Strong coupling of single emitters to surface plasmons," *Phys. Rev. B*, **76**, 035420 (2007).

27. A. N. Sudarkin and P. A. Demkovich, "Excitation of surface electromagnetic waves on the boundary of a metal with an amplifying medium," *Sov. Phys. Tech. Phys.* **34**, 764 (1989)
28. M. A. Noginov, G. Zhu, M. Bahoura, J. Adegoke, C. E. Small, B. A. Ritzo, V. P. Drachev and V. M. Shalaev, "Enhancement of surface plasmons in an Ag aggregate by optical gain in a dielectric medium," *Opt. Lett.* **31**, [20], 3022 (2006).
29. M. Ambati, S. H. Nam, E. Ulin-Avila, D. A. Genov, G. Bartal, and X. Zhang, "Observation of Stimulated Emission of Surface Plasmon Polaritons," *Nano Lett.* **8** [11], 3998 (2008).
30. I. De Lion, P. Berini, "Theory of surface plasmon-polariton amplification in planar structures incorporating dipolar gain media," *Phys. Rev. B*, **78**, 161401 (2008).
31. G. C. des Francs, P. Bramant, J. Grandidier, A. Bouhelier, J. -C. Weeber, and A. Dereux, "Optical gain, spontaneous and stimulated emission of surface plasmon polaritons in confined plasmonic waveguide," *Opt. Exp.*, **18**, [16], 16327 (2010).
32. I. D. W. Samuel, G. A. Turnbull, "Polymer lasers : recent advances," *Mater. Tod. Sept.*, 28 (2004).
33. F. Hide, M. A. Díaz-García, B. J. Schwartz, M. R. Andersson, Q. Pei, A. J. Heeger, "Semiconducting polymers: a new class of solid-state laser materials," *Sci.* **273**, 1833 (1996).
34. D. M. O'Carroll, I. Lieberwirth, G. Redmond, "Microcavity effects and optically pumped lasing in single conjugated polymer nanowires," *Nat. Nanotech.* **2**, 180 (2007).
35. D. M. O'Carroll, C. E. Petoukhoff, J. Kohl, B. Yu, C. M. Carter, and S. Goodman, "Conjugated polymer-based photonic nanostructures," *Polym. Chem.*, **4**, 5181 (2013).
36. H. Becker, H. Spreitzer, W. Kreuder, E. Kluge, H. Schenk, I. Parker, Y. Cao, "Soluble ppvs with enhanced performance-a mechanistic approach," *Adv. Mater.* **12**, 42 (2000).
37. X. Yang, and J. Loos, "Toward high-performance polymer solar cells: the importance of morphology control," *Macromolecules* **40**, 1353–1362 (2007).
38. G. Heliotis, E. Gu, C. Griffin, C. W. Jeon, P. N. Stravrinou, M. D. Dawson, D. D. C. Bradley, "Wavelength-tunable and white-light emission from polymer-converted micropixelated InGaN ultraviolet light-emitting diodes," *J. Opt. A*, **8**, 445 (2006).
39. K. H. An, M. Shtein, and K. P. Pipe, "Surface plasmon mediated energy transfer of electrically-pumped excitons," *Opt. Express* **18**(5), 4041-4048 (2010).
40. G. C. des Francs, P. Bramant, J. Grandidier, A. Bouhelier, J. -C. Weeber, and A. Dereux, "Optical gain, spontaneous and stimulated emission of surface plasmon polaritons in confined plasmonic waveguide," *Opt. Express* **18** (16), 16327-16334 (2010).
41. A. E. Ostfeld and D. Pacifici, "Plasmonic concentrators for enhanced light absorption in ultrathin film organic photovoltaics," *Appl. Phys. Lett.* **98**, 113112-113112-3, (2011).
42. S. Chénais and S. Forget, "Recent advances in solid-state organic lasers," *Polym. Int.* **61**, 390-406 (2011).
43. J. Frischeisen, D. Yokoyama, A. Endo, C. Adachi, and, W. Brütting, "Increased light outcoupling efficiency in dye-doped small molecule organic light-emitting diodes with horizontally oriented emitters," *Org. Electron.* **12**(5), 809-817 (2011).
44. L. H. Smith, J. A. E. Wasey, I. D. W. Samuel, and W. L. Barnes, "Light out-coupling efficiencies of organic light-emitting diode structures and the effect of photoluminescence quantum yield," *Adv. Funct. Mater.* **15**, 1839-1844 (2005).
45. E. Abbe, "Beiträge zur Theorie des Mikroskops und der mikroskopischen Wahrnehmung," *Archiv f. Mikroskop. Anat.* **9**, 413 (1873).
46. L. Novotny and B. Hecht, *Principles of Nano-Optics*, Cambridge University Press, (2006).
47. <http://en.wiktionary.org/wiki/evanesce>.

48. A. Ishimaru, *Electromagnetic Wave propagation, Radiation, and Scattering*, Prentice Hall, New Jersey (1991).
49. B. Oliver, "Assembly of hybrid photonic architectures from nanophotonic constituents," **480** [7376], 193 (2011).
50. J. Zenneck, "On the propagation of plane electromagnetic waves along a planar conductor surface and its relationship to wireless telegraphy," *Ann. Phys.* **23**, 848 (1907).
51. A. Sommerfeld, "On the propagation of waves in the wireless telegraphy," *Ann. Phys.* **28**, 665 (1909).
52. U. Fano, "The theory of anomalous diffraction gratings and of quasi-stationary waves on metallic surfaces (Sommerfeld's waves)," *J. Opt. Soc. Am.* **31**, 213 (1941).
53. R. W. Wood, "On a remarkable case of uneven distribution of light in a diffraction grating spectrum," *Phil. Mag.* **4**, 396 (1902).
54. S. Enoch and N. Bonod, "*Plasmonics*, Springer Series in Optical Sciences 167, 39 © Springer-Verlag Berlin Heidelberg (2012).
55. R. H. Ritchie, "Plasma losses by fast electrons in thin films," *Phys. Rev.* **106**, 874 (1957).
56. R. A. Ferrell, "Predicted radiation of plasma oscillations in metal films," *Phys. Rev.* **111**, 1214 (1958).
57. E. A. Stern, and R. A. Ferrell, "Surface plasma oscillations of a degenerate electron gas," *Phys. Rev.* **120**, 130 (1960).
58. C. J. Powell, J. L. Robins, and J. B. Swan, "Effects of contamination on the characteristic loss spectrum of tungsten," *Phys. Rev.* **110**, 657 (1958).
59. C. J. Powell, and J. B. Swan, "Origin of the characteristic electron energy losses in aluminum," *Phys. Rev.* **115**, 4 (1959).
60. C. J. Powell, "The origin of the characteristic electron energy losses in ten elements," *Proc. Phys. Soc. (London)* **76**, 593 (1960).
61. E. A. Stern and R. A. Ferrell, "Surface plasma oscillations of a degenerate electron gas," *Phys. Rev.*, **120**, 130 (1960).
62. C. J. Powell and J. B. Swan, "Origin of the characteristic electron energy losses in aluminum," *Phys. Rev.*, **115**, 869 (1959).
63. C. J. Powell and J. B. Swan, "Origin of the characteristic electron energy losses in magnesium," *Phys. Rev.*, **116**, 81 (1959).
64. C. J. Powell and J. B. Swan, "Effect of oxidation on the characteristic loss spectra of aluminium and magnesium," *Physical Review*, 18 (1960).
65. E. Burstein, W. P. Chen, Y. J. Chen, and A. Hartstein, "Surface polaritons - propagating electromagnetic modes at interfaces," *J. Vac. Sci. Technol.* **11**, 1004 (1974).
66. E. Kretschmann, and H. Raether, "Radiative decay of nonradiative surface plasmons excited by light," *Z. Naturforsch. Teil, A* **23**, 2135 (1968).
67. V. M. Shalaev, "Optical negative-index metamaterials," *Nat. Photon.* **1**, 41 (2007).
68. K. Kneipp, Y. Wang, H. Kneipp, L. T. Perelman, I. Itzkan, R. R. Dasari, and M. S. Feld, "Single molecule detection using surface-enhanced raman scattering (SERS)," *Phys. Rev. Lett.* **78**, 1667 (1997).
69. S. Nie, and S. R. Emory, "Probing single molecules and single nanoparticles by surface-enhanced raman scattering," *Science* **275**, 1102 (1997).
70. J. N. Anker, W. P. Hall, O. Lyandres, N. C. Shah, J. Zhao, and R. P. Van Duyne, "Biosensing with plasmonic nanosensors," *Nat. Mater.* **7**, 442 (2008).
71. W. L. Barnes, A. Dereux, and T. W. Ebbesen, "Surface plasmon subwavelength optics," *Nat.* **424**, 824 (1988).
72. R. Petit, editor, *Electromagnetic theory of gratings*, Springer-Verlag, Berlin, 1980.
73. C. Kittel, *Introduction to solid state physics*, Wiley, New York, 1996.
74. W.A. Benjamin, *Elementary Excitations in Solids*, New York (1964).

75. J. Babiskin and J.R. Anderson, *American Institute of Physics Handbook*, Eds., McGraw Hill. New York (1972).
76. R. E. Peierls, *Quantum Theory of Solids*, Oxford, London (1956).
77. E. D. Palik, *Handbook of Optical Constants of Solids*, Academic Press, Boston, 1985.
78. A. Vial, A.S Grimault, D Macías, D. Barchiesi, and M. L. de la Chapelle, "Improved analytical fit of gold dispersion: application to the modelling of extinction spectra with the FDTD method," *Phys. Rev. B* **71** (8), 085416 (2005).
79. H. A. Lorentz, *The Theory of Electrons*, New York, Dover, (1952).
80. M. A. Ordal, Robert J. Bell, R. W. Alexander, Jr, L. L. Long, and M. R. Querry, "Optical properties of fourteen metals in the infrared and far infrared: Al, Co, Cu, Au, Fe, Pb, Mo, Ni, Pd, Pt, Ag, Ti, V, and W," *App. Opt.*, **24** [24], 4493 (1985).
81. J. A. Dionne, L. A. Sweatlock, A. Polman, and H. A. Atwater, "Planar metal plasmon waveguides: frequency-dependent dispersion, propagation, localization, loss beyond the free electron model," *Phys. Rev. B* **72**, 075405 (2005).
82. F. A. Burton and S. A. Cassidy, "A complete description of the dispersion relation for thin metal film plasmon-polaritons," *J. Lightwave. Tech*, **8**, [12], 1843 (1990).
83. P. Ferguson, R. F. Wallis, M. Belakhovsky, J. P. Jadot, and J. Tomkinson, "Surface plasma waves in silver and gold," *Surface. Sci.* **76**, 483 (1978).
84. J. J. Burke and G. I. Stegeman, "Surface-polariton-like waves guided by thin, lossy metal films," **33**, [8], 5186 (1986).
85. H Raether, "Surface Plasmons on Smooth and Rough Surfaces and Gratings", Springer Tracts in Modern Physics, 111 (1988).
86. Interplay of physical structure and photophysics for a liquid crystalline polyfluorene Global Organic Electronic Market Analysis and Forecast 2011-2016, Transparency Market Research.
87. O. Worsfold, J. Hill, S. Y. Heriot, A. M. Fox, D. D. C. Bradley, T. H. Richardson, "Langmuir and langmuir-blodgett (LB) film properties of poly (9,9-dioctylfluorene)," *Mater. Sci. Eng., C* **23**, 541-544 (2003).
88. J. Teetsov, M. A. Fox, "Photophysical characterization of dilute solutions and ordered thin films of alkyl-substituted polyfluorenes," *J. Mater. Chem.* **9**, 2117-2122 (1999).
89. S. H. Chen, A. C. Su, C. H. Su, S. A. Chen, "Crystalline forms and emission behavior of poly(9,9-di-n-octyl-2,7-fluorene)," *Macromolecules* **38**, 379-385 (2005).
90. M. Grell, D. D. C. Bradley, G. Ungar, J. Hill, K. S. Whitehead, *Macromolecules* **32**, 5810-5817 (1999).
91. G. Helitos, D. D. C. Bradley, G. A. Turnbull and I. D. W. Samuel, "Light amplification and gain in polyfluorene waveguides", *Appl. Phys. Lett.* **81**, [3], 415 (2002).
92. F. Galbrecht, "Novel polyfluorene based copolymers for optoelectronic applications," Herstellung und Verlag: Books on Demand GbBH, Norderstedt, (2010).
93. D. O'Carroll, G. Redmond, " Polyfluorene Nanowire Active Waveguides as Sub-Wavelength Polarized Light Sources," *Physica E* **40** [7] 2468 (2008).
94. D. O'Carroll, D. Iacopino, A. O'Riordan, P. Lovera, É. O'Connor, G. A. O'Brien, G. Redmond, "Poly(9,9-dioctylfluorene) Nanowires with Pronounced Beta-Phase Morphology: Synthesis, Characterization and Optical Properties," *Adv. Mater.* **20**, [42] (2008).
95. D. Sarid, "Long-range surface-plasma waves on very thin metal films," *Phys. Rev. Lett.* **47**, 1927 (1981).
96. H. Raether, *Surface Plasmons*, Springer-Verlag, Berlin, (1988).
97. T. W. Ebbesen, H. J. Lezec, H. F. Ghaemi, T. Thio & P. A. Wolff, "Extraordinary optical transmission through sub-wavelength hole arrays," *Nat.*, **391**, 667 (1998).

98. J. N. Farahani, D. W. Pohl, H. J. Eisler, and B. Hecht, "Single quantum dot coupled to a scanning optical antenna: a tunable superemitter," *Phys. Rev. Lett.* **95**, [1], 017402 (2005).
99. P. Anger, P. Baharadwaj, and L. Nobotny, "Enhancement and quenching of single-molecule fluorescence," *Phys. Rev. Lett.*, 96, [11], 113002 (2006).
100. K. R. Catchpole, and A. Polman, "Plasmonic solar cells," *Opt. Express* **16**, [26], 21793–21800 (2008).
101. Y. Wang, T. Yang, M. T. Tuominen, and M. Achermann, "Radiative rate enhancements in ensembles of hybrid metal-semiconductor nanostructures," *Phys. Rev. Lett.* **102**, [16], 16300 (2009).
102. M. A. Noginov, G. Zhu, A. M. Belgrave, R. Bakker, V. M. Shalaev, E. E. Narimanov, S. Stout, E. Herz, T. Suteewong, and U. Wiesner, Demonstration of a spaser-based nanolaser, *Nature* **460**, [7259], 1110 (2009).
103. R. F. Oulton, V. J. Sorger, T. Zentgraf, R. M. Ma, C. Gladden, L. Dai, G. Bartal, and X. Zhang, "Plasmon lasers at deep subwavelength scale", *Nature* **461**, [7264], 629 (2009).
104. K. H. Drexhage, "Interaction of light with monomolecular dye layers," *Progress in Optics*, E. Wolf, ed., North-Holland, Amsterdam, (1974).
105. I. Gryczynski, J. Malicka, Z. Gryczynski, and J. R. Lakowicz, "Surface Plasmon-Coupled Emission with Gold Films," *J. Phys. Chem. B* **108**, [33], 12568 (2004).
106. I. Gryczynski, J. Malicka, W. Jiang, H. Fischer, W. C. W. Chan, Z. Gryczynski, W. Grudzinski, and J. R. Lakowicz, "Surface-plasmon-coupled emission of quantum dots," *J. Phys. Chem. B* **109**, [3], 1088 (2005).
107. W. L. Barnes, "Fluorescence near interfaces: the role of photonic mode density," *J. Mod. Opt.*, **45**, 661 (1998).
108. H. Morawitz and M. R. Philpott, "Coupling of an excited molecule to surface plasmons," *Phys. Rev. B* **10**, 4863 (1974).
109. C. F. Eagen, W. H. Weber, S. L. McCarthy, and R. W. Terhune, "Time dependent decay of molecular fluorescence," *Chem. Phys. Lett.* **75**, 274 (1980)
110. A. Neogi, T. Kuroda, A. Tackeuchi, and E. Yablonovitch, "Enhancement of spontaneous recombination rate in a quantum well by resonant surface plasmon coupling," *Phys. Rev. B*, **66**, 153305 (2002).
111. J. Vockovic, M. Loncar, and A. Scherer, "Surface plasmon enhanced light-emitting diode," *IEEE J. Quantum Electron.* **36**, [10], 1131 (2000).
112. F. Gan, *Laser Materials*, World Scientific, Singapore, 324 (1975).
113. J. Zhu, *Mat. Sci. Eng. A.* 454-455, 685 (2007).
114. A. Murphy and R. J. Pollard, 3rd International Congress on Advanced Electromagnetic Materials in Microwaves and Optics, London, 2009 (unpublished).
115. A. Murphy, J. McPhillips, W. Hendren, C. McClatchey, R. Atkinson, G. Wurtz, A. V. Zayats, and R. Pollard, *Nanotech.* **22**, 045705 (2011).
116. B. Apter, O. Guilatt, and U. Efron, *Appl. Opt.* **50**, 5457 (2011).
117. G. I. Stegeman, J. J. Burke, and D. G. Hall, "Surface-polaritonlike waves guided by thin, lossy metal films," *Opt. Lett.*, **8**(7), 383-385 (1983).
118. F. Yang, J. R. Sambles, and G. W. Bradberry, "Long-range surface modes supported by thin films," *Phys. Rev. B* **44**(11), 5855-5872 (1991).
119. M. N. Zervas, "Surface plasmon-polariton waves guided by thin metal films," *Opt. Lett.* **16**(10), 720-722 (1991).
120. M. Campoy-Quiles, G. Heliotis, R. Xia, M. Ariu, M. Pintani, P. Etchegoin, and D. D. C. Bradley, "Ellipsometric characterization of the optical constants of polyfluorene gain media," *Adv. Funct. Mater.* **15**(6), 925-933 (2005).
121. The value of the phase of the first oscillator term is misprinted in [21]. Donal D. C. Bradley, Director of the Centre for Plastic Electronics, Lee-Lucas Professor of

- Experimental Physics, Imperial College London, South Kensington Campus, London SW7 2AZ, UK provided the correct value of -0.981 (personal communication in 2012).
122. G. Heliotis and D. D. C. Bradley, M. Goossens, S. Richardson, G. A. Turnbull, and I. D. W. Samuel, "Operating characteristics of a travelling-wave semiconducting polymer optical amplifier," *Appl. Phys. Lett.* **85**(25), 6122-6124 (2004).
 123. R. Xia, M. Campoy-Quiles, G. Heliotis, P. Stavrinou, K. S. Whitehead, and D. D.C. Bradley, "Significant improvements in the optical gain properties of oriented liquid crystalline conjugated polymer films," *Synth. Met.* **155**(2), 274-278 (2005).
 124. N. Liu, A. Ruseckas, N. A. Montgomery, I. D. W. Samuel, and G. A. Turnbull, "Semiconducting polymer waveguides for end-fired ultra-fast optical amplifiers," *Opt. Express* **17**(24), 21452-21458 (2009).
 125. M. P. Nezhad, K. Tetz, and Y. Fainman, "Gain assisted propagation of surface plasmon polaritons on planar metallic waveguides," *Opt. Express* **12**(17), 4072-4079 (2004).
 126. E. Kretschmann, "Decay of non radiative surface plasmons into light on rough silver films. Comparison of experimental and theoretical results," *Opt. Commun.* **6**(2), 185187 (1972).
 127. A. Kolomenski, A. Kolomenskii, J. Noel, S. Peng, H. Schuessler, "Propagation length of surface plasmons in a metal film with roughness," *Appl. Opt.* **48**(30), 5683-5691 (2009).
 128. D. L. Mills, "Attenuation of surface polaritons by surface roughness," *Phys. Rev. B* **12**(10), 4036-4046 (1975).
 129. W. L. Barnes, "Fluorescence near interfaces: the role of photonic mode density," *J. Mod. Optic* **45**(4), 661-669 (1998).
 130. J. Kohl, J. Pantina, D. M. O'Carroll, "Enhancing surface plasmon leakage at the metal/semiconductor interface: towards increased light outcoupling efficiency in organic optoelectronics," *Opt. Express*, **22** [7], 7644-7656 (2014).
 131. S. H. Chen, A. C. Su, S. A. Chen, "Noncrystalline Phases in Poly(9,9-di-*n*-octyl-2,7-fluorene)," *J. Phys. Chem. B*, **109**, 10067 (2005).
 132. L. Yang, "Using an in-vacuum CCD detector for simultaneous small- and wide- angle scattering at beamline X9," *J. Synchrotron Rad.* **20**, 211-218 (2013).
 133. M. Allaire, L. Yang, "Biomolecular solution X-ray scattering at the National Synchrotron Light Source," *J. Synchrotron Rad.* **18**, 41-44, (2011).
 134. <http://www.bnl.gov/ps/x9/software/view.asp>
 135. <http://www.bnl.gov/ps/x9/software/view-gtk.pdf>.
 136. M. D. Foster, "X-ray scattering methods for the study of polymer interfaces," *Critical Reviews in Analytical Chemistry*, **24** (3), 179-241(1993).
 137. W. Bras, A. J. Ryan, "Sample environments and techniques combined with small angle X-ray scattering. *Advances in Colloid and Interface Science* **75**, 1-43 (1998).
 138. R. J. Kline, M. D. McGehee, M. F. Toney, "Highly oriented crystals at the buried interface in polythiophene thin-film transistors," *Nature Mater.* **5**, 222-228 (2006).
 139. O. Glatter O, Kratky *Small Angle X-ray Scattering*, Academic Press. (1982).
 140. S.G. Podorov, A. Nazarkin, "*Wide-Angle X-Ray Diffraction Theory versus Classical Dynamical Theory*," *Recent Res. Devel. Optics*, **7**(2009).
 141. M. Ariu, D. G. Lidzey, D. D. C. Bradley, "Influence of film morphology on the vibrational spectra of dioctyl substituted polyfluorene (PFO)," *Synth. Met.* **111**, 607 (2000).
 142. E. Prodan and P. Norlander, *Nano Lett.* **3**, 543 (2003). J. McPhillips, A. Murphy, M. P. Jonsson, W. R. Hendren, R. Atkison, F. Höök, A. W. Zayats, and R. J. Pollard, *ACS Nano* **4**, 2210 (2010).
 143. S. J. Oldenburg, S. K. Westcott, R. D. Averitt, and N. J. Halas, *J. Chem. Phys.* **111**, 4729 (1999).
 144. Y. Sun, B. Mayers, and Y. Xia, *Adv. Mater.* **15**, 641 (2003).

145. H. W. Liang, S. C. Ruan, M. Zhang, H. Su, and I. L. Li, *Laser Phys.*, **23**, 125001 (2013).
146. C. E. Rayford II, G. Schatz, and K. Shuford, *Nanoscape* **2**, 27 (2005).
147. W. Zhang, S. H. Brongersma, O. Richard, B. Brijs, R. Palmans, L. Froyen, and K. Maex, *Microelectron. Eng.* **76**, 146 (2004).
148. R. D. Averitt, D. Sarkar, and N. J. Halas, *Phys. Rev. Lett.* **78**, 4217 (1997).
149. E. Prodan, C. Radloff, N. J. Halas, and P. Norlander, *Science* **302**, 419 (2003).
150. A. Moradi, *J. Phys. Chem. Solids* **69**, 2936 (2008).
151. A. Moradi, *Physica B* **405**, 2466 (2010).
152. J. J. Ju, S. Park, M. Kim, J. T. Kim, S. K. Park, Y. J. Park, and M. H. Lee, *J. Lightwave Technol.* **26**, 0733 (2008).
153. A. Boltasseva, T. Nikolajsen, K. Leosson, K. Kjaer, M. S. Larsen, and S. I. Bozhevolnyi, *J. Lightwave Technol.* **23**, 413 (2005).
154. R. Charbonneau, C. Scales, I. Breukelaar, S. Fafard, N. Lahoud, G. Mattiussi, and P. Berini, *J. Lightwave Technol.* **24**, 477 (2006).
155. R. Charbonneau, N. Lahoud, G. Mattiussi, and P. Berini, *Opt. Exp.* **13**, 977 (2005).
156. S. I. Bozhevolnyi, V. S. Volkov, E. Devaux, J. Laluet, and T. W. Ebbesen, *Nature* **440**, 508 (2006).
157. A. Boltasseva and S. I. Bozhevolnyi, *IEEE J. Sel. Topic. Quantum Electron.* **12**, 1233 (2006).
158. Z. Han, L. Liu, and E. Forsberg, *Opt. Commun.* **259**, 690 (2006).
159. S. Park and S. H. Song, *Electron. Lett.* **42**, 402 (2006).
160. T. Nikolajsen, K. Leosson, and S. I. Bozhevolnyi, *Appl. Phys. Lett.* **88**, 5833 (2004).
161. S. J. Oldenburg, R. D. Averitt, S. L. Westcott, and N. J. Halas, *Chem. Phys. Lett.* **288**, 243 (1998).
162. R. D. Averitt, S. L. Westcott, and N. J. Halas, *J. Opt. Soc. Am. B* **16**, 1824 (1999).
163. A. Moradi, *Opt. Commun.* **282**, 3368 (2009).
164. A. O. Pinchuck and G. C. Schatz, *Mater. Sci. Eng. B* **149**, 251 (2008).
165. Y. H. Ye, Y. W. Jiang, M. W. Tsai, Y. T. Chang, C. Y. Chen, D. C. Tzuang, Y. T. Wu, and S. C. Lee, *Appl. Phys. Lett.* **93**, 263106 (2008).
166. R. Perahia, T. P. Mayer Alegre, A. H. Safavi-Naeini, and O. Painter, *Appl. Phys. Lett.* **95**, 201114 (2009).
167. R. Zia, M. D. Selker, P. B. Catrysse, and M. L. Brongersma, *J. Opt. Soc. Am. A* **21**, 2442 (2004).
168. J. Aizpurua, P. Hanarp, D. S. Sutherland, M. Käll, G. W. Bryant, and F. J. García de Abajo, *Phys. Rev. Lett.* **90**, 057401-1 (2003).
169. T. B. Wang, X. W. Wen, C. P. Yin, and H. Z. Wang, *Opt. Express* **17**, 24096 (2009).
170. A. Pors, M. Willatzen, O. Albrektsen, and S. I. Bozhevolnyi, *J. Opt. Soc. Am. B* **27**, 1680 (2010).
171. J. Kohl, M. Fireman, D. M. O'Carroll, "Surface plasmon and photonic mode propagation in gold nanotubes with varying wall thickness," *Phys. Rev. B* **84**, 235118 (2011).
172. J. McPhillips, A. Murphy, M. P. Jonsson, W. R. Hendren, R. Atkison, F. Höök, A. W. Zayats, and R. J. Pollard, *ACS Nano* **4**, 2210 (2010).
173. <http://rsb.info.nih.gov/ij/download.htm>.
174. P. W. Milonni, J. H. Eberly, *Lasers*, John Wiley & Sons, New York, 1988.
175. O. Svelto, D. C. Hanna, *Principles of Lasers*, Plenum Press, New York, 1998.
176. J. H. Park, and A. J. Steckl, "Laser action in Eu-doped GaN thin-film, cavity at room temperature," *Appl. Phys. Lett.* **85**, [20], 4588 (2004).
177. M. D. McGehee, R. Gupta, S. Veenstra, E. K. Miller, M. A. Díaz-García and A. J. Heeger, "Amplified spontaneous emission from photopumped films of a conjugated polymer," *Phys. Rev. B* **58**, [11], 7035 (1998).

178. L. Dal Negro, P. Bettotti, M. Cazzanelli, D. Pacifici, and L. Pavesi, "Applicability conditions and experimental analysis of the variable stripe length method for gain measurements," *Opt. Comm.* 229, 337 (2004).